
Simultaneous Inversion of Receiver Functions, Multi- Mode Dispersion, and Travel-Time Tomography for Lithospheric Structure Beneath the Middle East and North Africa

**Charles J. Ammon
Minoo Kosarian
Robert B. Hermann**

**Saint Louis University
Office of Research Services
3634 Lindell Blvd.
Saint Louis, MO 63108-3342**

Final Report

1 February 2006

APPROVED FOR PUBLIC RELEASE; DISTRIBUTION UNLIMITED.



**AIR FORCE RESEARCH LABORATORY
Space Vehicles Directorate
29 Randolph Road
AIR FORCE MATERIEL COMMAND
Hanscom AFB, MA 01731-3010**

This technical report has been reviewed and is approved for publication.

AFRL-VS-HA-TR-2006-1047

/signed/

ROBERT RAISTRICK
Contract Manager

/signed/

ROBERT BELAND, Chief
Battlespace Surveillance Innovation Center

This report has been reviewed by the ESC Public Affairs Office (PA) and is releasable to the National Technical Information Service (NTIS).

Qualified requestors may obtain additional copies from the Defense Technical Information Center (DTIC). All others should apply to the National Technical Information Service.

If your address has changed, if you wish to be removed from the mailing list, or if the addressee is no longer employed by your organization, please notify AFRL/VSIM, 29 Randolph Rd., Hanscom AFB, MA 01731-3010. This will assist us in maintaining a current mailing list.

Do not return copies of this report unless contractual obligations or notices on a specific document require that it be returned.

Using Government drawings, specifications, or other data included in this document for any purpose other than Government procurement does not in any way obligate the U.S. Government. The fact that the Government formulated or supplied the drawings, specifications, or other data does not license the holder or any other person or corporation; or convey any rights or permission to manufacture, use, or sell any patented invention that may relate to them.

This report is published in the interest of scientific and technical information exchange and its publication does not constitute the Government's approval or disapproval of its ideas or findings.

REPORT DOCUMENTATION PAGE

*Form Approved
OMB No. 0704-0188*

Public reporting burden for this collection of information is estimated to average 1 hour per response, including the time for reviewing instructions, searching existing data sources, gathering and maintaining the data needed, and completing and reviewing this collection of information. Send comments regarding this burden estimate or any other aspect of this collection of information, including suggestions for reducing this burden to Department of Defense, Washington Headquarters Services, Directorate for Information Operations and Reports (0704-0188), 1215 Jefferson Davis Highway, Suite 1204, Arlington, VA 22202-4302. Respondents should be aware that notwithstanding any other provision of law, no person shall be subject to any penalty for failing to comply with a collection of information if it does not display a currently valid OMB control number. PLEASE DO NOT RETURN YOUR FORM TO THE ABOVE ADDRESS.

1. REPORT DATE (DD-MM-YYYY) 01-02-2006		2. REPORT TYPE Final Report		3. DATES COVERED (From - To) 1 May 2002 - 31 Jan 2006	
4. TITLE AND SUBTITLE Simultaneous Inversion of Receiver Functions, Multi-Mode Dispersion, and Travel-Time Tomography for Lithospheric Structure Beneath the Middle East and North Africa		5a. CONTRACT NUMBER DTRA01-02-C-0038			
		5b. GRANT NUMBER			
		5c. PROGRAM ELEMENT NUMBER S49012			
		5d. PROJECT NUMBER DTRA			
6. AUTHOR(S) Charles J. Ammon*, Minoo Kosarian* and Robert B. Hermann**		5e. TASK NUMBER OT			
		5f. WORK UNIT NUMBER A1			
				8. PERFORMING ORGANIZATION REPORT NUMBER	
7. PERFORMING ORGANIZATION NAME(S) AND ADDRESS(ES) St. Louis University Office of Research Services 3634 Lindell Blvd. Saint Louis, MO 63108-3342		9. SPONSORING / MONITORING AGENCY NAME(S) AND ADDRESS(ES) Air Force Research Laboratory 29 Randolph Road Hanscom AFB, MA 01731-3010		10. SPONSOR/MONITOR'S ACRONYM(S) AFRL/VSBYE	
				11. SPONSOR/MONITOR'S REPORT NUMBER(S) AFRL-VS-HA-TR-2006-1047	
12. DISTRIBUTION / AVAILABILITY STATEMENT Approved for Public Release; Distribution Unlimited.					
¹ Penn State University ² Saint Louis University		³ Lawrence Livermore National Laboratory ⁴ Los Alamos National Laboratory			
13. SUPPLEMENTARY NOTES [*] Penn State University ^{**} Saint Louis University					
14. ABSTRACT <p>An important component to understanding the evolution of the continental lithosphere is to improve our knowledge on lower continental composition. Contribution towards this goal, we perform receiver function analysis using teleseismic waveforms recorded at permanent and temporary broadband seismic station located in Middle East, Europe, Asia, and North Africa. Two hundred and twenty six stations recording a total of about 6,000 teleseismic events producing more than 100,000 seismograms have been investigated. The distribution includes 72 stations in the Middle East, 57 stations in Europe, 60 stations in Asia, and 37 stations in central and north Africa. We have examined receiver functions for 213 of stations (best data) in the period of 1990 - 2004 and applied the receiver function stacking procedure of Zhuand Kanamori [2000] to estimate Poisson's ratio and crustal thickness. We have divided the research area according to five tectonics environments, explicitly Shields, Platform, Paleozoic orogenic belts, Mesozoic-Cenozoic orogenic belts, and rift zones based on Condie's [1989] simplified classifications. The results from this study shows lower value of Poisson's ratio $\sigma = 0.25$ for Shield and Platform compare to the Orogenic-belts with $\sigma = 0.27$. Crustal thickness for Shield and Platform show the value of 38 km and 43 km respectively, while for the Orogenic belts we found a value of 37 km for Paleozoic belts and 39 km for Mesozoic-Cenozoic belts, although the range of thicknesses for the younger active regions is large. Since our ultimate goal is to provide an improved imaged of global continental structure and composition, we combine our observations with receiver functions results from other published analysis. In total we have integrated observations from 374 stations located in different geologic setting and the results indicate the value of $\sigma = 0.26$ for Poisson's ratio and $H = 38$ km for crustal thickness in Shield, $\sigma = 0.27$ with $H = 43$ km for the Platform and $\sigma = 0.28$ with $H = 36-39$ km for the Orogenic belts</p>					
15. SUBJECT TERMS Seismic velocity Seismic propagation					
16. SECURITY CLASSIFICATION OF:			17. LIMITATION OF ABSTRACT	18. NUMBER OF PAGES	19a. NAME OF RESPONSIBLE PERSON Robert J. Raistrick
a. REPORT UNCLAS	b. ABSTRACT UNCLAS	c. THIS PAGE UNCLAS	SAR	248	19b. TELEPHONE NUMBER (include area code) 781-377-3726

Chapter 1

Introduction & Method Overview

Of the many successes in recent seismic verification research, significant advances in the application of kriging to construct travel time and seismic phase amplitude correction surfaces from available sparse calibration points (Schultz et al, 1998; Phillips, 1999; Phillips et al 1998; Rodgers et al 1999; Pasmanos, 2000) are perhaps most notable. Information gleaned from well placed calibration events significantly reduces mislocation to the extent that in some instances may remove the need for regional crustal models to improve seismic event locations. Of course the success of location and event-size methods relying on kriged correction surfaces requires calibration events with ground-truth location information. Not all places of interest have sufficient events or ground truth information and some extrapolation is required to incorporate the knowledge into standard processing and analysis procedures. In these regions, basic investigations into the character of crustal propagation are required for several reasons. First to help improve event location, and second to prepare for and aid the ultimate goal of event identification. If a unique event is observed, significant resources are directed toward a timely identification. Implications for national security dictate that the identification be robust, which requires that we exploit all available observations and tools.

One of the principal problems in identifying and locating small seismic events is the low-amplitude of observed signals. Without data from a nearby station, we are forced to deal with seismic observations that are small in amplitude and composed of short-period signals that are strongly distorted by propagation. At a few thousand kilometers from the source, the largest signals generated by a shallow event are short-period surface waves. To reliably identify and measure these signals some waveform processing such as phase-match filtering (Herrin and Goforth, 1977) will

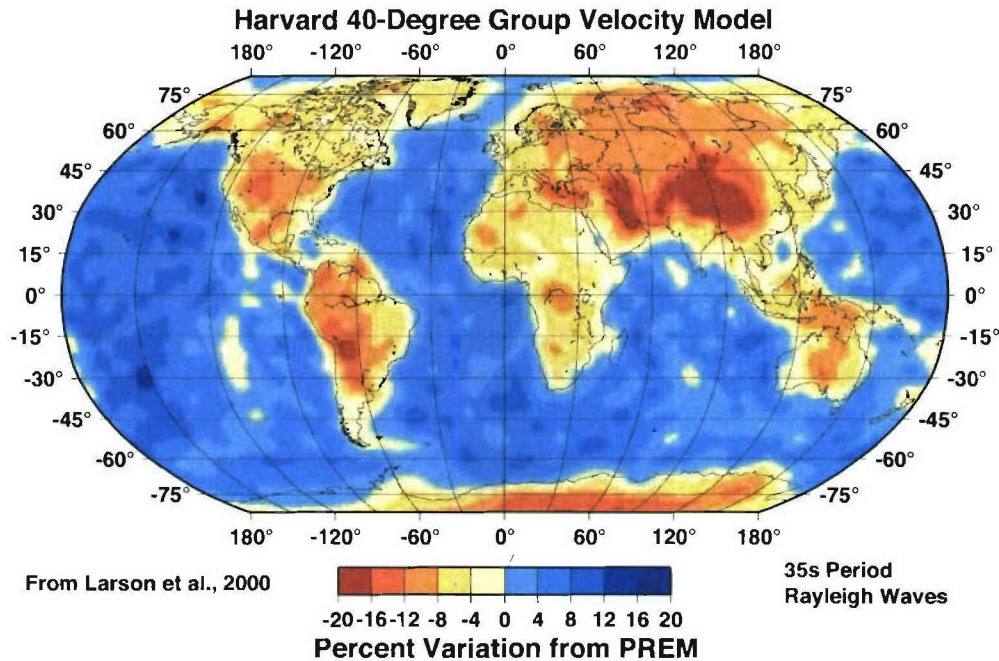


Figure 1.1: Global group velocity variations from the Harvard global mapping project [Larson and Ekstrom, 2001]. Although the period range is too long for the study of small events (which have little useful long-period energy), the models provide valuable information on structure for regional studies of the lithosphere that increase resolution using shorter period observations.

be necessary. The construction of optimal phase-match filters requires knowledge of the dispersive character of the upper crust between the source and the seismometer and that knowledge can be derived from either direct measurements of the dispersion of calibration signals (when available) or indirect knowledge of the shear velocity of the shallow Earth along the wave path. Undoubtedly the best approach to estimating surface-wave dispersion along a specific path is direct observation. Calibration events with ground-truth location information can provide region-specific dispersion characteristics for areas of interest that have well-studied seismic activity. Unfortunately not all places of interest have frequent events or ground truth information and some extrapolation is required to incorporate the knowledge in standard processing and analysis procedures.

Confident and reliable characterization of regional structure requires effort. With sufficient observations of paths crossing the area of interest we can use tomographic

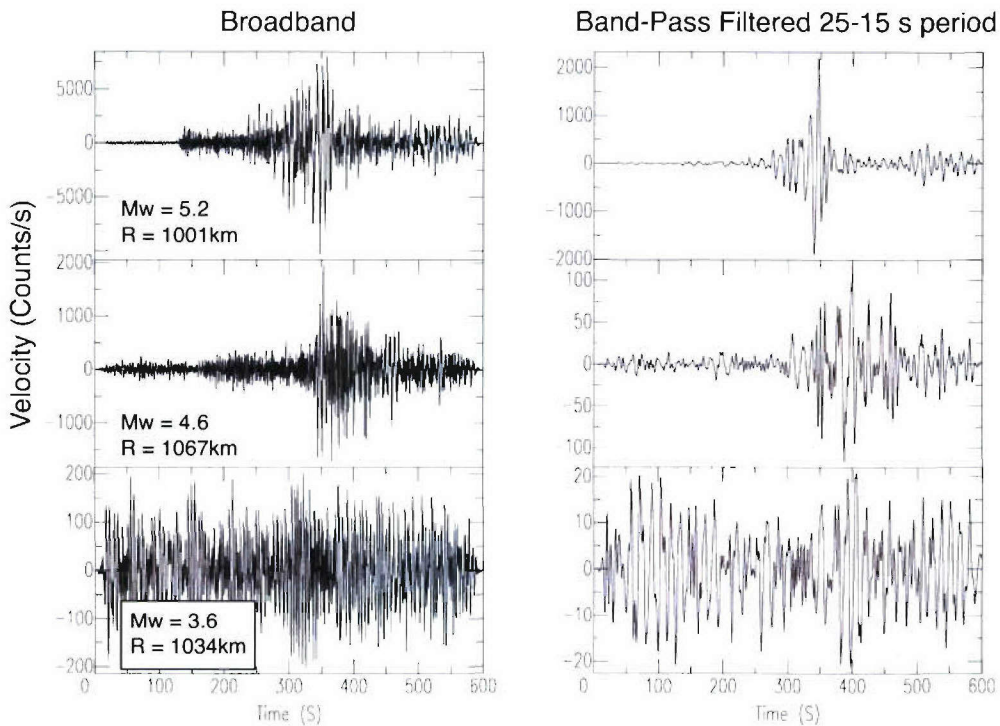


Figure 1.2: Illustration of the variation of signal frequency content for a source-receiver distance of about 1000 km. The signals on the left were generated by earthquakes in the Tien Shan region and recorded at station WMQ in central Asia. Those on the right are band-pass filtered version of the raw signals with a filter passing periods between 25 and 15 second (spanning the 20s Ms measurement range). The surface wave of the M_w 3.6 event is visible in the noisy trace at the bottom. Enhancing the signal to make an Ms measurement would require an appropriate short-period phase-match filter. M_w values are from moment-tensor inversion (Ghose et al., 1998).

imaging methods to construct a smooth version of the regional dispersion structure. Much effort, and much success has been achieved in efforts to map surface-wave dispersion variations across the planet (Figure 1.1). This approach has shown great promise as researchers apply the method to intermediate and short-period surface-wave observations, but the task becomes more difficult as one proceeds to periods less than 15 to 20 seconds. These periods, which are critical to enhancing signals from small events (Figure 2), are difficult to observe routinely and Rayleigh-wave dispersion tomograms for the short periods (and the longest periods) often have the least number of observations in tomographic analyses. Compounding the problem is the fact that short-period surface waves are sensitive to structures that are small enough to require more paths to image accurately. One approach to constructing the necessary knowledge is to combine the longer-period tomography observations with other seismic data to improve regional shear velocity maps which can then be used to predict path-dependent, short-period, surface-wave dispersion. That is the avenue we propose to pursue with the goal of constructing site-specific structure map of the crust and upper mantle beneath China.

Composite Seismic Data Inversions

Seismic studies of earth structure have historically proceeded with a divide and conquer approach. Different parts of seismograms were isolated and modeled by different methodologies and often different researchers. The divide and specialize strategy has computational advantages that are much less important today, but our experience in combining historically disjoint observations remains limited. Subsurface geology generally has a broad wavenumber spectrum (Figure 2), containing sharp, or high-wavenumber, changes in velocity near Earth's surface, at the sediment-basement transition, near the crust-mantle boundary (usually), and in the upper-mantle transition zone, and smooth low-wavenumber variations in regions of relatively uniform geologic structure. Access to the full spectrum of earth structure requires that we exploit signals that span a wide frequency range and that are sensitive to the entire spectrum of heterogeneity. For example, surface-waves, travel times, and direct-wave amplitudes are sensitive to smooth variations in earth structure; reflected and converted waves are sensitive to the velocity contrasts. Combining seismic data in joint inversions is an obvious approach to improve estimates of earth structure. Refraction seismologists have long used seismic wave travel times, amplitudes, and gravity variations to study the structure along one-dimensional surface profiles that illuminate the two-dimensional subsurface geology. To successfully combine data in an inversion, we must insure that all the data are sensitive to the same (or related)

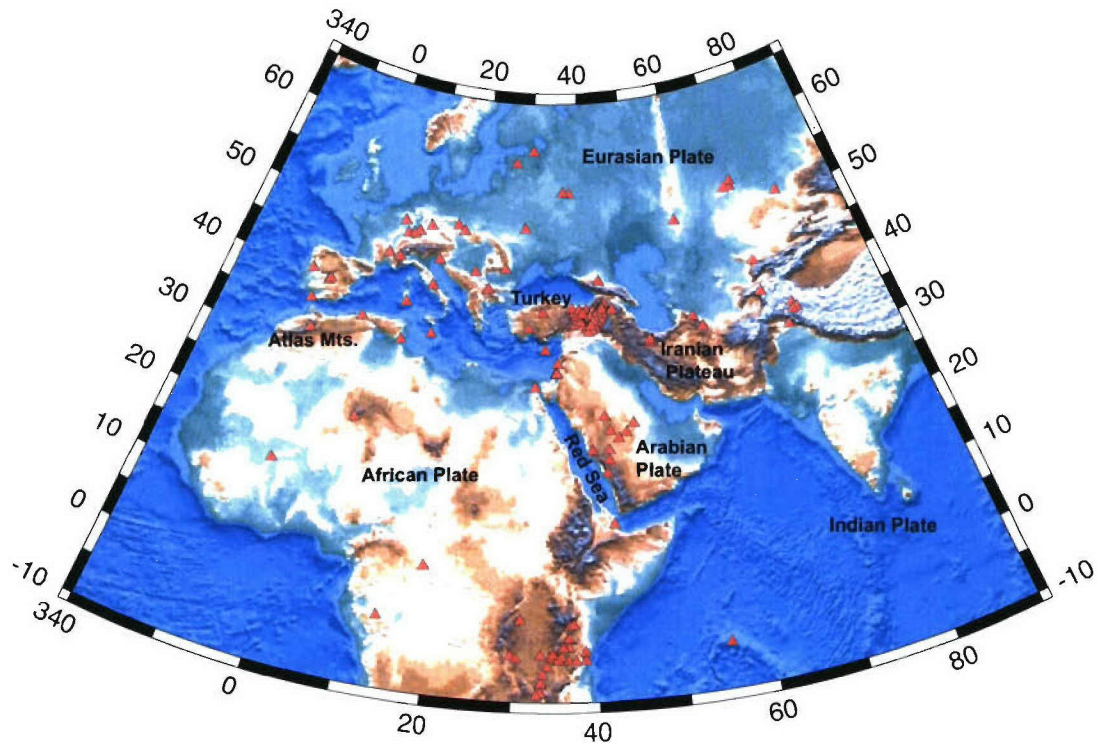


Figure 1.3: Each triangle represents a seismic station for which we analyzed receiver functions. Not all stations had structures suitable for a joint inversion of receiver functions and surface-wave dispersion; some receiver functions indicated strong heterogeneity, for which simple plane-layered modeling is inappropriate.

physical quantities and that they sample or average structure over comparable length scales. Recent advances in surface-wave tomography have provided an opportunity to combine localized surface-wave dispersion estimates with other data such as P- and S-wave receiver functions.

No one doubts that using all available data to construct earth models is the appropriate direction for future studies, but few careful studies of the problems and specific benefits of joint inversions are documented in the literature. Some recent studies have included modeling complete waveform (usually intermediate-to-long period body and surface waves) to extract source or path structure information. Although waveform inversion is simple and straight forward, it is unclear if it is the best way to extract information about earth structure. Unlike a surface-wave dispersion study where the observations at a particular period are equally weighted, the period-dependent weighting in a waveform is not even and simple norms such as L1 and L2 misfit measures are easily dominated by Airy phases. Such observations are also not completely independent since both the body and surface-wave group delays can be affected by mislocation and origin time errors. Finally, we note one other reason for utilizing dispersion measurements. The mechanism by which different seismic waves traveling through Earth average heterogeneity is an area that requires some investigation. Does a one-dimensional parameterization of subsurface structure contain biases resulting from an uneven averaging of the structure by the seismic wave field? To avoid such issues we chose to invert tomographically separated variations in dispersion parameters and receiver functions, which sample the structure within a few 10s of kilometers of the seismic recording station. This insures a relatively local sampling to the station and in some instances better justifies the simple one-dimensional parameterization.

We have successfully applied the joint inversion of receiver functions on data from across western Eurasia and central and northern Africa (Figure 1.3). We illustrate the recent results of our efforts at joint receiver-function fundamental surface-wave inversion later, but our work has produced two important results that deserve mention before we elaborate into a detailed discussion. First, the addition of intermediate-period group velocities (10 to 50 seconds period band) to receiver functions greatly reduces trade off between depth and velocity above velocity contrasts in receiver-function models by adding constraints on broad averages of the crustal shear velocity (receiver functions provide solid information on the thickness and magnitude of the major velocity transitions in the crust). Second, initial applications (in regions of relatively simple structure) have produced models that agree well with existing estimates of structure from refraction profiling.

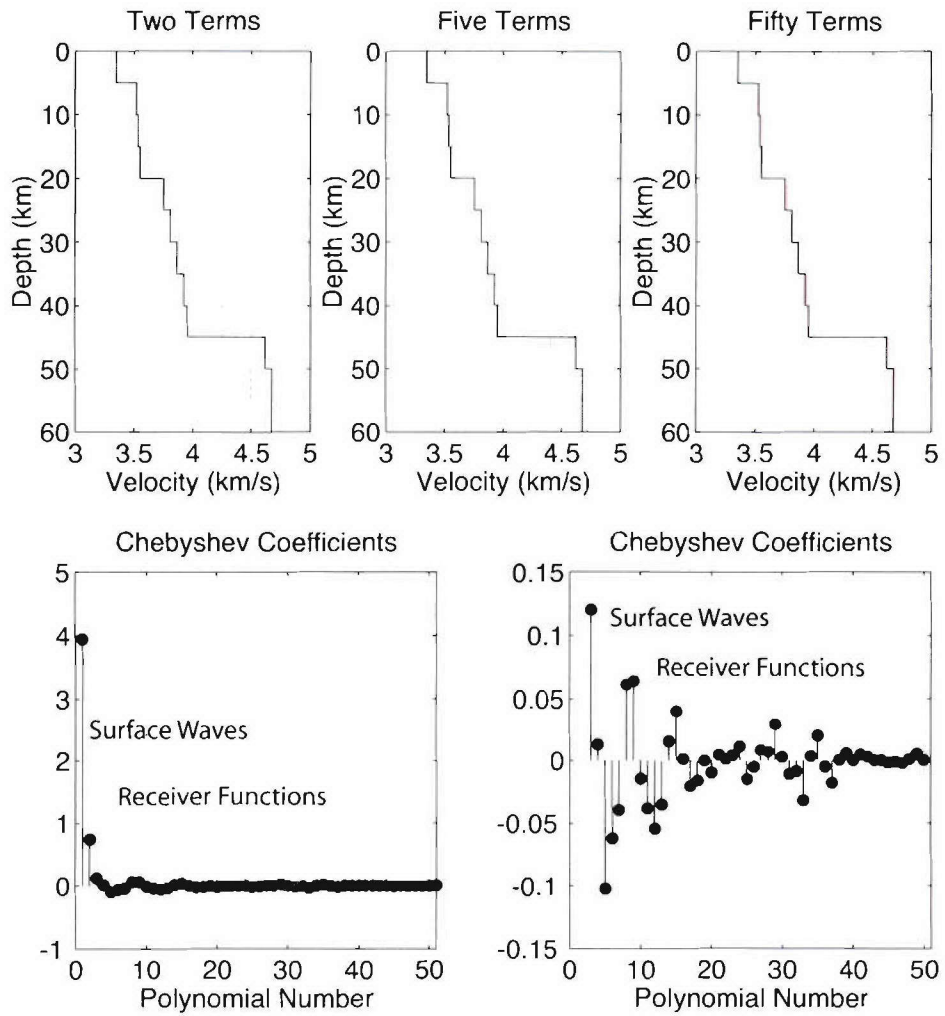


Figure 1.4: Expansion of a shear-velocity model (dark line in top panel) in terms of Chebyshev Coefficients. The top panel shows the sum of two, five and fifty terms respectively. The lower panels show the model spectra, that on the right focuses on the smaller amplitude, higher wavenumber coefficients. In practice, the two data sets are band limited and do not cover the entire spectrum of the model - the illustration is conceptual.

Receiver Functions

Receiver functions represent the response of a location structure to an incoming plane wave (e.g. Phinney, 1964; Langston, 1979). The response consists of the direct P-wave arrival followed by smaller amplitude P and S waves which reverberate in the local structure. By modeling the arrival time and amplitude of the reverberations we can extract information on the structure surrounding a seismometer with a radius of about 40 km (Owens et al. 1984). The use of teleseismic P waves makes the technique suitable for temporary deployments since sufficient observations accrue quickly (provided earthquake sources in the distance range of 30 to 90 degrees are available, which is true of most locations). To isolate the near-receiver response, the vertical component of ground motion is deconvolved from the horizontals, removing the signature of the source and near-source structure (Langston, 1979). The cost of the deconvolution procedure is the loss of P-wave multiples in the resulting time series which is easily accounted for in synthetic waveforms and results in an enhanced sensitivity to shear-velocity (Langston, 1979; Owens et al., 1984; Ammon, 1991). Receiver functions are primarily sensitive to the sharpness of velocity contrasts beneath the receiver and the vertical travel time between the contrasts (Ammon et al., 1990), and receiver function waveforms are relatively easy to model. Owens et al (1984) formulated the first time-domain receiver function inversion and Ammon et al. (1990) extended the procedure to include reflectivity waveform modeling, smoothness constraints, and investigations of initial model dependence on the results.

Receiver Function Estimation. When the data are high-quality and the receiver structure is not too complex, the choice of a deconvolution procedure does not make much difference. However, when the noise in the seismograms is substantial, or the receiver structure is complex, different deconvolution approaches have strengths and weaknesses. We computed receiver functions using the iterative time-domain deconvolution procedure described by Ligorra and Ammon (1999). We prefer the iterative approach, which is based on the Kikuchi and Kanamori (1982) source-time function estimation algorithm, for several reasons. First, in the iterative approach the receiver function is constructed by a sum of Gaussian pulses which produces a flat spectrum at the longest periods. The flat long-period spectrum can be viewed as a priori information that helps reduce side-lobes that may result of spectral or singular-value truncation stabilization procedures. The reduction of side-lobes eases the interpretation and helps stabilize low-frequency receiver functions. Second, the iterative approach constructs a causal receiver function, which is what we expect in all cases of reasonable earth structure. This is a subtle difference from spectral

techniques (e.g. Langston, 1979; Park and Levin, 2000) which can always introduce a component to the signal before the P-wave. The acausal component of the spectral signal may be small, but still important to the satisfaction of the convolutional model that defines a receiver function

$$(1.1) \quad R(t) = Z(t) * E_R(t).$$

where $R(t)$ and $Z(t)$ are the radial and vertical components of ground motion, and $E_R(t)$ is the radial receiver function (a similar equation holds for the transverse component). The point is that even when the receiver function estimation is unstable, spectral deconvolutions may satisfy (1.1) quite well. The iterative time-domain approach, which can be restricted to produce the best causal solution, may not always satisfy (1.1). Experienced modelers have always been able to identify failed receiver functions, but the misfit to (1.1) available from iterative deconvolutions provides quantitative information that can be used when stacking signals, or in extreme cases, to discard obviously failed deconvolutions. In our case we find using a threshold cut-off of 80-90% of the radial power fit allows us to quickly discard poorly constrained deconvolution results, enabling an efficient and objective select of the data to include in further analysis. We generally allow the iterative inversion to include more than 600 arrivals in the receiver-function estimate. For longer time windows, we allow up to 1200. The important point is not to under sample the response by including a limited number of iterations in the deconvolution (a sign of under-sampling are flat regions in the receiver-function estimate).

The receiver function data flow used in our analysis is summarized in Figure 1.5. The original P-waveforms are obtained from the IRIS DMC for all events with magnitudes greater than 5.5. Each three component P-waveform is visually examined and the P-wave arrivals are marked. Events with good visual signal-to-noise ratios are used with the iterative deconvolution method outlined in Ligorria and Ammon [1999]. Those that have convolution misfits less than 20% are included in later analyses that include receiver-function stacking and shear- velocity inversion.

Poissons Ratio & Crustal Thickness Estimation. As a first step in the receiver function analysis we use the receiver function stacking method of Zhu and Kanamori (2000) to estimate the crustal thickness and V_p/V_s velocity ratio (or Poissons ratio). The stacking method makes a rather limiting assumption of a uniform crust but the analysis provides good estimates of these quantities when the structure is relatively simple. The estimated values of Poissons ratios can be used in subsequent inversions which require some assumed value of bulk crustal Poissons ratio. We summarize our results in Figure 3. Although it is difficult to just cluster regions of the continent into simple classifications, we follow Zandt and Ammon

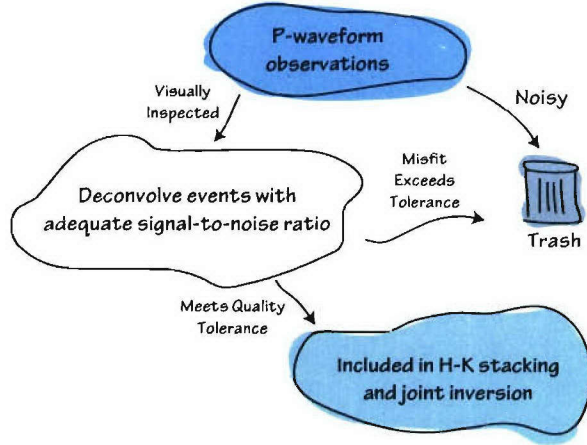


Figure 1.5: Sketch of the data processing flow for the receiver function estimation used in the project.

(1995) and separate our data into tectonic-age based groups with the exception of Tibet, which we remove keep as a separate subset of the Mesozoic-Cenozoic regions. Our results are similar to those of Zandt and Ammon (1995) with the exception that our larger survey of shields (including Archean shields) does not show an unusually high Poissons ratio as was suggested in the earlier data set. Only 7 stations are common to both studies, so the differences are a sampling result. Interestingly, we see no differences between Archean and Proterozoic shields. Crustal thickness estimates agree on average with the global crustal model 2.0, but at times the differences are significant (greater than 5 km). The mean difference between our results and Crust 2.0 is about 1 km and the standard deviation of the differences is about 7 km, which is larger than the resolution we have on stations with stable receiver functions (probably between, 2.5 to 5 km). The numbers agree more closely when we rank our estimates using the complexity of the observed receiver functions. At the bottom of Figure 3 we show the estimated V_p/V_s values for each station. The shaded region shows a liberal range that is typical for the continental crust. For the most part our results are showing up lower than average (Zandt and Ammon, 1995).

Fundamental-Mode Surface-Wave Dispersion

In the time domain, surface waves often have uneven period-dependent weighting due to the existence of Airy phases and differences in source excitation. Dispersion

measurements equalize the weighting and have been used to estimate earth structure for more than four decades (e.g. Haskell, 1954, Brune, 1969; Der, et al., 1970; Braile and Keller, 1975). Observed dispersion can be used to constrain portions of the subsurface structure along the propagation path but substantial trade-off in the details of the lower crust and upper mantle are difficult to control without additional information. Further, dispersion measurements represent an average between the source and the receiver, and thus average the structure over a potentially large path. To estimate local variation near a receiver we will rely on dispersion estimates from tomographic analyses that geographically localize dispersion observations. The mathematics of the problem are quite simple. In the same way a linearized receiver function is formulated to iteratively estimate the variations in velocity beneath the receiver, the dispersion measurements are used to iteratively solve the nonlinear problem relating the observed frequency-dependent velocities on to the shear-wave velocity along the path. Partial derivatives are readily computed using perturbation theory (e.g. Rodi et al., 1975).

A companion collaboration of this work was the continued improvement of the group-velocity dispersion models for the MENA region by researchers at LLNL [Pasyanos and Walter, 1999]. We updated the dispersion models three times during our analyses, as the information was provided by LLNL. We focus little discussion in this report on the model since the work was done elsewhere by others. However, our work would not have been possible without the related effort at LLNL and earlier studies by groups at Harvard [Larson and Ekstrom, 2000].

Shear-Velocity Inversion with Constraints

The receiver function is sensitive to velocity transitions and vertical travel times, surface-wave dispersion measurements are sensitive to averages of the velocities, and relatively insensitive to sharp velocity contrasts. The complementary nature of the signals makes them ideal selections for joint study because they can fill in resolution gaps of each data set. Ammon and Zandt (1993) pointed this out in a study of the Landers region of southern California (although for their specific case, available observations were unsuitable to resolve subtle features in the lower crust) and Ozalaybey et al. (1997) and Last et al. (1997) have performed complementary analyses of surface-wave dispersion and receiver functions. The mechanics of the inversion are relatively simple since partial derivatives of dispersion observations (Herrmann, 1995) and receiver functions waveforms (e.g., Randall, 1989, Ammon et. al, 1990) can be calculated quickly and accurately.

The inversion is formulated to allow convenient adjustment of the relative importance of the different signals on the resulting models. We use an iterative least-squares approach to minimize a functional, $S(x)$, which contains two terms corresponding to the two set of observations (N receiver function sample points, y , and M dispersion observations, z) adjusted to an approximate unit variance. A control parameter, p , is used to adjust the importance of each set of observations.

No a priori approach is available to select an optimal weighting parameter, and the choice is made best after a systematic study of the inversions produced with a range of weights on each set of observations. At times the appropriate value of the trade-off parameter can be made by studying the fits. You may not want to fit part of a waveform that you know may be corrupted by off-azimuth arrivals, or you may not want to fit a rough portion of a noisy dispersion curve. These seismological decisions are not easily coded, but the decisions are easy after a careful study of the matches to the signals for a range of inversion weights. The overriding philosophy is simply to construct a model that suitably matches the observed dispersion and receiver functions.

Iterative Jumping Inversion Scheme

We used a jumping algorithm to jointly invert multiple receiver functions (such as those with different bandwidths or corresponding to different P-wave incidence angles) and surface-wave observations for shear-wave velocity [Constable et al., 1987]. The jumping scheme allows us to implement a smoothness constraint in the inversion by minimizing a model roughness norm [Constable et al., 1987; Ammon et al., 1990] that can trade-off with the prediction error. Our inversion weighting scheme accounts for the different number of data points and different physical units of each data set, and incorporates an a priori parameter that allows to investigate the relative influence of each data set in the resulting models [Julia et al. 2000]. Our model parameters are velocities of fixed-thickness layers overlying a half-space. The system of equations to be inverted is

$$(1.2) \quad \begin{pmatrix} pD_s \\ qD_r \\ \sigma\Delta \end{pmatrix} \cdot m = \begin{pmatrix} r_s \\ r_r \\ 0 \end{pmatrix} + \begin{pmatrix} pD_s \\ qD_r \\ \sigma\Delta \end{pmatrix} \cdot m_o$$

where D_s and D_r are the partial derivative matrices for the dispersion measurements and the receiver function estimates, respectively, r_s and r_r are the corresponding vectors of residuals, m is the vector of S-wave velocities, m_o is the starting model, and Δ is a matrix that constructs a depth-dependent weighted second difference of the

model. The partial derivative matrices and the vectors of residuals are normalized to equalize the different number of data points and physical units in the data sets. A number of trade-off parameters must be specified before inversion. The influence factor, p , controls the trade-off between fitting receiver functions and dispersion curves, and the smoothness parameter, σ , controls the trade-off between data fitting and model smoothness. The parameter $q = 1 - p$, so that p is meaningless outside the range $0 \leq p \leq 1$.

We begin with an example illustrating the inversion. Figure 4 is a plot of the observed and predicted radial receiver functions and fundamental mode group velocity values for station SODA located near the western edge of the Arabian Shield. The receiver function sampled the structure into the Shield and away from the coast. The resulting shear-velocity profile is shown on the right. The shear-velocity model layers are one-km thick for depths down to eight km, two-km thick from 8 to 50 km depth and five-km thick from 50 to 100 km depth, beneath which is a uniform half-space. The trade-off parameters for the inversion, and , were chosen empirically, after a systematic study of the inversion results produced for a range of values, as described in Julia et al. [2000]. The starting model was a uniform 8.0 km/s P-wave velocity half-space. The resulting model is relatively simple, with a strong, shallow velocity gradient with a two layer crust underlain by a transitional lower crust. The upper mantle is smooth, but contains a low velocity zone below 50 km.

Although simple, this model poses some interpretational challenges. First the shallow structure appears to be too slow when compared with more detailed models of shallow shield structure which suggest an average velocity of 3.2 km/s for the top kilometer [Mokhtar et al., 1988]. Our surface low-velocity structure is 3-to-4 km thick, much more than the 400 m layer in higher-frequency studies. After considerable numerical experimentation we found it necessary to omit the shortest periods for Love waves ($T = 5$ and 9 s) to remain consistent with geologic and seismic constraints on shallow structure of the Shield [e.g. Mokhtar et al., 1988].

Also worth close inspection is the need for the decrease in velocity throughout the upper mantle in the model. The half-space velocity is significantly low for a shield and a simple check of the long-period dispersion shows values that are much lower than those commonly observed. The models deepest velocities are controlled by the long-period Rayleigh waves, and not surprisingly, since our longest periods is 60 s, we cannot uniquely resolve much of the deeper structure in the model. However, although our observations cannot unambiguously constrain the deep structure, they are sensitive to deep features in the model, particularly an infinitely deep half-space located at such a shallow depth. Our concern is that the anomalous structure in the mantle may still trade off with features in the crust. To minimize the extent

that deep velocity features may influence crustal features, we decided to constrain our results to transition smoothly into a priori mantle structures. Although we do not know *a priori* the deep structure, we are confident that PREM [Dziewonski and Anderson, 1980] or slight modifications from PREM velocities are certainly a better choice than an unconstrained component in our band-limited inversion. In practice we can implement constraints to be consistent with global aspherical shear velocity models since we need only know the values of deeper mantle shear velocity beneath the station (which we can get for the shear-wave models). Of course we can also (and plan to) include longer-period tomographic dispersion measurements from other studies into our inversion.

Including *a priori* Velocity Information

The upper mantle. The upper mantle low velocity zone in Figure 5 may be a consequence of the limited resolving power at depth of our data set. To test the hypothesis we incorporated a priori information to compel the deepest layers in our model to resemble values from global mantle models like S12WM13 model [Su et al., 1994]. We chose to constrain our solution by appending the following set of equations to the original system (1) [Jackson, 1972],

$$(1.3) \quad W \cdot m = W \cdot m_{\text{apriori}}$$

where W is a diagonal matrix of constraint weights and m contains *a priori* predefined velocity values. Equation 1.2 becomes

$$(1.4) \quad \begin{pmatrix} pD_s \\ qD_r \\ \sigma\Delta \\ \epsilon W \end{pmatrix} \cdot m = \begin{pmatrix} r_s \\ r_r \\ 0 \\ 0 \end{pmatrix} + \begin{pmatrix} pD_s \\ qD_r \\ \sigma\Delta \\ \epsilon W \end{pmatrix} \cdot m_o$$

The scalar weight ϵ is redundant, but it allows us to adjust the importance of the *a priori* velocity weights relative to the model fits and roughness with one convenient parameter. We also thicken the model to move the half-space to a depth of 500-km, well below the depth of influence in our band width. The resulting models are satisfactory in that they predict dispersion values more consistent with global observations than do the truncated-depth models.

Chapter 2

Bulk Properties of the Continental Crust

The continental crust covers approximately 41% of the Earth's surface and accounts for 79% of the volume of the Earth's crust [Condie, 1997]. Approximately 71% of the continental crust lies above the mean sea level [McLennan, 1992]. The continental crust is a composite of materials fractionated from the primordial mantle "geochemical reservoir" by geologic processes operating during the 4500 *Ma* history of the Earth. The continental crust is usually divided into 10 continents and four submerged microcontinents. The mean elevation of continental crustal material is about 125 meters above sea-level (including the 29% that lies beneath the ocean). The continental crust ranges in thickness from about 10-80 km. The average values for the crust is about 40 km [Mooney, 1994], although previous estimates of 35 or 38 are often used in calculations. The crust is thickest beneath active orogenic regions, and probably the thickest crust lies beneath Tibet and the Bolivian Altiplano. Including the ocean sediment of continental affinity, the volume of continental crust is estimated to be approximately $7.35 \times 10^9 \text{ km}^3$ [McLennan, 1992]. The lengthy history of the crust produces a complex assemblage of materials with a variety of densities and elastic parameters. Assuming a mean density of 2800 kg/m³, the mass of the crust is approximately 2.06×10^{22} kg, representing about 0.35% of the total mass of the Earth [McLennan, 1992].

The single outstanding feature of continental crustal chemistry is the enrichment of the incompatible trace elements. From the concentrations shown in Figure 2, we can also see that the amount of enrichment correlates well with the affinity of a given element to the liquid produced by a mantle melt. The bulk chemistry of

the continental is approximately that of tonalite, with approximately 65% SiO₂ [O’Nions, 1992]. In general, the lower crust is thought to be more mafic than the upper crust, indicating an increase importance of basalt in the lower crust. Crustal xenoliths strongly indicate that the lower crust is more mafic than the upper crust. Exposed sections of the lower crust agree with this general trend, but are not as basaltic in character as the samples found in xenoliths [Rudnick, 1992]. The continental crust is the only repository of information for a major part of the earth history [McLennan, 1992] since the relatively young age of the oceans (200 Ma) supplies information on earth evolution for only a small fraction of the age of the Earth. Models of crustal evolution are primarily based on geochemical (isotopic) evidence although recent efforts at global surveys using seismic data are adding new information to the problem [Nelson, 1991; Durrheim and Mooney, 1991 and 1994]. Early in Earth history, the planet had very little, if any, crust. Continued bombardment by planetismals and debris remaining from solar system formation continually broke up the slag forming above the mantle. Eventually, the rate of bombardment slowed enough to allow the formation of crust. We have samples of continental crustal material back to about 3800 Ma., so only the first 700 Ma are without record [O’Nions, 1992] (the oldest terrestial material, zircons from western Australia have been dated to approximately 4200 Ma.). The estimated mean age of the crust is about 2200–300 Ma.

Poisson’s Ratio

Poisson’s Ratio, σ , is an elastic parameter that is often used to characterize different rock types. Physically, Poisson’s Ratio can be defined if you consider an experiment stretching an elastic rod of diameter d and length L . As you stretch the rod, the length and the diameter will change. Poisson’s ratio is then defined as

$$\sigma \equiv \frac{\Delta d/d}{\Delta L/L}.$$

For most materials as you stretch the rod the diameter decreases, and so σ is positive. For most rocks, typical values of Poisson’s Ratio is on the order of 0.25, so the fractional change in diameter is about 1/4 that of the fractional change in length when the material is stretched.

For seismic applications, Poisson’s Ratio can be related to the seismic velocities of P and S waves, which can be measured. Let V_p represent the P-velocity and V_s

represent the S velocity. Then

$$\begin{aligned}\frac{V_p}{V_s} &= \sqrt{\frac{2(1-\sigma)}{1-2\sigma}} \\ &= \sqrt{\frac{1}{1-2\sigma}-1}.\end{aligned}$$

The inverse relationship is

$$\begin{aligned}\sigma &= \frac{\left(\frac{V_p}{V_s}\right)^2 - 2}{2\left(\frac{V_p}{V_s}\right)^2 - 2} \\ &= 1 - \frac{1/2}{1 - \left(\frac{V_s}{V_p}\right)^2}.\end{aligned}$$

The trick then is to relate σ to rock type. The relationship between σ and rock composition is not unique by any metric, but the information can be used in some instances to distinguish between different rock types. Even better is knowledge of both V_p , and V_s . The relationship between V_p/V_s and Poisson's ratio is one-to-one, so the two can be used interchangeably.

Receiver Functions for Simple Earth Models

In relatively simple structures, the waveform is a composite of P-to-S converted waves that reverberate in the structure beneath the seismometer. Modeling the amplitude and timing of those reverberating waves can supply valuable constraints on the underlying geology. If the main structural boundaries are approximately subhorizontal in the region of the recording station, the main features of the structure can be approximated using a sequence of nearly-horizontal interfaces bounding regions with strong contrasts in elastic properties. In that case, the arrivals generated by each sharp (that is, sharp relative to the shortest wavelength in the observations) looks something like the signal shown in Figure 2.1.

In more complex structures, the arrivals may also include scattered surface waves, and the response may be complicated.

The travel times of these waves can be simply expressed in terms of the horizontal and vertical slownesses, p and η_α and η_β . The horizontal slowness, p is also called

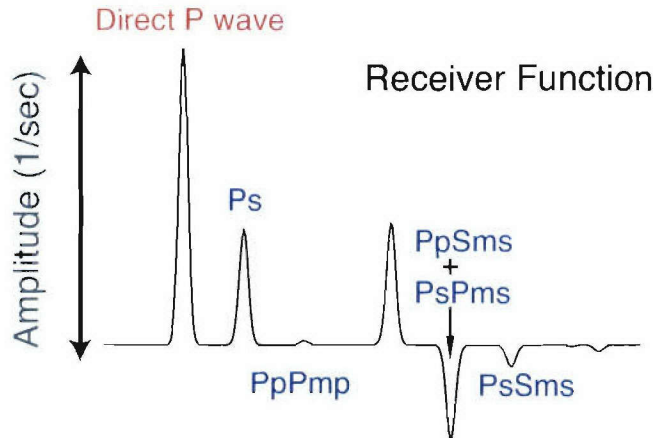


Figure 2.1: Canonical receiver function for layer over a half-space model.

the ray parameter, and can be estimated from the slope of travel-time curves. The vertical slownesses are related to the seismic velocity and the ray-parameter by

$$\eta_\beta \equiv \sqrt{\frac{1}{V_s^2} - p^2}$$

and

$$\eta_\alpha \equiv \sqrt{\frac{1}{V_p^2} - p^2}$$

In a receiver function, as a consequence of the deconvolution, all times are specified relative to the initial P-wave arrival. Then

$$\begin{aligned} T_{Ps} &= (\eta_\beta - \eta_\alpha) \cdot h \\ T_{PpPmS} &= (\eta_\beta + \eta_\alpha) \cdot h \\ T_{PsPmS} = T_{PpSPmS} &= 2 \cdot \eta_\beta \cdot h \end{aligned}$$

The amplitudes of the arrivals in a receiver function depend on the incidence angle of the impinging P-wave and the size of the velocity contrasts generating the conversions (Ps) and multiples (PsPhs, PpShs, PpPhs). The arrival times of the converted phase and multiples depend on the depth of the velocity contrast, the P and S velocity between the contrast and the surface, and the P-wave incidence angle, or ray parameter. The relative amplitudes of the later arrivals and their frequency content depend on the nature of the velocity transition - e.g. is it broad or relatively sharp velocity change?

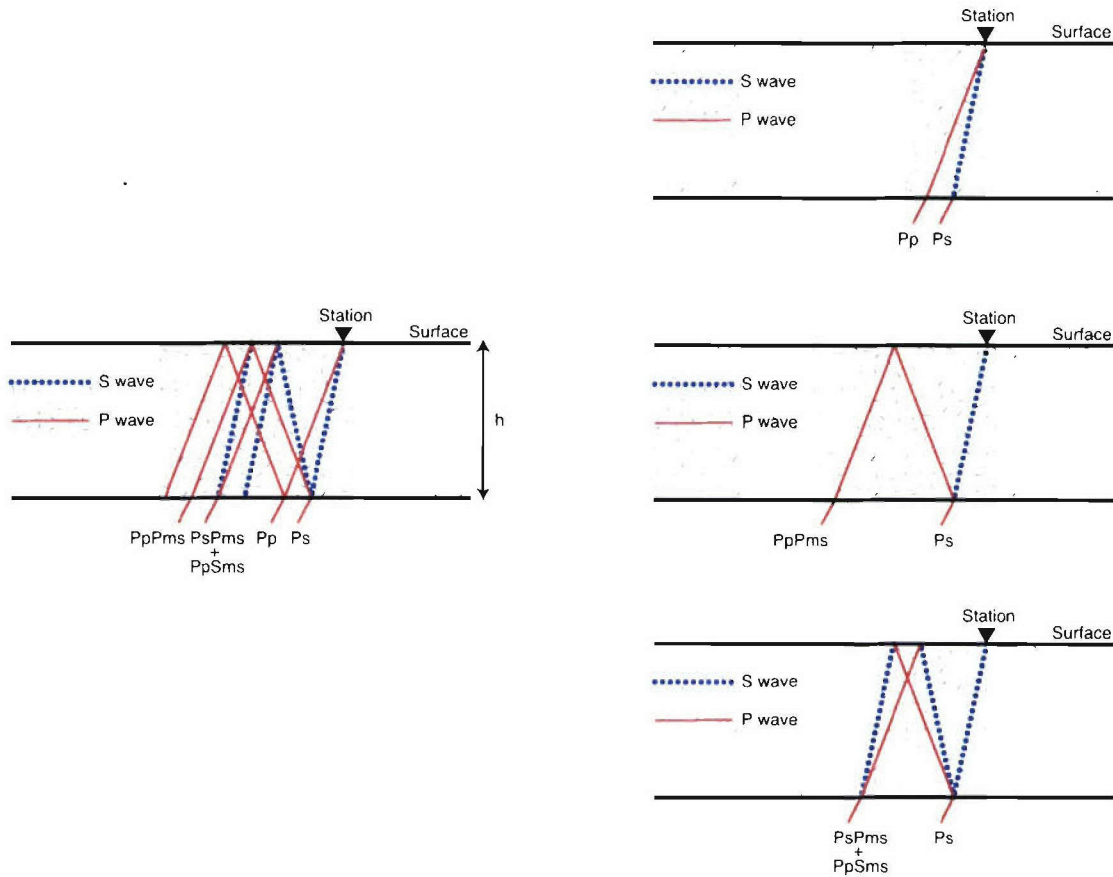


Figure 2.2: Ray paths for the main arrivals in a receiver function generated by a simplified crustal model. Each cross section is cut along the plane containing the receiver and the source. The left panel shows all the rays for the largest arrivals, the panels on the right separate the converted phases from the multiples for clarity.

Poisson-Ratio Estimation Using Amplitude Stacking

This Poisson's Ratio panel in *Lithospheric Structure in Africa and Western Eurasia* is a simple implementation of the $h - \kappa$ stacking algorithm of Zhu and Kanamori [2000]. h represents thickness, and κ represents the Vp/Vs ratio. A grid-search is performed for a range of thickness and Poisson Ratio's assuming a constant P-velocity. For each thickness and velocity, the arrival times of the Ps , $PpPmP$, $PsPmS$, and $PpSmS$ phases (Figure 2.1) are computed and the receiver function amplitudes corresponding to these times are summed. The optimal estimates for the values of these parameters is that which produces the maximum amplitude. Since the second set of multiples $PsPmS$, and $PpSmS$ have the opposite polarity of the Ps and $PpPmS$ multiple, the former amplitude is subtracted to the others. Also, since the quality of the multiples varies and is generally not as good as the Ps phase quality, a weighted sum of these amplitudes is employed. If we let $P(h, \sigma)$ represent the sum for a particular thickness, h , and Poisson's Ratio, σ , then we have

$$(2.1) \quad P(h, \sigma) = W_{Ps}R(T_{Ps}) + W_{PpPmS}R(T_{PpPmS}) - W_{PpSmS}R(T_{PpSmS})$$

where the W 's represent weights and $R(t)$ represents the receiver function. A cartoonish vision of the ray paths are shown in Figure 2.2. Note that implicit in the assumptions of this method is a simple, uniform crust underlain by a flat crust-mantle transition.

The choice of weights in Equation (2.1) is subjective. Most values are adjusted by trial and error with an eye on sensitivity. We use a slightly different approach (Figure 2.3) in that we examine the stacking images for each of the three phases used to produce a common receiver function $h - \kappa$ stack. With this approach, we can determine the consistency of the phases used in the stacks. We also examine the moveout of the different phases as a function of ray parameter. If one of the phases corresponds to a poorly defined feature, we can decrease it's weight. For example, in Figure 2.3, the Ps and $PpPmS$ phases are consistent, but the later multiple arrivals are inconsistent with the other two. This suggests not using the second set of multiples ($PsPmS$ and $PpSmS$) in the stacking. We have run bootstrap error estimates on many of the data, and together with the consistency of the results and a comparison based with all of the stations that we have analyzed, we grade each estimate across the range of A, B, C, D, and F. While inherently fuzzy, these grades provide experienced quality assessments for those wishing to use the results.

To perform the stacking we must also estimate the vertical slownesses, which depend on the ray parameter (computed from travel-time curves), and the assumed average P-wave speed for the crust. The results are sensitive to the assumed velocity so the

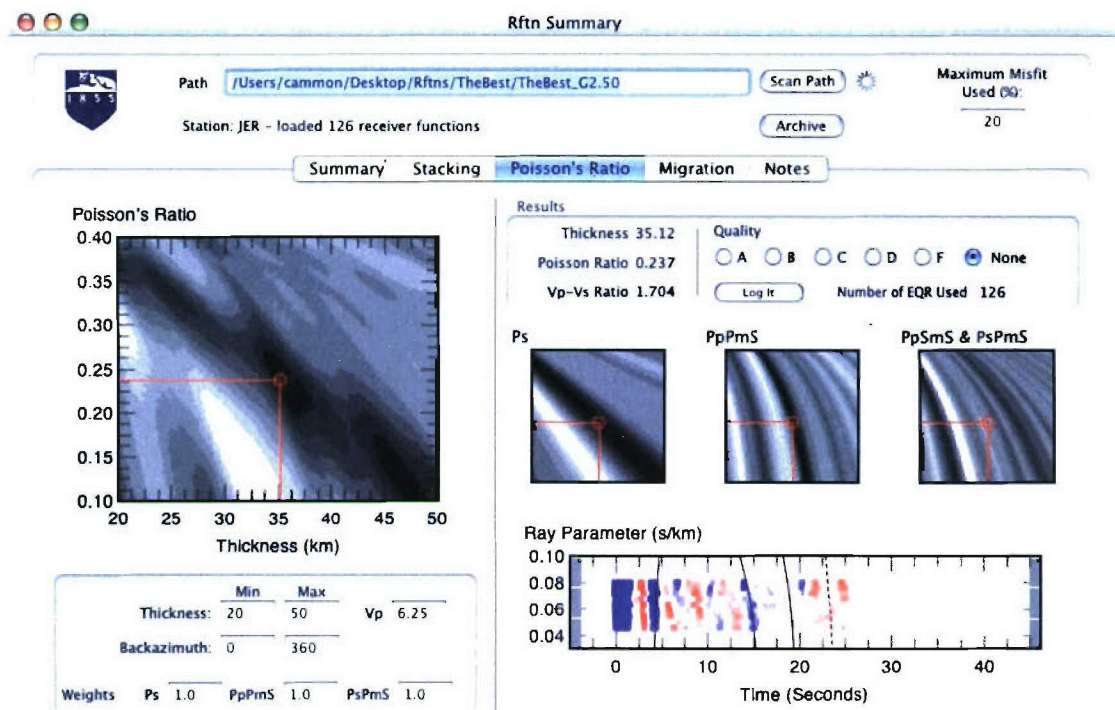


Figure 2.3: Sample receiver-function stacking example.

speed that you use is important. We used the average speed obtained at each station from Crust 2.0 (actually a slowness average), which allows a direct comparison between our results and the reference model, and keeps our results as consistent with the global reference as possible.

Poisson's Ratio & Crustal Thickness Estimates

In this section we present a summary view of the results of receiver-function stacking to estimate the crustal thickness and Poisson's ratio across the study region. All of our results are assigned a quality rank, which is listed along with all estimates in appendix. Here, we summarize the results graphically and compare our measurements with those from previous studies.

Comparison With Zandt and Ammon [1995]. Values for crustal thickness and Poisson's Ratio estimated by Zandt and Ammon [1995] are summarized in Figure 2.4. The study includes 76 measurements, and was performed by picking the arrival times of the converted and multiple phases, not using the less subjective stacking approach developed later. Experience suggests that careful picking produces results compatible with the stacking results. Zandt and Ammon separated their results into crustal provinces guided by the map of basement age found in Condie [1993]. The results for most provinces included much scatter with the exception of shields, which were uniformly high in Poisson's ratio. The average thicknesses for each crustal age province produced a systematic variation with age as shown in Figure 2.4. The results of the study were based predominately on two large earthquakes from 1994 (the large, deep Bolivia and Fiji events) and were heavily biased to North America - a result of the global seismic network configurations at the time. Only a handful of stations are common to the present analysis and the 1995 study, so direct quantitative comparisons are unavailable.

Comparisons With Crust 2.0. One of the more interesting comparisons that we can make is with the predominantly refraction (P-wave speed) constructed model Crust 2.0 [Bassin *et al.*, 2000]. Crust 2.0 is a model widely used in global and regional seismic waveform modeling, and forms the basis for crustal corrections in long-period shear-velocity imaging efforts. Crust 2.0 contains a detailed map of crustal thickness, but has a low spatial resolution of variations in Poisson's Ratio or equivalently, the V_p/V_s ratio. Thicknesses are compared in Figure 2.6, which is useful only for first-

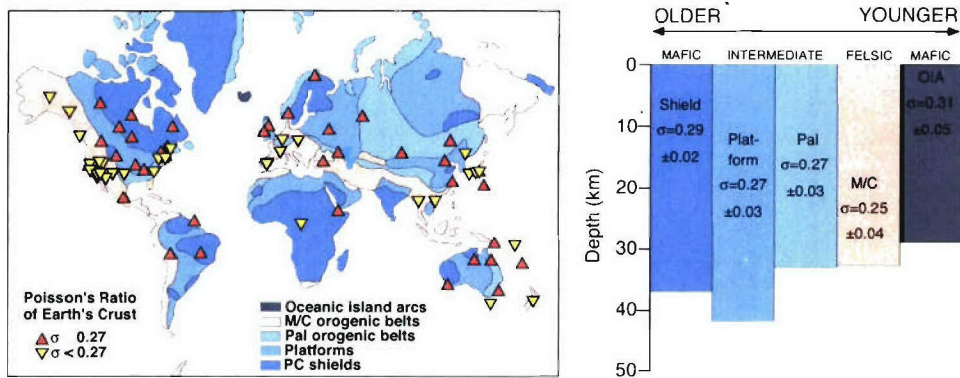


Figure 2.4: Global variations in Poisson's ratio observed by Zandt and Ammon (1995). The simplified geologic map is based on REFERENCE.

order comparison of the two sets of results. Many observations agree to within 2.5 km, probably the resolution of either method, and most of the measurements are within about 3.5 kilometers of the values listed in Crust 2.0. About 90% of the observations are within 7 kilometers. As in Zandt and Ammon [1995], observations are separated into crustal province to illuminate age-dependent differences (which are not readily clear). The thickness values correlate reasonably well (Figures 2.5 and Figures 2.6). Our results for the Tanzania Craton suggest a thinner crust than that contained in Crust 2.0, but the other values are more consistent such as those in the Arabian Shield. Thicker crusts are observed in the shields in west-central Africa and on the western edge of the Tanzania Craton. The thinnest crusts are observed across north-central Europe (less than 30 km), the thickest in mountain belts, including the Urals, Tian Shan, and Pamir region.

In Figure 2.7 we compare the our V_p/V_s ratio estimates with those included in Crust 2.0. Crust 2.0 has an extremely simple variation in Poisson's ratio (there are few non receiver-function based estimates of this quantity [Zandt and Ammon, 1995]. Individual results are uncorrelated, but are bounded by the range of values assumed in Crust 2.0. Table 2.1 summarizes our results by crustal age province, and we include the Crust 2.0 values sampled at the same locals for reference. Quantitative comparison between the two populations is difficult, the information is simply not contained in Crust 2.0.

For completeness, we also summarize the results geographically, using the maps shown in Figure (2.8). The sparsity of stations makes drawing conclusions difficult. But, as mentioned earlier, the thinnest crusts are located in north-central Europe,

Table 2.1: Crustal Thickness & Poisson's Ratio By Age Province.

		Shield (37)	Platform (19)	Pal. Orogen (23)	M-C Orogen (62)
This Study	H (km)	38	41	36	35
ABC Data	σ	0.25	0.26	0.26	0.26
CRUST 2.0 (1998)	H (km)	39	40	36	35
Zandt & Ammon (1995)	σ	0.27	0.27	0.27	0.27
Holbrook et al. (1992)	H (km)	36.9	41.5	33.4	32.6
	σ	0.29	0.27	0.27	0.25

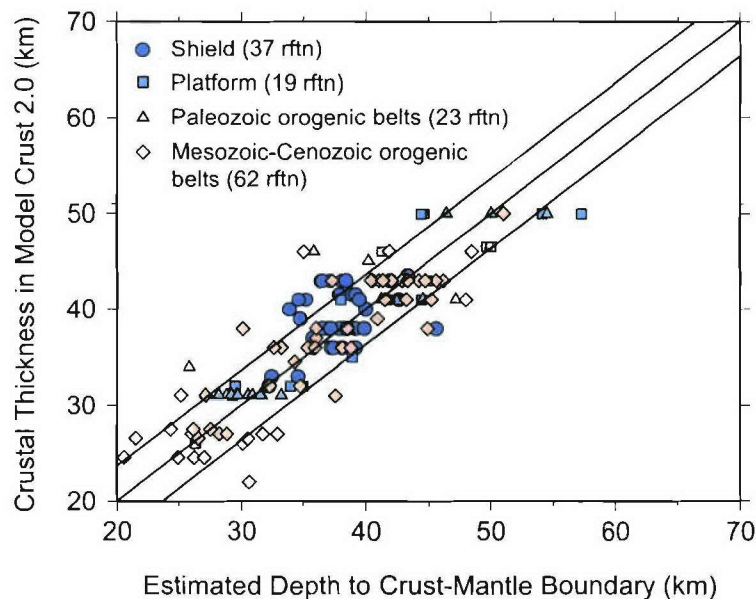


Figure 2.5: Observed differences between the crustal thickness estimated using receiver function stacking and those estimated in the construction of model Crust 2.0. The diagonal lines indicate one standard deviation in the difference between the two crustal thickness estimates. Horizontal trends usually indicate stations within the same cells in model Crust 2.0.

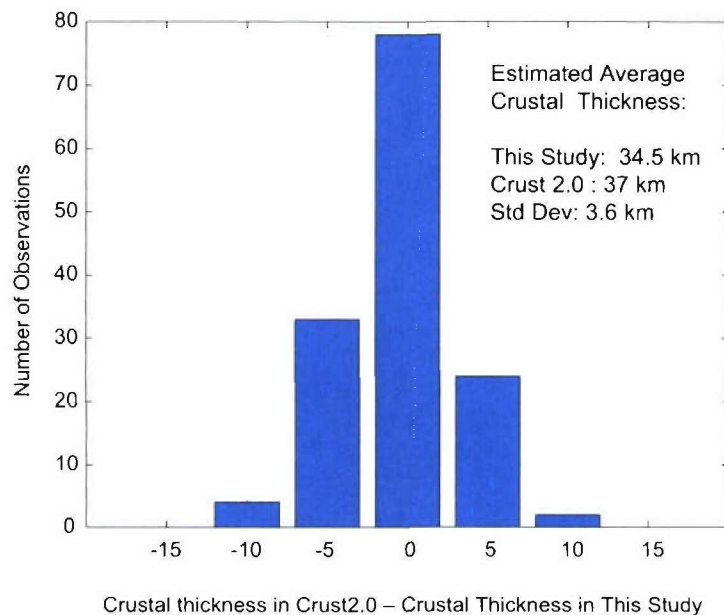


Figure 2.6: Distribution of differences between the crustal thickness estimated using receiver function stacking and those estimated in the construction of model Crust 2.0. The average shown in the chart is not adjusted for crustal province, so it only useful as a comparison of the results samples as the crust is in this study.

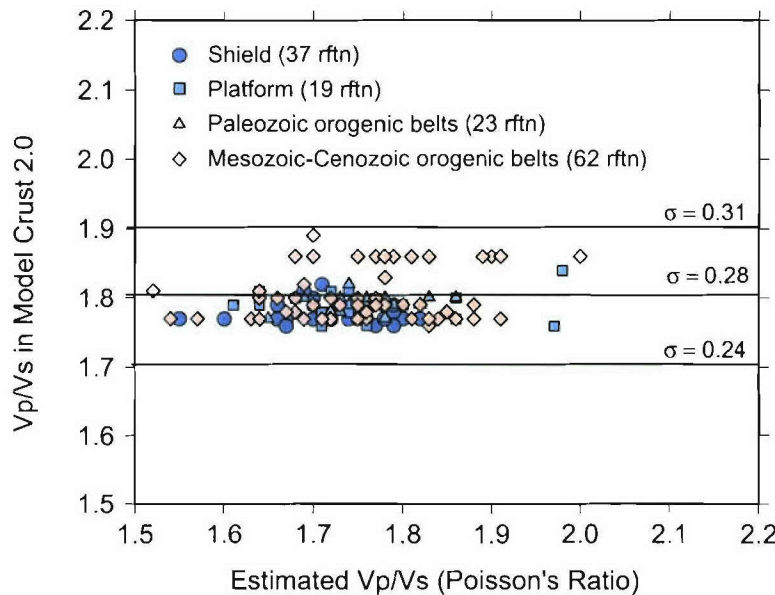


Figure 2.7: Observed differences between the the V_p/V_s ratio estimated using receiver function stacking and those contained in model Crust 2.0.

the thickest beneath active orogens. Shield values are intermediate, but slightly thicker in western Africa. A similar summary for V_p/V_s ratios is presented in Figure 2.9.

We also performed a literature search of results from across the globe, including receiver-function estimates of V_p/V_s ratios from North America, Japan, Australia. The results are shown in Figure 2.10, which also contains a summary of studies already discussed. The histogram labeled Holbrook et al. (1992) include thickness values from about 90 active-source seismic experiment, but included only 11 V_p/V_s ratio estimates. One remarkable result is the systematic crustal thickness pattern observed from the different receiver function observations - crustal thickness increases by 2-5 km with the addition of sediments on top of shield to form Platforms, then decreases beneath the Paleozoic orogens. The patterns beneath the active Mesozoic-Cenozoic regions are much more difficult to simplify, as the scatter of values within that provinces is large. The unusual nature of the Tibetan crust is highlighted in the global summary.

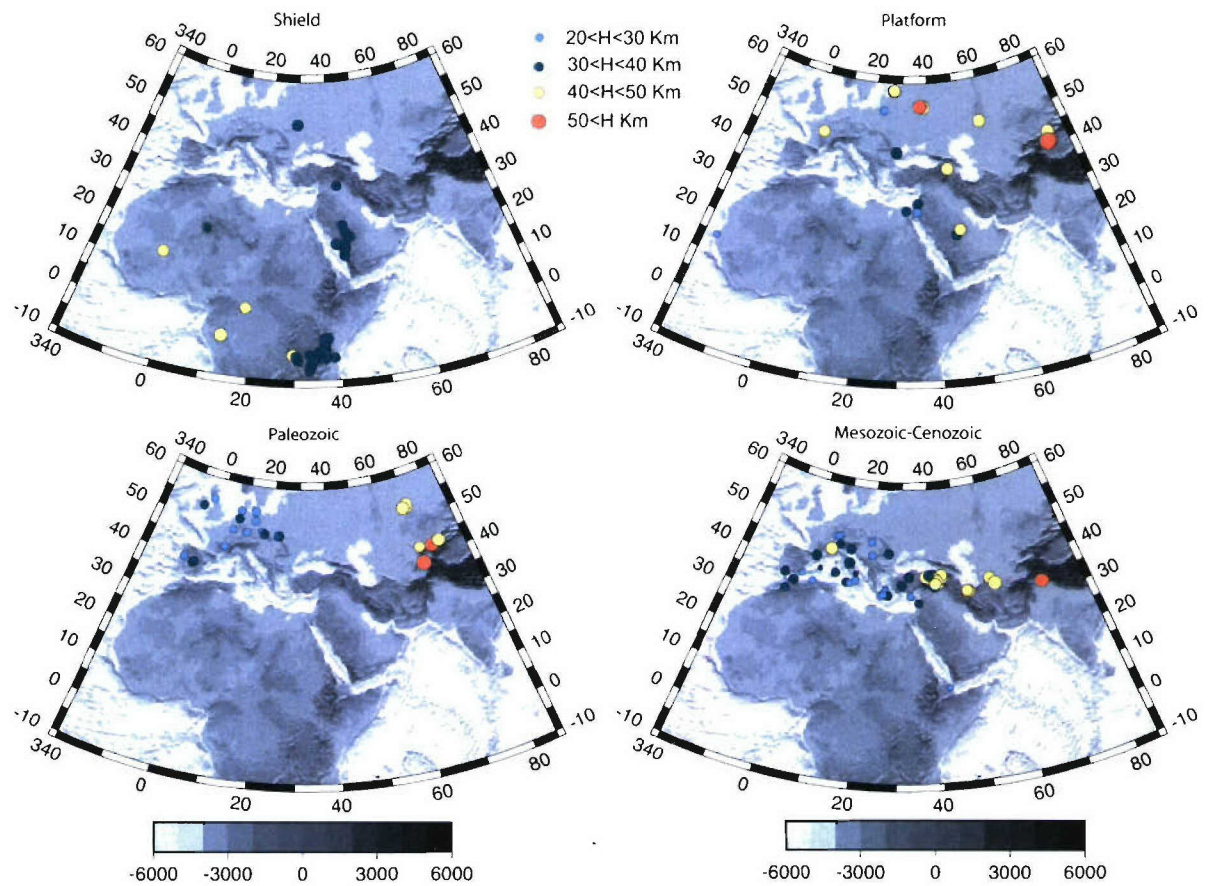


Figure 2.8: Observed crustal thicknesses from receiver function stacking.

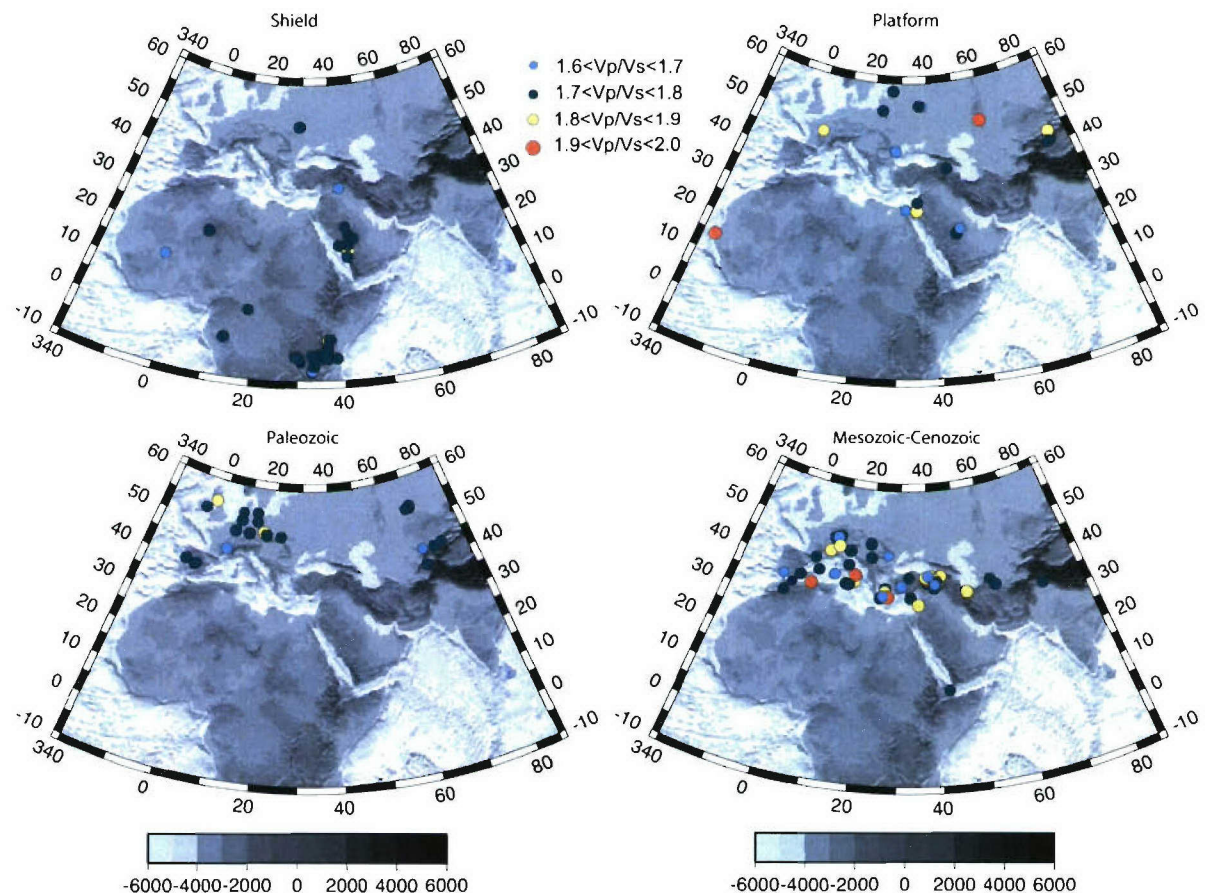


Figure 2.9: Observed crustal V_p/V_s ratios from receiver function stacking.

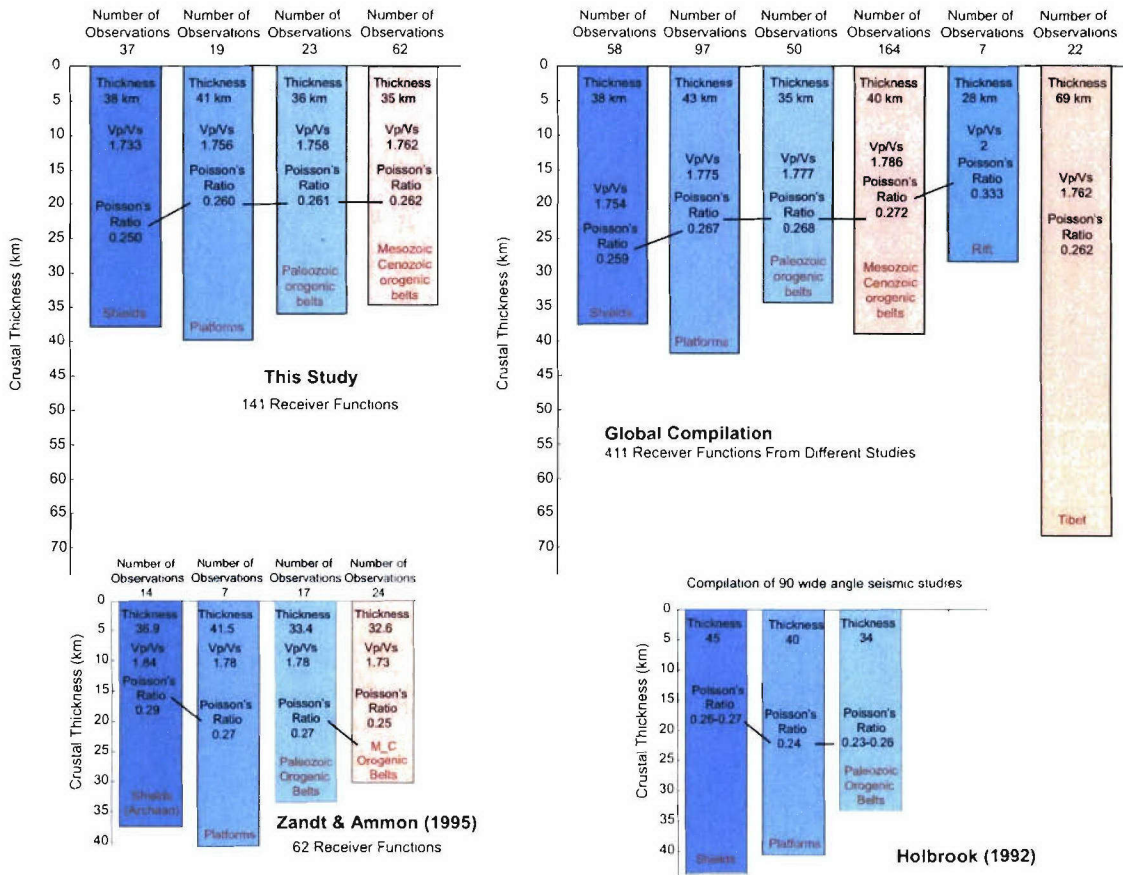


Figure 2.10: Graphical comparison of results from earlier studies, this work, and a search of the scientific literature for receiver function stacking estimates across the globe.

Chapter 3

Shear-Velocity Estimation

As described in the introduction, subsurface geology generally has a broad wavenumber spectrum containing spatially localized broadband-wavenumber changes in velocity near Earth's major geologic boundaries and smooth low-wavenumber variations in regions of relatively uniform geologic structure. Access to the full spectrum of earth structure requires that we exploit signals that span a wide frequency range and that are sensitive to the entire spectrum of heterogeneity. Surface-waves, travel times, and direct-wave amplitudes, for example, are sensitive to smooth variations in earth structure; reflected and converted waves are sensitive to velocity contrasts. Combining seismic data in joint inversions is an obvious approach to improve estimates of earth structure. To successfully combine data in an inversion, we must insure that all the data are sensitive to the same (or related) physical quantities and that they sample or average structure over comparable length scales. Advances in surface-wave tomography have provided an opportunity to combine localized surface-wave dispersion estimates with other data such as P- and S-wave receiver functions.

Surface-wave dispersion measurements are sensitive to broad averages, or low wavenumber components of earth structure. They provide valuable information on the absolute seismic shear velocity but are relatively insensitive to sharp, high-wavenumber velocity changes. Generally surface-wave inversions must be constrained using a particular layer parameterization (e.g. near-surface, upper-crust, lower crust, mantle lid, deep mantle), resemble an a priori model, or substantially smoothed to stabilize earth-structure estimation. Despite these drawbacks, surface-wave dispersion values contain important constraints on the subsurface structure, and the general increase in depth sensitivity with depth allows an intuitive understanding of their constraints on structure. Additionally, modeling dispersion values facilitates a

broadband inversion by reducing the dominance of Airy phases, which pose problems when constructing broad-band misfit norms to model seismograms directly. Perhaps most important for our application is the ability to localize Earths dispersion properties using seismic tomography. The idea is now well established and global dispersion models exist for a broad range of frequencies (e.g. Larson and Ekstrm, 2001; Stevens et al., 2001). The localization of dispersion allows us to isolate the variations in properties spatially and global models of surface-wave dispersion exist and are readily available for application to other studies such as the proposed work. We employ two dispersion models in our inversions - a low-frequency model of Harvard (Larson and Ekstrom, 2001) and the Lawrence Livermore Model of Michael Pasyanos (Pasyanos and Walter, 2001, personal communications - for updates). The Harvard models contain smooth variations as a function of period, but have no information below periods of 30 seconds (important for upper crustal constraints). The LLNL model has shorter period information, but can be rough from period-to-period. We generally apply a simple smoothing operator to the raw curves before using the LLNL results in an inversion.

Receiver function waveforms are a composite of P-to-S (or S-to-P) converted waves that reverberate within the structure near the seismometer. Modeling the amplitude and timing of those reverberating waves can supply valuable constraints on the underlying geology. In general, the receiver functions sample the structure over a range of 10s of kilometers from the station in the direction of wave approach (the specific sample width depends on the depth of the deepest contrast). Stations sited near geologic boundaries can produce different responses for different directions. Recent innovations in receiver function analysis include more detailed modeling of receiver function arrivals from sedimentary basin structures (e.g. Clitheroe et al., 2000), anisotropic structures (e.g. Levin and Park, 1997; Savage 1998), estimation of Poissons ratio (e.g. Zandt et al., 1995; Zandt and Ammon, 1995; Zhu and Kanamori, 2000, Ligorra, 2000), reflection-like processing of array receiver functions (e.g. Chevrot and Girardin, 2000; Ryberg and Weber, 2000) and joint inversions (e.g. Ozalaybey et al., 1997; Du and Foulger, 1999; Julia et al., 2000).

Ammon and Zandt (1993) used surface-wave dispersion observations to try and distinguish between competing models of the Mojave desert, but Ozalaybey et al., (1997) pioneered a formal, joint inversion of these data. They nicely illustrated the value of even a limited band of dispersion values to help reduce the trade-off between crustal thickness and velocity inherent in receiver function analyses. Specifically, they used Rayleigh-wave phase velocities in the 20-25 second period range to help produce stable estimates of crustal thickness in the northern and central Basin & Range. The limited bandwidth did not permit resolution of details in the crust and they limited their inversion (or at least their interpretation) to depths above 40

km. More recent authors have exercised the approach and combined the data with additional a priori model constraints (Du and Foulger, 1999; Julia et al., 2000). Recent accomplishments in global and regional tomography now provide a more complete band of dispersion measurements to combine with receiver functions that allow us to improve the resolution of earlier works.

Seismic inversion is not a simple exercise. Each result requires performing dozens of inversions to assess the stability of the result and/or identify the robust features in the solution. For the inversion of dispersion curves, we often experimented with adjusting the bandwidth of the observations or excluding Love or Rayleigh waves to explore the consistency and sensitivity of those data. After months of experiments and exploration of these issues we found that most of the time it was prudent to often ignore the Love wave measurements, which are less well constrained in the tomographic models than the corresponding Rayleigh wave dispersion values. The extent of the differences between these values is an interesting scientific target, but we do not believe that simply extracting curves from the models and showing that it is difficult to fit them simultaneously is sufficient documentation of the prevalence of anisotropy. The tomography for Love and Rayleigh are decoupled and the coverage and resolution of each differs. The result may be artificial differences in the dispersion values. What we can state is that we had a difficult time fitting Love and Rayleigh dispersion curves simultaneously. But we could fit the receiver function with either curve.

An Example Inversion In the joint inversion of a waveform with a dispersion curve, we also have to deal with the weighting of the two different data sets. If the data constrain orthogonal components of the model, the results are not too sensitive to the relative weights applied to the data sets. We have taken two approaches to solving this problem, first we have run a large number of inversions with different weighting factors to identify an influence parameter (relative weight) for the two data sets. Second, we have used a multiple objective optimization approach [Ammon, 2003], to map out a more objective weight selection approach. Both analyses suggest roughly the same value. For ease of reference, we repeat equation 3 here

$$\begin{pmatrix} pD_s \\ qD_r \\ \sigma\Delta \\ \epsilon W \end{pmatrix} \cdot m = \begin{pmatrix} r_s \\ r_r \\ 0 \\ 0 \end{pmatrix} + \begin{pmatrix} pD_s \\ qD_r \\ \sigma\Delta \\ \epsilon W \end{pmatrix} \cdot m_o$$

where the subscript r identifies receiver function quantities and the subscript s identifies surface-wave quantities. σ and ϵ control the importance of smoothing and *a priori* model constraints.

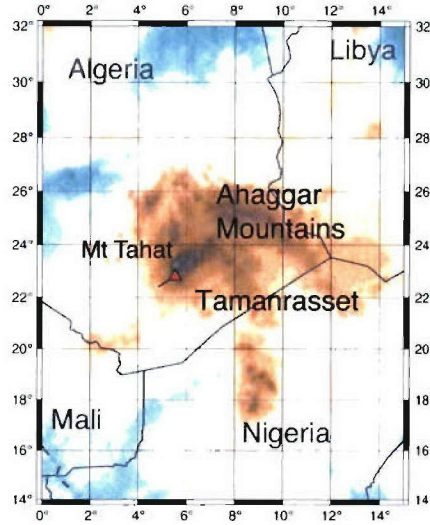


Figure 3.1: Location map for station TAM, used in the example inversions.

As an example, we present the several inversions of the data recorded at station TAM, Tamanrassett, Algeria (Figure 3.1). TAM is located within the Hoggar swell, an uplifted region in north-central Africa. Observations from the southwest are particularly clear at TAM and we use those for our illustration. We used a simple crustal model resting on a PREM mantle as the initial model, and ran each inversion for 5 iterations. Although we applied smoothing in the inversion, we did not incorporate any *a priori* information other than requiring the model to blend in to PREM below a depth of 200 km. Figure 3.2 shows the results for a receiver-function dominated inversion (influence parameter $p = 0.05$, $q = 1 - p = 0.95$). Love wave dispersion values are shown for reference but were not used in the inversion. Also shown is a low-frequency receiver function, which also was left out to simplify the inversion (but we have the capability and usually include different bandwidth receiver functions in the inversions). Even with most of the weight on the receiver function, the fit to the Rayleigh waves is reasonable. The solution obtained after reversing the weights is shown in Figure (3.3). The result here is smoother and the fit to the Rayleigh-wave dispersion values is excellent, but the fit to the receiver function, which requires some sharp boundaries, has degraded.

We can perform a systematic variation in the influence parameter to compute an optimal weight. The results of the systematic search are shown in Figure 3.4. The chart is a standard multiple objective optimization misfit diagram, that shows the ideal misfits and the misfits found for a range of influence parameter (labeled points). The point closest to the ideal fit is roughly 0.40. Inversion results for this balanced

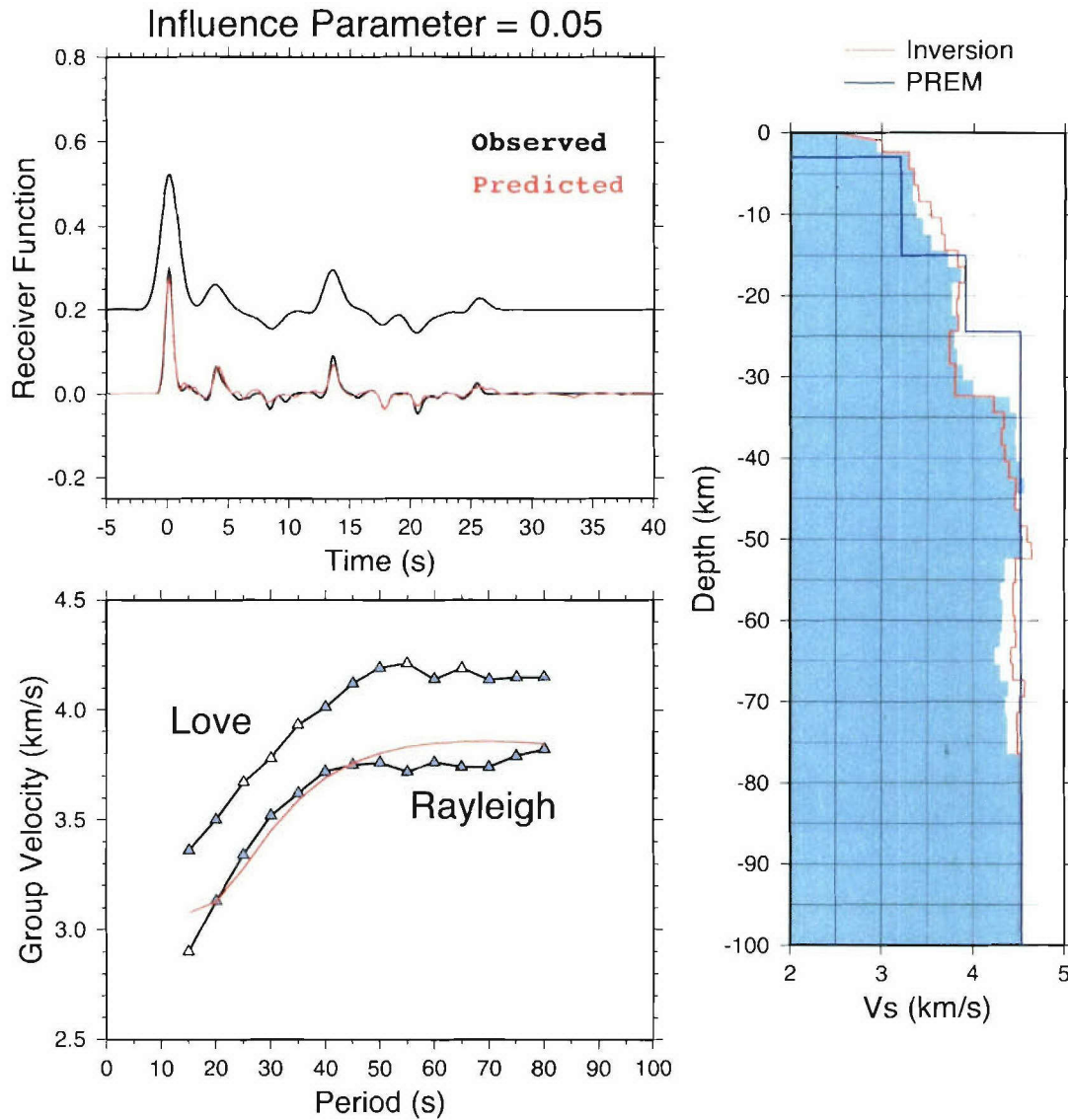


Figure 3.2: Sample inversion showing the fits to a broadband receiver function and Rayleigh dispersion. In this example the influence parameter is 0.05, which produces an inversion dominated by the receiver function. The model outlined in green is that obtained from a more balanced weight.

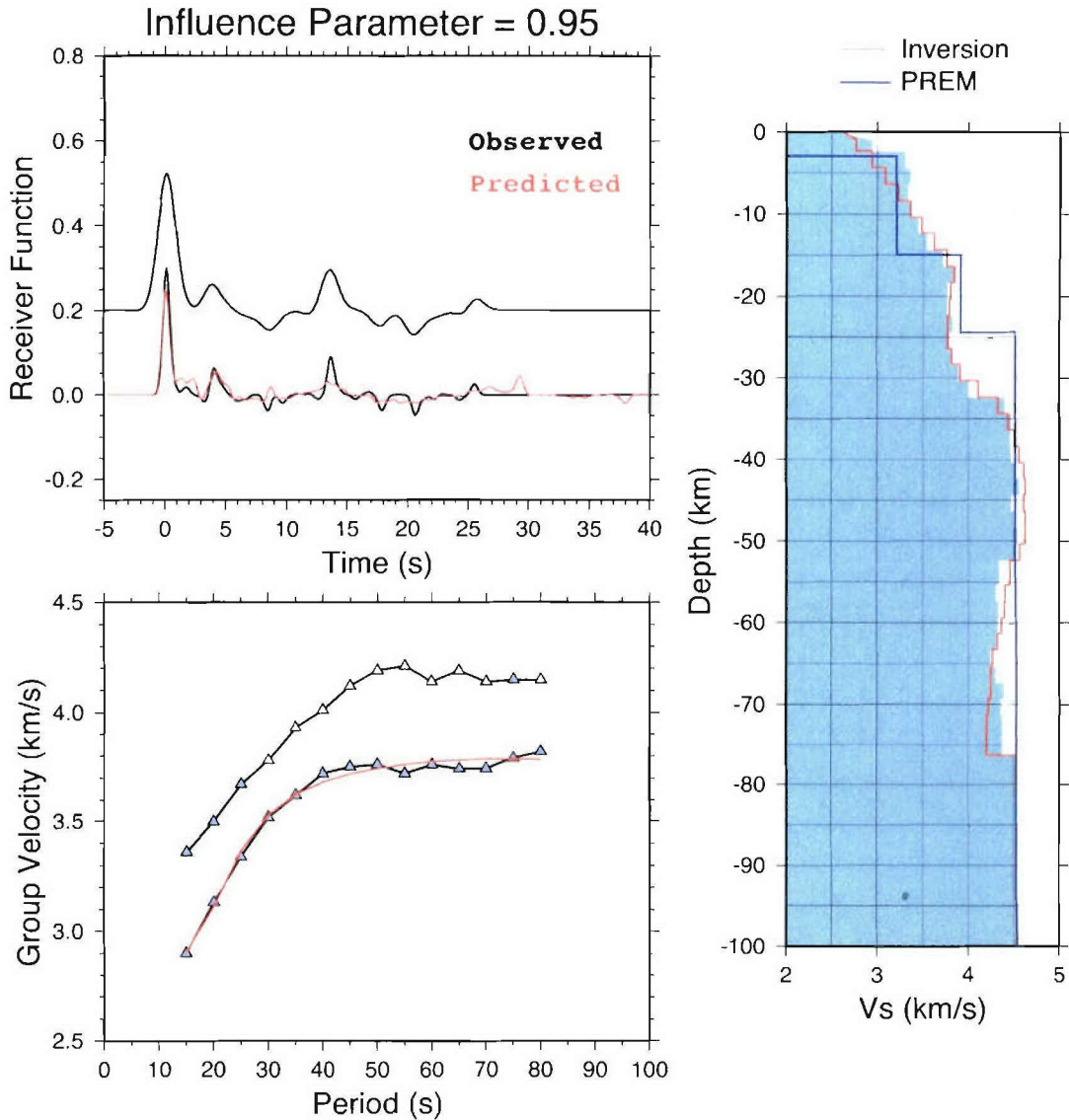


Figure 3.3: Sample inversion showing the fits to a broadband receiver function and Rayleigh dispersion. In this example the influence parameter is 0.95, which produces an inversion dominated by the dispersion (in this case, the Rayleigh waves). The model outlined in green is that obtained from a more balanced weight.

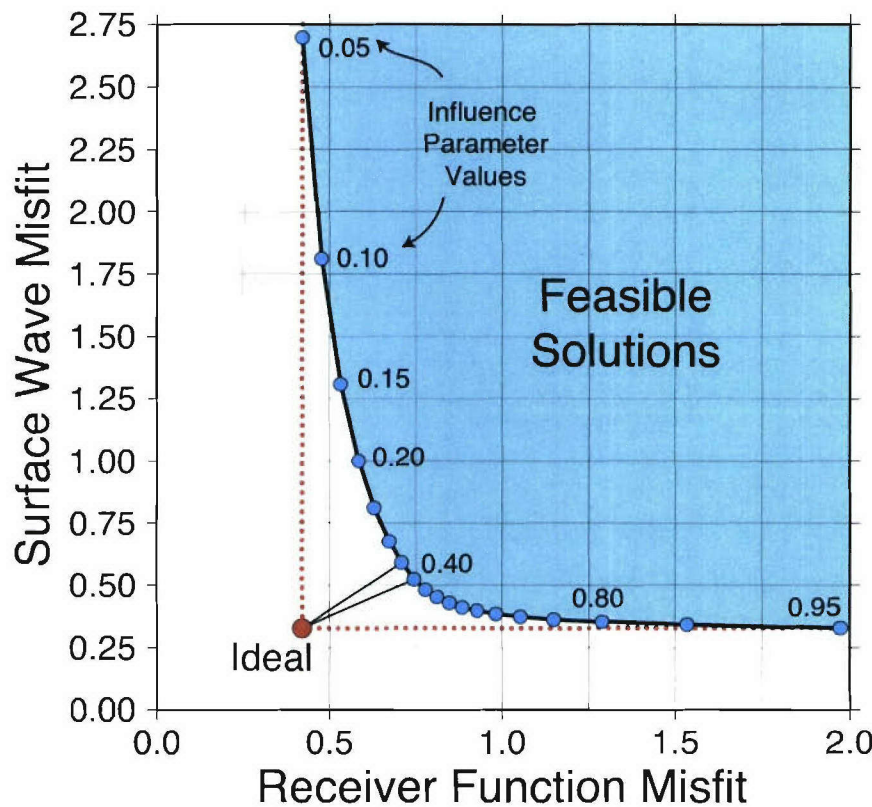


Figure 3.4: Multiple objective optimization misfit diagram showing the variation in misfit to the two data sets as for a range of influence parameters. The optimal influence parameter produces misfits closest to an ideal solution fit, that is identified by the point with coordinates given by the lowest misfit for each data set.

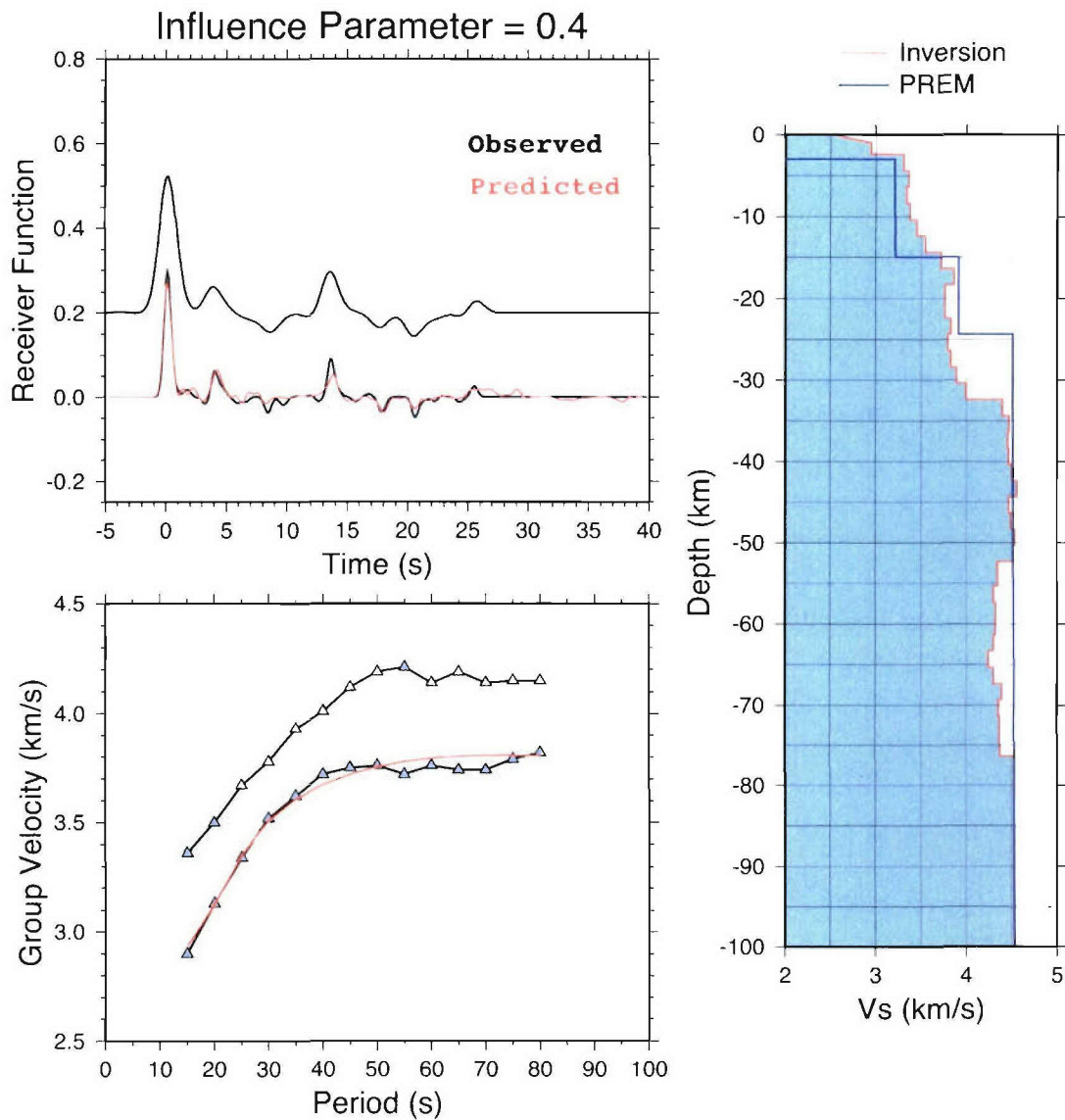


Figure 3.5: Sample inversion showing the fits to a broadband receiver function and Rayleigh dispersion. In this example the influence parameter is 0.40, which produces a balanced inversion.

weight are shown in Figure 3.5. The fit to both data sets in this case is superb (probably better than warranted) and the model is relatively smooth, but contains sharp features where needed, such as near the surface and near the crust-mantle boundary.

Shear-Velocity Models

Earth is not always amendable to simplified models of its structure. We have produced a library of one-dimensional shear velocity inversions to the lithosphere. These models are at best approximations to the true structure and should be thought of as only a first approximation to what's really at depth. But computer programs always provide and answer, but the answers vary in reliability. In an appendix we provide the results of all 171 shear-wave speed inversions. Not all of the results are reliable. We have ranked the receiver function quality in the tables contained in the appendices. Before using any results you should check the quality of the data. Checking the quality of the dispersion values is more difficult, since they are provided by another group and the inherent difficulties associated with estimating reliable uncertainties in tomography. These issue complicate the use of our shear-velocity models, and necessitate that people using the information must have a basic understanding of the nature of geophysical inverse problems and some understanding of seismic wave propagation.

The shear-velocity models can depend strongly on the group velocities used in the inversion. We have performed inversions using both the LLNL [Pasmanos and Walter, 2002] and the Harvard models Larson and Ekstrom, 2001]. When the dispersion models differ substantially, our estimates of the absolute velocities will diverge; velocity contrasts, controlled by the receiver functions, will be similar, but their depth may change to maintain the time lags of the corresponding arrivals observed on the receiver functions. Convergence in tomographic models to uniform dispersion models is the only way to remove such ambiguity.

Relatively Simple Radial Receiver Function Observations. A number of stations, predominantly on shields, exhibit relatively simple receiver function responses that are dominated by relatively sharp crust-mantle boundary arrivals. We list the simplest stations in Table 3.1 since these may provide ideal stations for studies needing to observe clear teleseismic observations for magnitude or for teleseismic depth estimation. One must remember that almost all receiver responses depend to

some extent on the incidence and angle and back azimuth, so some care will always be needed using these observations. Note that networks beginning with the letter X were temporary - the IRIS PASSCAL deployments.

Table 3.1: Stations With Simple Radial Receiver Function Observations

Network Code	Station Code(s)
AS	KAAO
CZ	DPC
G	ECH, SSB, TAM
GE	MALT, MTE, STU,
GT	BGCA
II	ESK, RAYN,
IU	KMBO, KOWA, MSKU
KZ	CHK, ZRN
MN	VSL, WDD
XD (Tanzania)	AMBA, KOND, LONG, MBWE, MITU, MTOR, PUGE, RUNG
XI (Arabia Shield)	AFIF, HALM, RANI, SODA,

Exceedingly Complex Receiver Function Observations. We list stations with exceedingly complex receiver functions in Table 3.2. Models derived from these data are unreliable and should not be used. In a few instances the complexity may be the result of sparse data, but some are simply indicative of seismic stations located in complex environments, and several are island stations, where the structure often has strong lateral variations. Other reasons for complexity may be proximity to large basins such as that found near station SFUC in southwestern Spain.

Table 3.2: Stations With Exceedingly Complex Structure

Network Code	Station Code(s)
GE	APEZ, MELI, SFS, SFUC, ZKR
MN	AIO, AQU, CEL, CUC, GFA, IDI, TUE, VAE
XG	HAMR, KARS, TTB01
XI	RIYD

Near-Surface Complexity Observations. Receiver functions are also quite useful for identifying regions with near-surface structural complexity. Most of the complex stations fall into this category, since they invariably have long-duration radial (and tangential) receiver functions that ring on for tens of seconds. Some observations also show substantial near surface complexity that lasts less than 10 seconds. This is generally an indication of near-receiver reverberations in a shallow structure underlain (or containing) strong elastic contrasts. At times the indication is simply a shift in the P-wave arrival in the receiver function, other times the P-wave is overwhelmed by a very strong P_s conversion from a less than a few kilometers depth. Stations whose receiver functions exhibit these characteristics are list in Table 3.3.

Table 3.3: Stations With Strong Near-Surface Structure Complexity

Network Code	Station Code(s)
G	MBO
GE	APEZ, CSS, FODE, KRIS, KWP, MELI, MRNI, NAI, PUL, RGN, SFS, SFUC, SKD, VSU, ZKR
II	ABKT, GAR, KIV
IU	TOL
MN	AIO, AQU, CEL, CII, CUC, IDI, MEB, TUE, VAE
SR	MAIO
XG	BYKN, DGSU, EZRM, HAMR, HINS, HUB03, KARS, TTB01
XI	RIYD

Using & Simplifying the Models

To some extent this simplifying assumption allows some freedom for those seeking to use the models as a starting point. Probably the best constrained parameters in the models are the vertical shear-wave travel times, which are constrained by the P_s wave observed on most of the receiver functions. Complexities in receiver functions tend to introduce more roughness into the structure, in an effort to fit small but common oscillations following the P-wave. These arrivals are at the level of waves scattered from lateral heterogeneity, and thus inferences drawn on one dimensional structures from them are not well constrained. They remain in the inversion results because the simple L2 norm metric of misfit does not distinguish them from the

larger, more important arrivals that are reasonably well fit (i.e. the residuals of the features are of comparable amplitudes). Some simplification is justified when using the models for other purposes. How much a model can be adjusted could be tested by comparing receiver functions and dispersion values for the original and modified models. Small changes in the models may not strongly affect the data used to constrain the model, but could improve predictions of other data substantially. For example, even a minor adjustment of the wave speed gradient beneath the crust could strongly affect Pn and Sn amplitudes. Modifications are best made with an eye on the original fits to the data and with some appreciation of what is geologically reasonable (Figure 3.6).

Software Availability

An implementation of the methods described above has been publicly available for about two years. The tools are integrated into Herrmann's Computer Programs in Seismology, and include documentation.

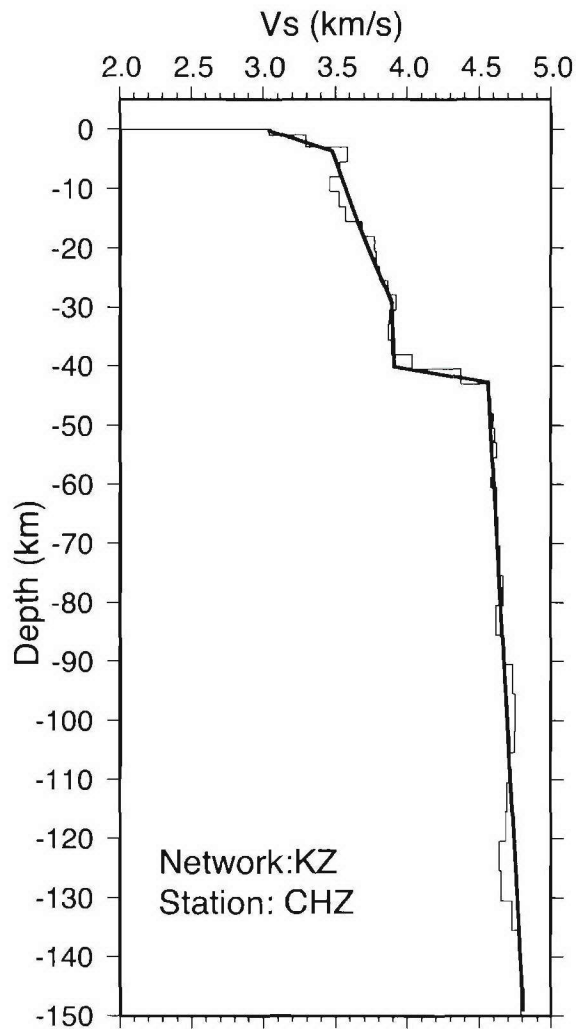


Figure 3.6: The shear-speed models are at best approximations to the true structure. Some simplification is justified when using the models for other purposes. How much a model can be adjusted could be tested by comparing receiver functions and dispersion values for the original and modified models. Modifications are best made with an eye on the original fits to the data and with some appreciation of what is geologically reasonable.

Appendix A

Station Summary Tables

In this appendix we include summary tables that list the locations, number of observations, and key results for each seismic station that we analyzed. The tables are arranged by crustal province, and each station is listed with its network code first, followed by the station code. We use a simple crustal classification based on the map found in Condie [1993] that includes shields, platforms, paleozoic orogenic regions, and mesozoic-cenozoic orogenic regions. Shields are platforms are generally similar, except for a sedimentary veneer, which covers the basement of platforms. Each result is ranked in the range from A to D, with A being the most reliable results. Specific uncertainties depend on the particular data used in any station analyses, but based on general assumptions, a rule of thumb uncertainty for crustal thickness is from 2 to 5 km. We've separated out three stations associated with the thick crust in the Pamir-Hindu Kush region. For information on Crust 2.0, please visit <http://mahi.ucsd.edu/Gabi/rem.dir/crust/crust2.html>.

Table A.1: Shield Station Observations

STATION	LAT	LON	ELV (m)	Data #	RFTN #	YEAR	LOCATION
G TAM 30<BAZ<80	22.8	5.53	1377	850	132	1990-04	Africa
G TAM 80<BAZ<360	22.8	5.53	1377	850	132	1990-04	Africa
GE NAI	-1.27	36.8	1992	62	23	1995	Africa
GT BGCA	5.17	18.42	676	353	208	1994-02	Africa
II MBAR	-6.01	30.74	1390	208	29	1999-02	Africa

continued on next page

Table A.1: *continued*

STATION	LAT	LON	ELV (m)	Data #	RFTN #	YEAR	LOCATION
IU FURI	8.9	36.69	2545	569	37	1997-02	Africa
IU KMBO	-1.12	37.25	1960	452	46	1995-02	Africa
IU KOWA	14.5	-4.01	321	39	5	1998-01	Africa
IU MSKU	-1.66	13.61	312	99	6	1999-00	Africa
XD AMBA	-8.11	33.26	1415	55	8	1994-95	Africa-Tanzania
XD BASO	-4.33	35.14	1694	77	12	1994	Africa-Tanzania
XD GOMA	-4.84	29.7	880	141	25	1994-95	Africa-Tanzania
XD HALE	-5.3	38.62	230	198	21	1994-95	Africa-Tanzania
XD INZA	-5.2	30.4	975	58	6	1994-95	Africa-Tanzania
XD KIBA	-5.32	36.57	1500	155	31	1994-95	Africa-Tanzania
XD KIBE	-5.37	36.47	997	228	20	1994-95	Africa-Tanzania
XD KOMO	-3.84	36.72	1114	157	24	1994-95	Africa-Tanzania
XD KOND	-4.9	35.8	1419	159	14	1994-95	Africa-Tanzania
XD LONG	-2.73	36.7	1380	127	22	1994-95	Africa-Tanzania
XD MBWE	-4.96	34.35	1100	136	19	1994-95	Africa-Tanzania
XD MITU	-6.1	34.06	1566	100	18	1994-95	Africa-Tanzania
XD MTAN	-7.91	33.32	1393	105	4	1994	Africa-Tanzania
XD MTOR	-5.25	35.4	1100	180	33	1994-95	Africa-Tanzania
XD PAND	-8.98	33.24	1248	101	12	1994-95	Africa-Tanzania
XD PUGE	-4.71	33.18	1350	113	20	1994-95	Africa-Tanzania
XD RUNG	-6.94	33.52	1230	160	25	1994-95	Africa-Tanzania
XD SING	-4.64	34.73	1462	187	21	1994-95	Africa-Tanzania
XD TARA	-3.89	36.02	1268	135	25	1994-95	Africa-Tanzania
XD TUND	-9.3	32.8	1660	126	14	1994-95	Africa-Tanzania
XD URAM	-5.08	32.08	1120	127	17	1994-95	Africa-Tanzania
MN WDD	35.87	41.52	41	474	57	1995-02	Arabian-Plate
IU KONO	59.65	9.6	216	3473	13	1991-04	Europe
IU KIEV	50.7	29.21	163	707	194	1995-03	Europe
XG HUB03	36.33	74.66	2469	446	48	1999-01	Middle-East
XG TRB01	35.6	75.22	2072	152	5	1996	Middle-East
XG TTB01	35.41	74.59	2610	17	5	1995	Middle-East
XI AFIF	23.93	43.04	1116	252	32	1995-97	Middle-East
XI BISH	19.92	42.69	1379	27	2	1995	Middle-East
XI HALM	22.84	44.32	930	343	31	1995-97	Middle-East
XI RANI	21.31	42.78	1001	204	18	1995-97	Middle-East
XI SODA	18.29	42.37	2876	289	41	1995-97	Middle-East
XI TAIF	21.28	40.34	2050	43	6	1996	Middle-East

continued on next page

Table A.1: *continued*

<i>STATION</i>	<i>LAT</i>	<i>LON</i>	<i>ELV</i> (m)	<i>Data</i> #	<i>RFTN</i> #	<i>YEAR</i>	<i>LOCATION</i>
XI UQSK	25.78	42.36	950	207	11	1996-97	Middle-East

Table A.2: Shield Station Results

STATION	H (km)	Vp/Vs	H(km) Crust2.0	Vp/Vs Crust2.0	TYPE Crust2.0	RANK	LOCATION
G TAM 30<BAZ<80	40	1.6	40	1.77	H1	B-C	Africa
G TAM 80<BAZ<360	33.8	1.79	40	1.77	H1	B-C	Africa
GE NAI	39.2	1.8	38	1.77	X5	B	Africa
GT BGCA	41.9	1.71	43	1.77	I1	A	Africa
II MBAR	34.7	1.55	39	1.77	G2	C	Africa
IU FURI	38.6	1.86	31	1.77	G9	C-D	Africa
IU KMBO	39.9	1.76	38	1.77	X5	A	Africa
IU KOWA	42.6	1.66	41	1.79	G3	C	Africa
IU MSKU	45.6	1.78	38	1.79	I2	C	Africa
XD AMBA	34.5	1.76	33	1.77	X2	B	Africa-Tanzania
XD BASO	38.2	1.67	38	1.77	X5	B-C	Africa-Tanzania
XD GOMA	43.3	1.78	43.5	1.77	GF	A	Africa-Tanzania
XD HALE	35.2	1.7	41	1.8	I3	B	Africa-Tanzania
XD INZA	38.9	1.77	41.5	1.76	GE	B	Africa-Tanzania
XD KIBA	39.2	1.72	36	1.77	IE	A	Africa-Tanzania
XD KIBE	38.1	1.7	36	1.77	IE	B	Africa-Tanzania
XD KOMO	37	1.71	38	1.77	X5	A	Africa-Tanzania
XD KOND	38.3	1.66	38	1.77	X5	A-B	Africa-Tanzania
XD LONG	38.5	1.7	38	1.77	X5	A-B	Africa-Tanzania
XD MBWE	36.5	1.75	38	1.77	X5	A	Africa-Tanzania
XD MITU	37.2	1.74	36	1.77	IE	A	Africa-Tanzania
XD MTAN	37.9	1.67	41.5	1.76	GE	B-C	Africa-Tanzania
XD MTOR	37.9	1.74	38	1.77	X5	A	Africa-Tanzania
XD PAND	32.4	1.8	33	1.77	X2	B	Africa-Tanzania
XD PUGE	35.7	1.77	37	1.76	G1	A	Africa-Tanzania
XD RUNG	39.2	1.79	41.5	1.76	GE	B	Africa-Tanzania
XD SING	38.5	1.78	38	1.77	X5	A-B	Africa-Tanzania
XD TARA	37.2	1.75	38	1.77	X5	A-B	Africa-Tanzania
XD TUND	34.6	1.7	33	1.77	X2	D	Africa-Tanzania
XD URAM	40.3	2	37	1.76	G1	C-D	Africa-Tanzania
MN WDD	35.7	1.69	36	1.81	ID	B	Arabian-Plate
IU KONO	32.2	1.71	32	1.82	T5	B-C	Europe
IU KIEV	39.5	1.79	41	1.78	DC	B	Europe
XG HUB03	50	1.66	65	1.76	R2	C-D	Middle-East
XG TRB01	71.6	1.69	65	1.76	R2	C	Middle-East
XG TTB01	68.8	1.68	65	1.76	R2	C	Middle-East

continued on next page

Table A.2: *continued*

<i>STATION</i>	<i>H</i> (km)	<i>Vp/Vs</i>	<i>H(km)</i> <i>Crust2.0</i>	<i>Vp/Vs</i> <i>Crust2.0</i>	<i>TYPE</i> <i>Crust2.0</i>	<i>RANK</i>	<i>LOCATION</i>
XI AFIF	36.4	1.75	43	1.77	I1	B	Middle-East
XI BISH	37.1	1.82	43	1.77	I1	B	Middle-East
XI HALM	34.6	1.79	41	1.79	D9	B	Middle-East
XI RANI	38.1	1.76	43	1.77	I1	B	Middle-East
XI SODA	38.4	1.74	43	1.77	I1	B	Middle-East
XI TAIF	37.4	1.74	36	1.77	IE	B	Middle-East
XI UQSK	36.5	1.74	43	1.77	I1	B	Middle-East

Table A.3: Platform Stations Observations

STATION	LAT	LON	ELV (m)	Data #	RFTN #	YEAR	LOCATION
G MBO	14.39	-16.96	3	81	12	2002-03	Africa
MN GFA	34.34	9.1	250	134	9	1990 1995-96	Africa
MN KEG	29.93	31.83	460	651	58	1990-99	Africa
GE SUW	54.01	23.18	152	1882	4	1995-04	Europe
G-GRC	47.295	3.074	191	336	35	2000-02	Europe
GE TIRR	44.46	28.41	77	82	11	2003-04	Europe
GE TRTE	58.4	26.7	0	654	42	1996-03	Europe
GE VSU	58.46	26.73	63	223	12	2003-04	Europe
G WUS	41.1	79.22	1457	2104	423	1990-02	Middle-East
GE BGIO	31.72	35.09	752	246	35	1994-96	Middle-East
GE EIL	29.67	34.95	717	210	138	2000-02	Middle-East
GE JER	31.77	35.2	770	495	89	1996-03	Middle-East
GE MHV	54.96	37.77	150	1669	263	1995-04	Middle-East
GE PUL	59.77	30.32	65	969	49	1998-03	Middle-East
II KIV 0<BAZ<90	43.96	42.69	1054	1350	284	1990-02	Middle-East
II KIV 90<BAZ<360	43.96	42.69	1054	1350	284	1990-02	Middle-East
II OBN	55.11	36.57	160	4512	244	1990-04	Middle-East
II RAYN	23.52	45.5	631	581	144	1997-02	Middle-East
IU GNI	40.15	44.74	1609	542	68	1991-02	Middle-East
KZ AKT	50.43	58.02	360	98	44	1994-99	Middle-East
KZ AKTK	50.43	58	360	702	77	1999-02	Middle-East
KZ PDG	43.32	79.48	1277	331	28	1999-02	Middle-East
XI RIYD	24.722	46.64	717	244	13	1996-97	Middle-East
XW AHQI	40.94	78.45	1959	72	29	1999-00	Middle-East

Table A.4: Platform Station Results

<i>STATION</i>	<i>H</i> (km)	<i>Vp/Vs</i>	<i>H(km)</i> <i>Crust2.0</i>	<i>Vp/Vs</i> <i>Crust2.0</i>	<i>TYPE</i> <i>Crust2.0</i>	<i>RANK</i>	<i>LOCATION</i>
G MBO	26.3	1.98	26	1.84	S8	C	Africa
MN GFA	36.7	1.89	36	1.8	DR	D	Africa
MN KEG	32.2	1.64	32	1.81	IH	B-C	Africa
G-GRC	29.3	1.77	31	1.8	M3	B	Europe
GE SUW	41.2	1.8	46	1.79	DE	C	Europe
GE TIRR	38.9	1.68	35	1.8	M4	B	Europe
GE TRTE	44.4	1.72	41	1.78	DC	B	Europe
GE VSU	42.6	1.74	41	1.78	DC	C	Europe
G WUS	54.1	1.71	50	1.76	QE	A-B	Middle-East
GE BGIO	33.9	1.74	32	1.81	T4	B-C	Middle-East
GE EIL	29.5	1.86	32	1.8	T6	B-C	Middle-East
GE JER	34.9	1.72	32	1.81	T4	A-B	Middle-East
GE MHV	49.6	1.61	46.5	1.79	H4	A-B	Middle-East
GE PUL	40.1	1.96	41	1.78	DC	C-D	Middle-East
II KIV 0<BAZ<90	38.3	1.92	43	1.78	PB	C-D	Middle-East
II KIV 90<BAZ<360	46	1.74	43	1.78	PB	C-D	Middle-East
II OBN	50	1.7	46.5	1.79	H4	B	Middle-East
II RAYN	38	1.77	41	1.79	D9	A	Middle-East
IU GNI	44.9	1.71	43	1.78	Q3	B	Middle-East
KZ AKT	44.6	1.97	50	1.76	PE	C-D	Middle-East
KZ AKTK	50.5	1.86	50	1.76	PE	C	Middle-East
KZ PDG	44.4	1.86	50	1.77	P4	B	Middle-East
XI RIYD	41.6	1.64	41	1.79	D6	B	Middle-East
XW AHQI	57.3	1.76	50	1.76	PE	B	Middle-East

Table A.5: Paleozoic Stations Observations

STATION	LAT	LON	ELV (m)	Data #	RFTN #	YEAR	LOCATION
CZ DPC 0<BAZ<80	50.36	16.41	760	936	170	1992-03	Europe
CZ DPC 80<BAZ<360	50.36	16.41	760	936	170	1992-03	Europe
G SSB	45.28	4.542	700	815	285	199002	Europe
GE DSB	53.25	-6.38	236	1741	89	1993-04	Europe
GE HLG	54.19	7.88	41	399	31	2001-04	Europe
GE IBBN	52.31	7.76	140	840	26	1999-04	Europe
GE KWP	49.63	22.71	463	1011	50	1999-04	Europe
GE MORC	49.78	17.54	740	895	275	1993-02	Europe
GE MTE	40.4	-7.54	815	402	64	1997-03	Europe
GE RGN	54.55	13.32	15	1591	134	1995-04	Europe
GE RUE	52.48	13.78	40	797	78	2000-04	Europe
GE SELV	37.24	-3.73	650	257	24	2002-03	Europe
GE SFS	36.47	-6.21	21	378	9	2001-04	Europe
GE WLF	49.7	6.15	295	845	211	1994-03	Europe
GR GRA1	49.69	11.22	499.5	2630	4	1990-04	Europe
II ESK	55.32	-3.21	242	2364	13	1990-04	Europe
IU GRFO	49.7	11.22	425	752	194	1994-02	Europe
IU PAB	39.54	-4.35	925	825	183	1992-02	Europe
IU TOL	39.9	-4.05	480	89	11	1991-92	Europe
II AAK 0<BAZ<80	42.64	74.49	1645	1200	172	1991-02	Middle-East
II AAK 80<BAZ<360	42.64	74.49	1645	1200	172	1991-02	Middle-East
II GAR	39	70.32	1300	115	23	1990-92	Middle-East
KN AML	42.13	73.69	3400	2298	339	1991-04	Middle-East
KZ BRVK	53.06	70.28	315	2390	514	1994-04	Middle-East
KZ CHK	53.68	70.6	120	690	144	1994-99	Middle-East
KZ KKAR	43.1	70.5	524.9	217	97	2003-04	Middle-East
KZ TLG	43.23	77.23	1120	1899	162	1994-02	Middle-East
KZ VOS	52.72	70.98	300	1364	330	1994-04	Middle-East
KZ ZRN	52.95	69	380	109	38	1994 & 1999	Middle-East

Table A.6: Paleozoic Station Results

STATION	H (km)	Vp/Vs	H(km) Crust2.0	Vp/Vs Crust2.0	TYPE Crust2.0	RANK	LOCATION
CZ DPC 0<BAZ<80	25.8	1.86	34	1.8	MD	B-C	Europe
CZ DPC 80<BAZ<360	29.8	1.74	34	1.8	MD	B	Europe
G SSB	27.1	1.69	31	1.8	M1	B	Europe
GE DSB	30.5	1.7	31	1.79	M5	B	Europe
GE HLG	28.8	1.74	31	1.82	C4	C	Europe
GE IBBN	30.9	1.76	31	1.8	M1	B-C	Europe
GE KWP	35.8	1.73	46	1.79	DE	B	Europe
GE MORC	31.6	1.79	31	1.79	M5	B	Europe
GE MTE	29	1.76	31	1.79	M5	B	Europe
GE RGN	29.6	1.73	31	1.8	M1	B	Europe
GE RUE	29.2	1.73	31	1.8	MH	B	Europe
GE SELV	41	1.84	32	1.81	T4	C-D	Europe
GE SFS	32	1.93	32	1.81	T4	D	Europe
GE WLF	28.8	1.78	31	1.8	M3	B	Europe
GR GRA1	29.2	1.83	31	1.8	M3	C-D	Europe
II ESK	28.2	1.82	31	1.79	M5	C	Europe
IU GRFO	29.7	1.76	31	1.8	M3	A	Europe
IU PAB	31.5	1.7	31	1.79	M5	A	Europe
IU TOL	33.2	1.73	31	1.79	M5	B	Europe
II AAK 0<BAZ<80	50	1.78	50	1.77	P4	B	Middle-East
II AAK 80<BAZ<360	53.6	1.63	50	1.77	P4	B	Middle-East
II GAR	54.5	1.75	50	1.77	P4	C	Middle-East
KN AML	53.3	1.93	45	1.77	PC	C-D	Middle-East
KZ BRVK	47.2	1.73	41	1.78	DC	B	Middle-East
KZ CHK	41.2	1.72	41	1.78	DC	B	Middle-East
KZ KKAR	40.2	1.65	45	1.77	PC	B	Middle-East
KZ TLG	46.4	1.72	50	1.77	P4	C	Middle-East
KZ VOS	38.2	2.1	41	1.78	DC	C-D	Middle-East
KZ ZRN	44.5	1.74	41	1.79	D9	B	Middle-East

Table A.7: Mesozoic-Cenozoic Stations Observations

STATION	LAT	LON	ELV (m)	Data #	RFTN #	YEAR	LOCATION
GE MELI	35.29	-2.94	40	732	18	1999-04	Africa
MN MDT	32.82	-4.61	1200	159	34	1990-91	Africa
						1994-95	
MN MEB	36.3	2.73	500	106	13	1992-93	Africa
G ATD	11.53	42.85	610	780	192	1993-02	Africa-Rift
G ECH	48.22	7.15	580	874	194	1990-02	Europe
GE APE	37.07	25.53	620	596	41	2000-04	Europe
GE APEZ	34.98	24.89	435	528	30	2000-03	Europe
GE CART	37.59	-1	65	1042	56	1997-04	Europe
GE FODE	35.38	24.96	50	556	41	2000-03	Europe
GE GVD	34.84	24.09	180	731	7	1999-03	Europe
GE KRIS	35.18	25.5	850	898	55	1998-04	Europe
GE MAHO	39.9	4.27	15	738	32	1999-04	Europe
GE MLR	45.5	25.95	1378	678	53	1994-02	Europe
GE PSZ	47.92	19.9	549	1046	178	1995-04	Europe
GE SANT	36.37	25.46	540	942	11	1998-04	Europe
GE SFUC	36.64	-6.17	88	406	38	1996-01	Europe
GE SKD	35.41	23.93	306	950	83	1998-04	Europe
GE STU	48.77	9.2	360	842	218	1994-03	Europe
GE ZKR	35.11	26.22	270	87	4	2003-04	Europe
II BFO	48.33	8.33	589	551	83	1996-02	Europe
MN AIO	37.97	15.23	751.4	248	2	2001-03	Europe
MN AQU	42.35	13.41	710	1033	140	1990-03	Europe
MN BGY	44.8	20.52	250	224	28	1991-95 1997-98	Europe
MN BNI	45.1	6.68	1395	549	48	1990-92 1996-03	Europe
MN CEL	38.26	15.89	702	50	5	2003-04	Europe
MN CII	41.72	14.03	910	405	7	1994-96 1999-02	Europe
MN CLTB	37.58	13.22	949	274	16	2001-04	Europe
MN CUC	39.99	15.81	637	81	9	2003-04	Europe
MN IDI	35.29	24.89	750	524	37	1996-04	Europe
MN TRI	45.71	13.25	161	222	71	1996-99 & 2003	Europe
MN TUE	46.47	9.35	1924	272	2	2001-04	Europe
MN VAE	37.47	14.35	735.1	280	1	2001-03	Europe
MN VSL	39.5	9.4	370	1001	229	1990-03	Europe

continued on next page

Table A.7: *continued*

<i>STATION</i>	<i>LAT</i>	<i>LON</i>	<i>ELV</i> (m)	<i>Data</i> #	<i>RFTN</i> #	<i>YEAR</i>	<i>LOCATION</i>
MN VTS	42.62	2.24	1490	391	141	1996-02	Europe
AS KAAO	34.54	69.04	19	1079	72	1977-82	Middle-East
GE CSS	34.96	33.33	396	1026	221	1999-04	Middle-East
GE ISP	37.84	30.51	1100	500	113	1996-03	Middle-East
GE KSDI	33.19	35.7	123	402	31	2002-04	Middle-East
GE MALT	38.31	38.43	1120	714	160	2000-04	Middle-East
II ABKT	37.93	58.12	678	622	293	1993-02	Middle-East
II NIL	33.65	73.27	629	652	23	1994-00	Middle-East
IL IR1	35.42	50.69	200	209	50	1976-79	Middle-East
IL IR2	35.67	50.9	200	209	18	1976-79	Middle-East
IL IR3	35.48	51.02	200	209	40	1976-79	Middle-East
IL IR4	35.24	50.9	200	209	17	1976-79	Middle-East
IL IR5	35.21	50.58	200	209	12	1976-79	Middle-East
IL IR6	35.47	50.43	200	209	7	1976-79	Middle-East
IL IR7	35.7	50.61	200	209	33	1976-79	Middle-East
IU ANTO	39.87	32.79	883	376	70	1992-98	Middle-East
SR MAIO	36.3	59.5	1000	572	84	1975-78	Middle-East
XG AGIN	38.94	38.71	945	356	30	1999-01	Middle-East
XG AHLT	38.75	42.48	1738	282	34	1999-01	Middle-East
XG BNGL	38.9	40.6	1160	440	72	1999-01	Middle-East
XG BTLS	38.43	42.12	1722	327	43	1999-01	Middle-East
XG BYBT	40.23	40.26	1684	301	29	1999-01	Middle-East
XG BYKN	38.17	41.78	816	230	41	1999-01	Middle-East
XG CMCY	39.92	43.2	1995	295	34	1999-01	Middle-East
XG DGRL	41.06	43.33	2027	358	48	1999-01	Middle-East
XG DGSU	39.13	42.73	1646	175	18	1999-01	Middle-East
XG DYBR	37.82	40.32	619	337	38	1999-01	Middle-East
XG ERGN	38.26	39.73	922	445	47	1999-01	Middle-East
XG EZRM	40.1	41.36	1910	442	29	1999-01	Middle-East
XG HAMR	39.61	42.99	1714	239	26	1999-01	Middle-East
XG HINS	39.35	41.7	1727	317	70	1999-01	Middle-East
XG HRPT	38.7	39.25	142	429	78	1999-01	Middle-East
XG HRSN	39.94	42.29	1800	446	32	1999-01	Middle-East
XG ILIC	39.45	38.57	1300	223	50	1999-01	Middle-East
XG IMRL	39.88	38.12	1708	172	7	1999-01	Middle-East
XG KARS	40.62	43.07	1904	190	39	1999-01	Middle-East
XG KOTK	40.22	43	1396	247	55	1999-01	Middle-East

continued on next page

Table A.7: *continued*

<i>STATION</i>	<i>LAT</i>	<i>LON</i>	<i>ELV</i> (m)	<i>Data</i> #	<i>RFTN</i> #	<i>YEAR</i>	<i>LOCATION</i>
XG KRLV	39.37	40.99	1894	381	34	1999-01	Middle-East
XG KTLN	37.95	41.7	791	228	20	1999-01	Middle-East
XG KYPR	37.56	41.17	1179	274	62	1999-01	Middle-East
XG MRDN	37.29	40.7	674	425	61	1999-01	Middle-East
XG MSDY	40.46	37.78	1152	458	52	1999-01	Middle-East
XG MUSH	38.76	41.48	1554	317	49	1999-01	Middle-East
XG SILN	38.14	41.04	917	237	38	1999-01	Middle-East
XG SIRN	40.2	39.12	1496	445	62	1999-01	Middle-East
XG UZML	39.71	39.72	1593	579	2	1999-01	Middle-East

Table A.8: Mesozoic-Cenozoic Station Results

STATION	H (km)	Vp/Vs	H(km) Crust2.0	Vp/Vs Crust2.0	TYPE Crust2.0	RANK	LOCATION
GE MELI	34.7	1.52	32	1.81	T4	C	Africa
MN MDT	33.2	1.72	36	1.77	IE	B	Africa
MN MEB	26.2	1.9	24.5	1.86	S3	C	Africa
G ATD	22.6	1.73	17	1.79	X4	B-C	Africa-Rift
G ECH	25.1	1.72	31	1.8	M3	C	Europe
GE APE	21.5	1.75	26.5	1.86	S4	B	Europe
GE APEZ	29.8	2.1	27	1.86	S5	D	Europe
GE CART	20.6	1.79	24.5	1.86	S6	C	Europe
GE FODE	31.7	1.7	27	1.86	S5	C	Europe
GE GVD	26	1.77	27	1.86	S5	C	Europe
GE KRIS	28.2	1.81	27	1.86	S5	C	Europe
GE MAHO	19.6	1.7	18	1.89	B8	B	Europe
GE MLR	34.26	1.64	34.5	1.8	MD	C	Europe
GE PSZ	27.5	1.75	27.5	1.8	ME	B	Europe
GE SANT	26.5	1.81	26.5	1.86	S4	C	Europe
GE SFUC	32.25	1.64	32	1.81	T4	C	Europe
GE SKD	37.5	1.96	26	1.84	S8	D	Europe
GE STU	24.3	1.75	27.5	1.79	MG	A	Europe
GE KRIS	28.2	1.81	27	1.86	S5	C	Europe
GE ZKR	32.9	2	27	1.86	S5	C	Europe
II BFO	26.1	1.66	27.5	1.8	MG	B	Europe
MN AIO	31.2	1.99	26.5	1.86	S4	D	Europe
MN AQU	37.52	1.7	31	1.79	M5	B	Europe
MN BGY	27.12	1.78	31	1.79	M5	B	Europe
MN BNI	44.9	1.86	38	1.77	PA	B	Europe
MN CEL	27	1.83	24.5	1.86	S6	B-C	Europe
MN CII	32	1.84	31	1.8	M1	C-D	Europe
MN CLTB	30.1	1.78	26	1.83	S7	C	Europe
MN CUC	17.9	1.91	24.5	1.86	S6	C	Europe
MN IDI	28.8	1.68	27	1.86	S5	C	Europe
MN TRI	36	1.77	37	1.8	M8	B	Europe
MN TUE	30.1	1.88	38	1.77	PA	C	Europe
MN VAE	26.5	1.79	26.5	1.86	S4	C-D	Europe
MN VSL	30.6	1.69	22	1.82	S1	B	Europe
MN VTS	38.1	1.73	36	1.79	MG	B	Europe
AS KAAO	45	1.89	38	1.79	DT	D	Middle-East
GE CSS	35.9	1.91	24.5	1.86	S6	C-D	Middle-East

continued on next page

Table A.8: *continued*

STATION	H (km)	Vp/Vs	H(km) Crust2.0	Vp/Vs Crust2.0	TYPE Crust2.0	RANK	LOCATION
GE ISP	36	1.68	38	1.78	P2	B-C	Middle-East
GE KSDI	30.5	1.89	26.5	1.86	S4	C	Middle-East
GE MALT	37.3	1.54	43	1.77	P6	B	Middle-East
II ABKT	41.8	1.7	46	1.79	DE	B-C	Middle-East
II NIL	51	1.76	50	1.78	PP	B	Middle-East
IL IR1	48	1.77	41	1.79	D9	C	Middle-East
IL IR2	43.2	1.82	41	1.79	D9	C	Middle-East
IL IR3	45.18	1.8	41	1.79	D9	C	Middle-East
IL IR4	42	1.96	41	1.79	D9	D	Middle-East
IL IR5	49	1.85	41	1.79	D9	D	Middle-East
IL IR6	44.7	1.87	41	1.79	D9	D	Middle-East
IL IR7	41.5	1.88	41	1.79	D9	C	Middle-East
IU ANTO	35	1.71	46	1.77	P1	B-C	Middle-East
SR MAIO	48.43	1.77	46	1.79	DE	C	Middle-East
XG AGIN	37.3	1.76	43	1.77	P6	B	Middle-East
XG AHLT	42.9	1.76	43	1.77	P6	B-C	Middle-East
XG BNGL	42.8	1.84	43	1.77	P6	B-C	Middle-East
XG BTLS	40.5	1.83	43	1.77	P6	C	Middle-East
XG BYBT	38.8	1.89	36	1.79	DQ	C	Middle-East
XG BYKN	46.2	1.63	43	1.77	P6	B-C	Middle-East
XG CMCY	41.7	1.83	43	1.77	P6	D	Middle-East
XG DGRL	37	1.86	39	1.76	Q2	C-D	Middle-East
XG DGSU	41	1.84	43	1.77	P6	C	Middle-East
XG DYBR	35.3	1.67	36	1.78	Q5	C	Middle-East
XG ERGN	45.2	1.7	43	1.77	P6	C-D	Middle-East
XG EZRM	40.3	1.79	36	1.79	DQ	C-D	Middle-East
XG HAMR	45.6	1.69	43	1.77	P6	C	Middle-East
XG HINS	44.2	1.57	43	1.77	P6	C	Middle-East
XG HRPT	35.6	1.81	43	1.77	P6	CD	Middle-East
XG HRSN	41	1.81	43	1.77	P6	C	Middle-East
XG ILIC	42	1.91	43	1.77	P6	C	Middle-East
XG IMRL	43.3	1.84	43	1.77	P6	C	Middle-East
XG KARS	36.5	2.17	39	1.76	Q2	D	Middle-East
XG KOTK	40.9	1.83	39	1.76	Q2	C	Middle-East
XG KRLV	40.4	1.83	43	1.77	P6	C	Middle-East
XG KTLN	24.7	2.19	36	1.78	Q5	D	Middle-East
XG KYPR	32.6	1.85	36	1.78	Q5	C	Middle-East

continued on next page

Table A.8: *continued*

<i>STATION</i>	<i>H</i> (km)	<i>Vp/Vs</i>	<i>H(km)</i> <i>Crust2.0</i>	<i>Vp/Vs</i> <i>Crust2.0</i>	<i>TYPE</i> <i>Crust2.0</i>	<i>RANK</i>	<i>LOCATION</i>
XG MRDN	35.9	1.76	36	1.78	Q5	B	Middle-East
XG MSDY	38.1	1.84	41	1.79	D6	C-D	Middle-East
XG MUSH	44.7	1.75	43	1.77	P6	C	Middle-East
XG SILN	41.3	1.64	43	1.77	P6	C	Middle-East
XG SIRN	38.5	1.68	38	1.8	D3	C	Middle-East
XG UZML	40.4	1.79	43	1.77	P6	D	Middle-East

Table A.9: Pamir Stations Observations

<i>STATION</i>	<i>LAT</i>	<i>LON</i>	<i>ELV</i> (m)	<i>Data</i> #	<i>RFTN</i> #	<i>YEAR</i>	<i>LOCATION</i>
XG HUB03	36.33	74.66	2469	446	75	1999-01	Middle-East
XG TRB01	35.6	75.22	2072	152	5	1996	Middle-East
XG TTB01	35.41	74.59	2610	17	5	1995	Middle-East

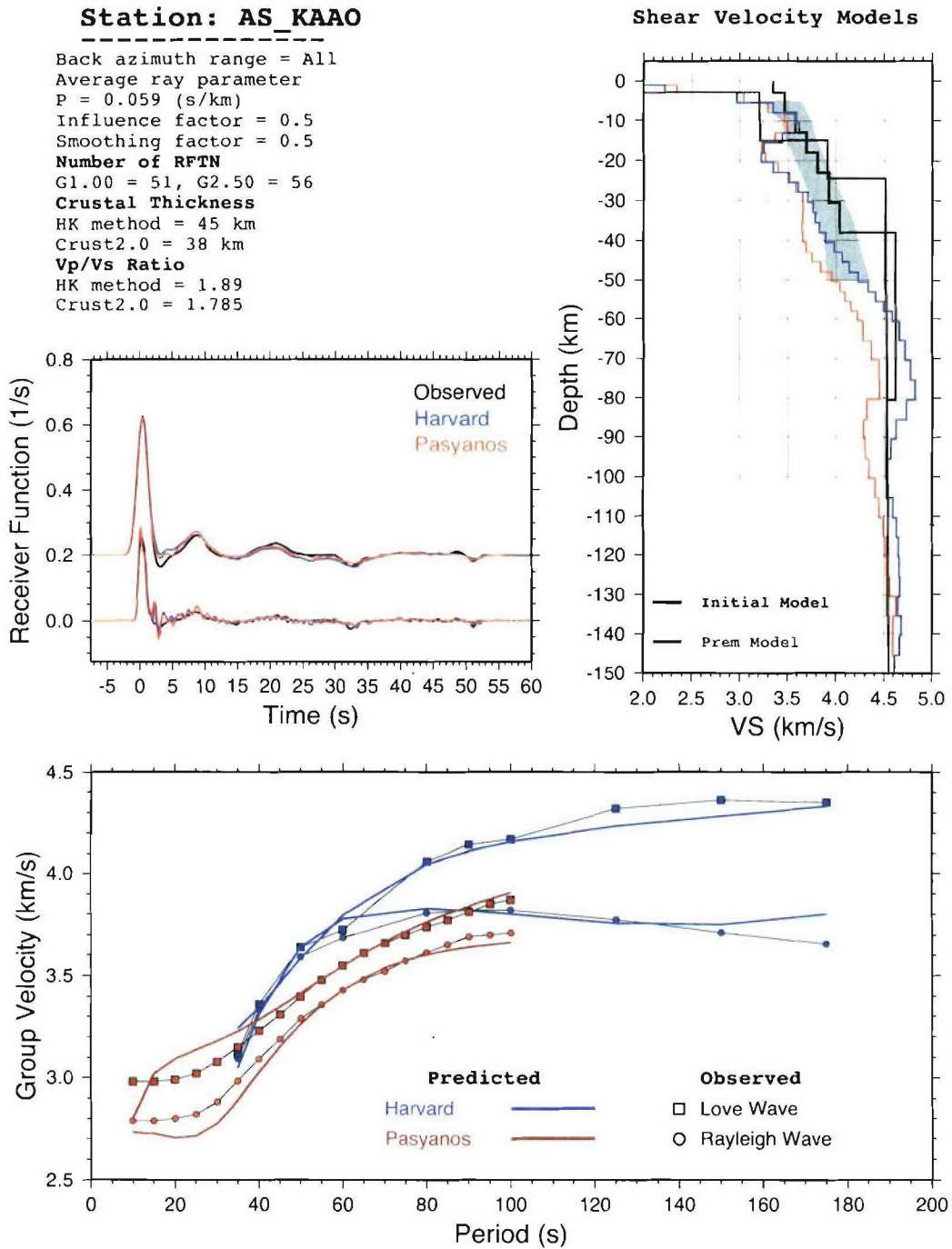
Table A.10: Pamir Station Results

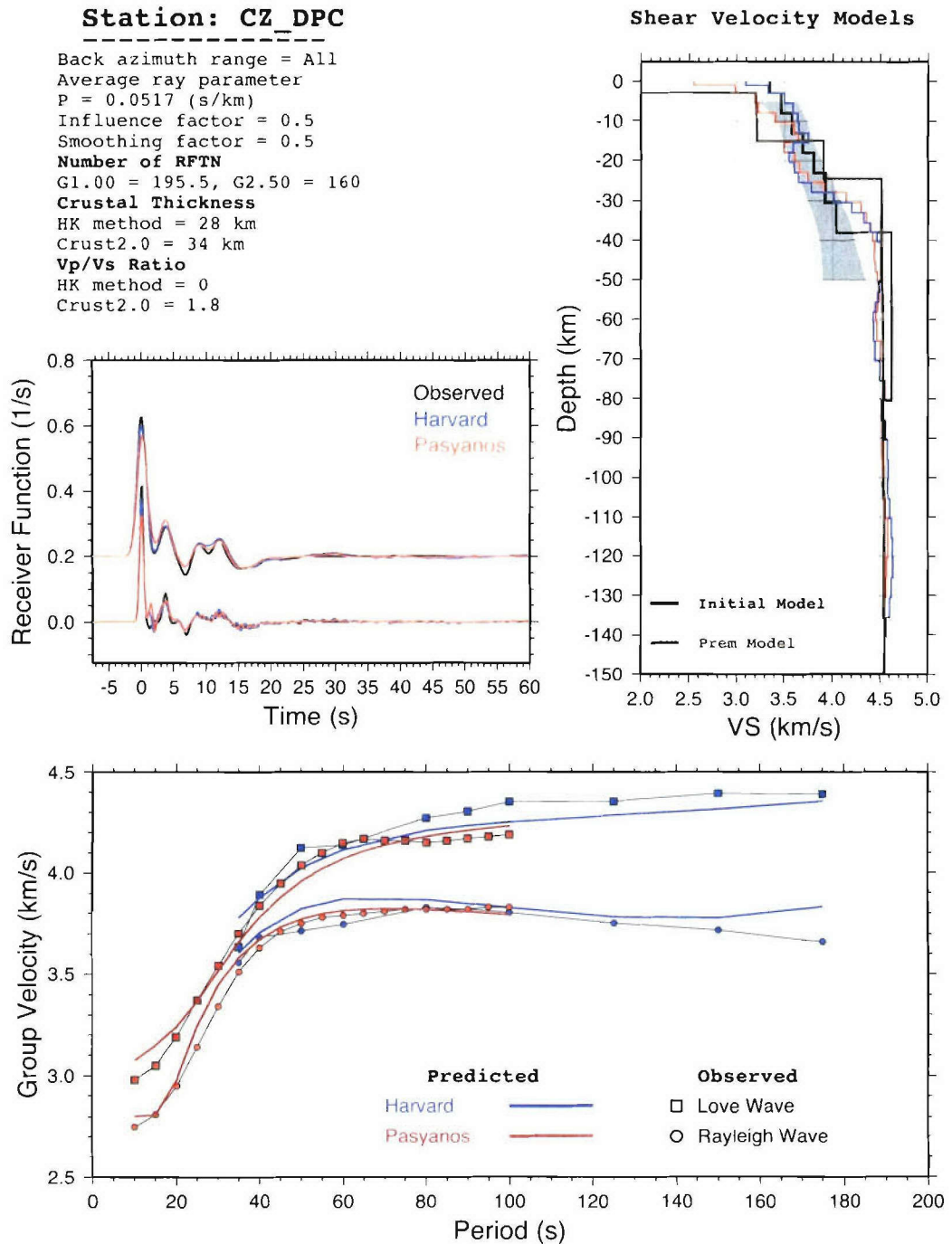
<i>STATION</i>	<i>H</i> (km)	<i>Vp/Vs</i>	<i>H(km)</i> <i>Crust2.0</i>	<i>Vp/Vs</i> <i>Crust2.0</i>	<i>TYPE</i> <i>Crust2.0</i>	<i>RANK</i>	<i>LOCATION</i>
XG HUB03	50	1.66	65	1.76	R2	C-D	Middle-East
XG TRB01	71.6	1.69	65	1.76	R2	C	Middle-East
XG TTB01	68.8	1.68	65	1.76	R2	C	Middle-East

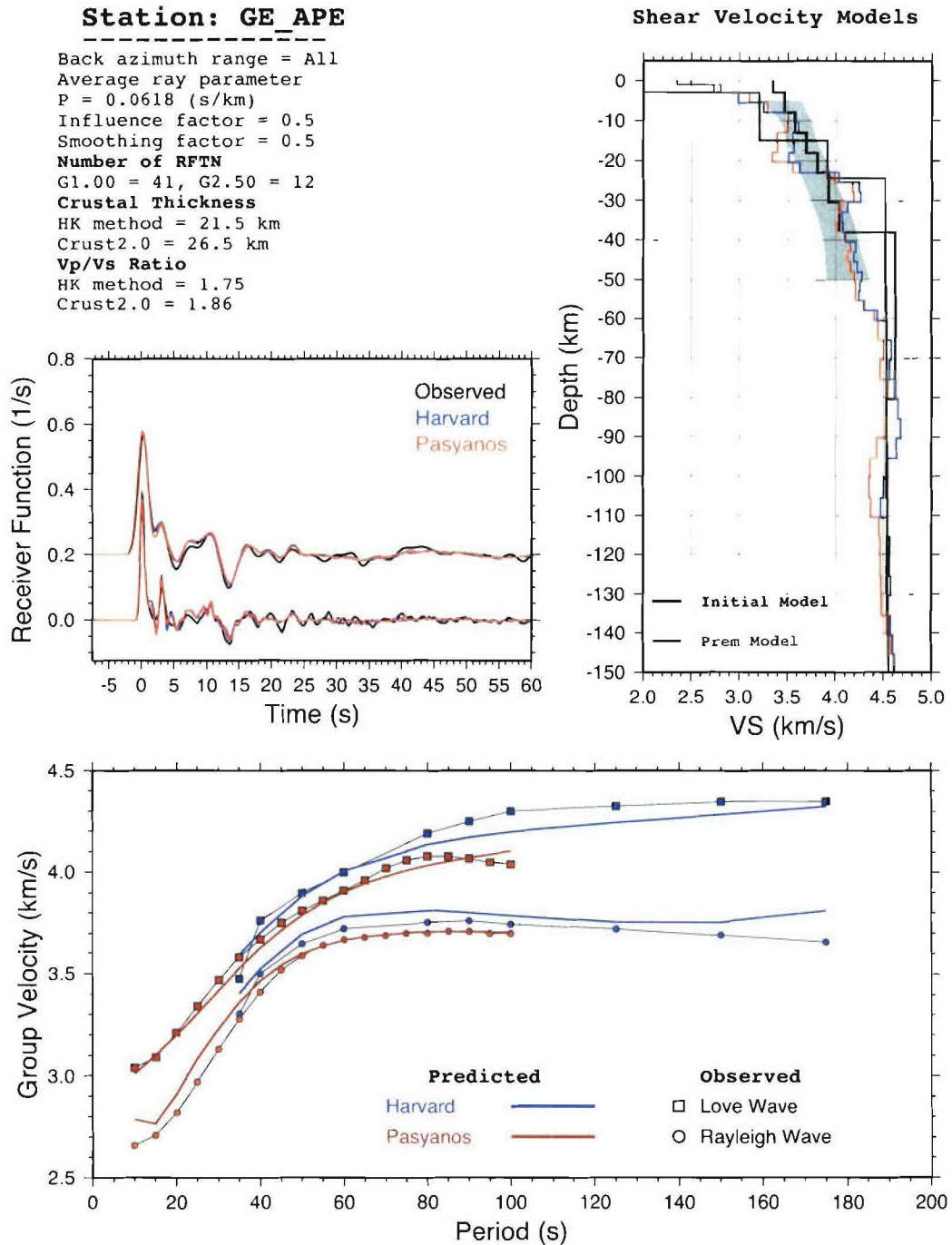
Appendix B

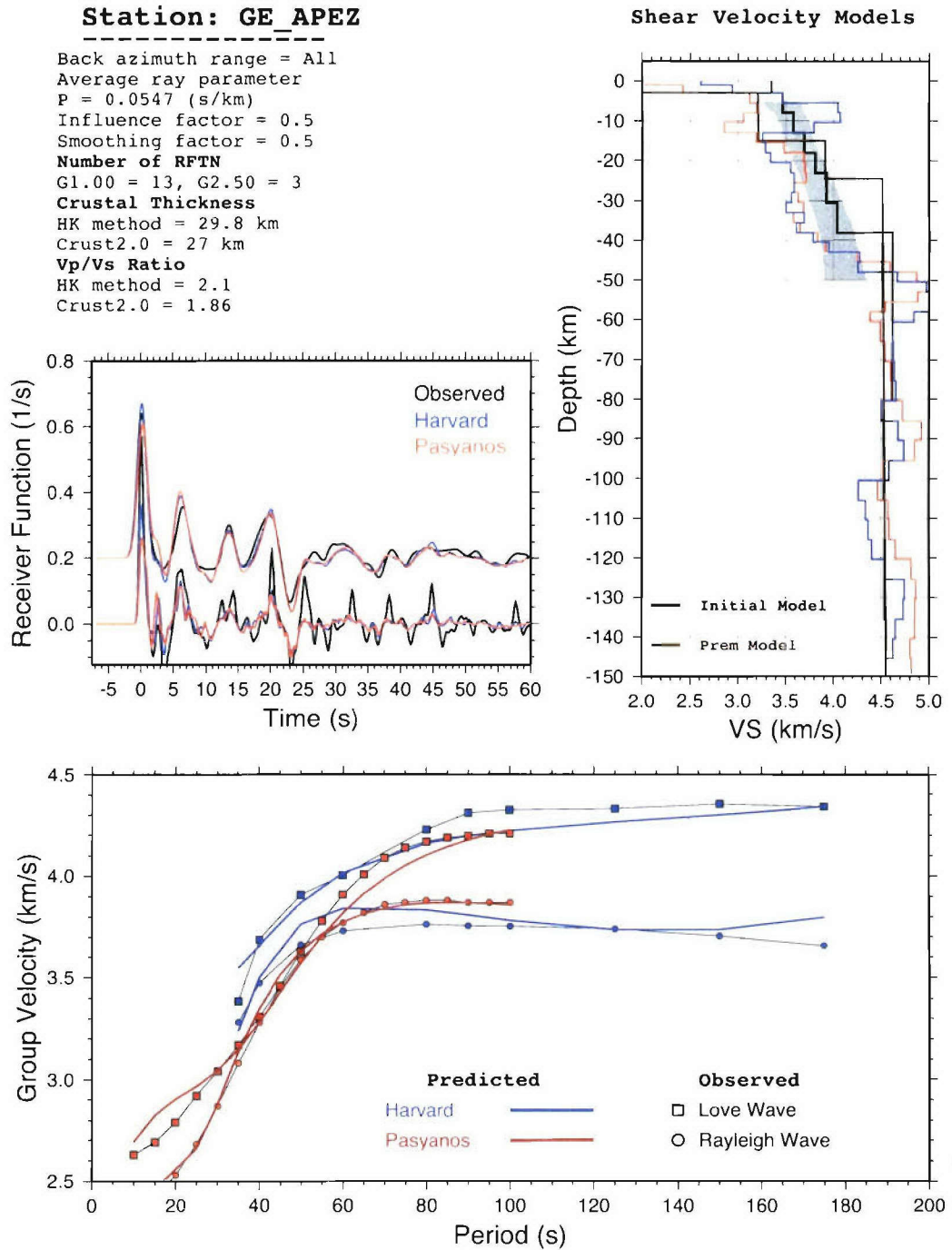
Inversion Summaries

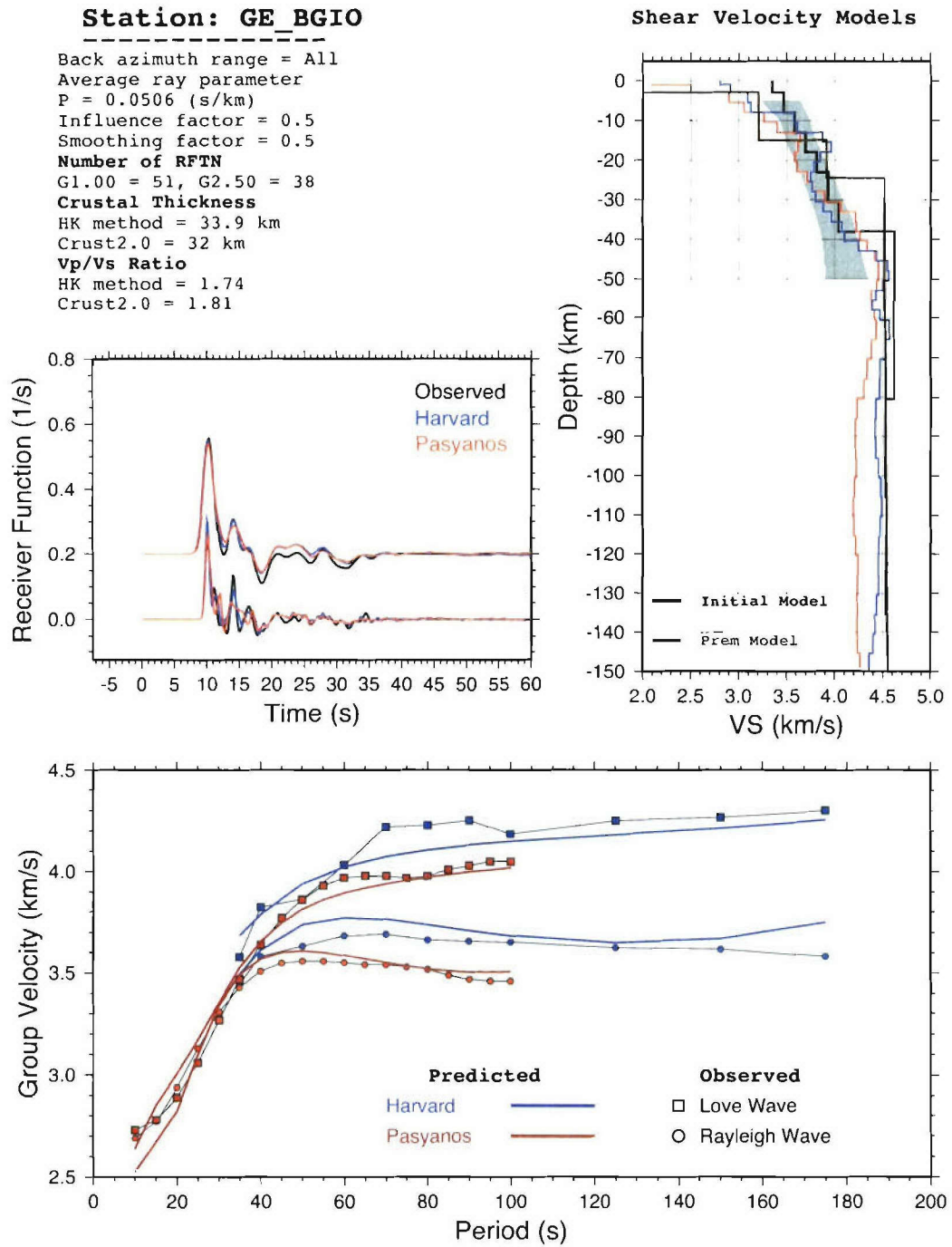
In this appendix we include summaries for each of the 171 stations for which we have attempted a shear-wave speed inversion. Please note, this is a complete summary and we do not believe that all observations could be explained with these relatively simple isotropic plane-layered earth models. These data generally result in wild shear-wave speed models, that are unacceptable in terms of simplicity or any understanding of rock physics. Data of quality D in the summary tables in the previous appendix identify stations that we think were too complicated or had too little data to produce a reliable result. Each page summarizes the results at one station. The upper left shows some summary results from the H-K stacking, and the azimuth and ray parameter ranges. Receiver functions from two band widths are included in each inversion. The red curves correspond to an analysis based on the Harvard group velocity model, the blue to the LLNL group velocity model. The gray region shows the range of typical crustal shear-wave speeds reported in Christensen and Mooney [1995].

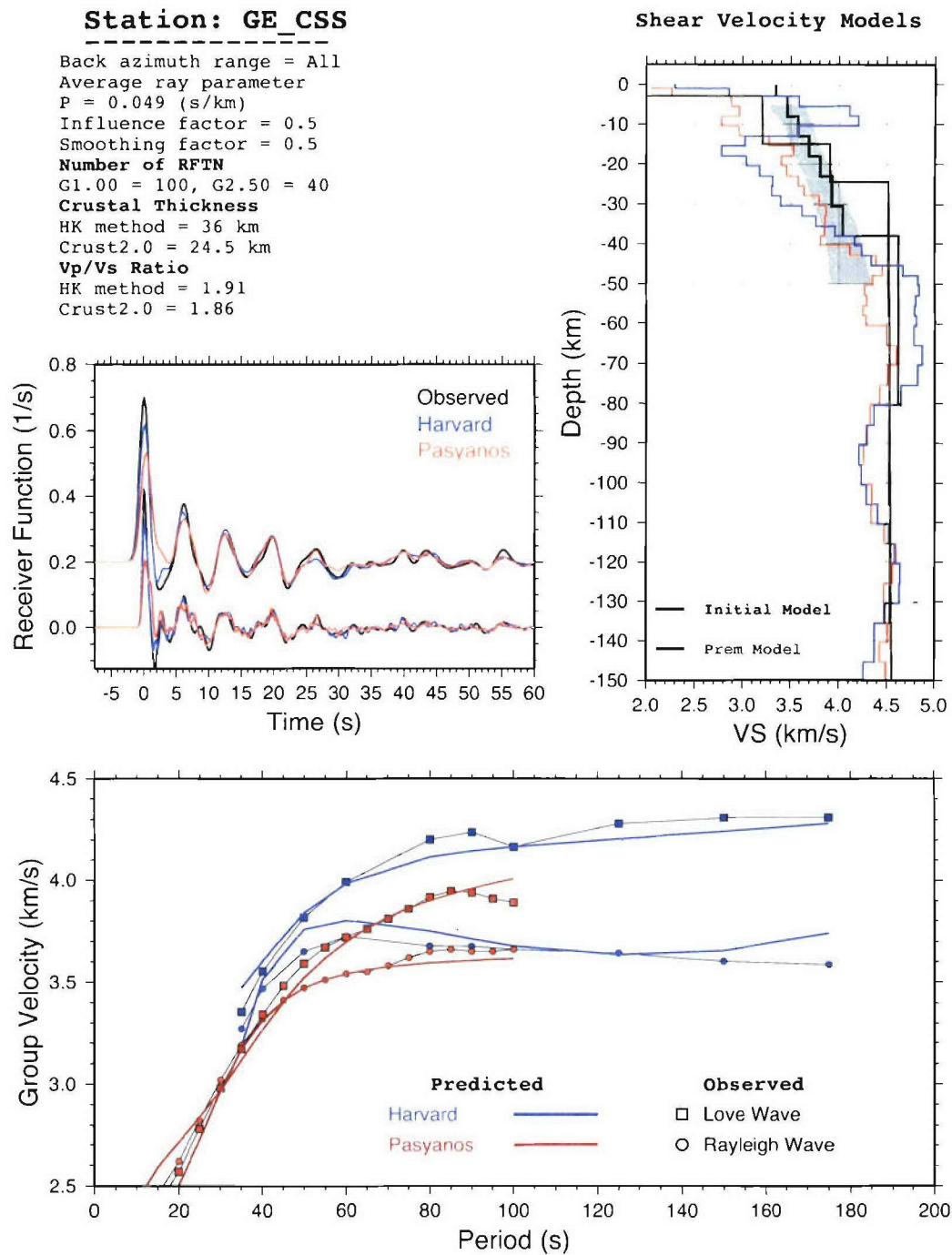


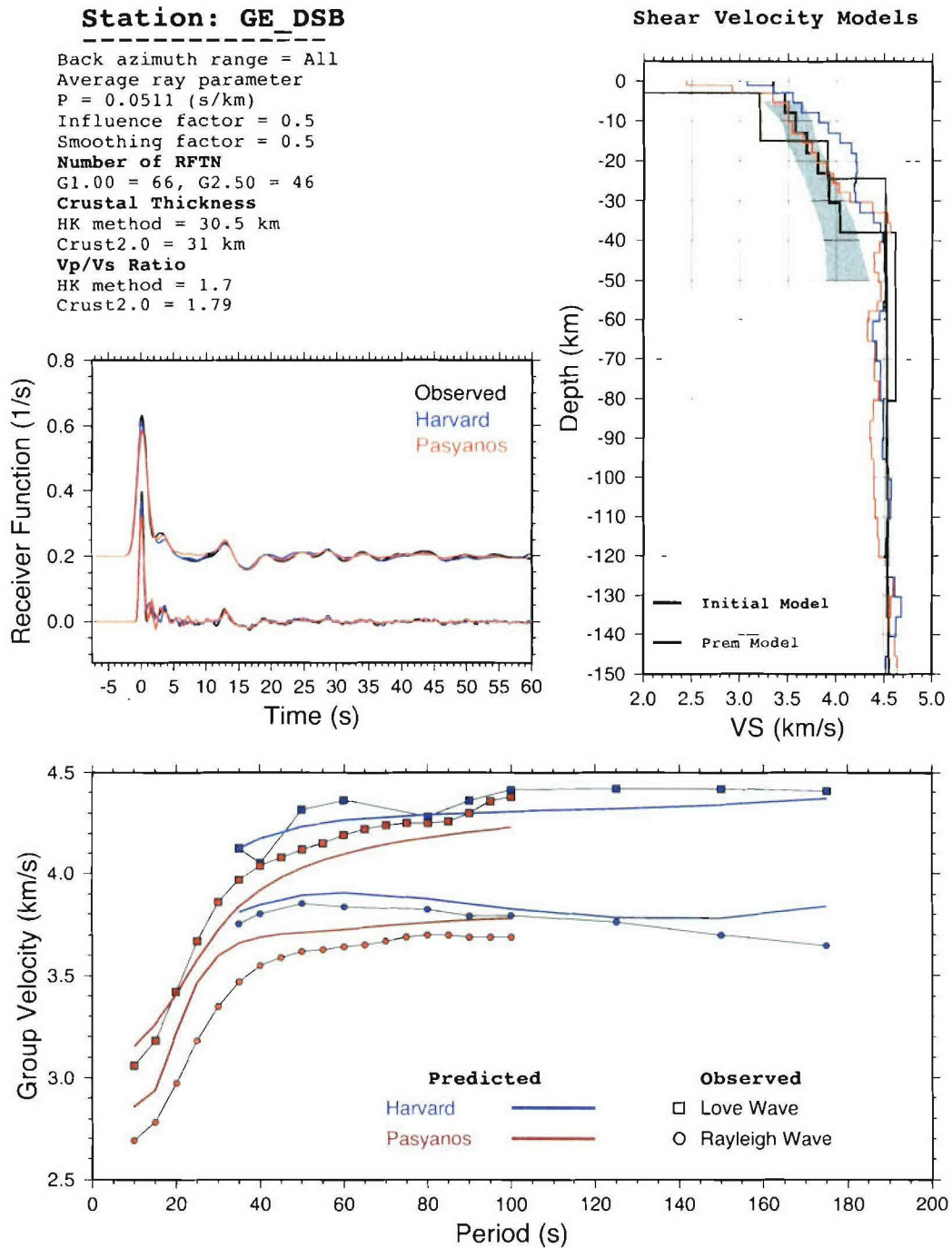


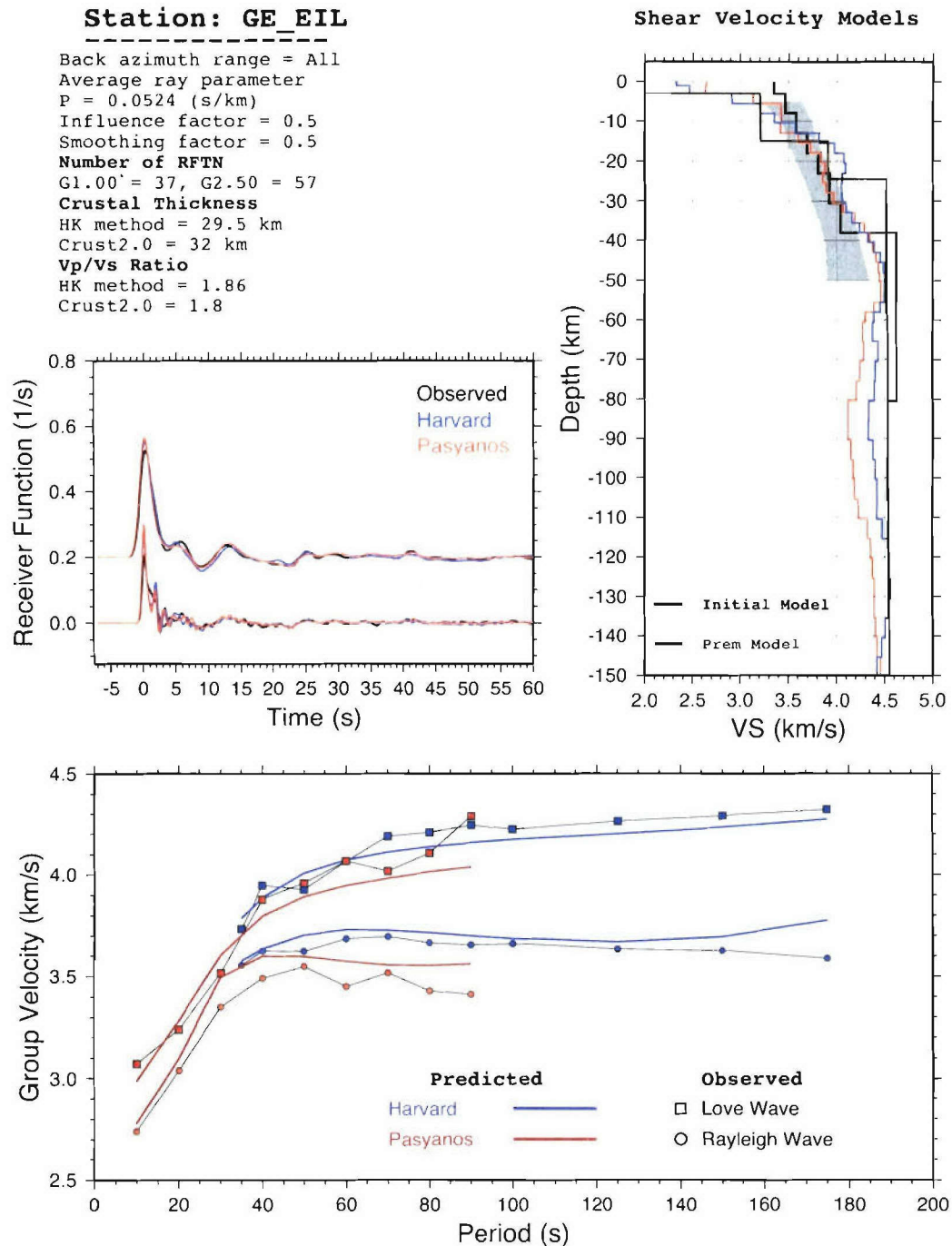


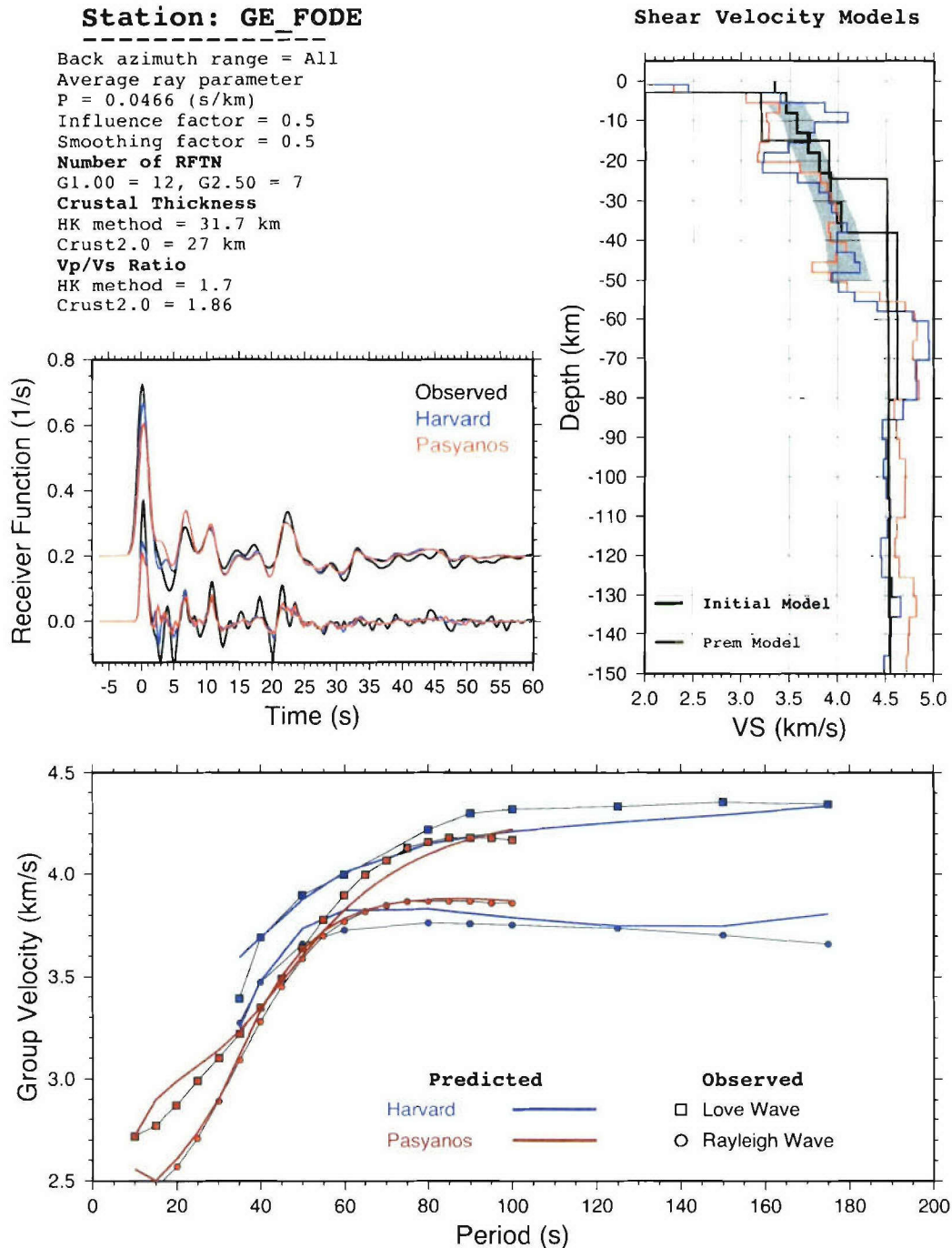


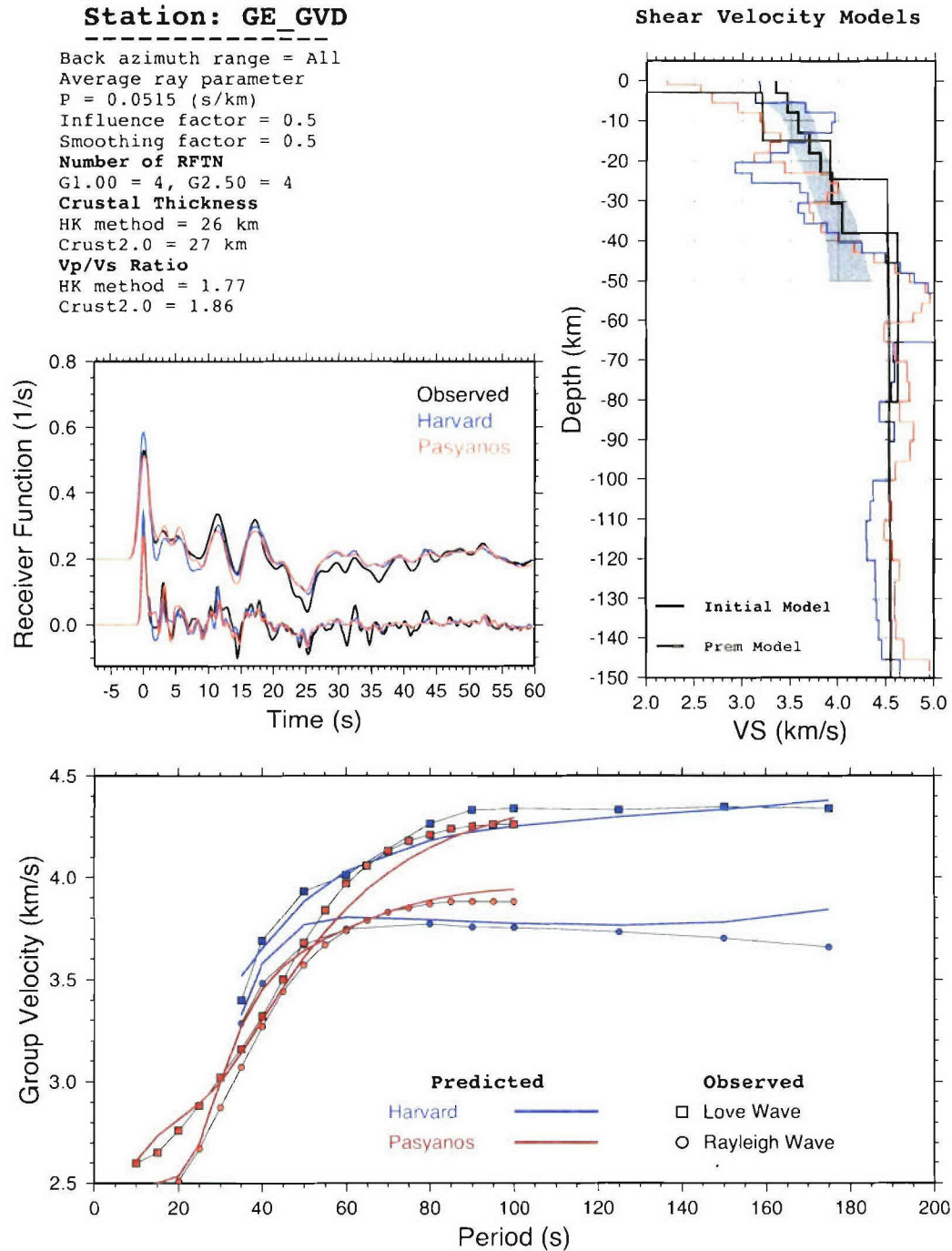


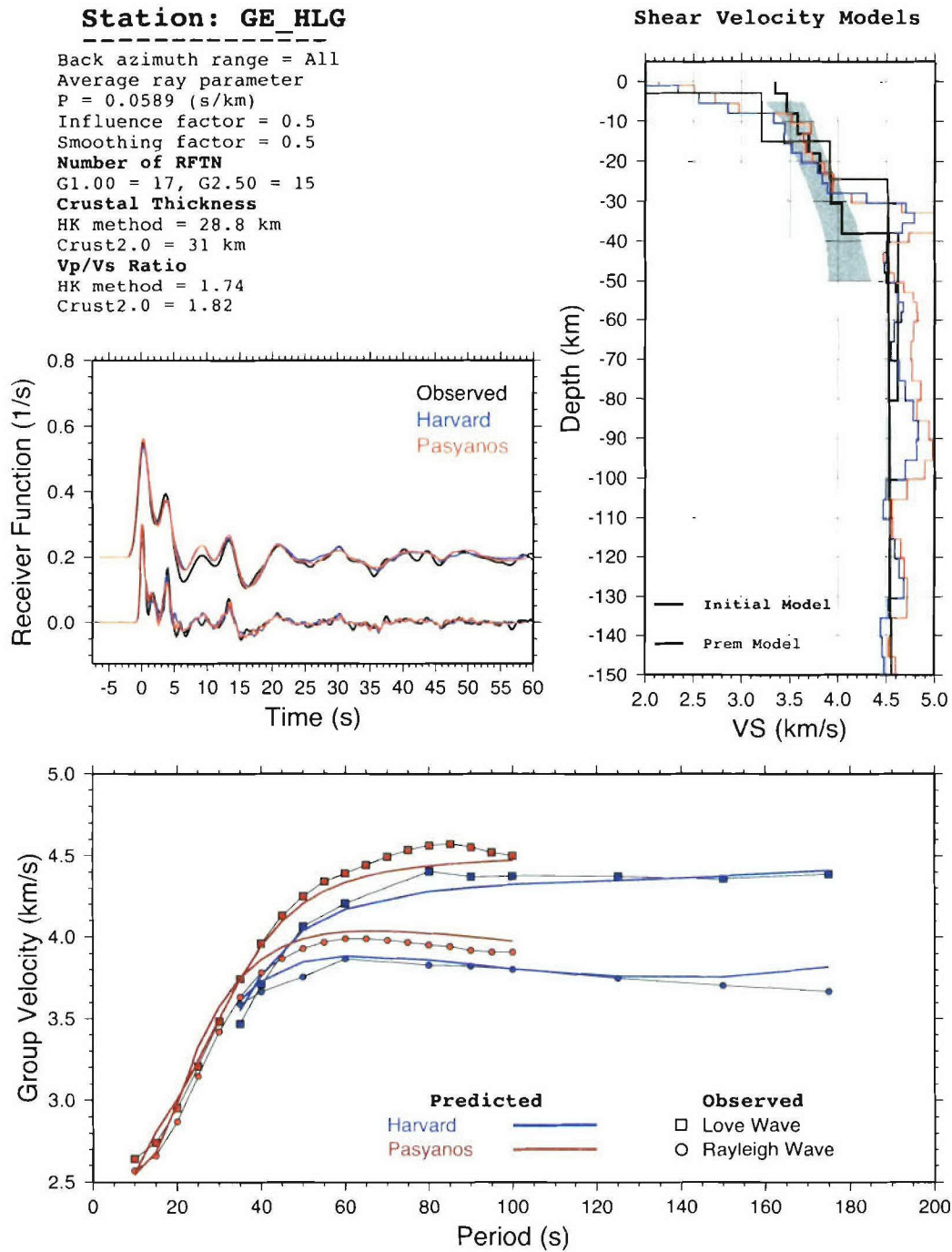


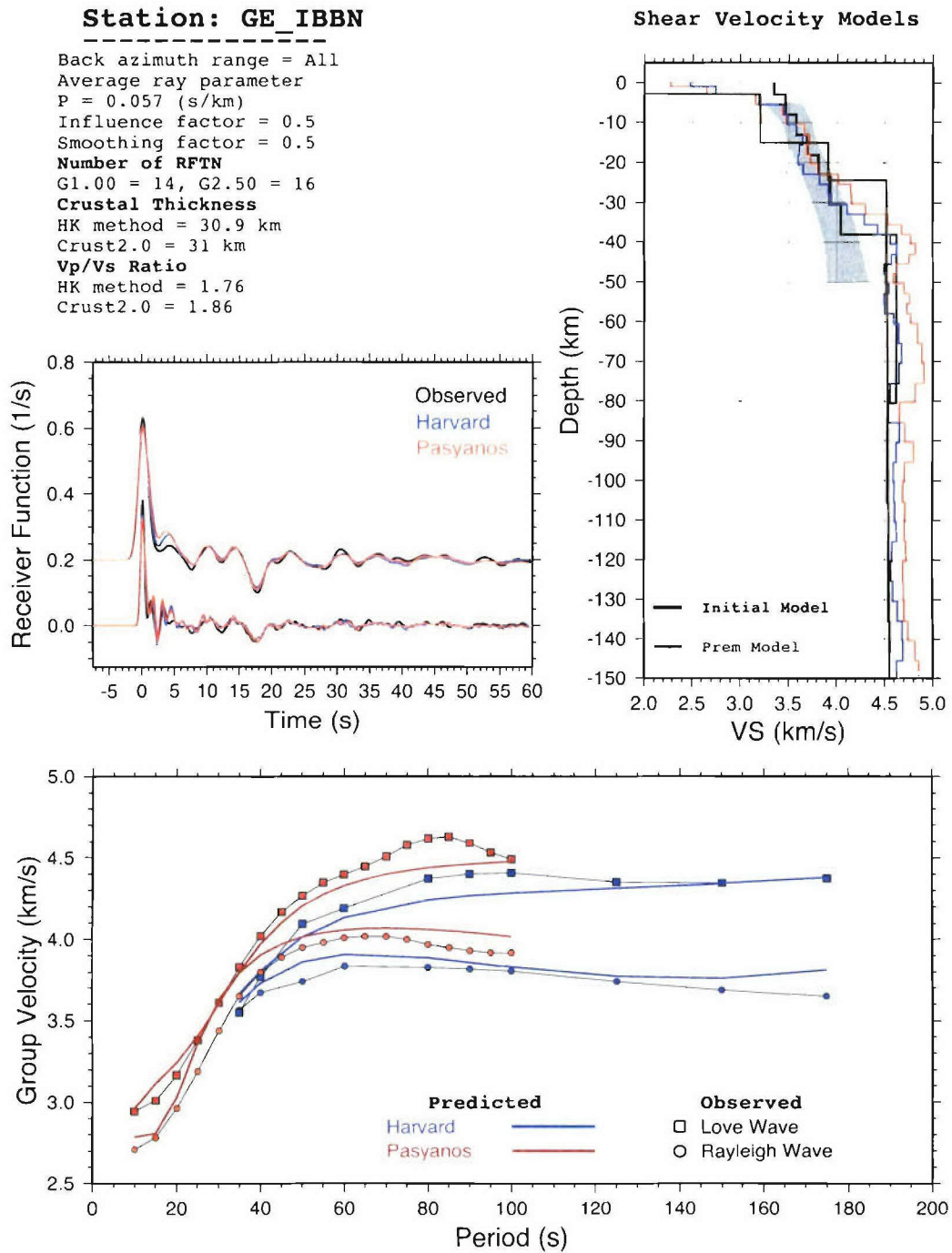


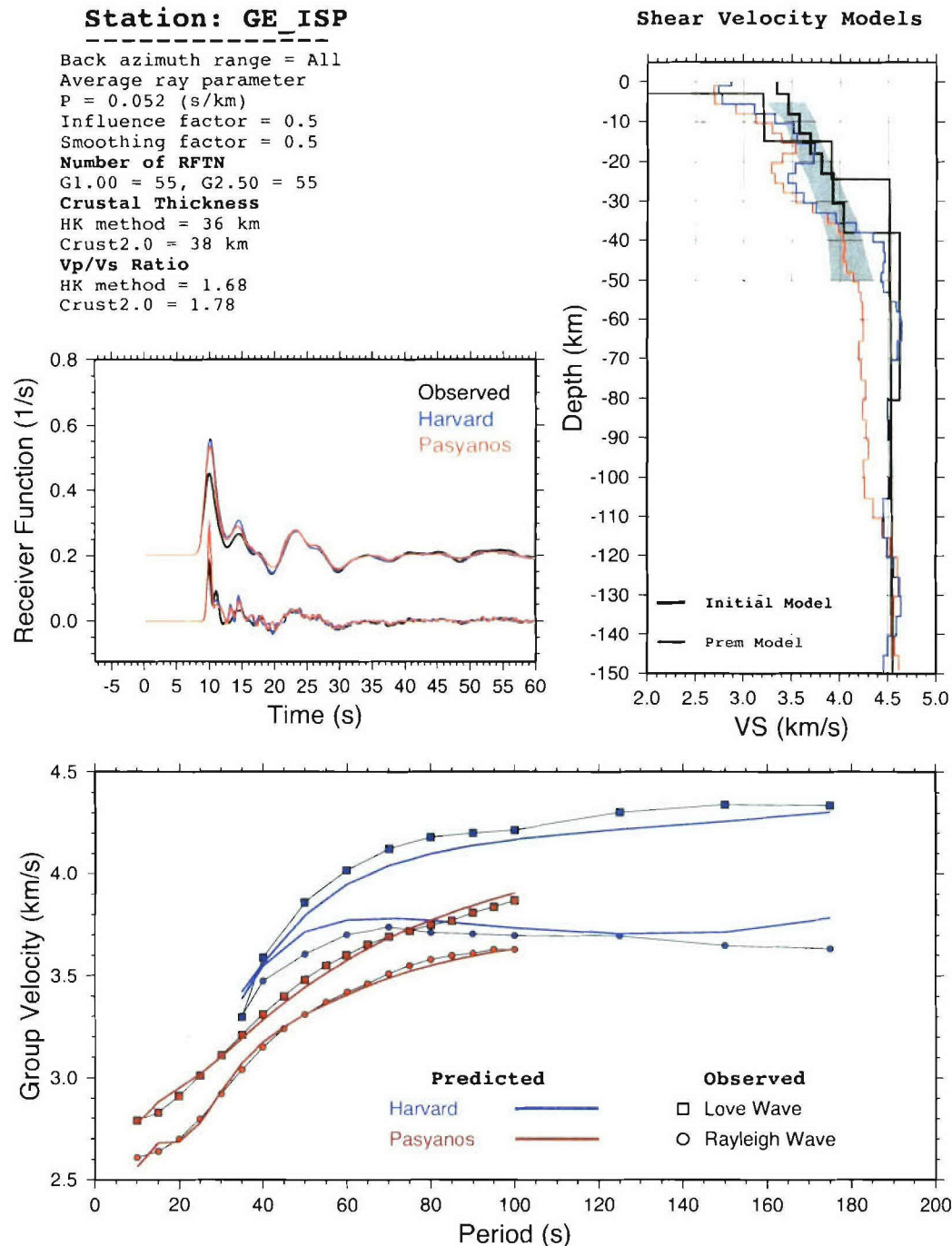


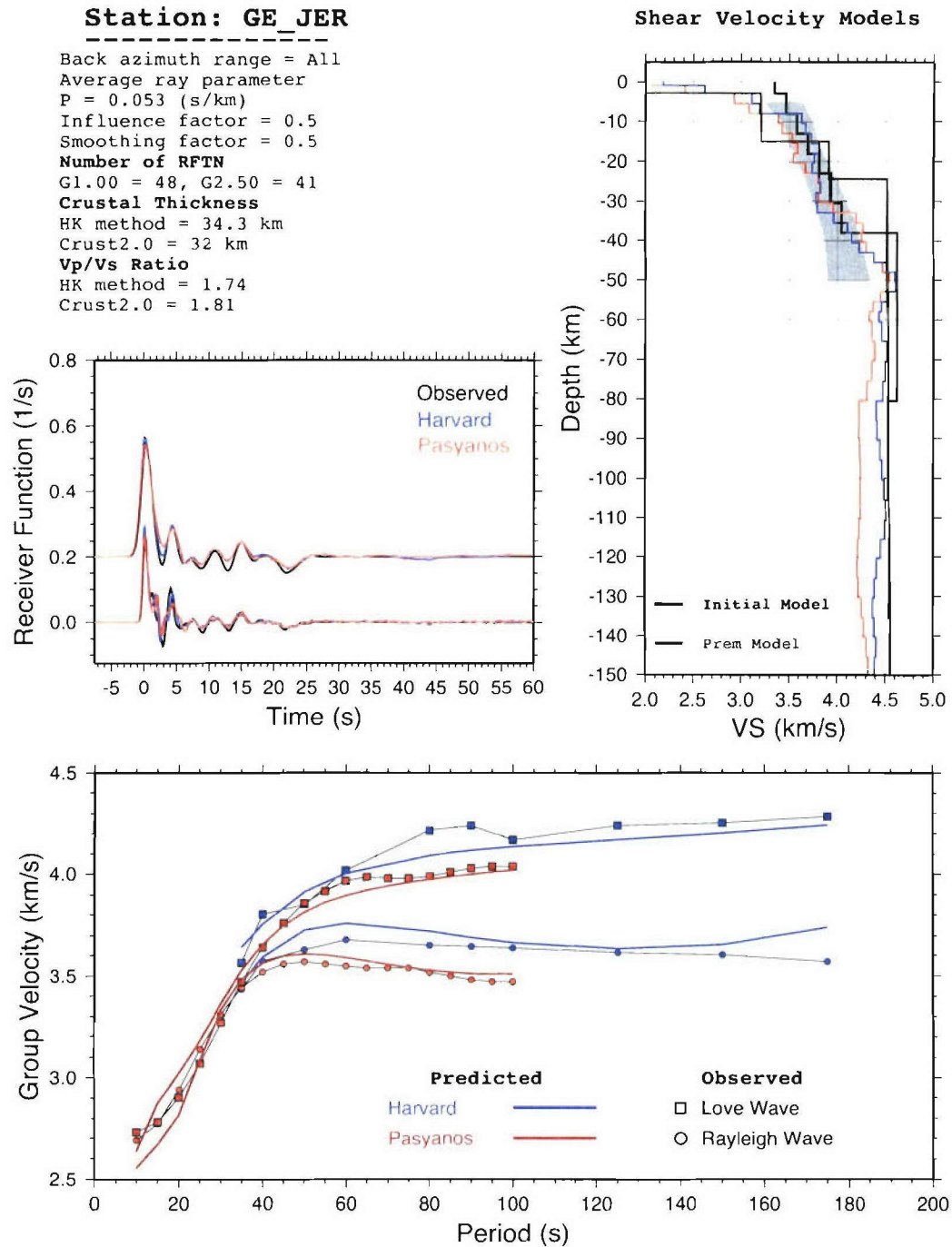


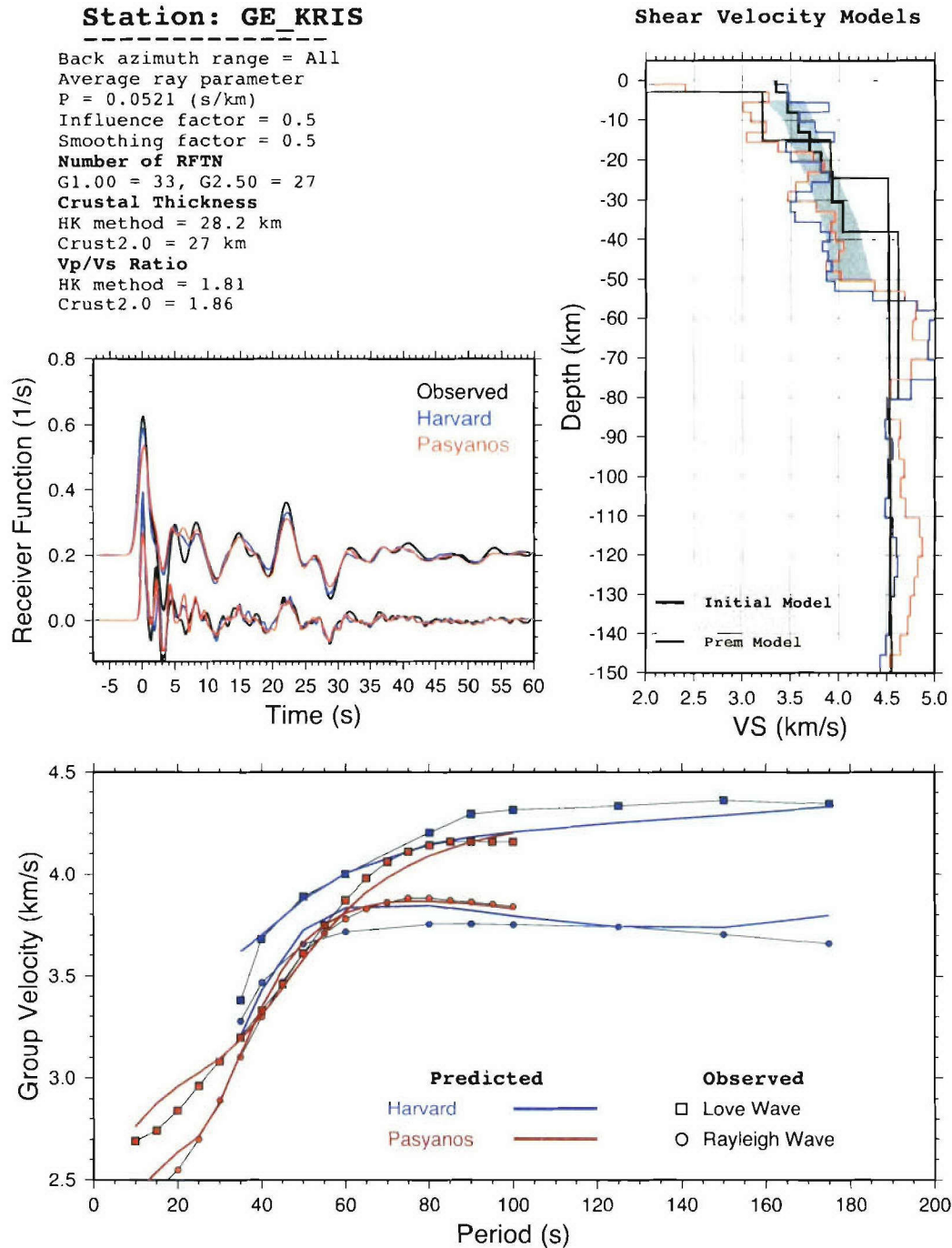


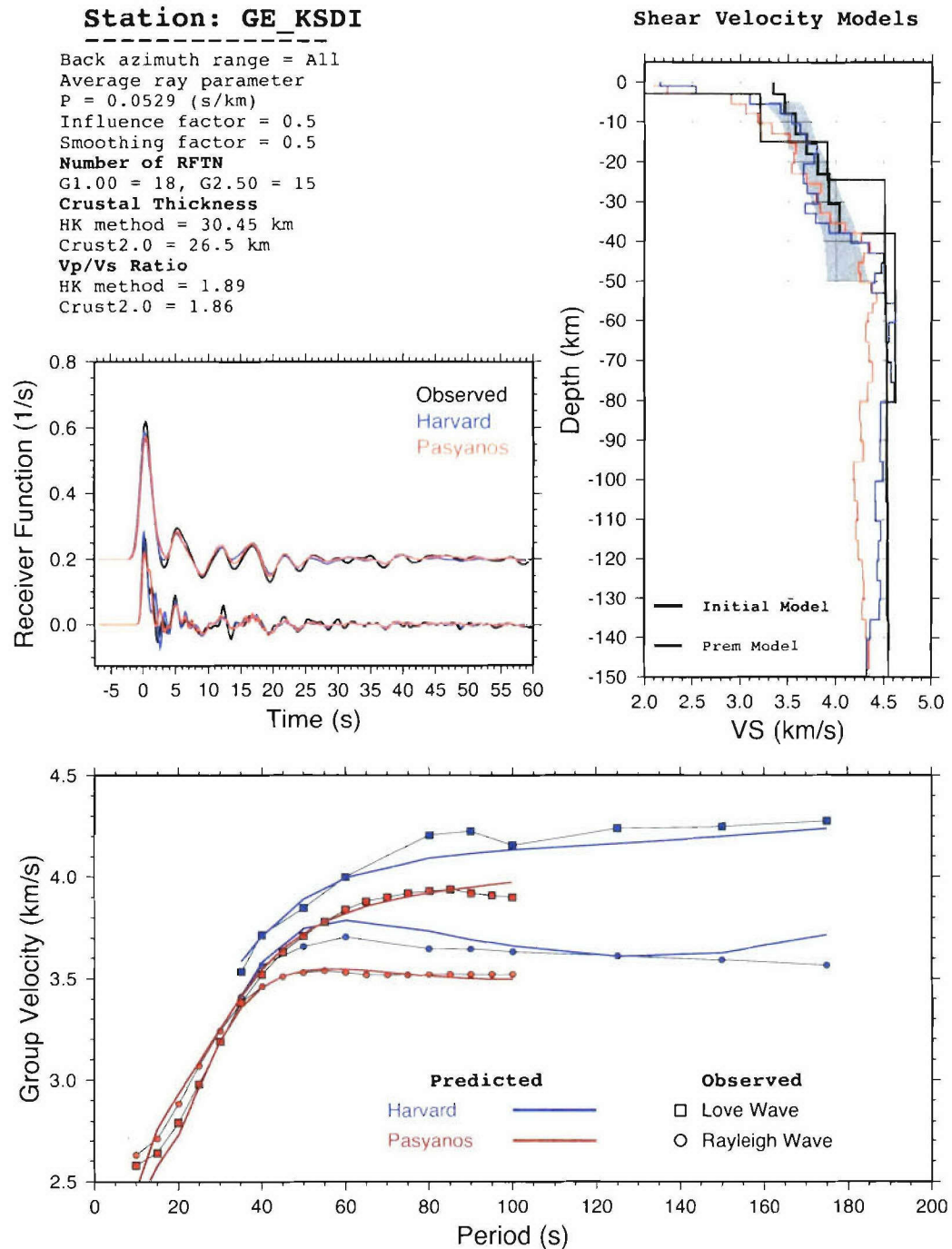


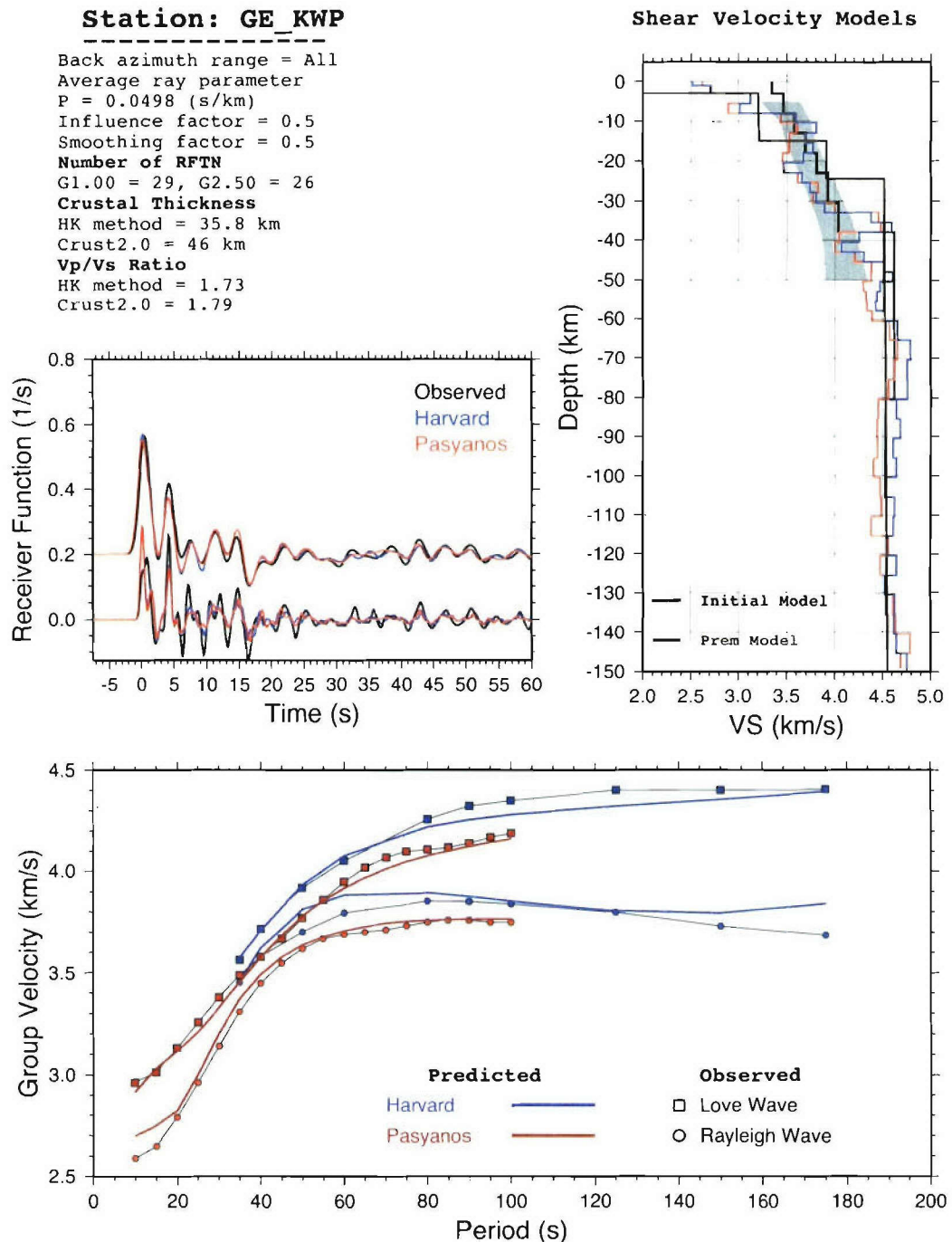


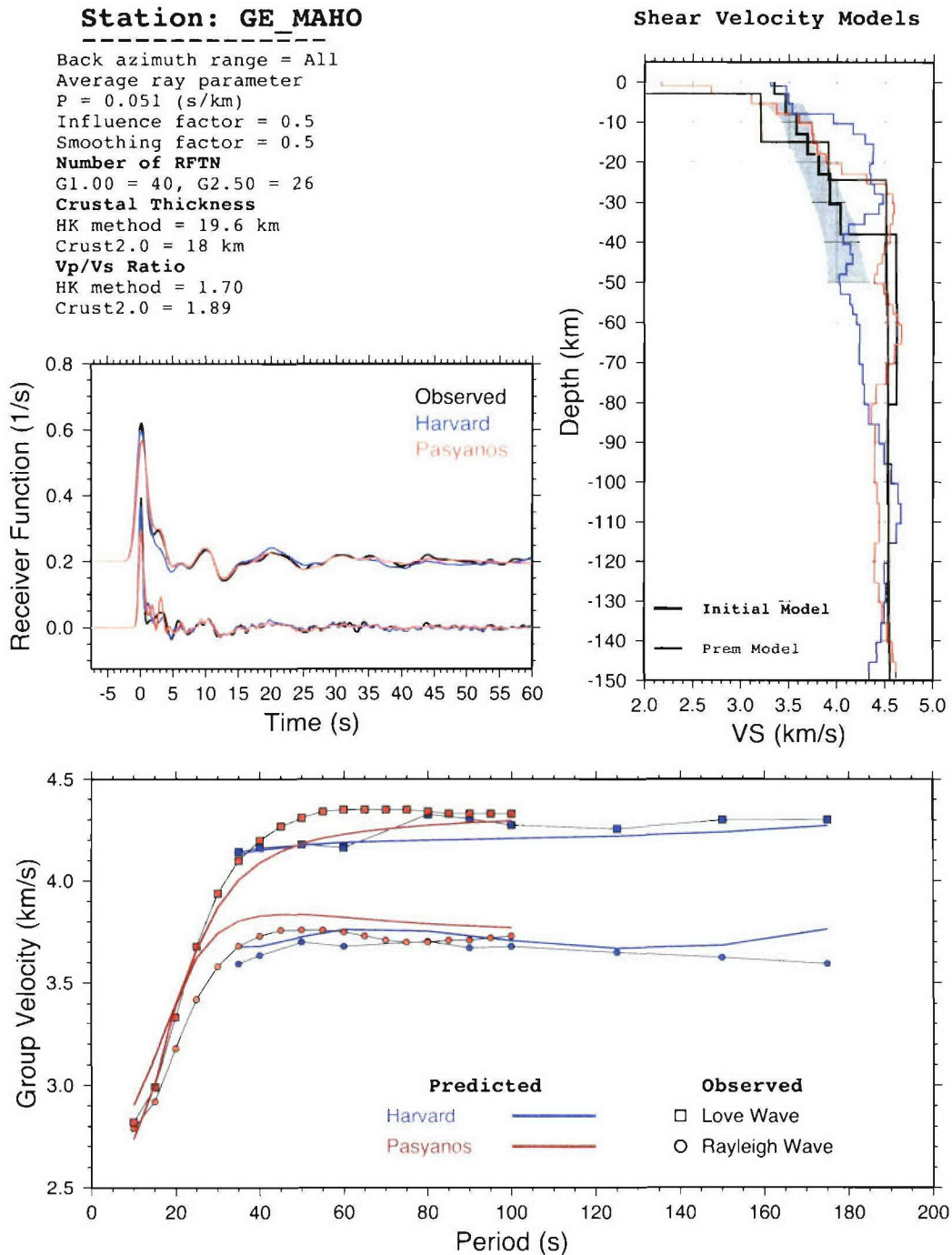


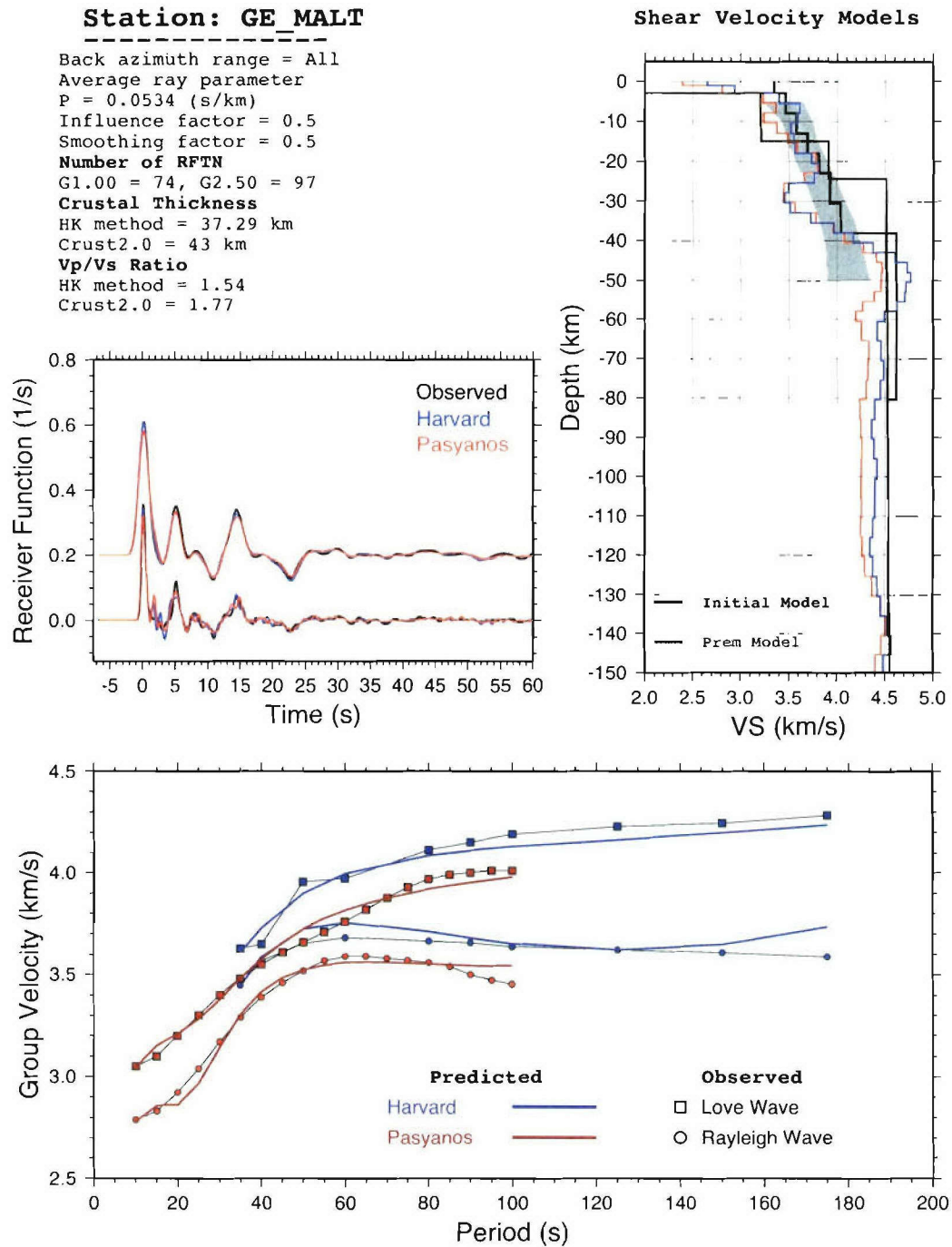


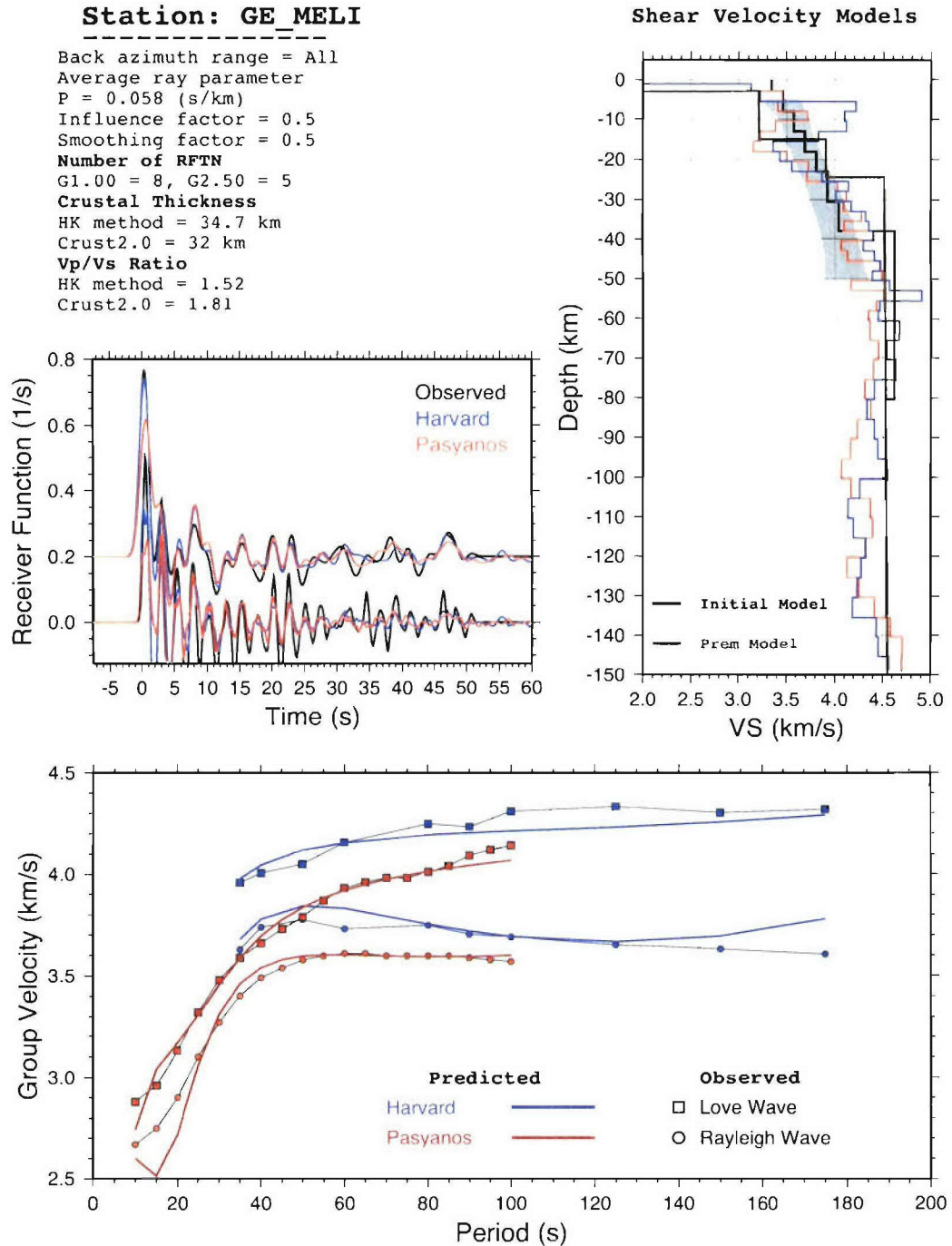


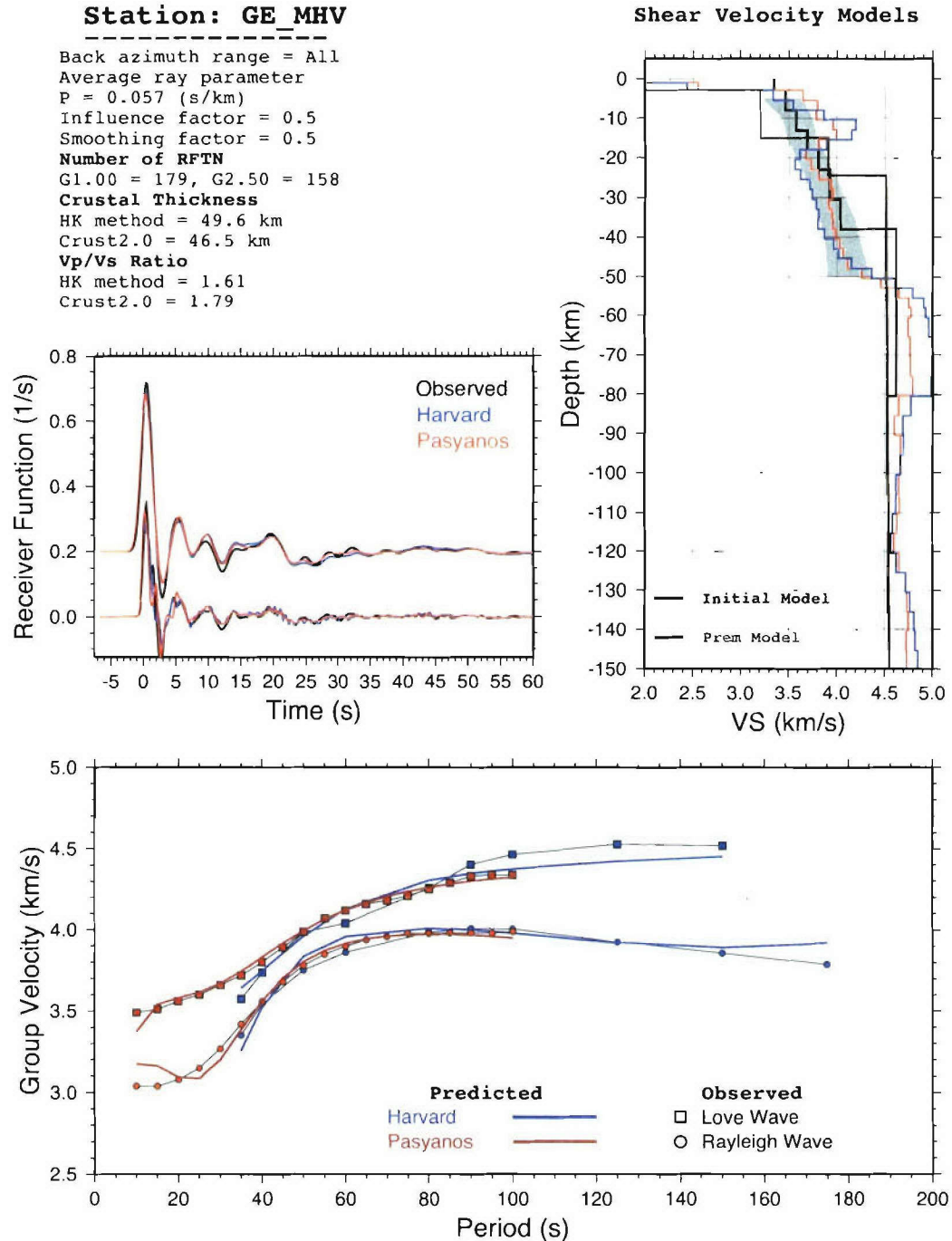


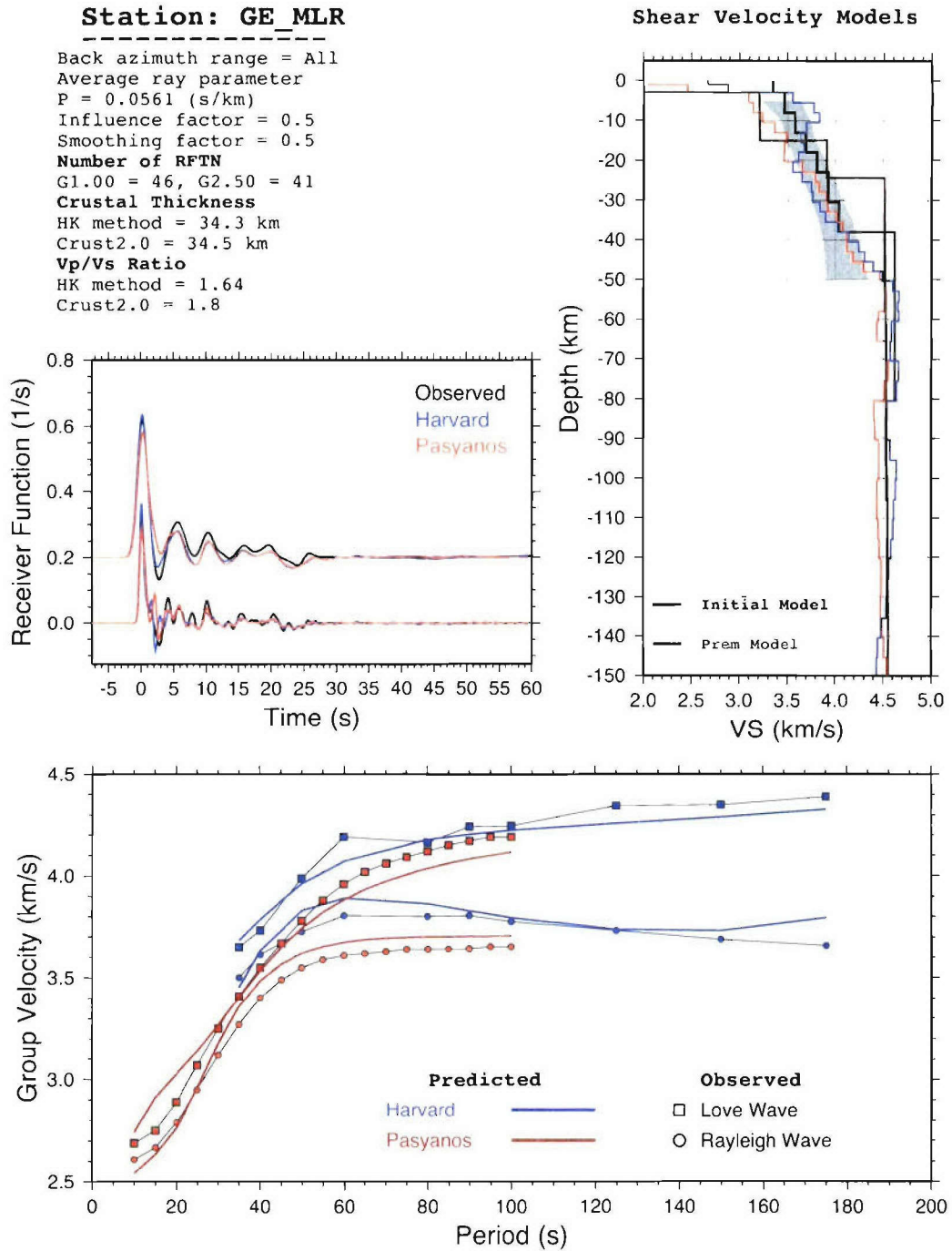


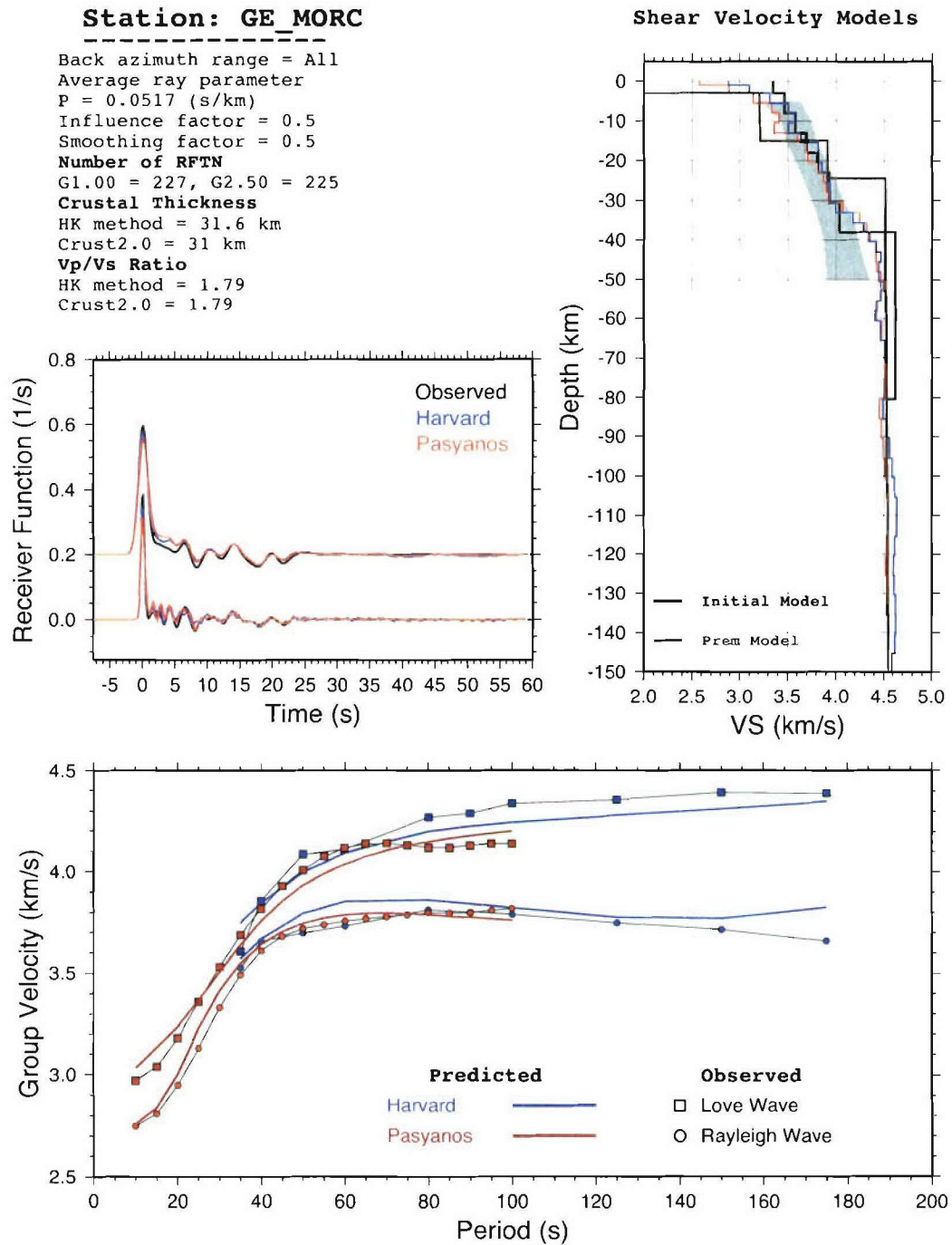


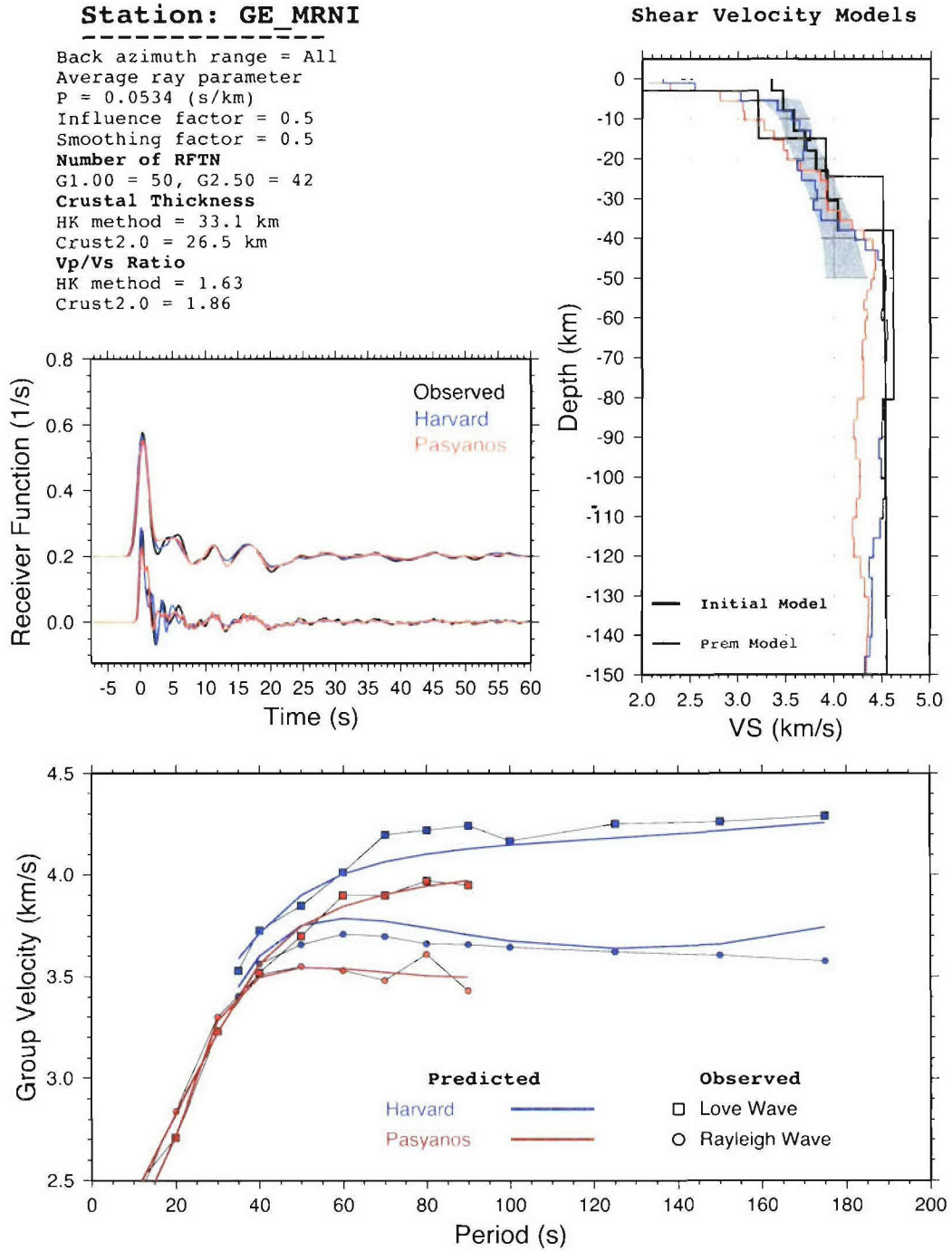


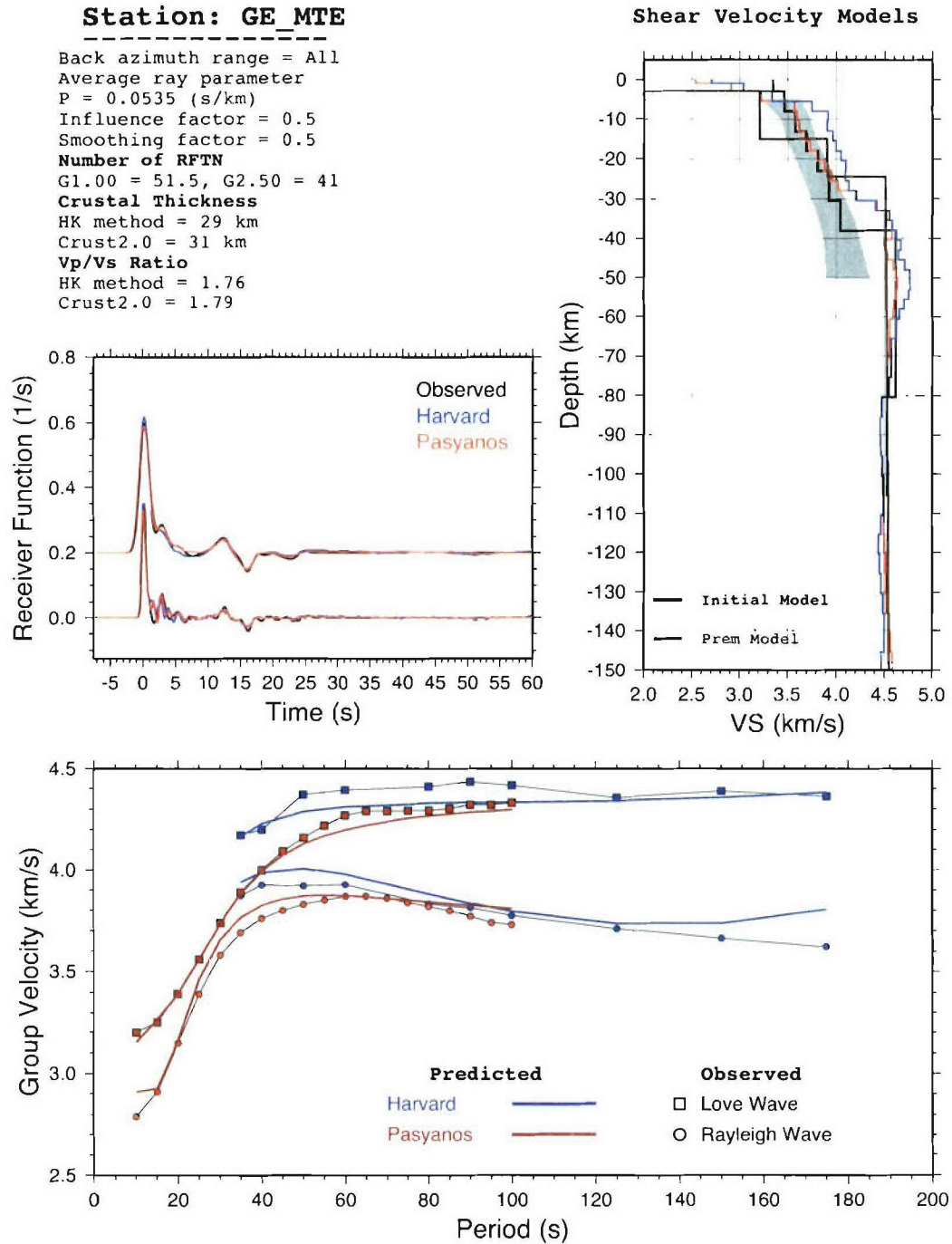


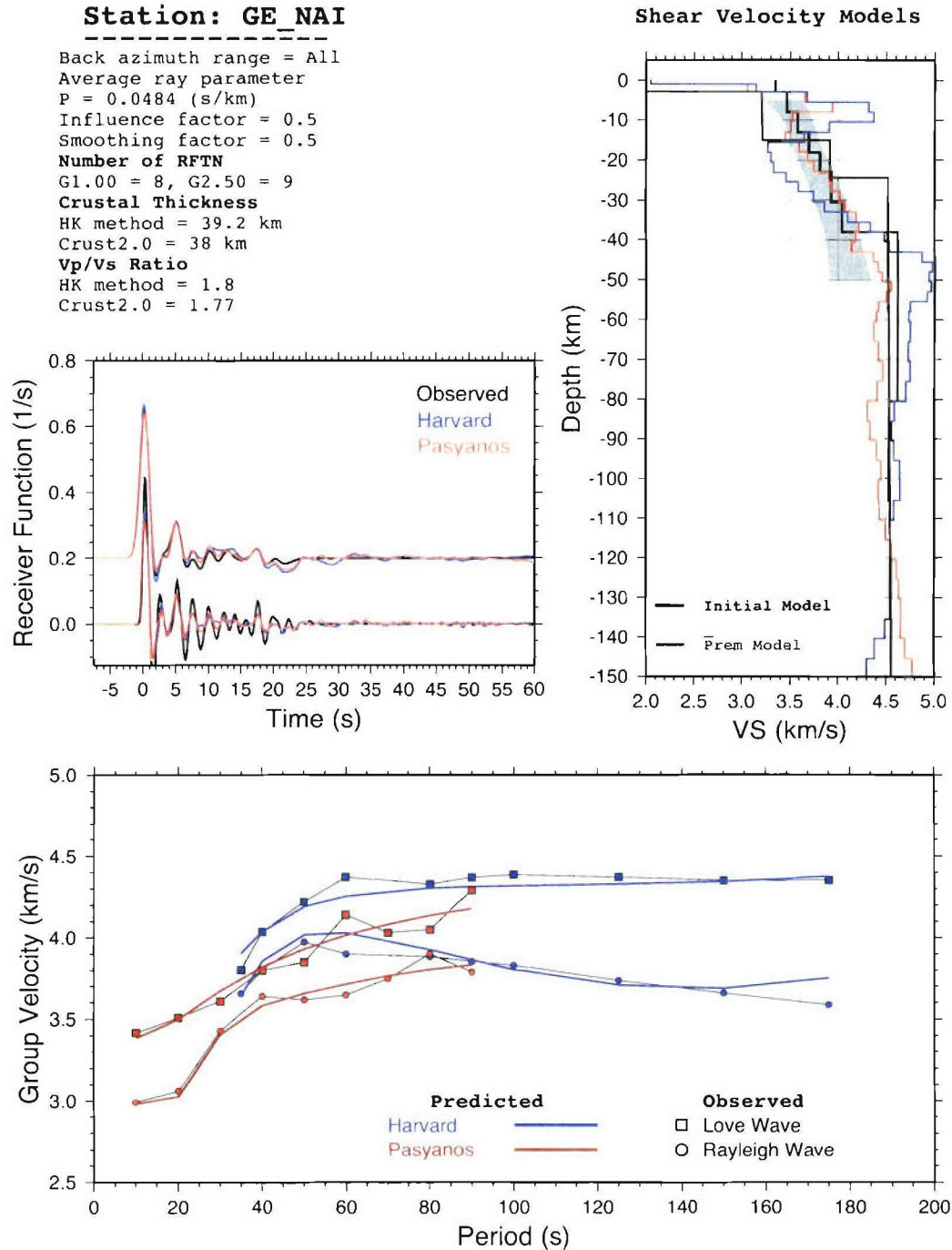


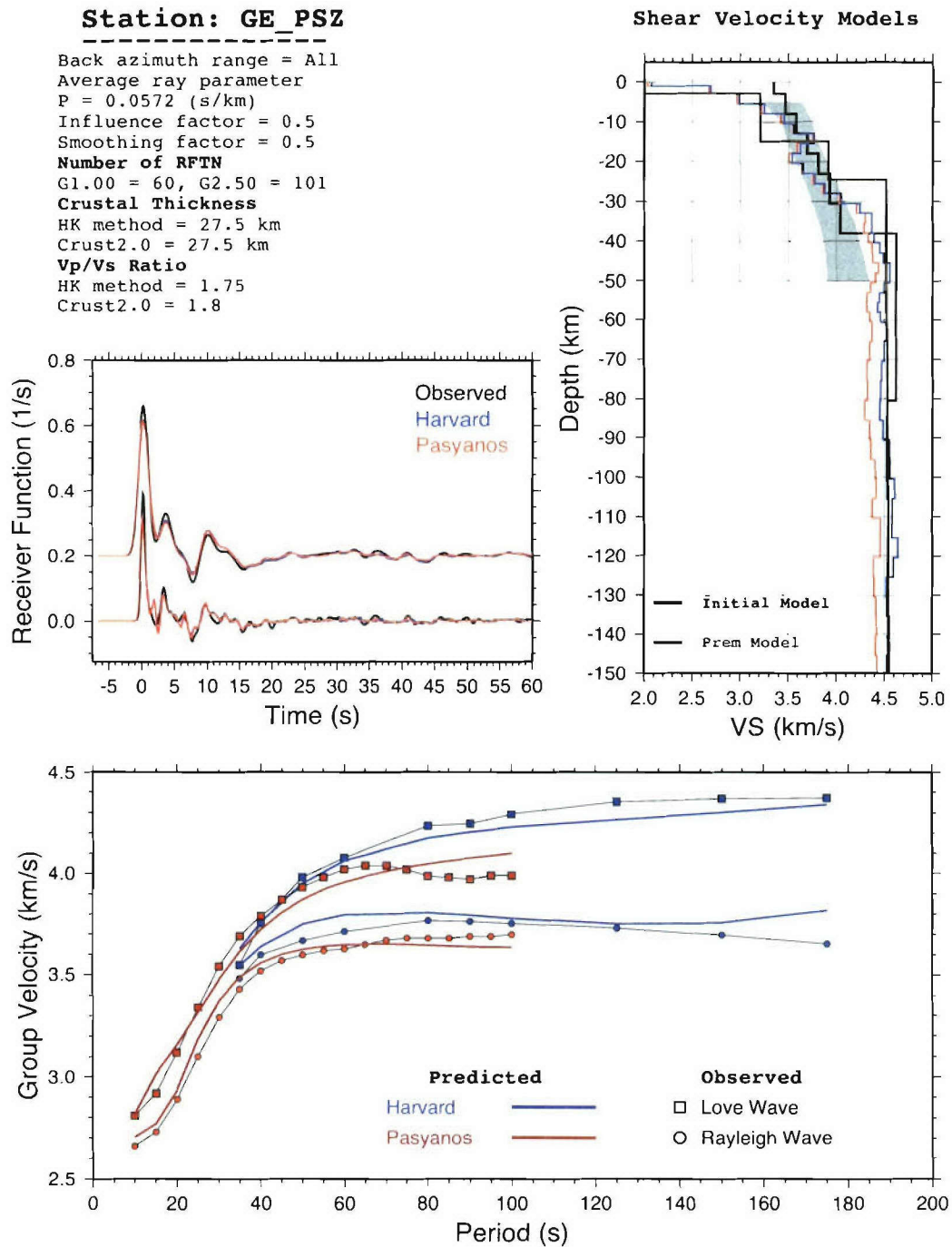


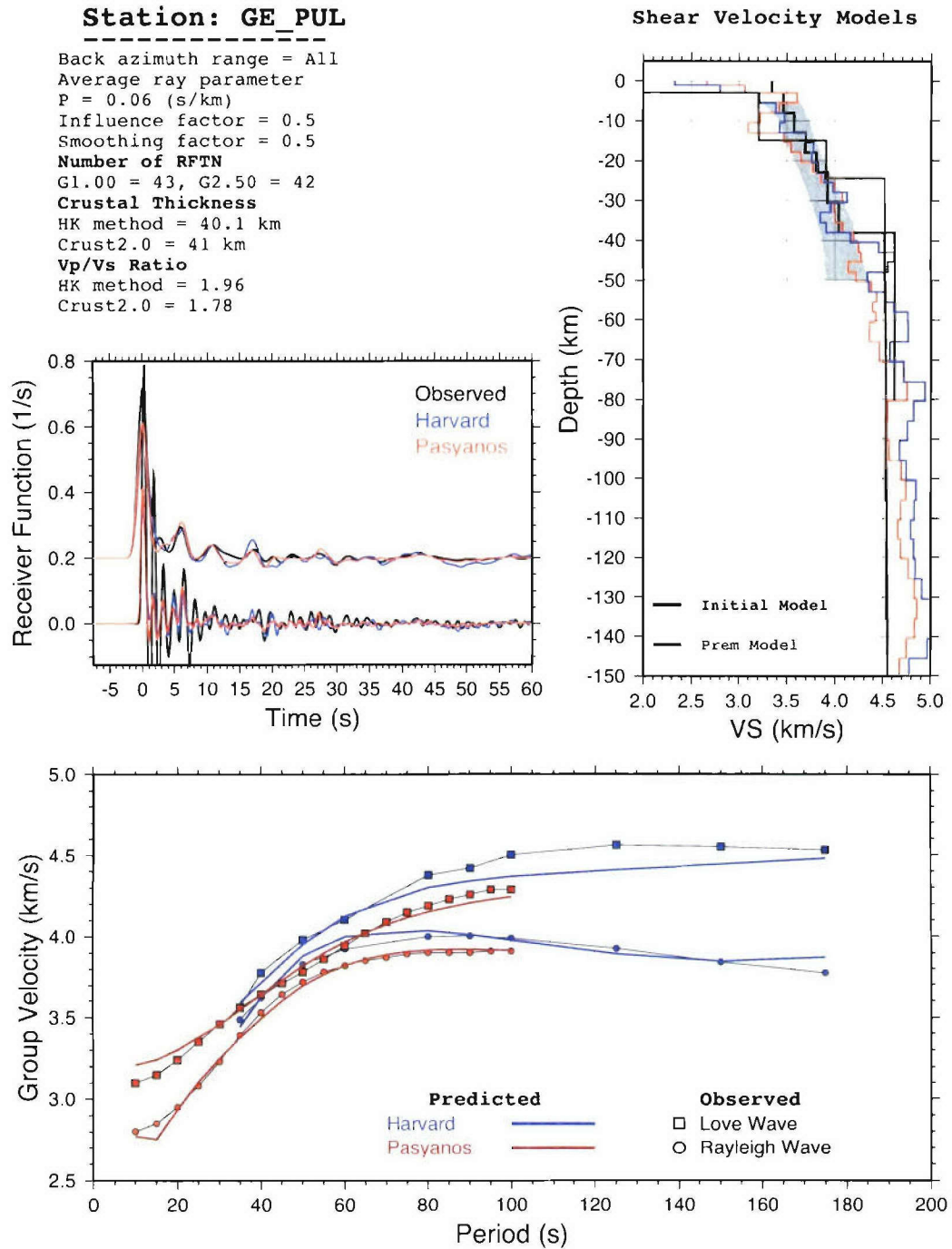


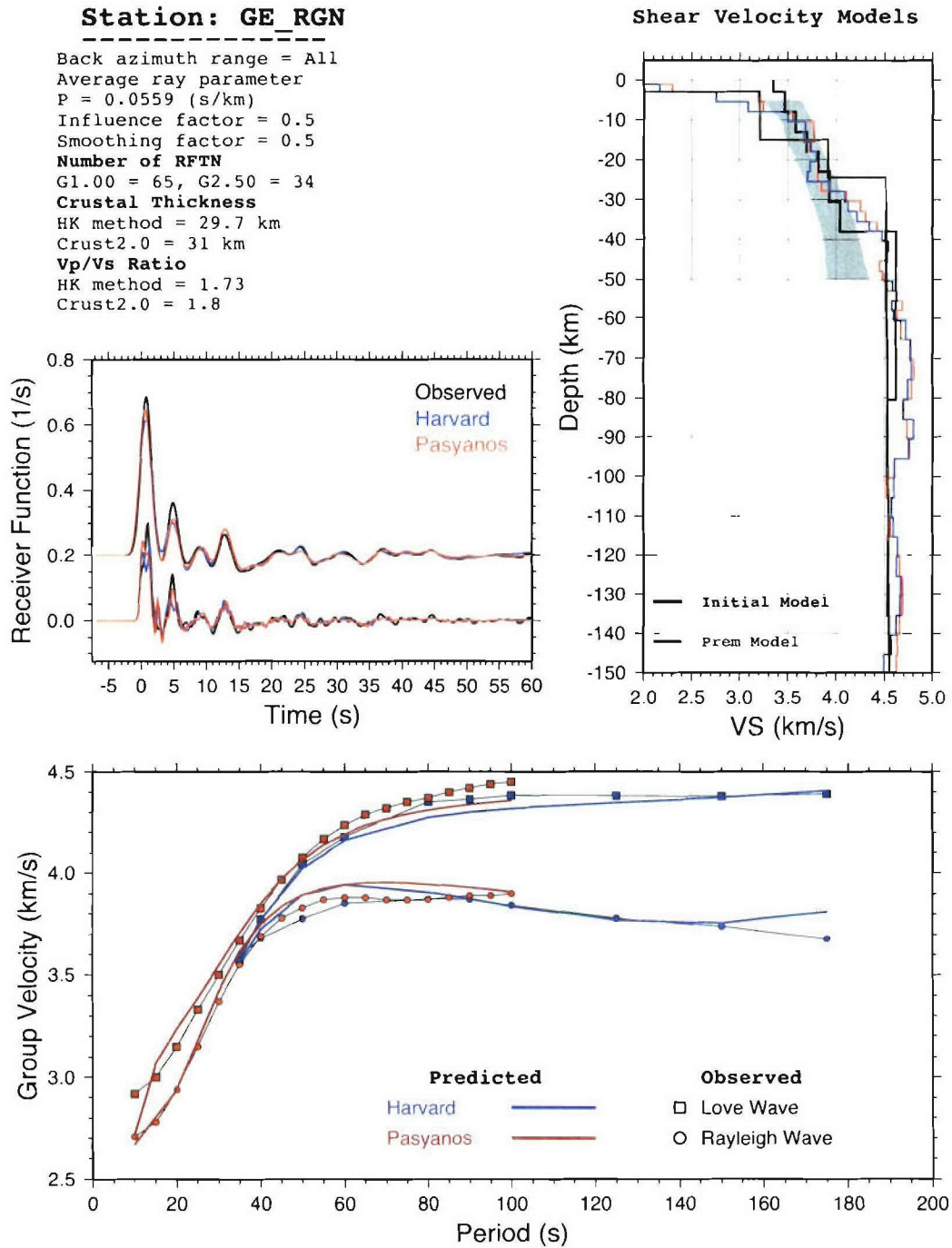


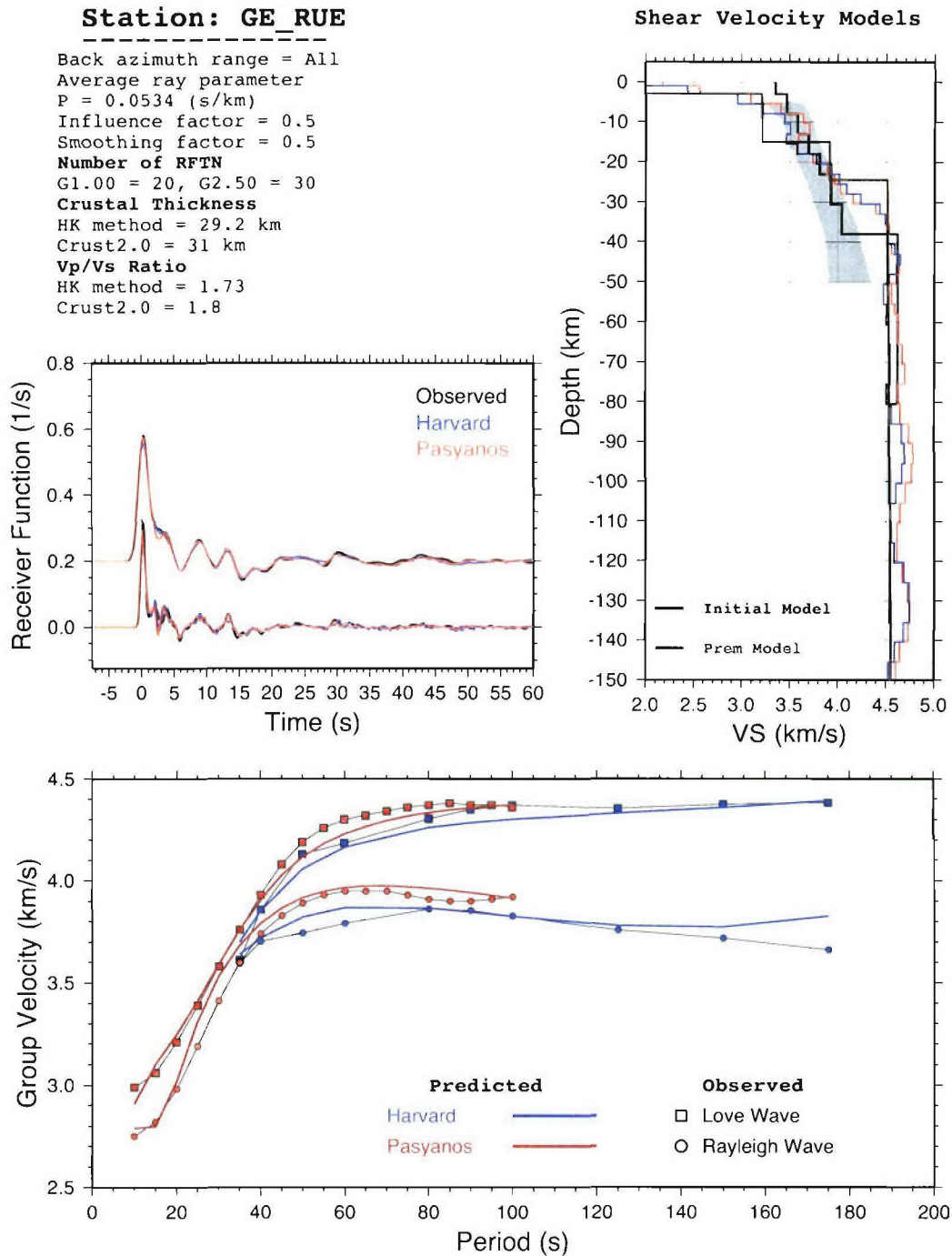


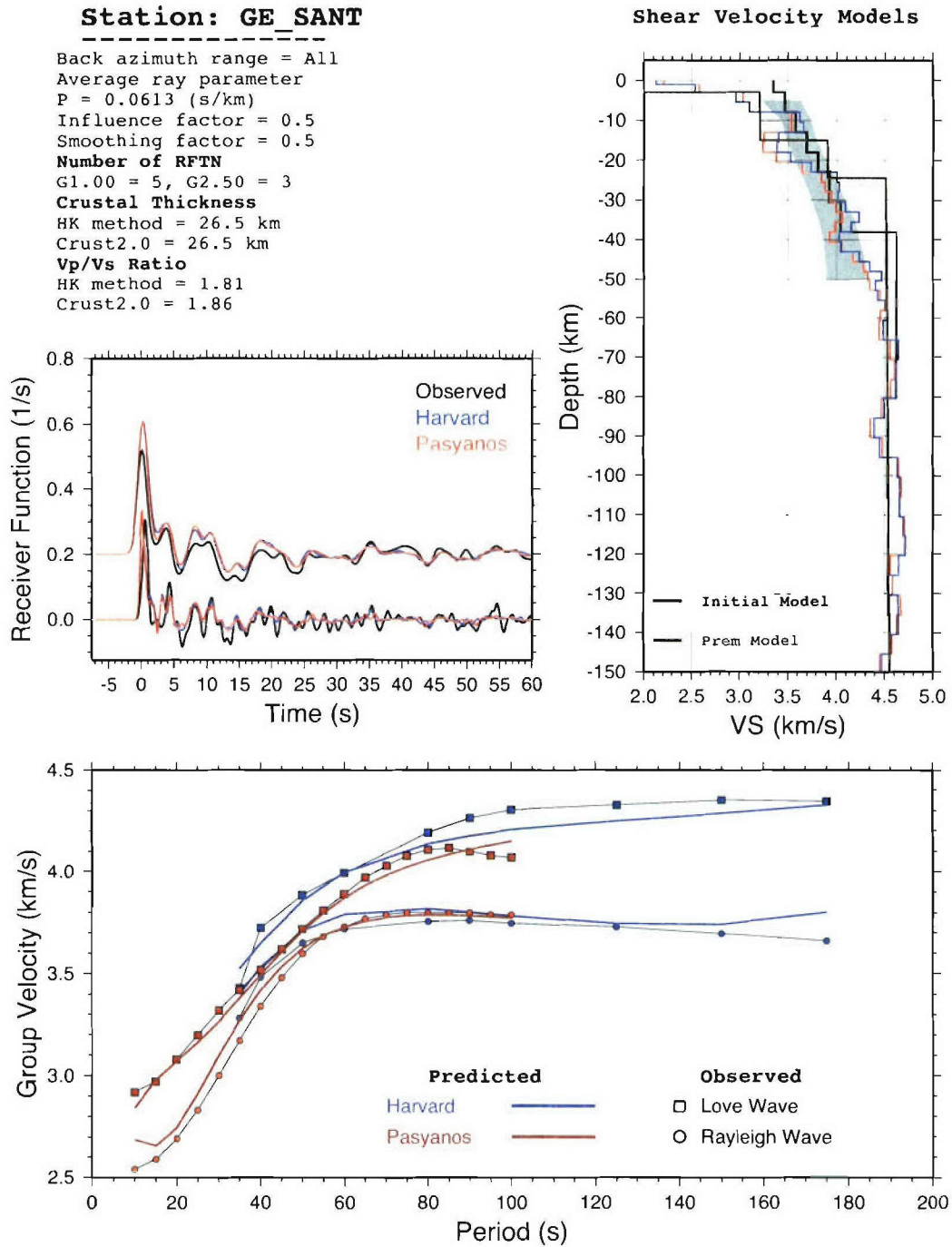


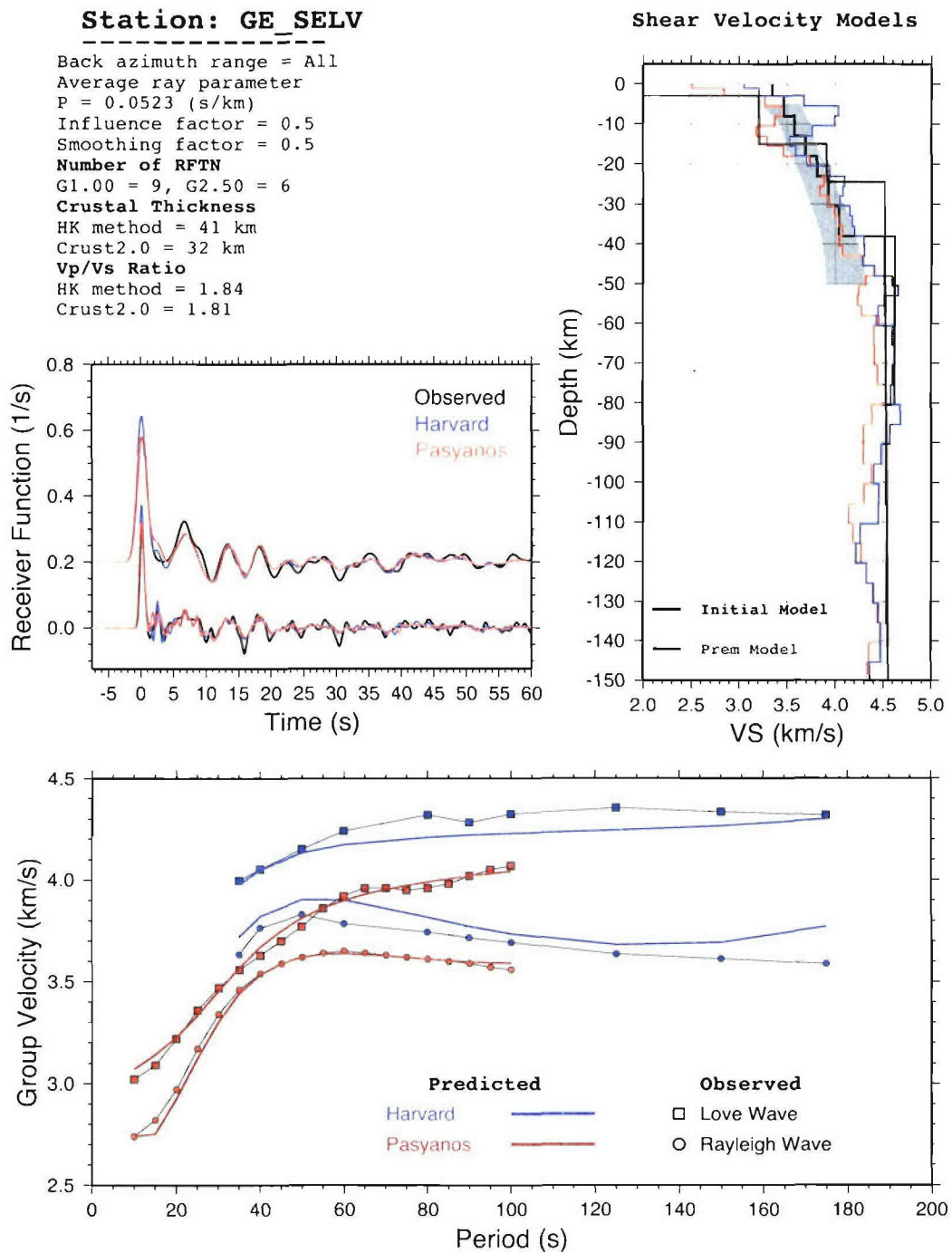


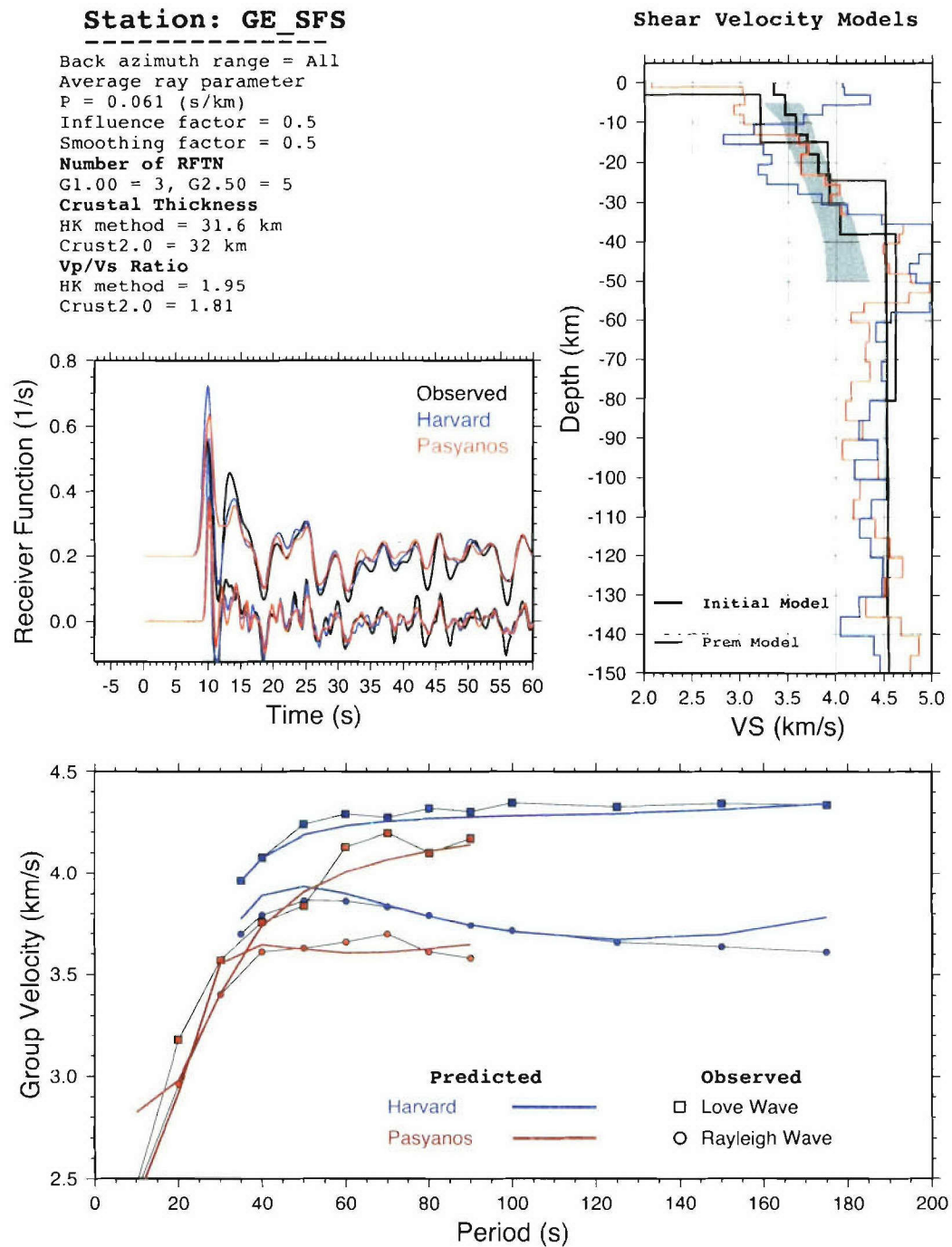


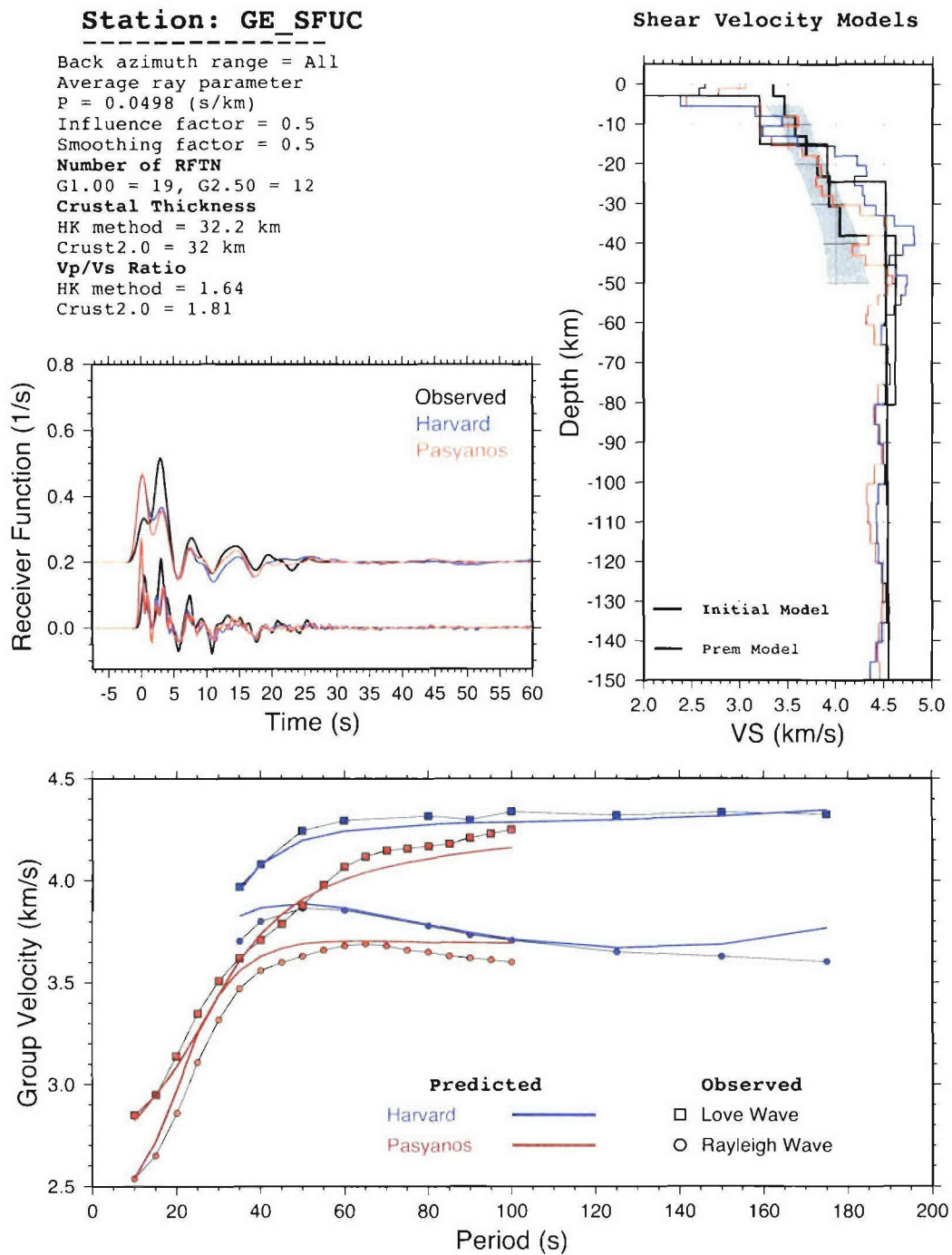


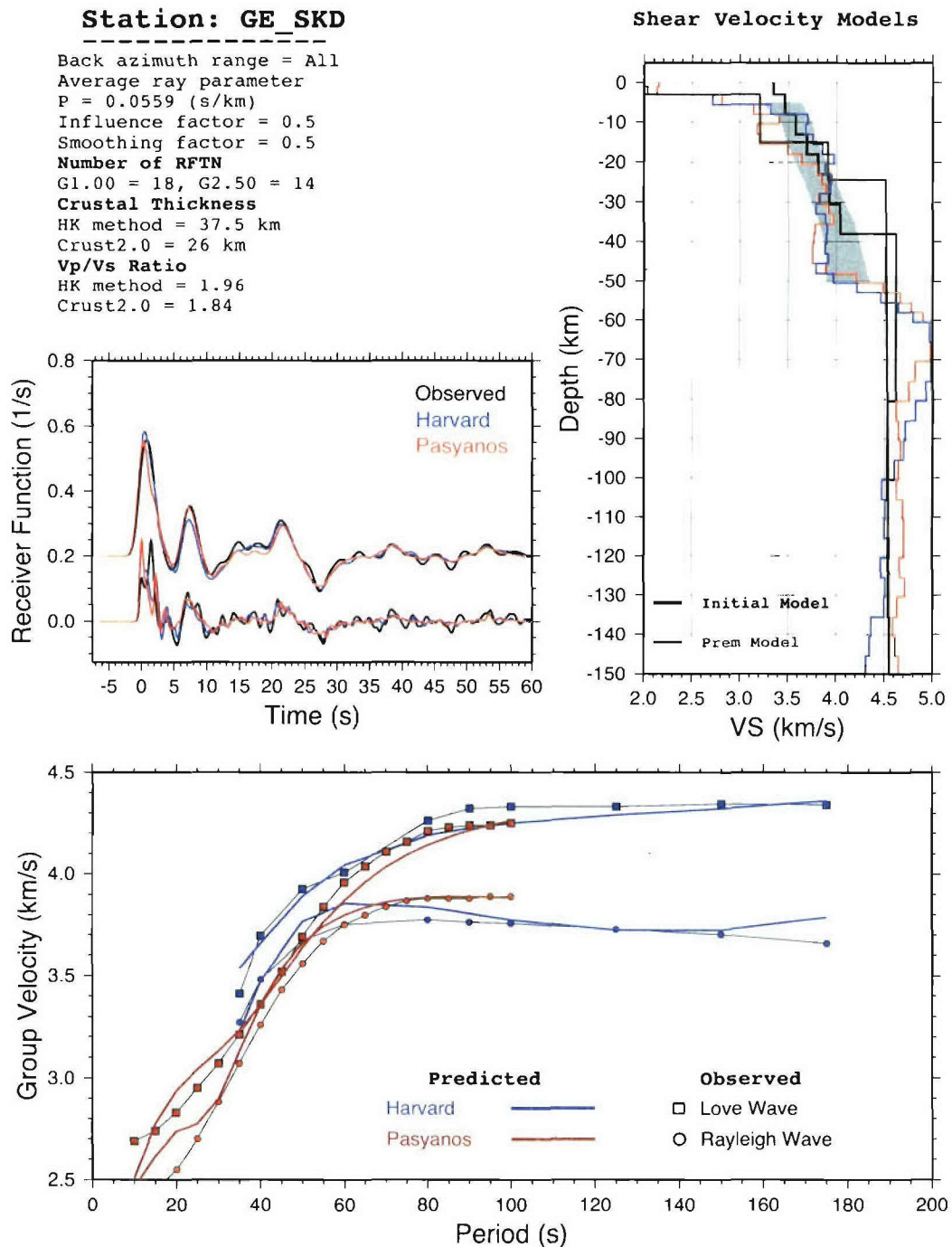


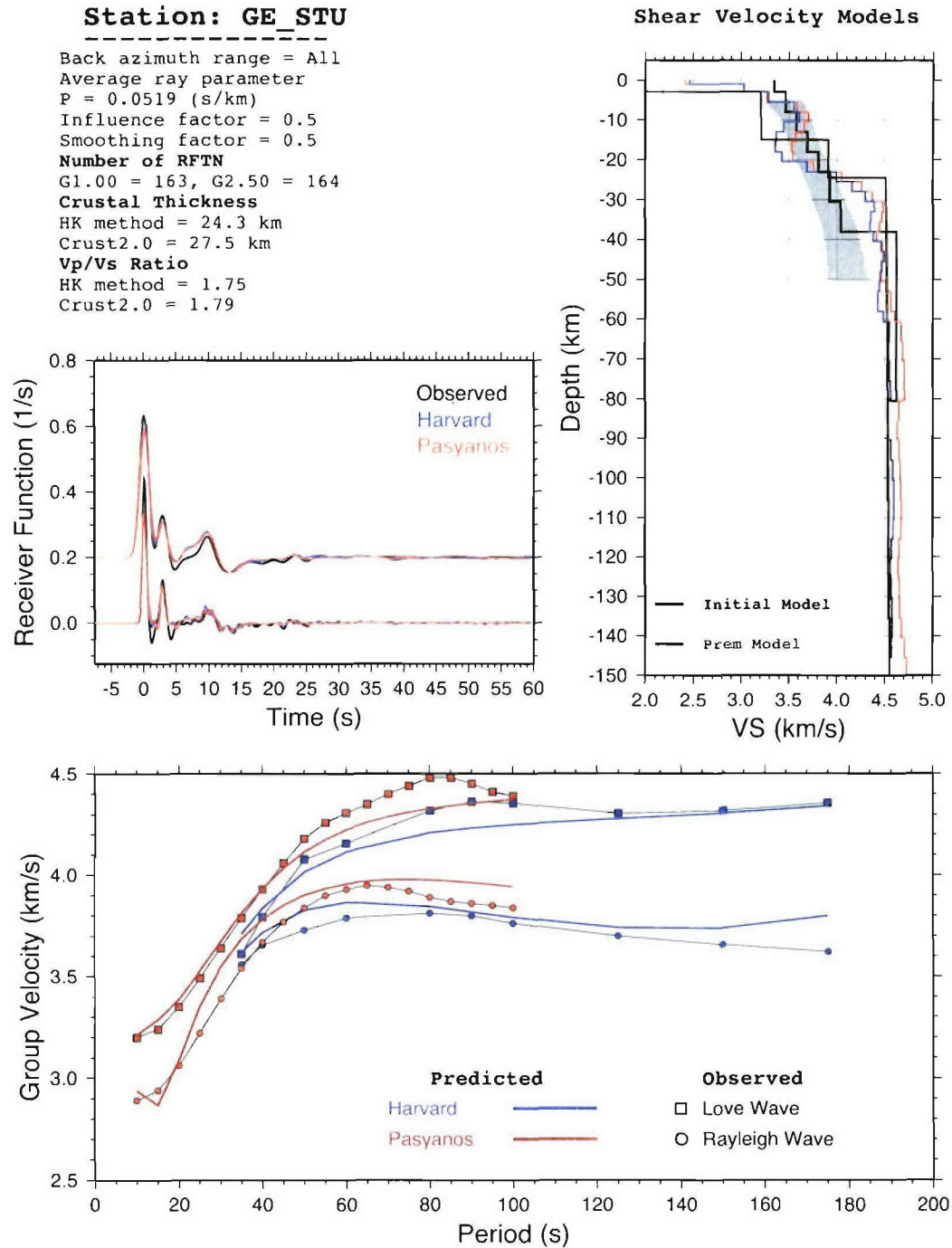


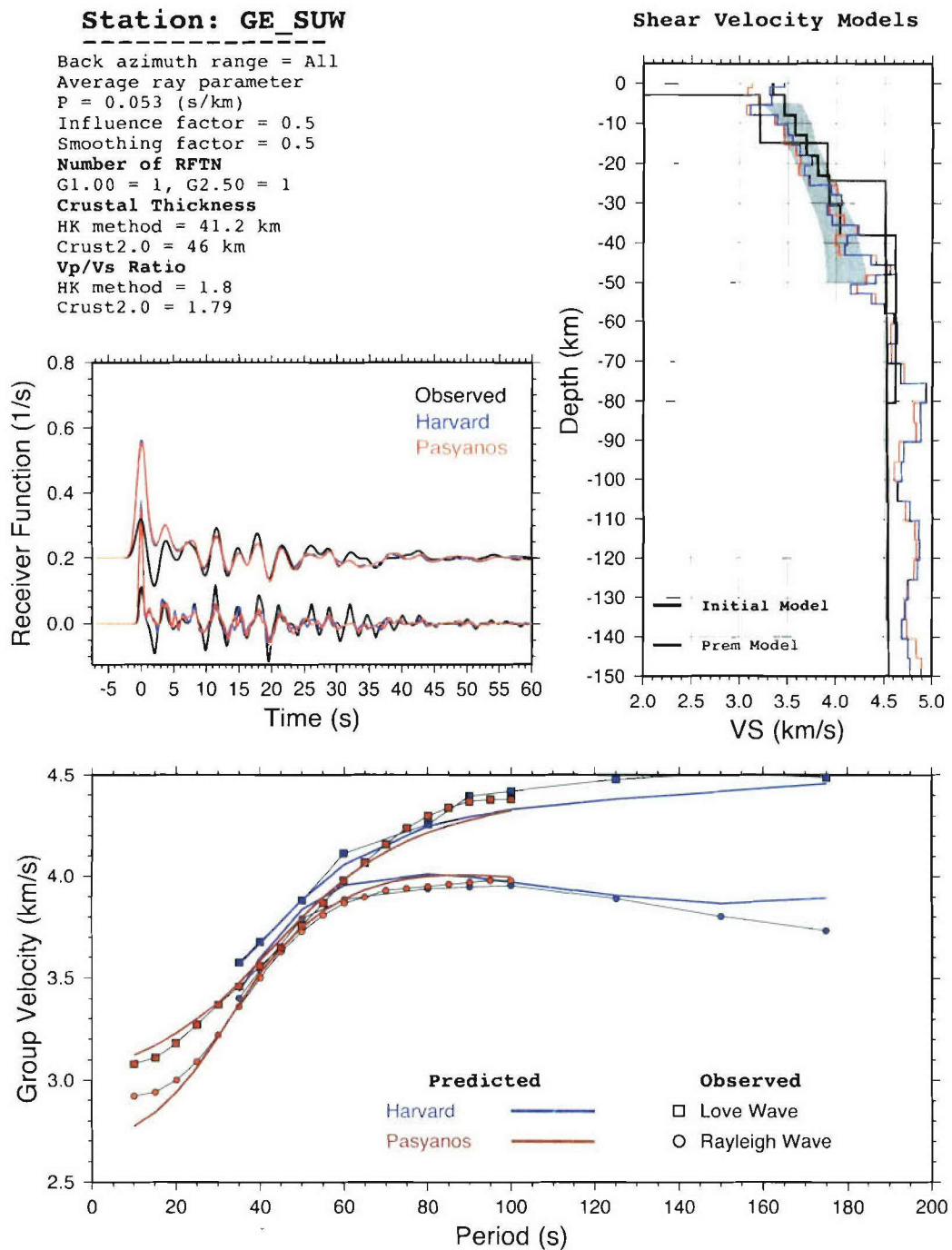


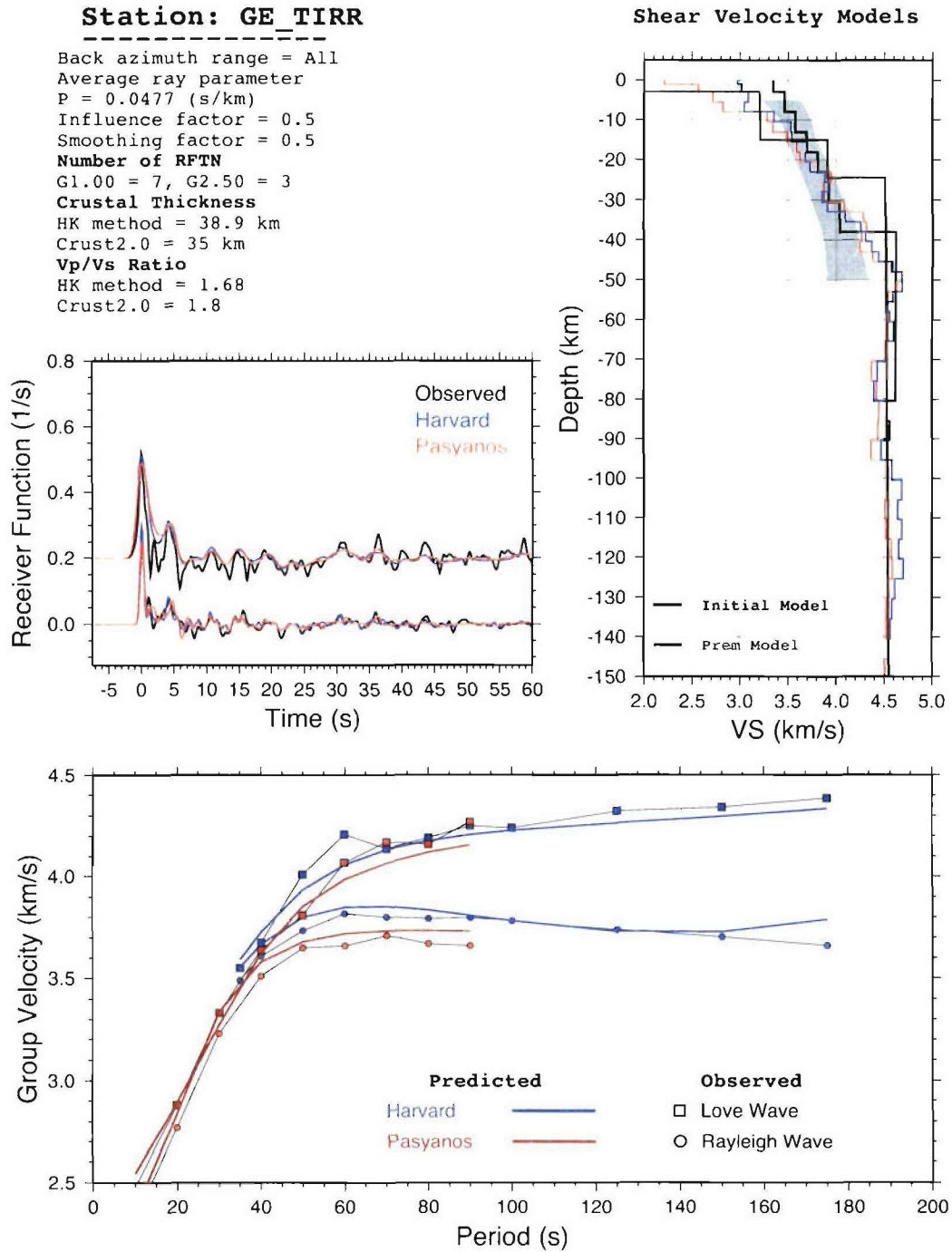


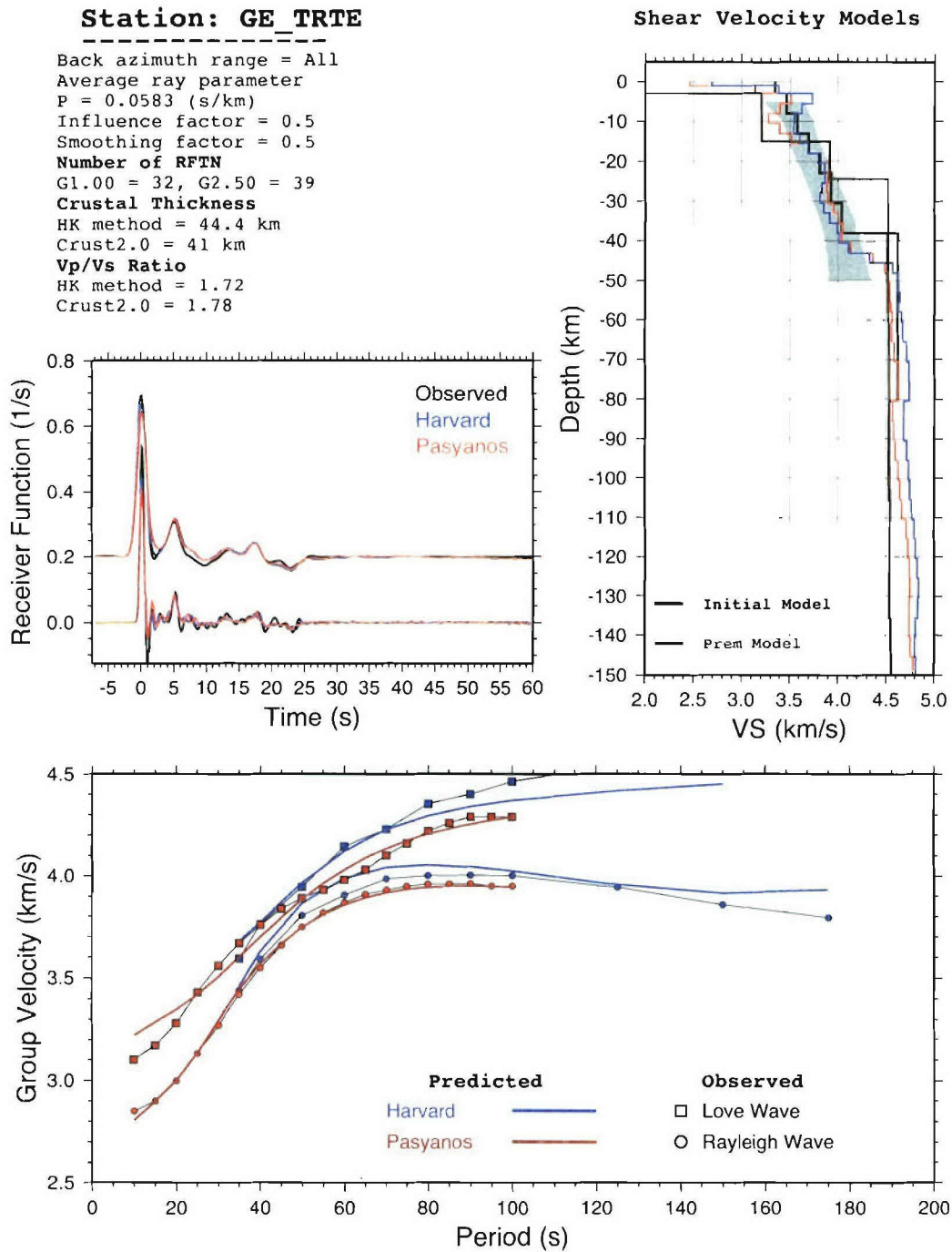


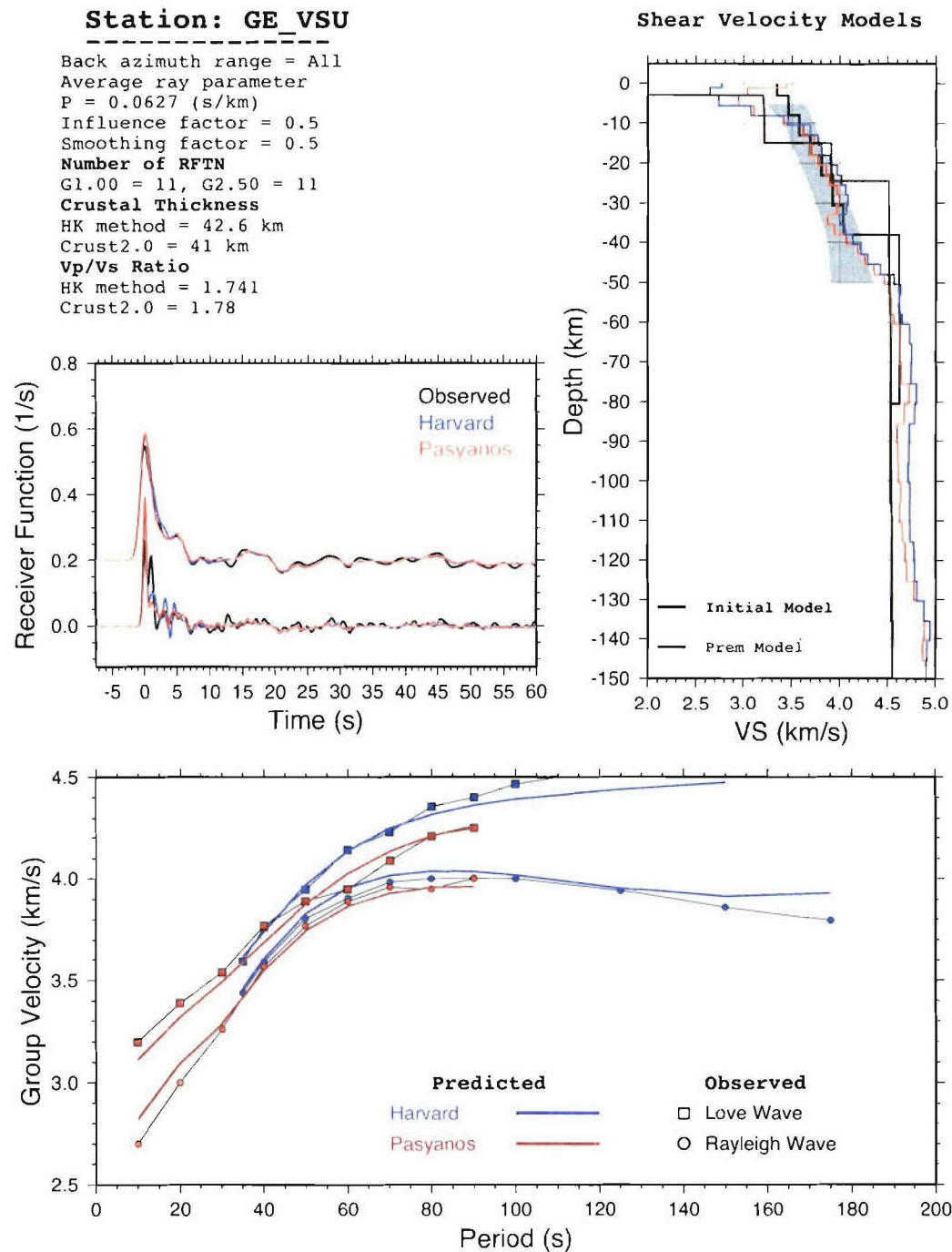


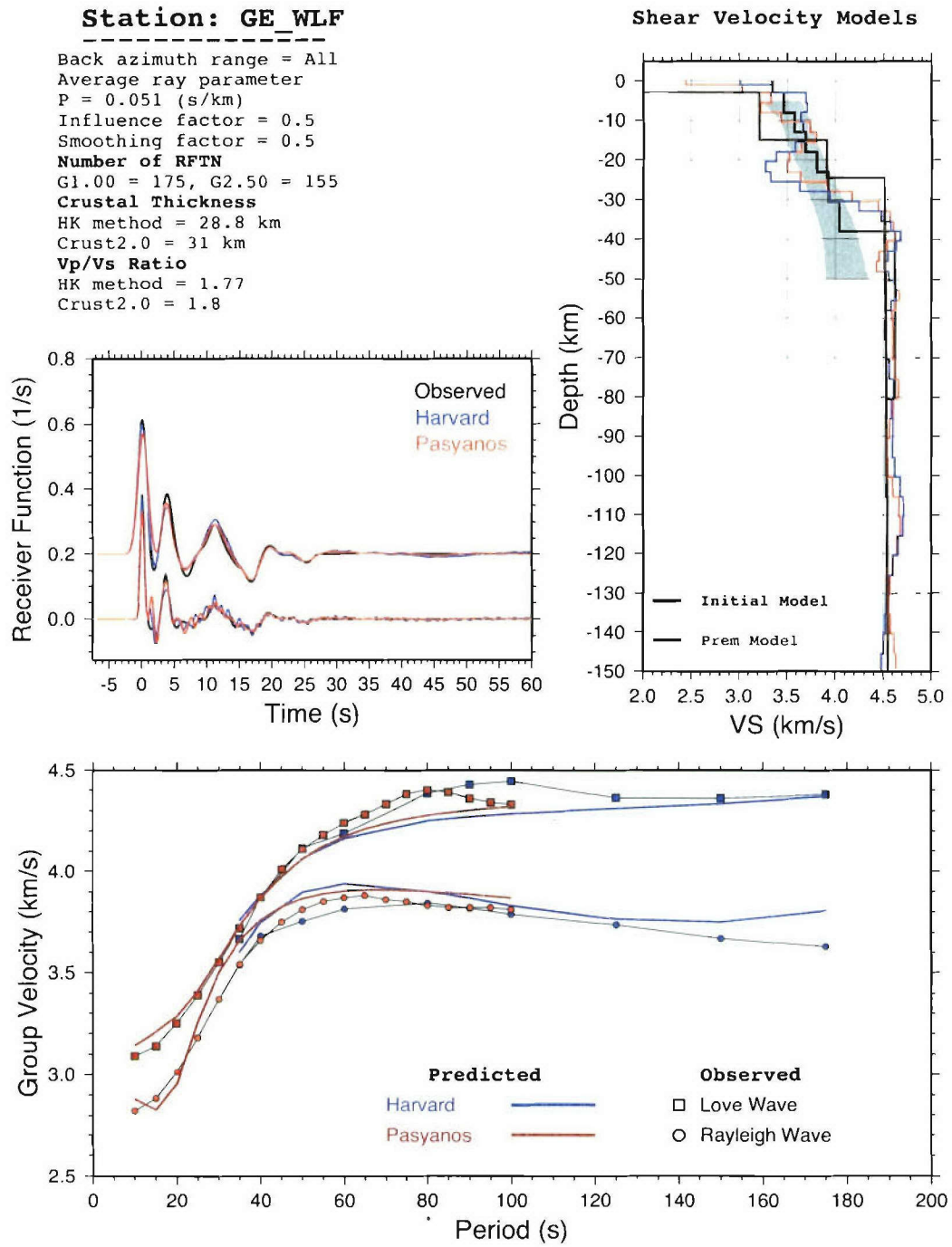


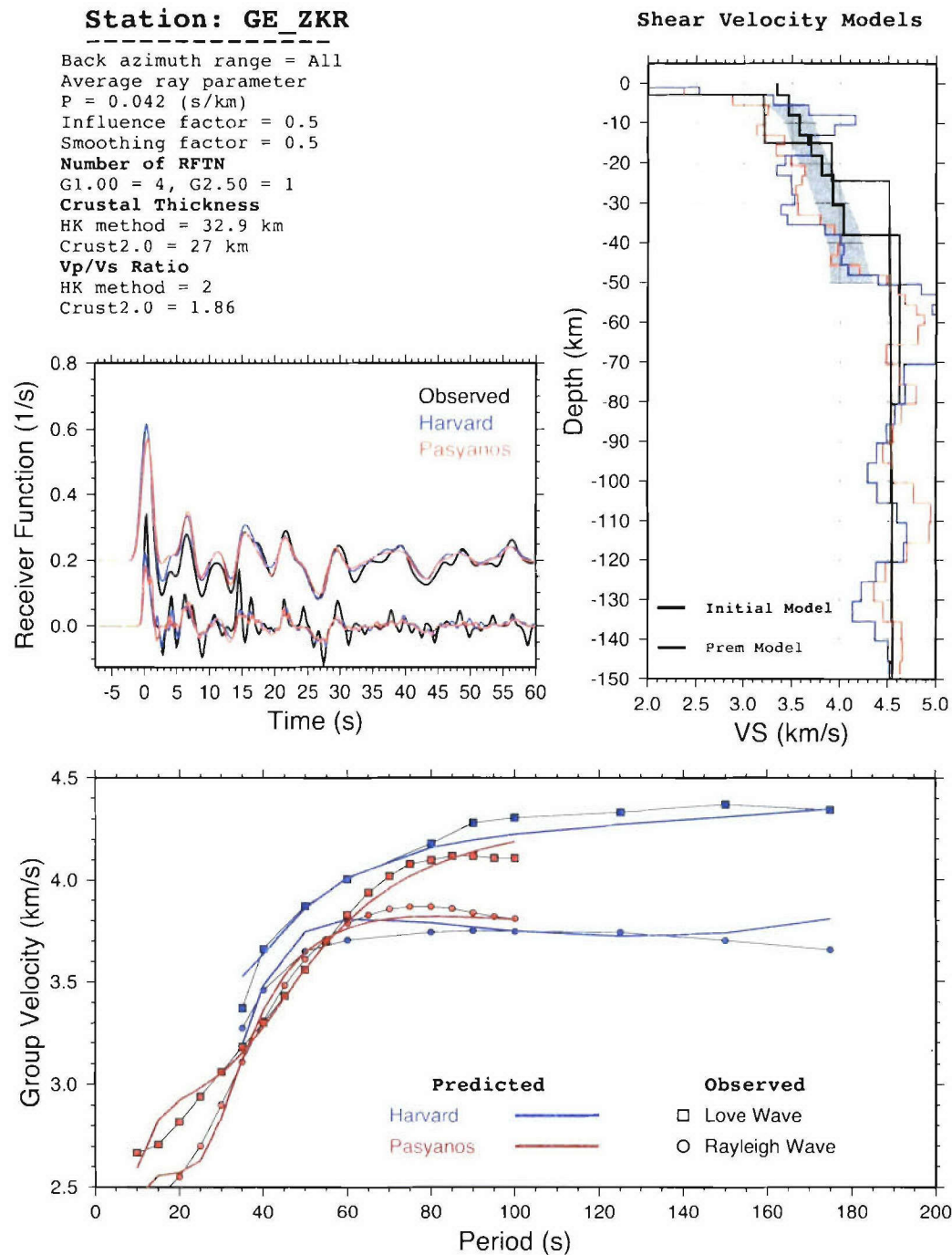


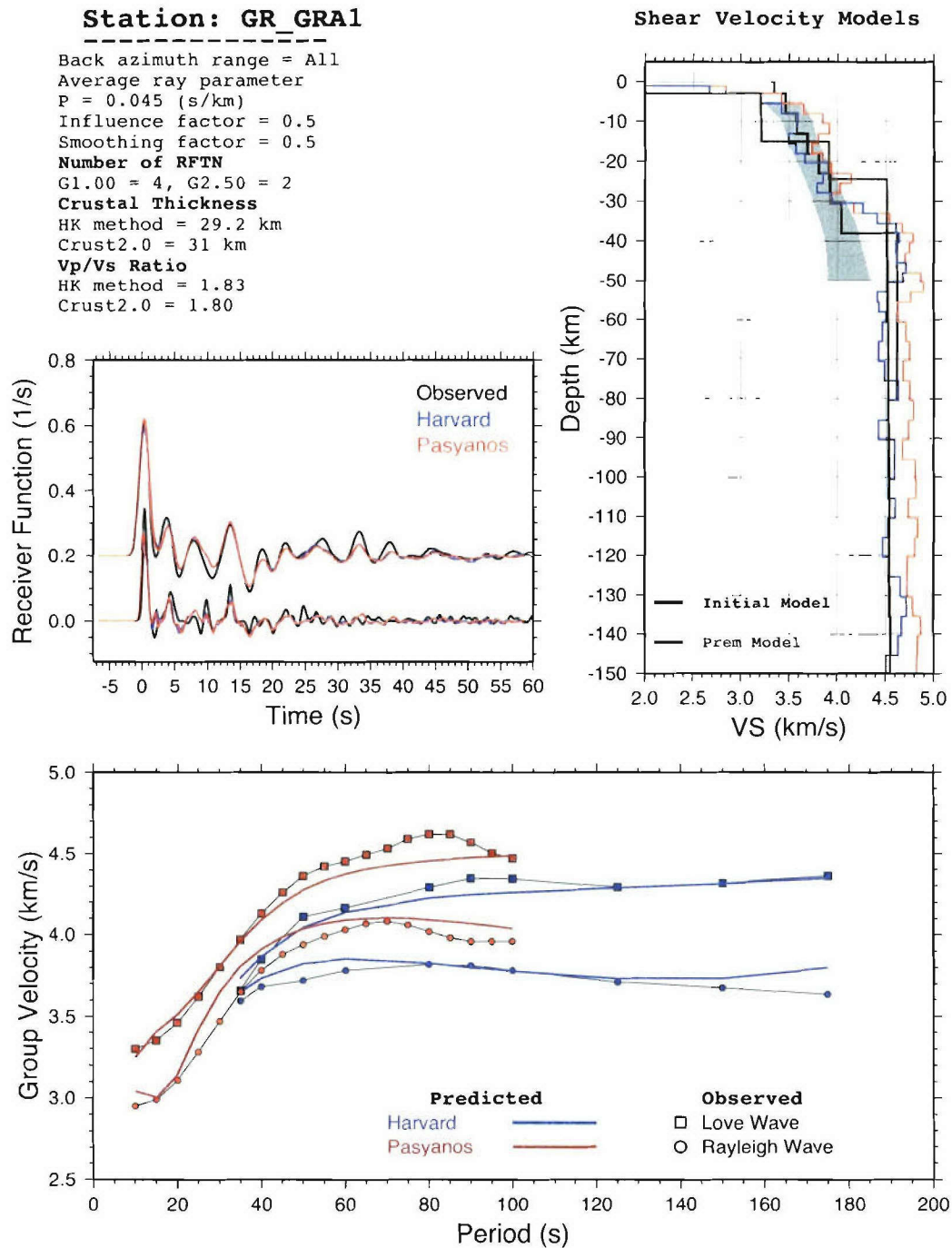


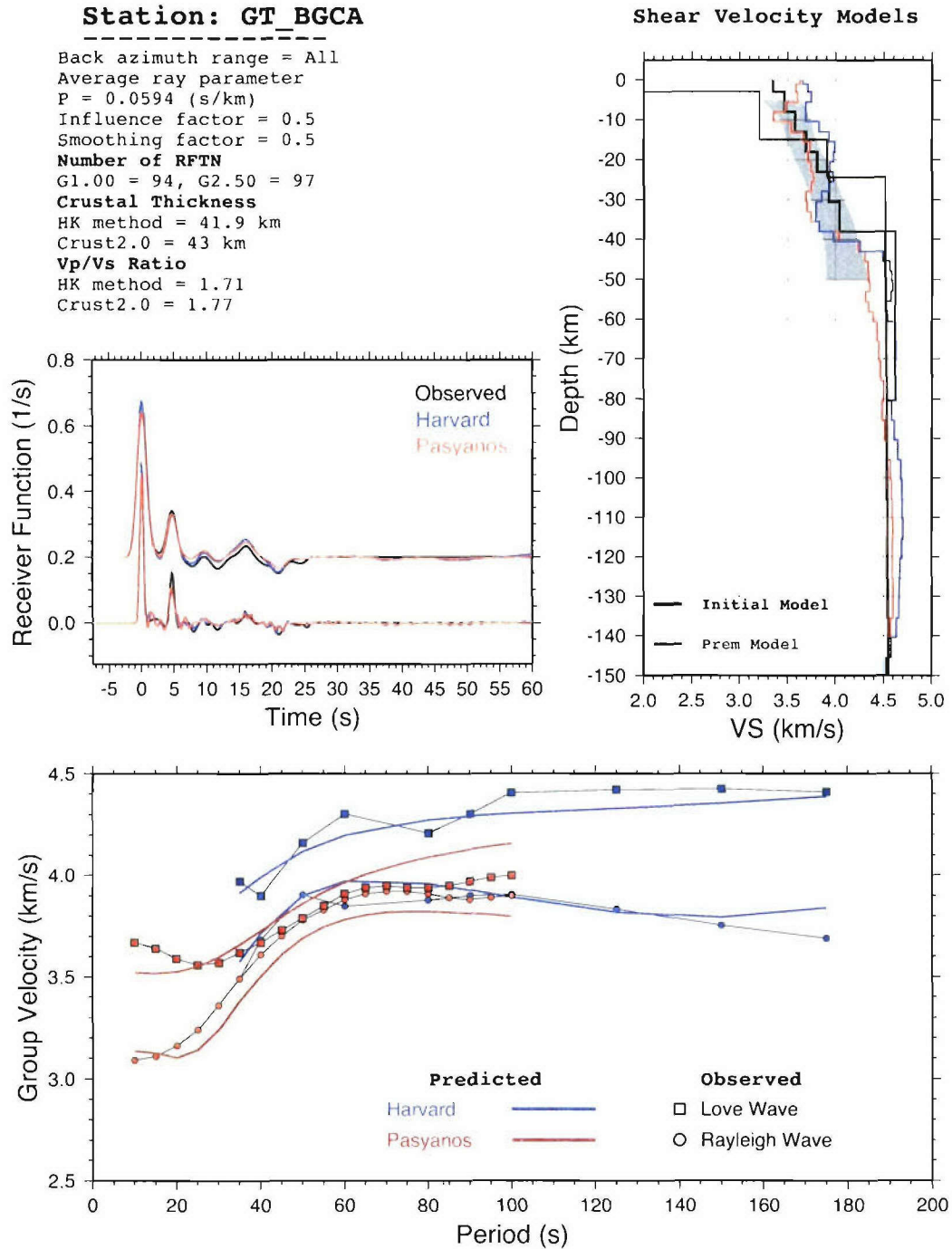


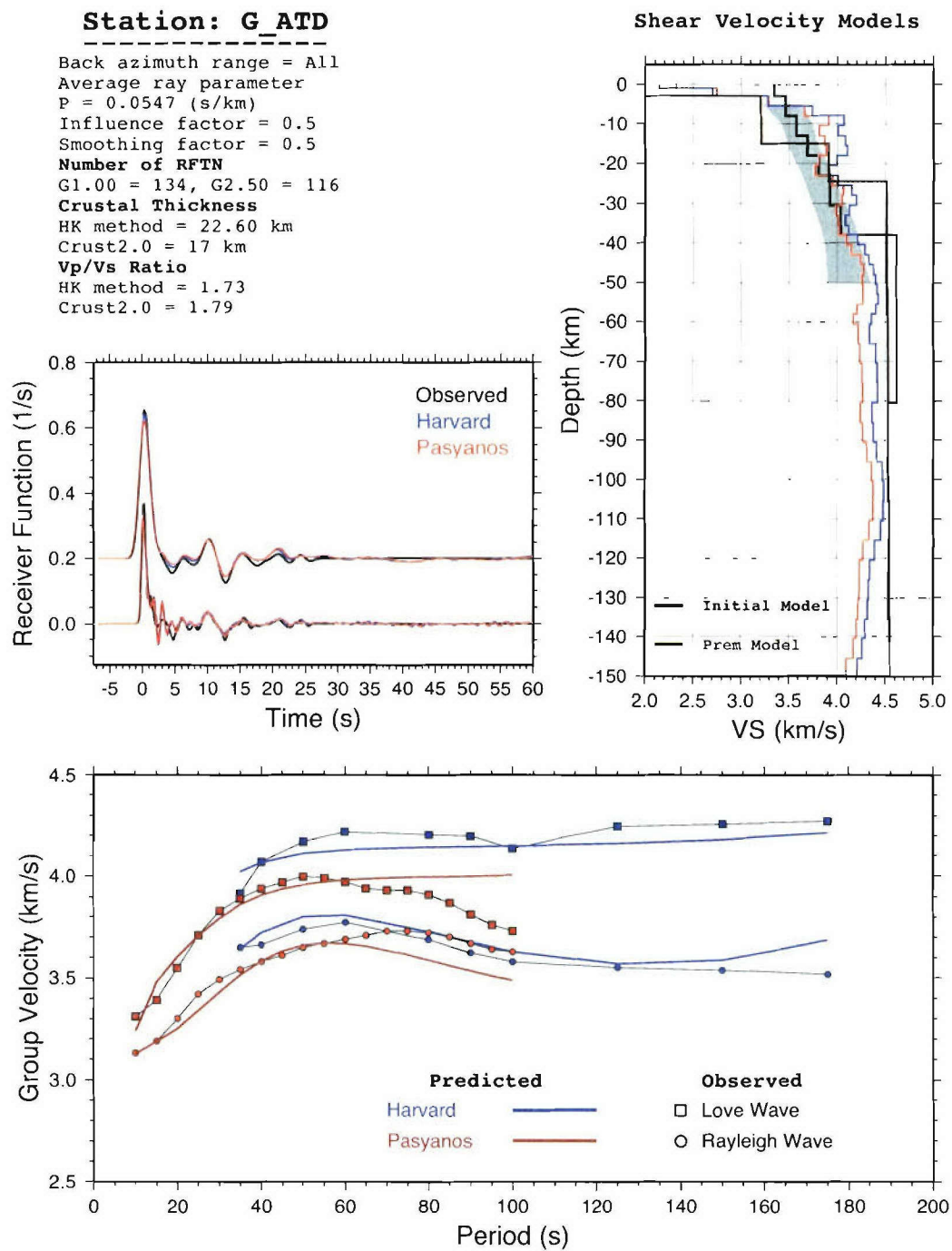


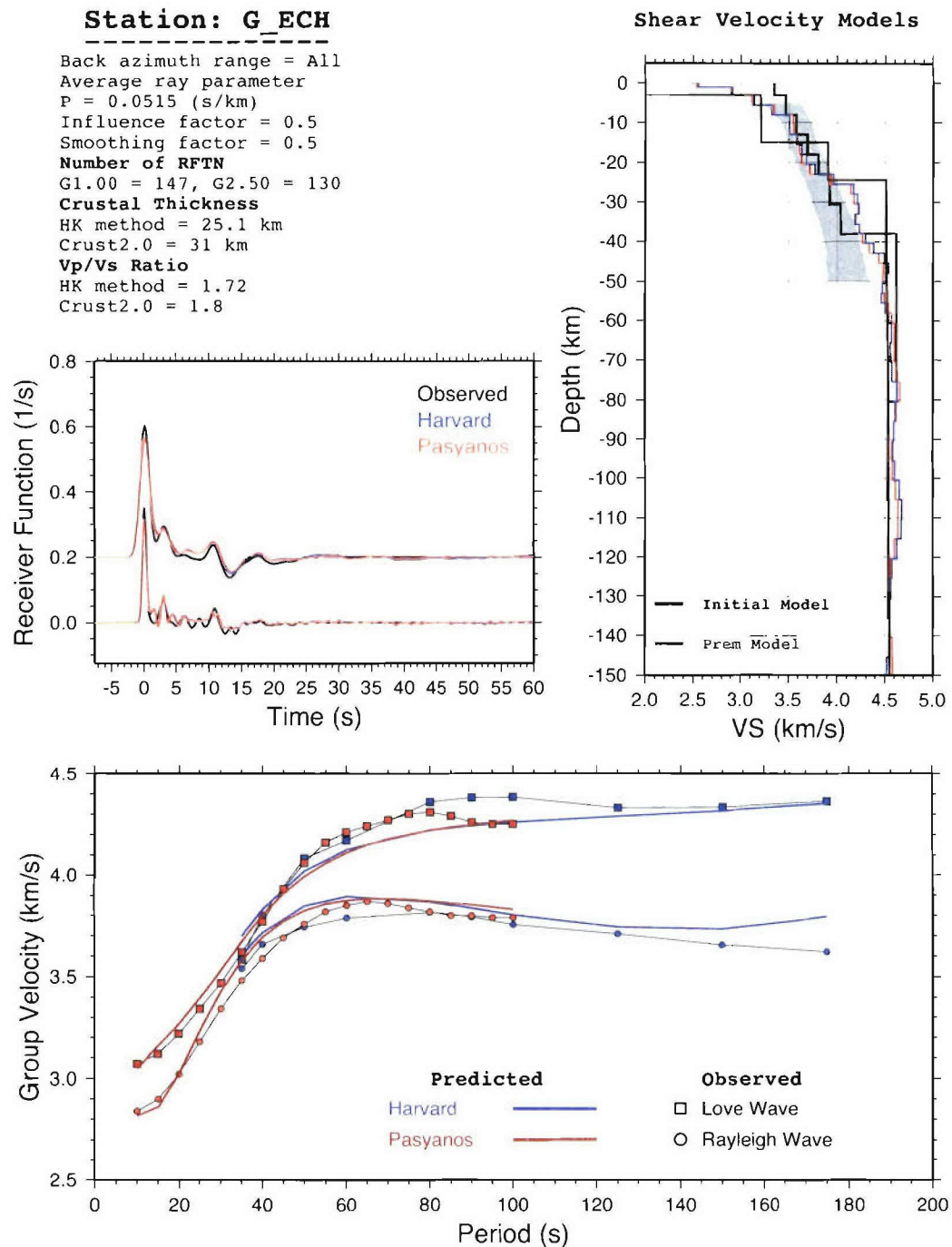


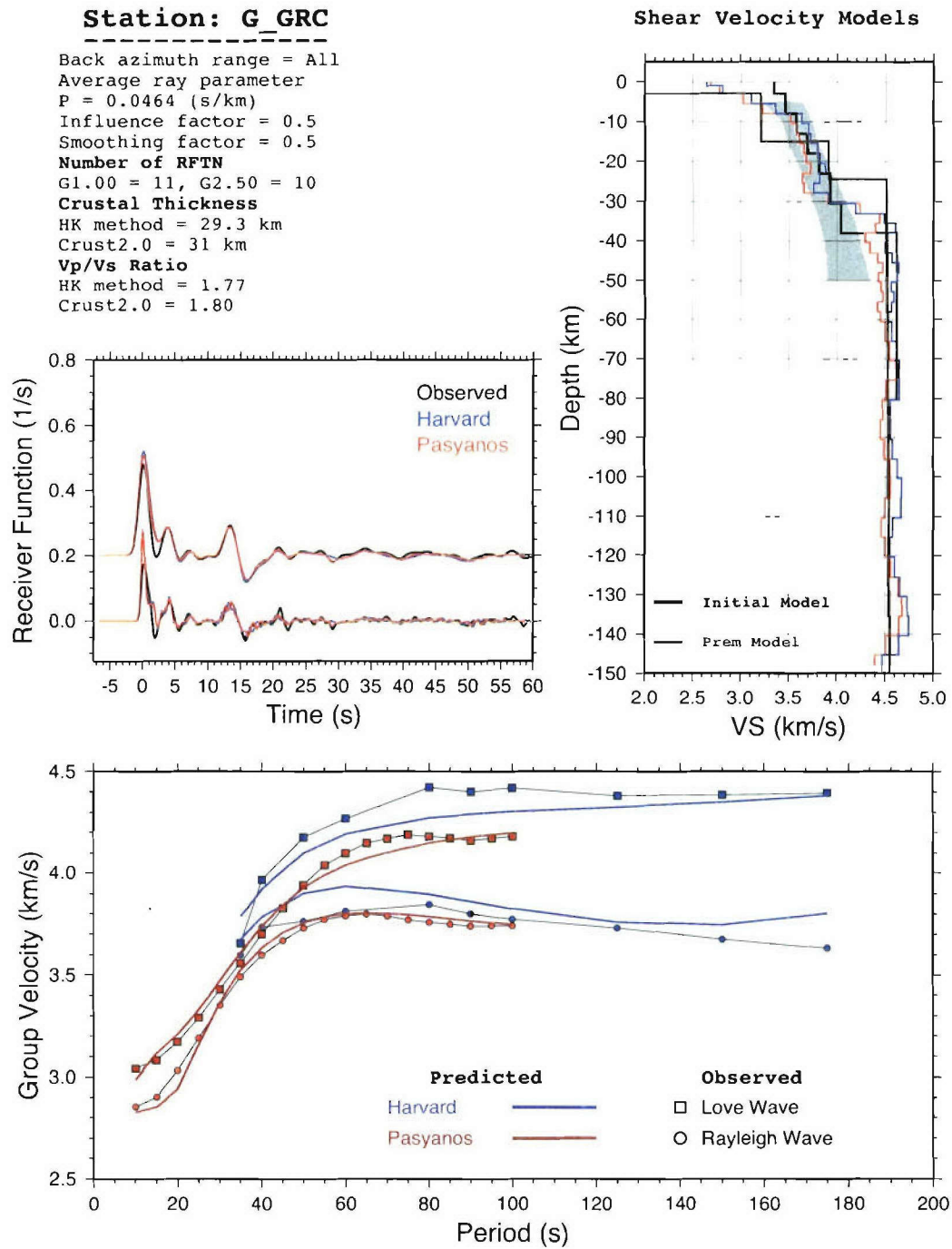


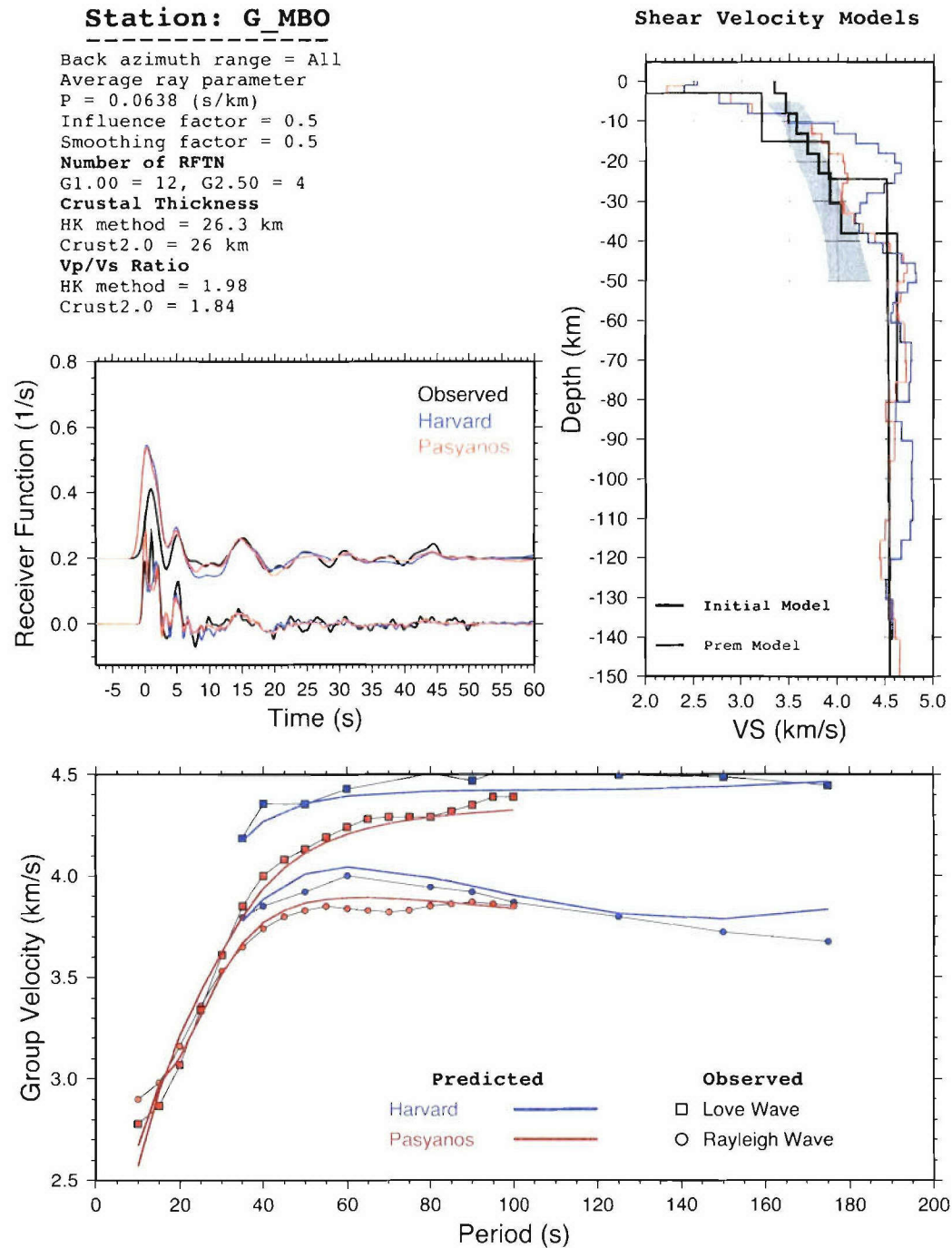


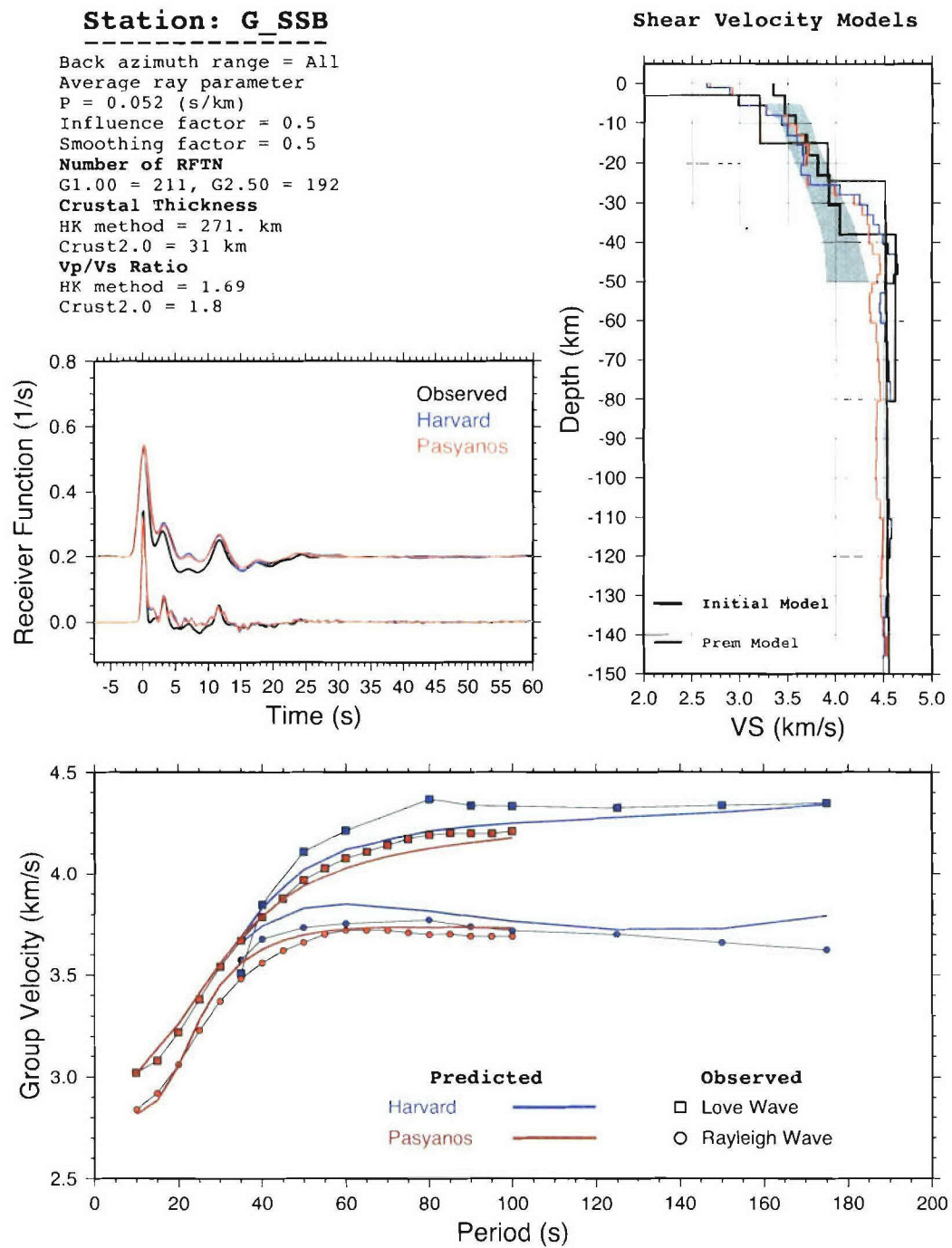


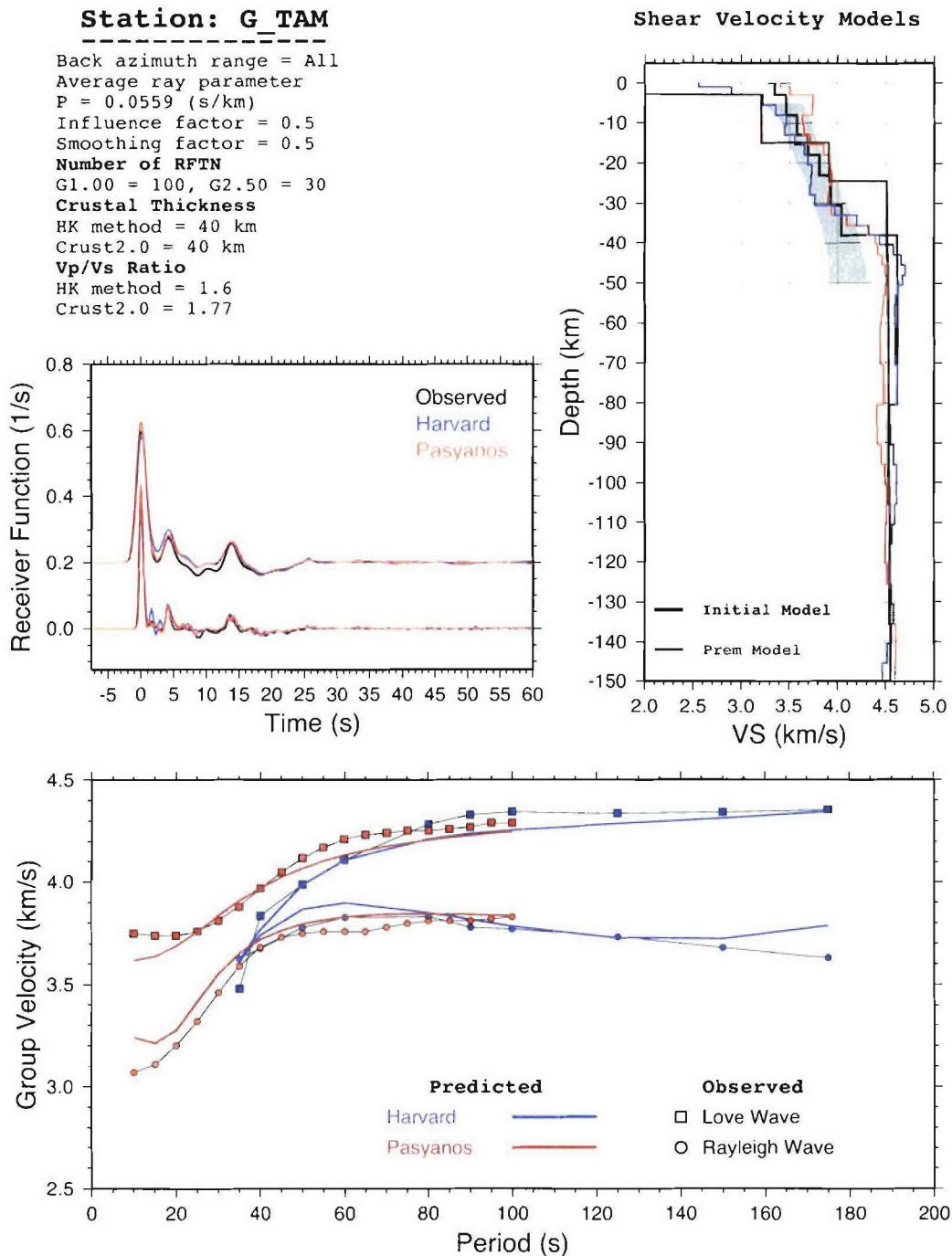


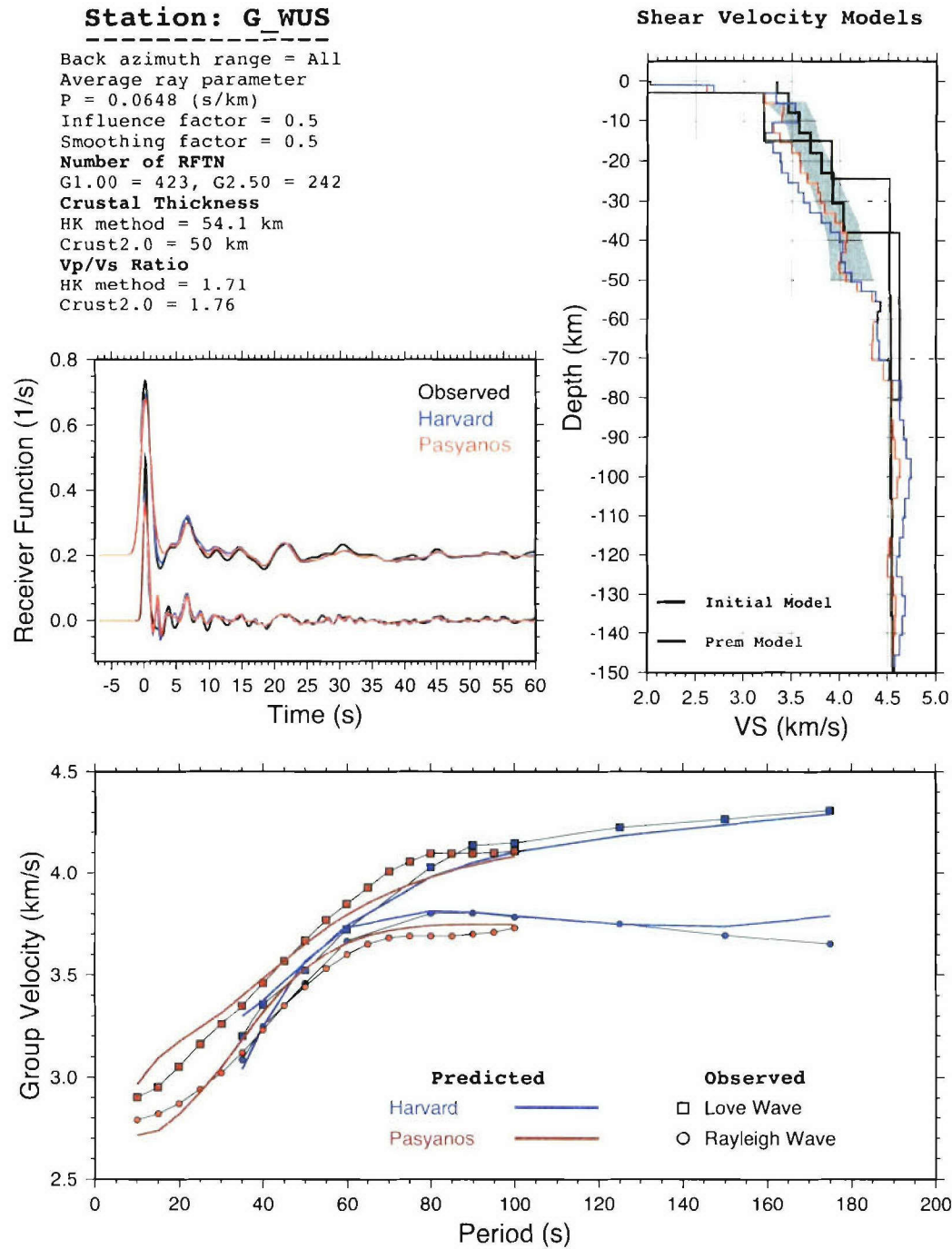


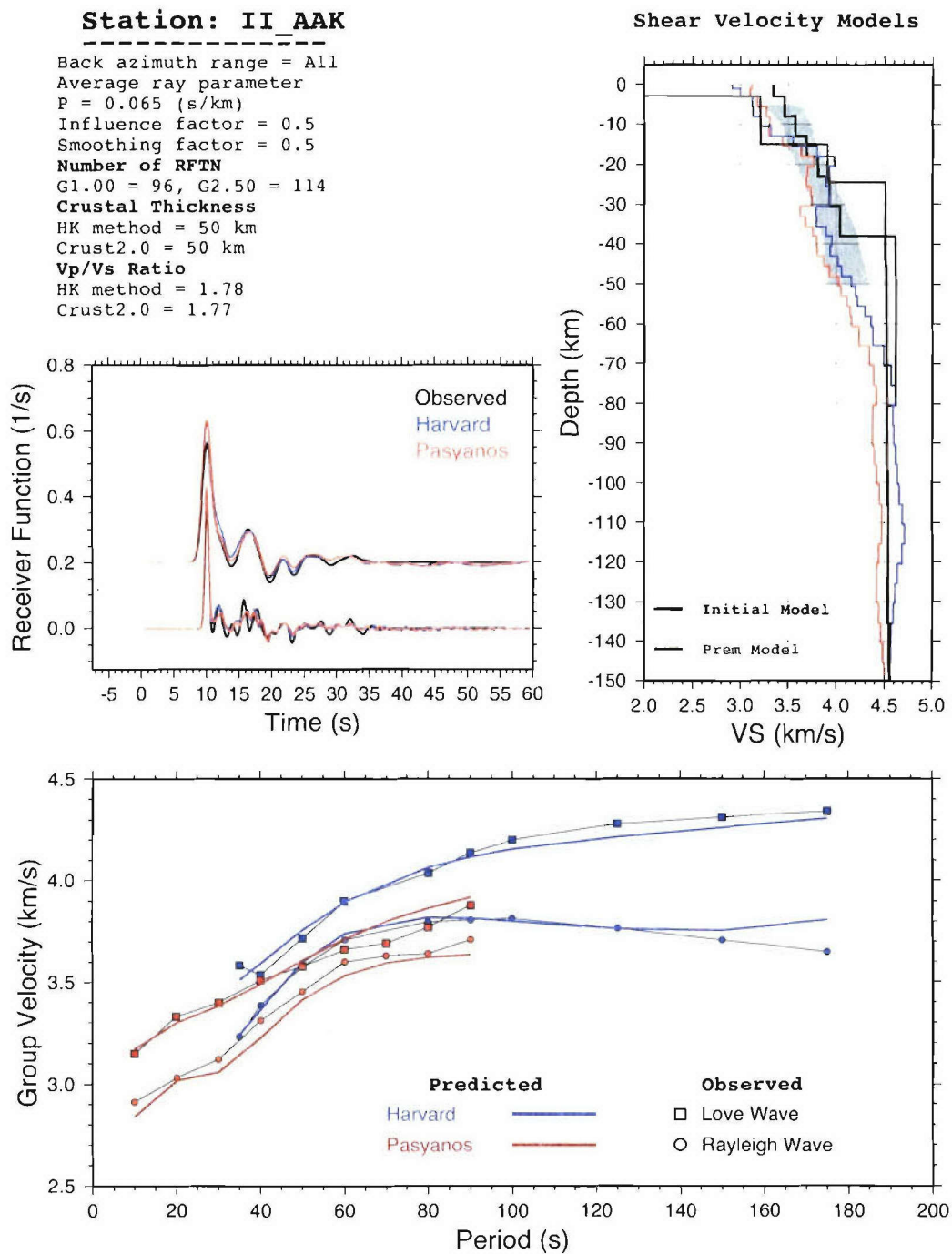


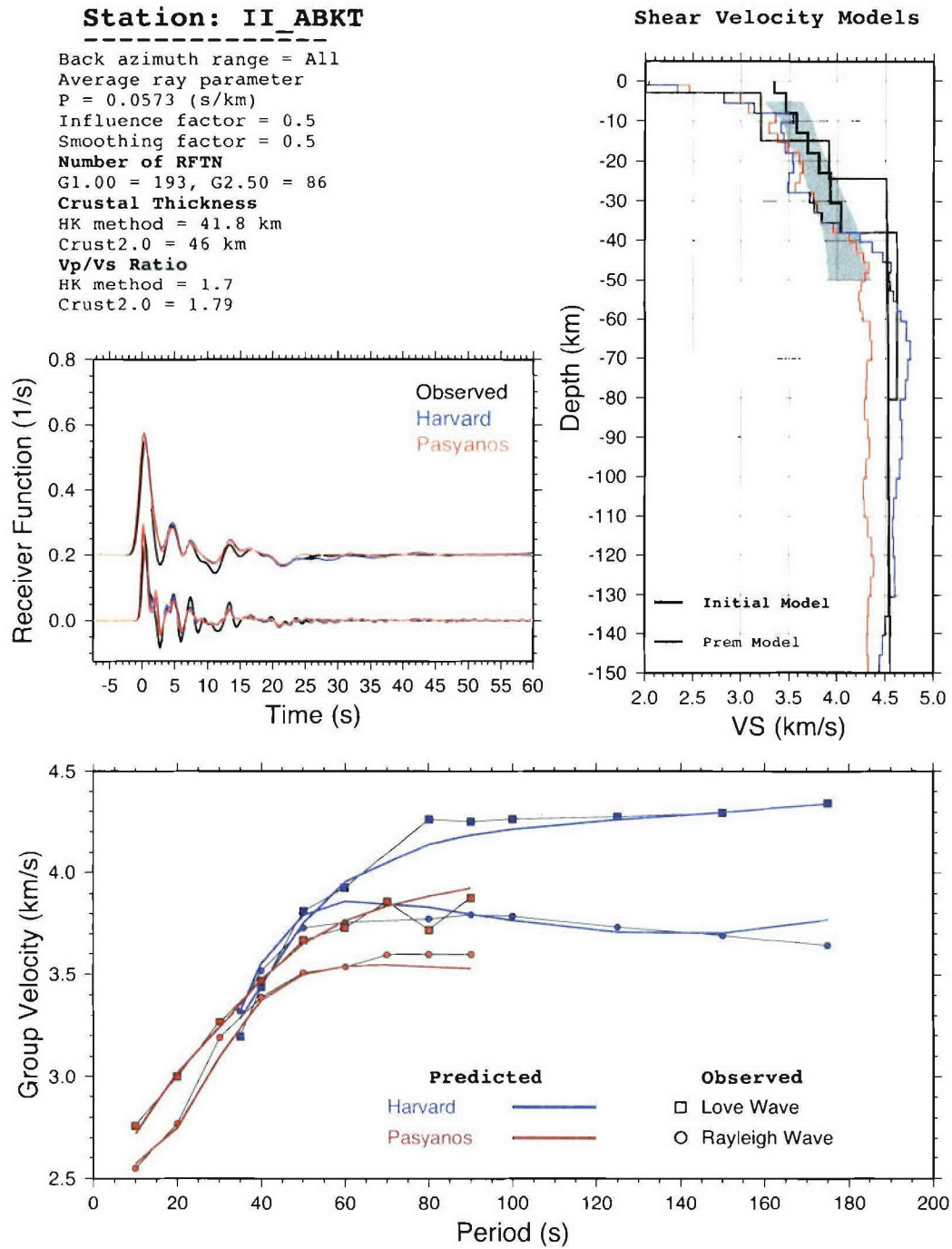


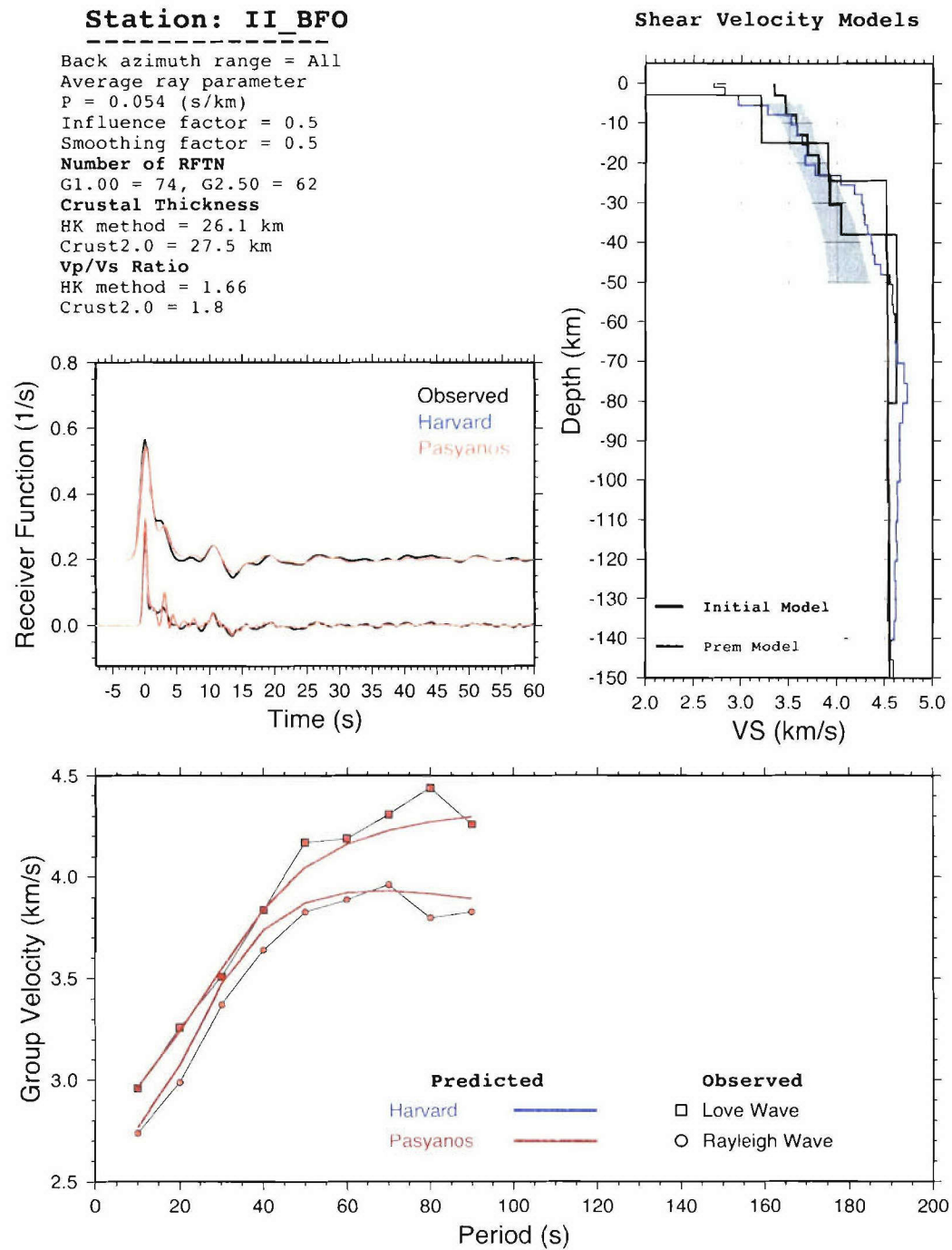


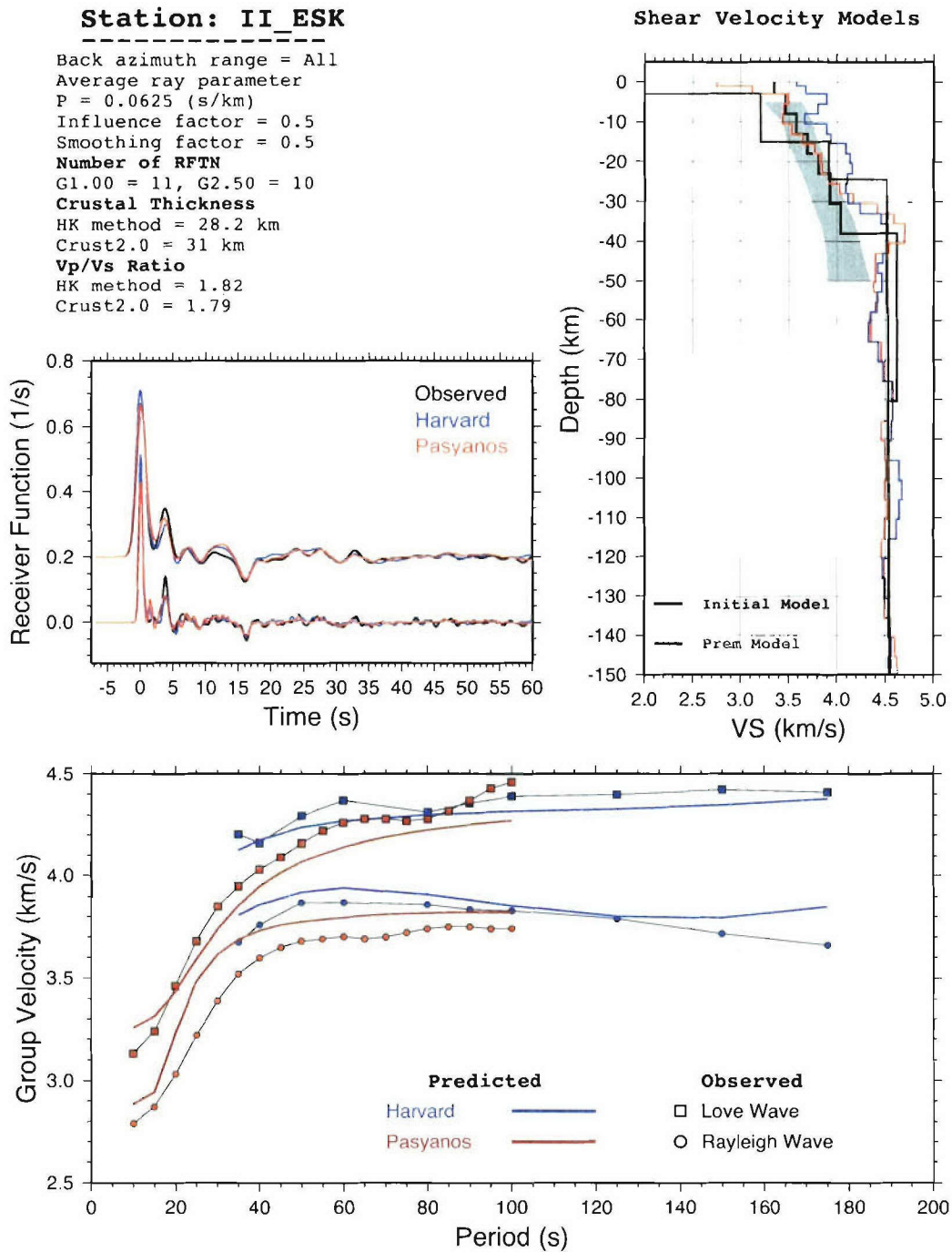


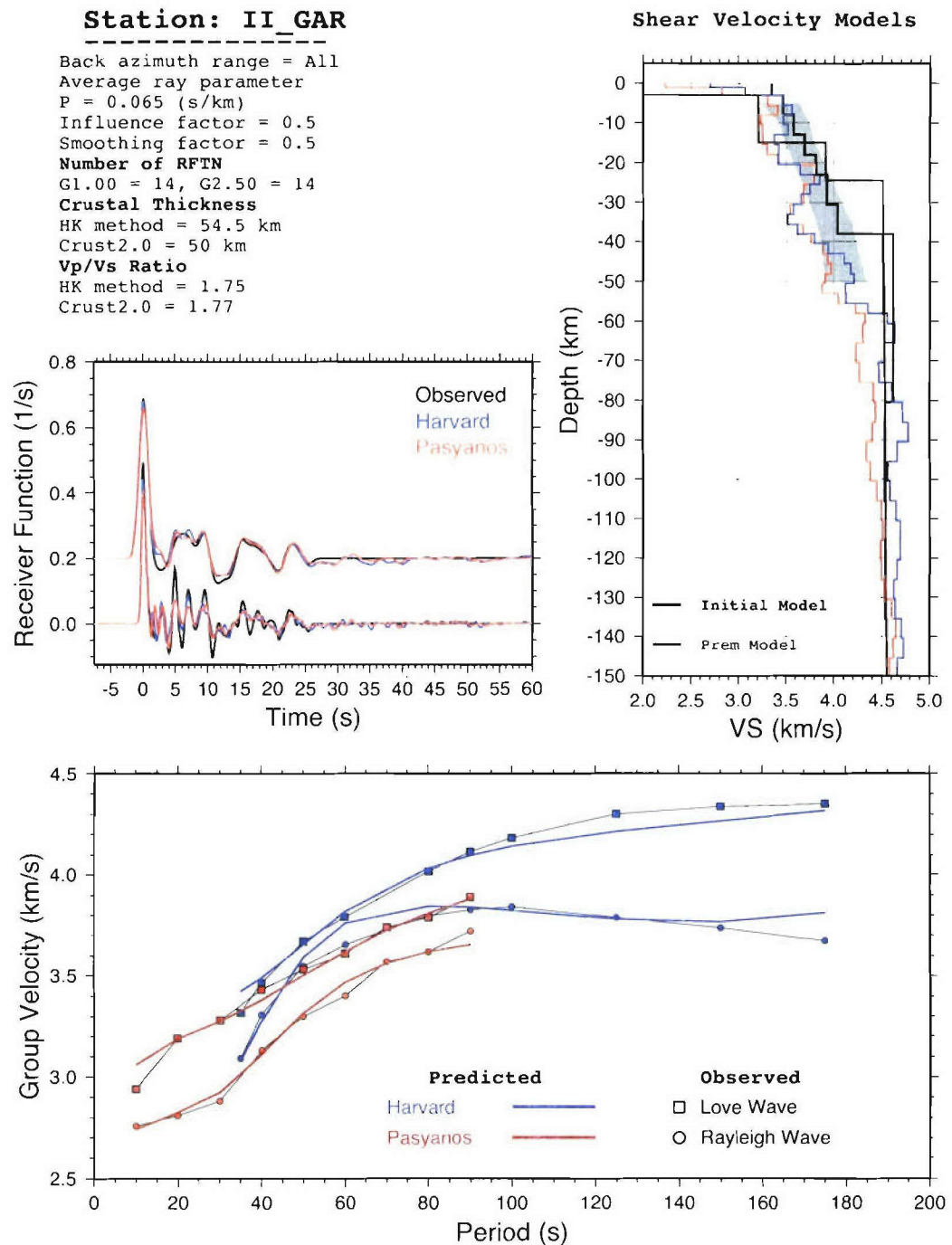


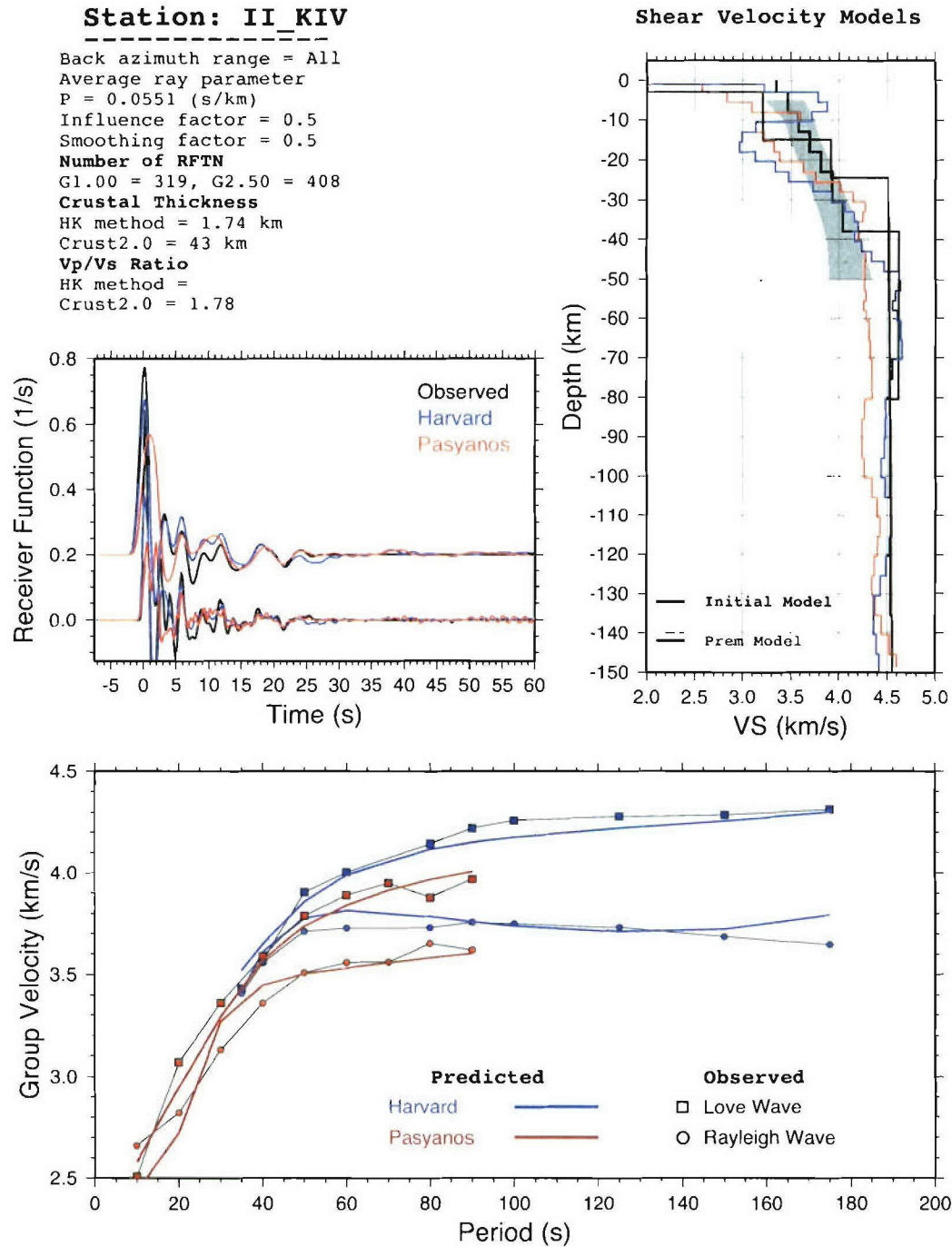


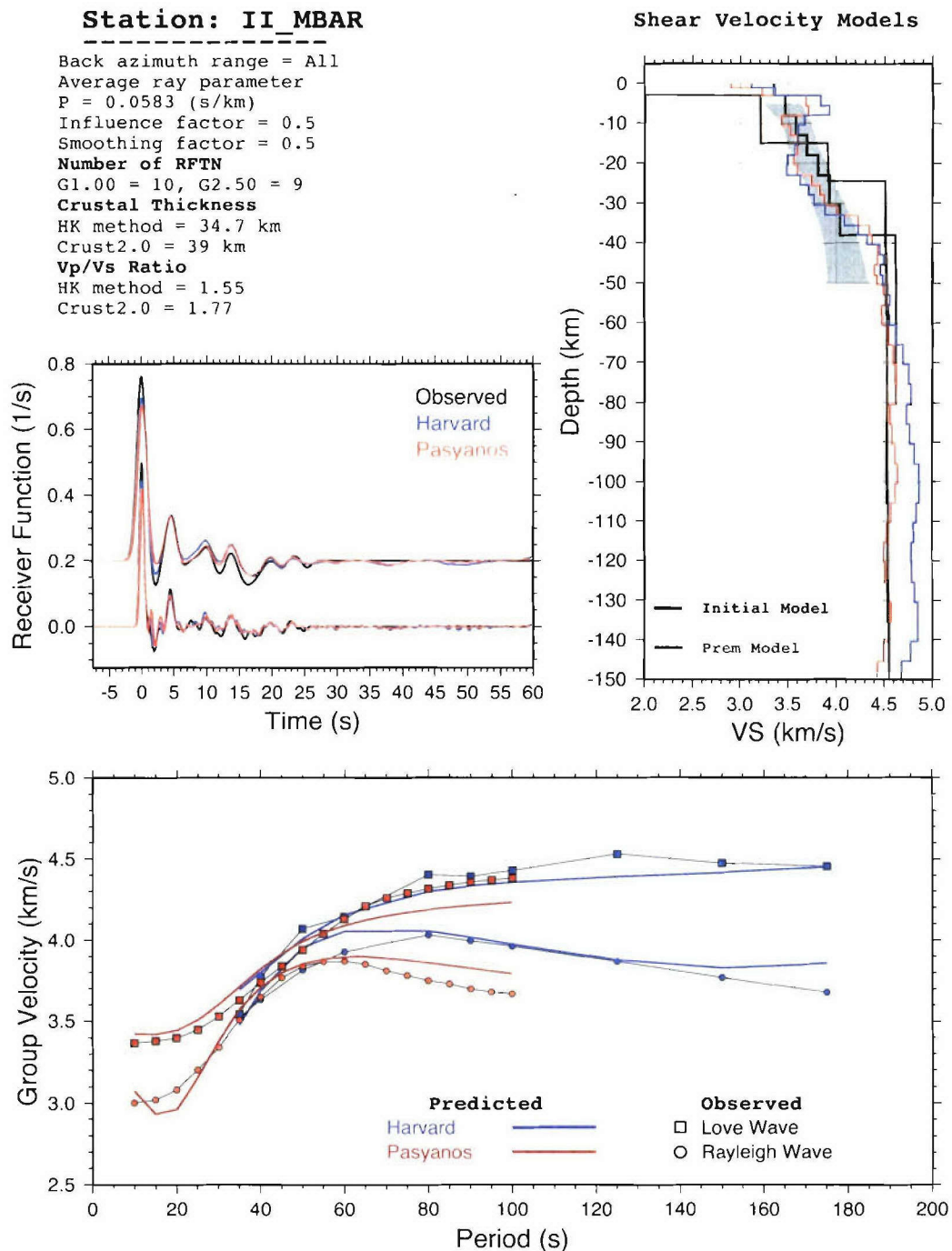


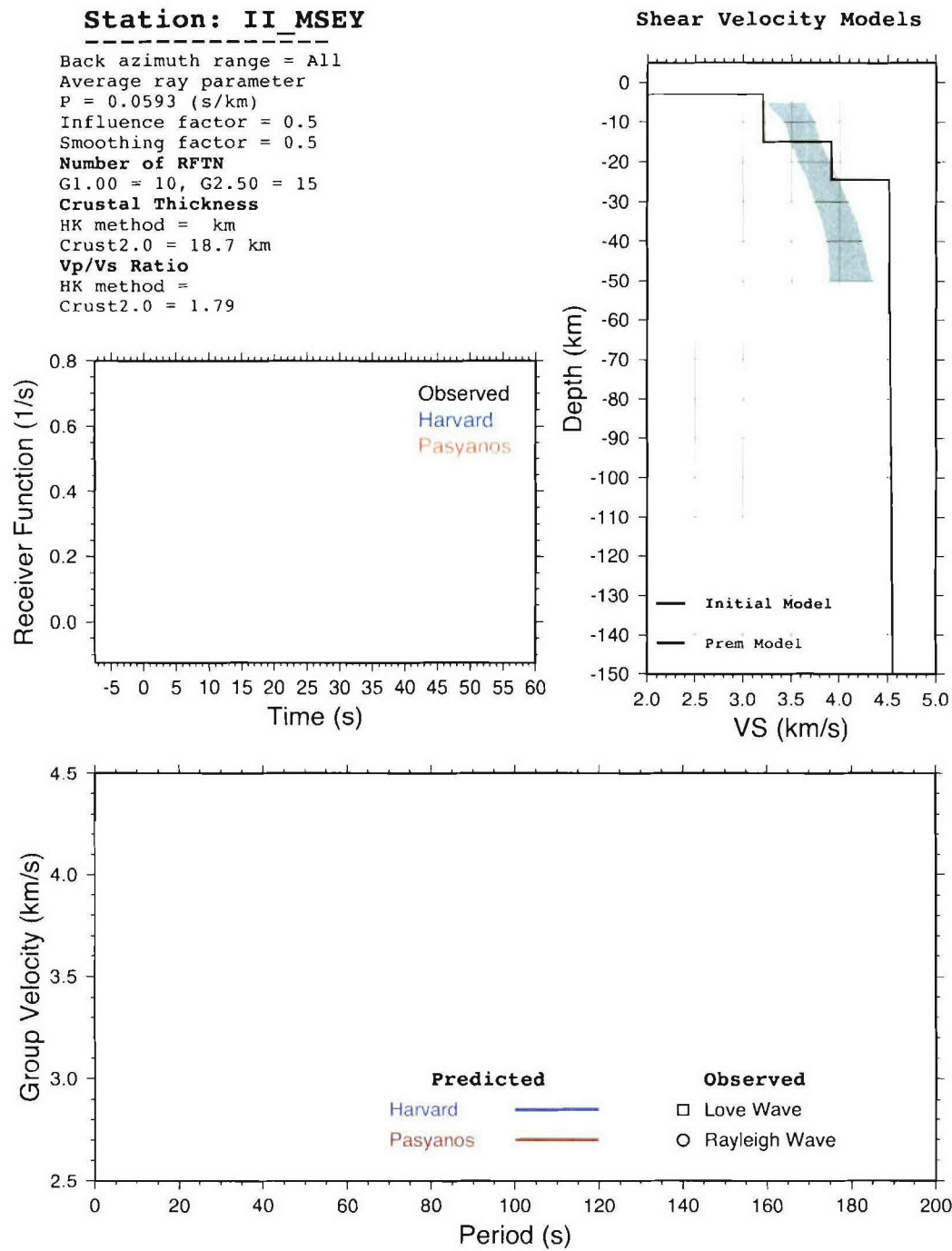


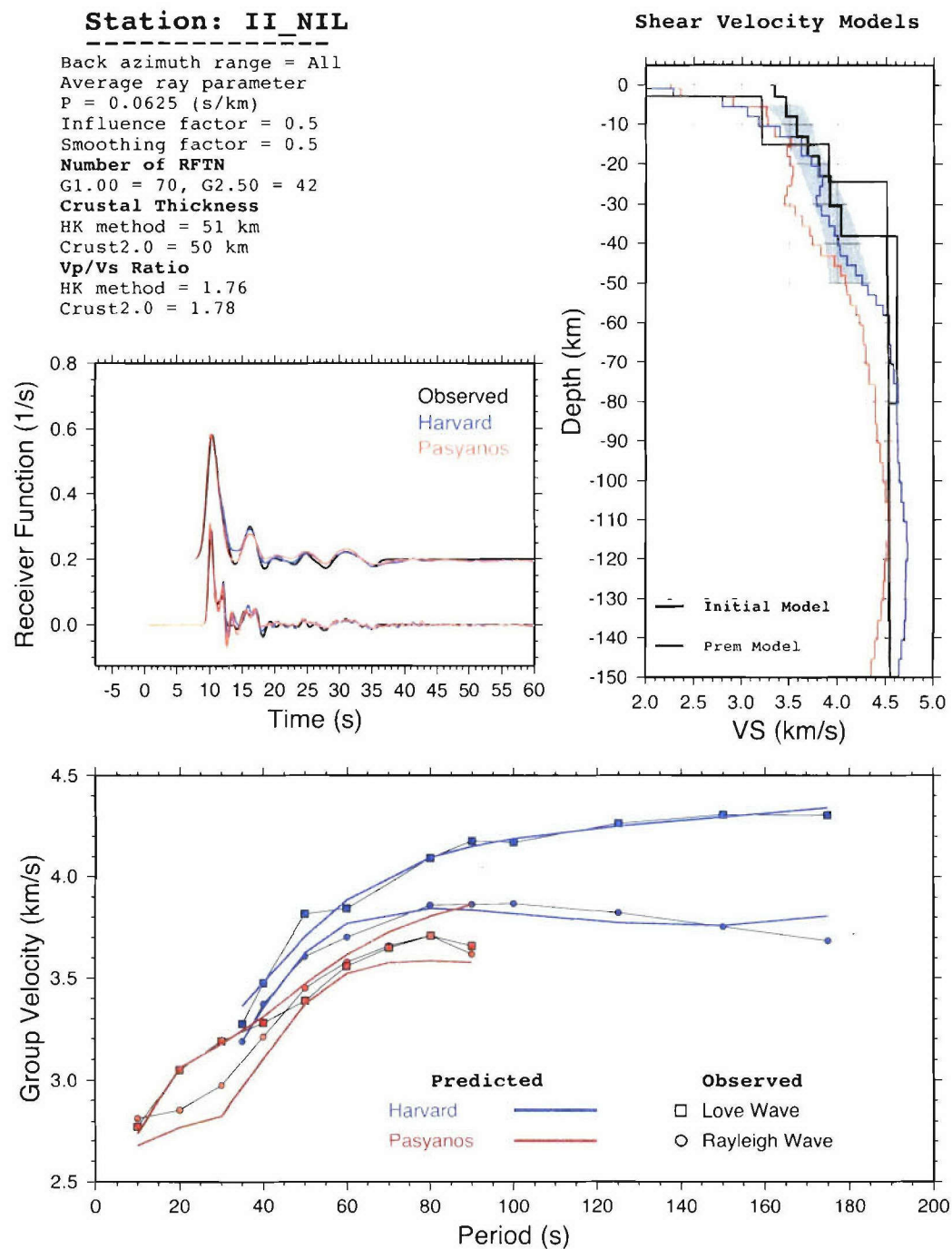


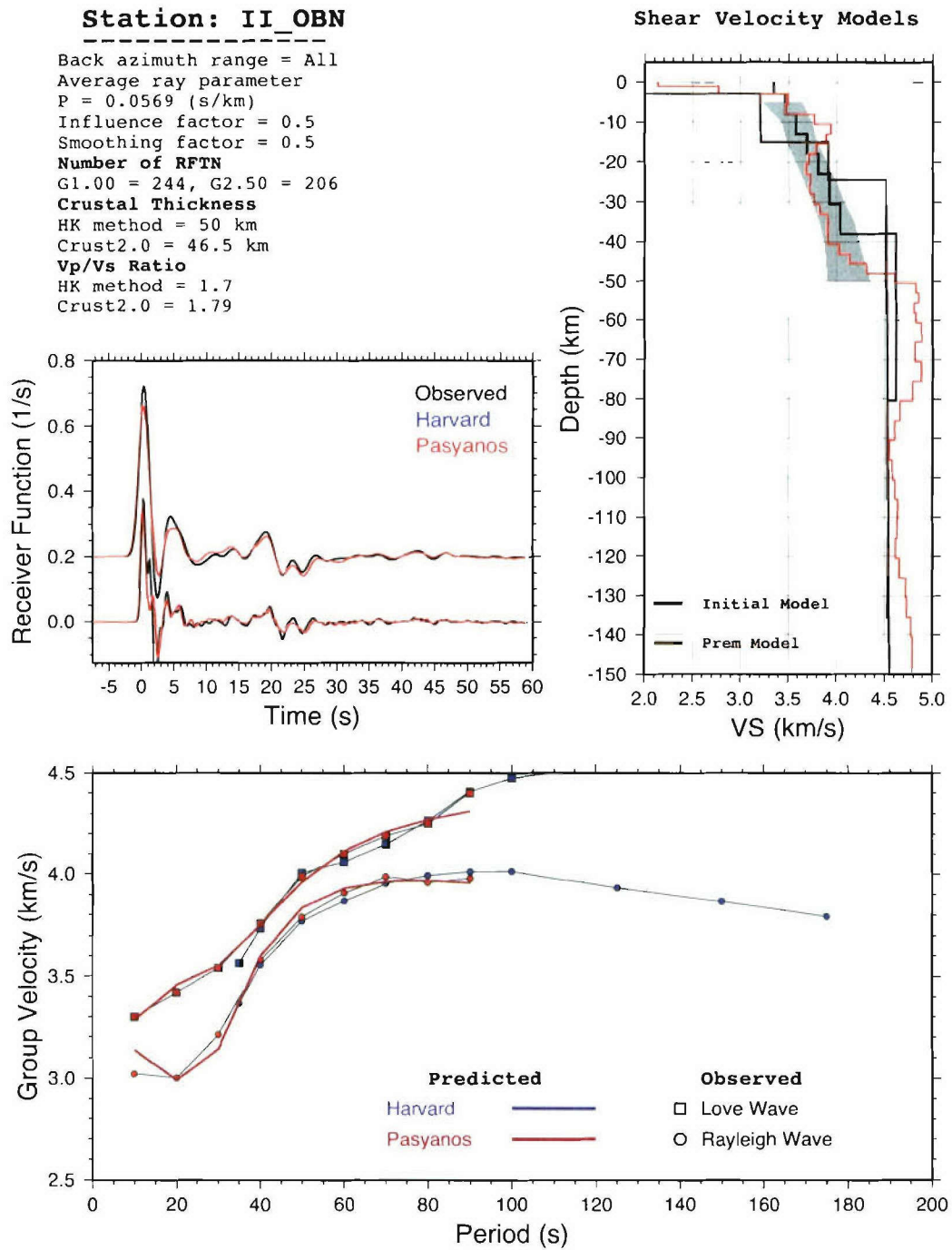


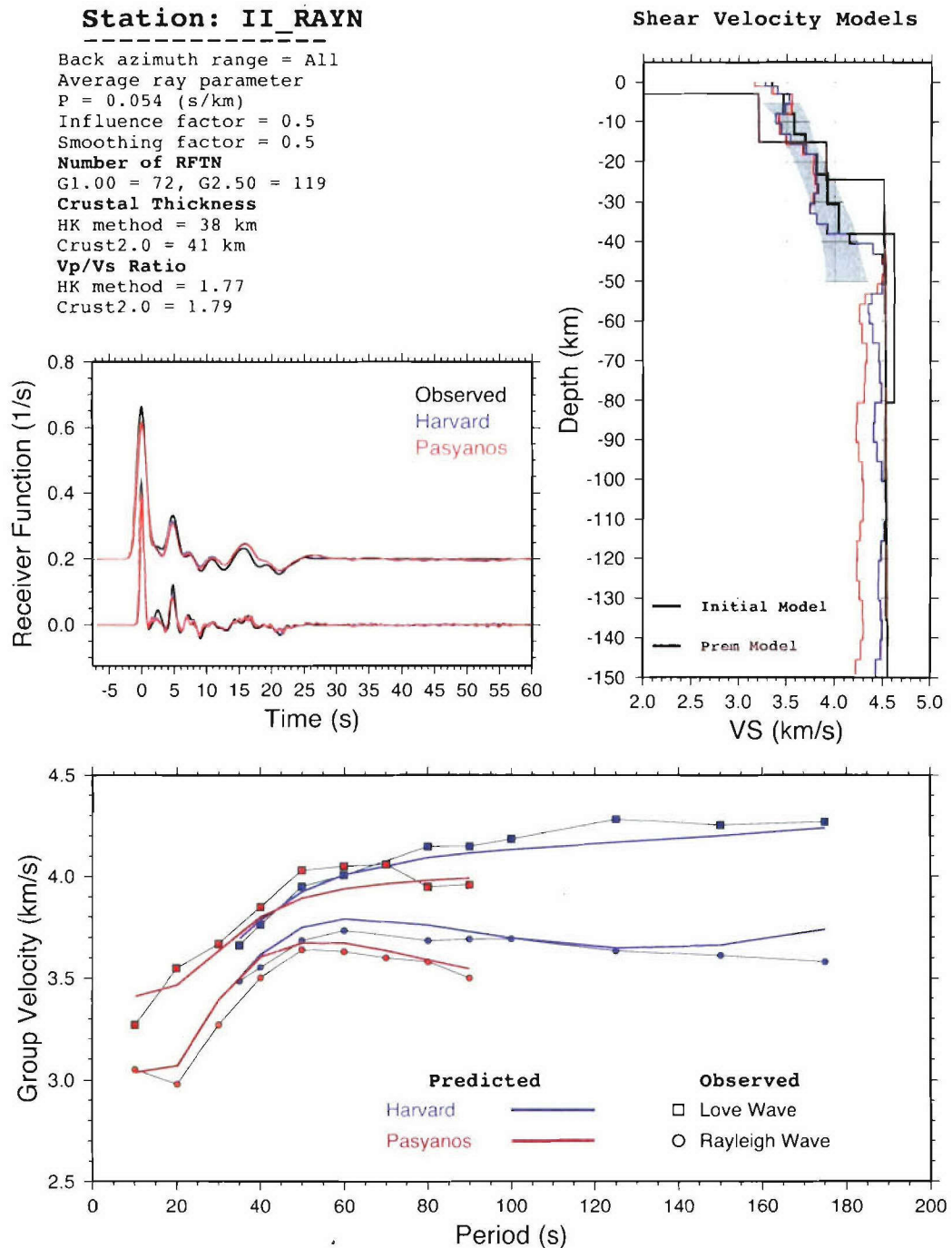


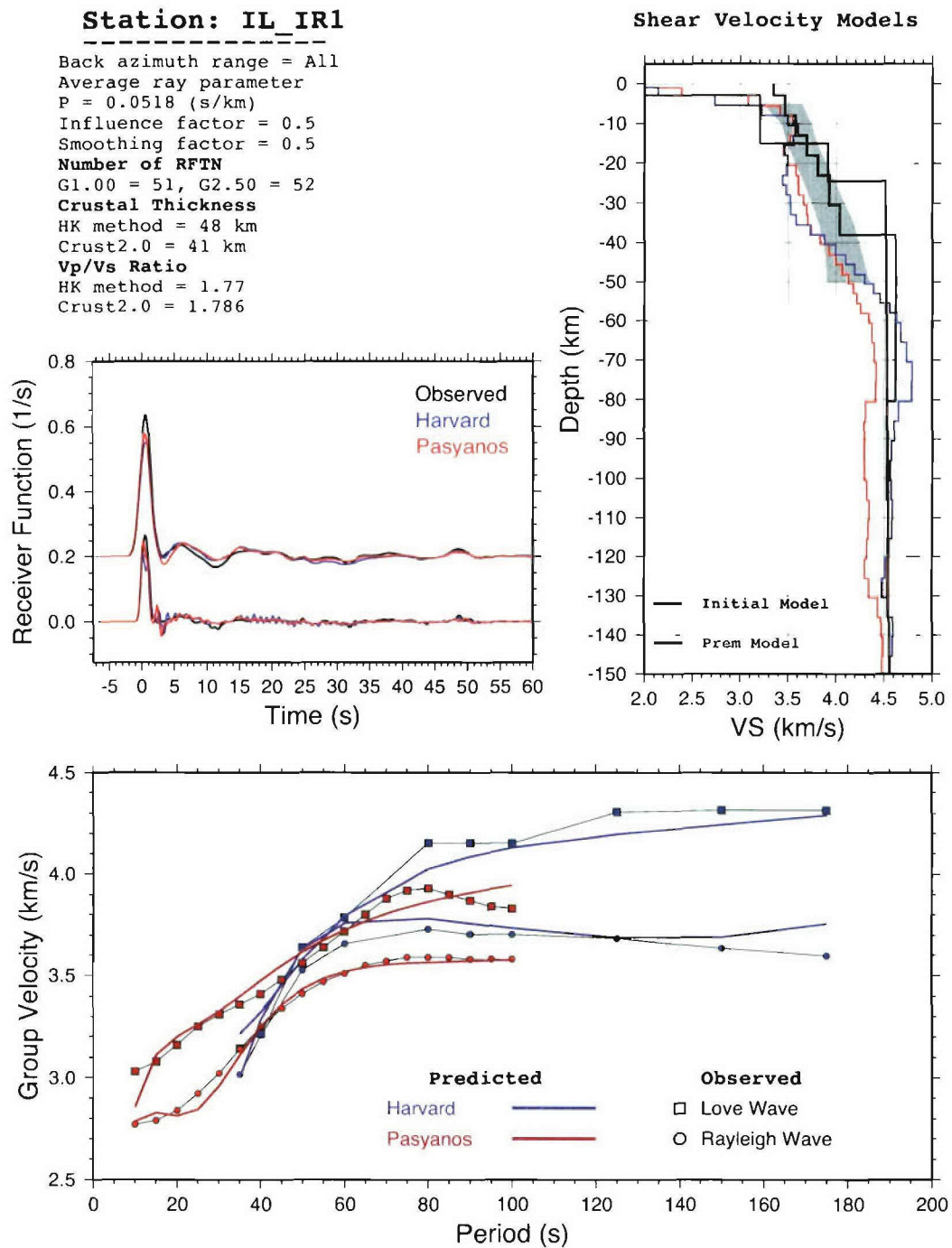


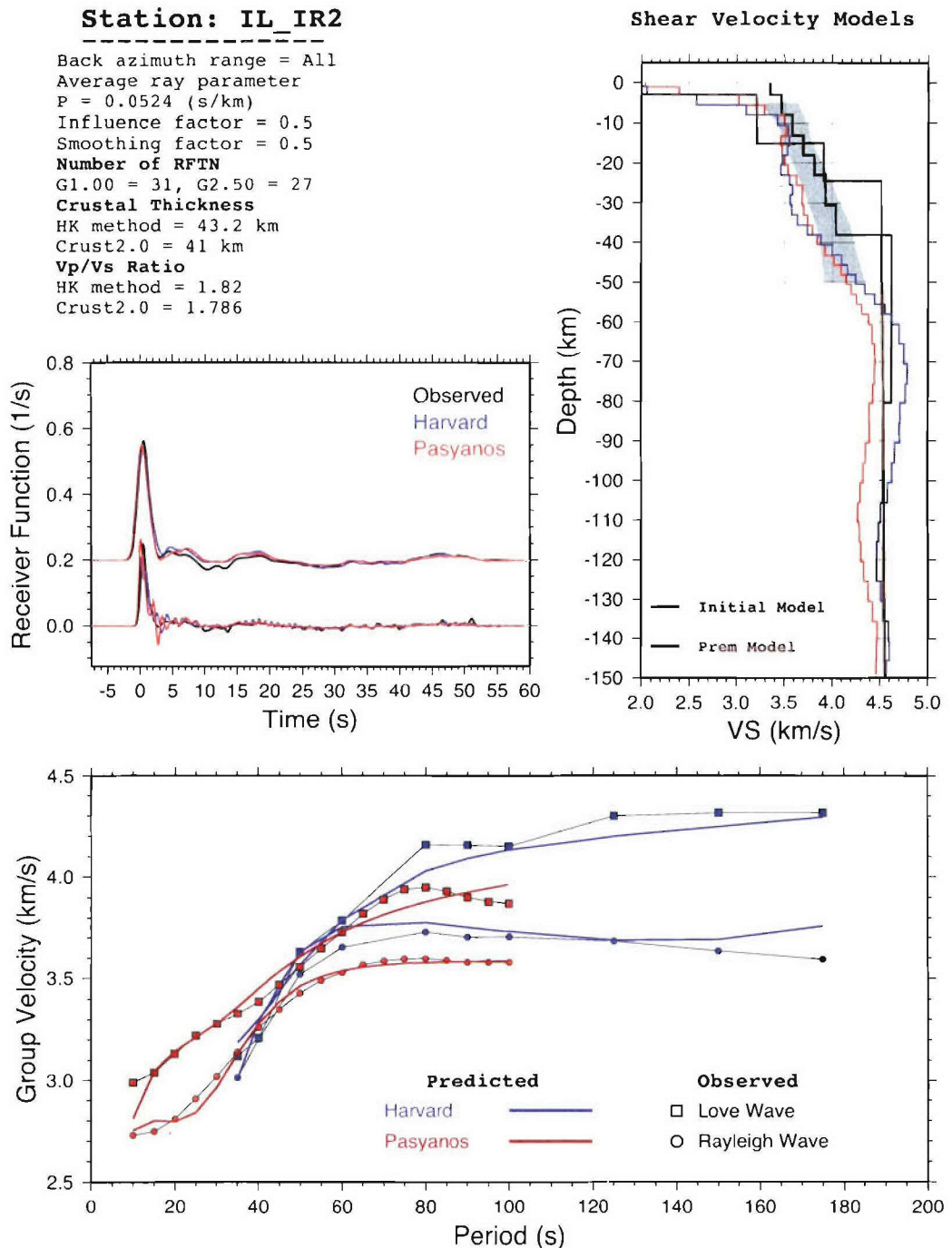


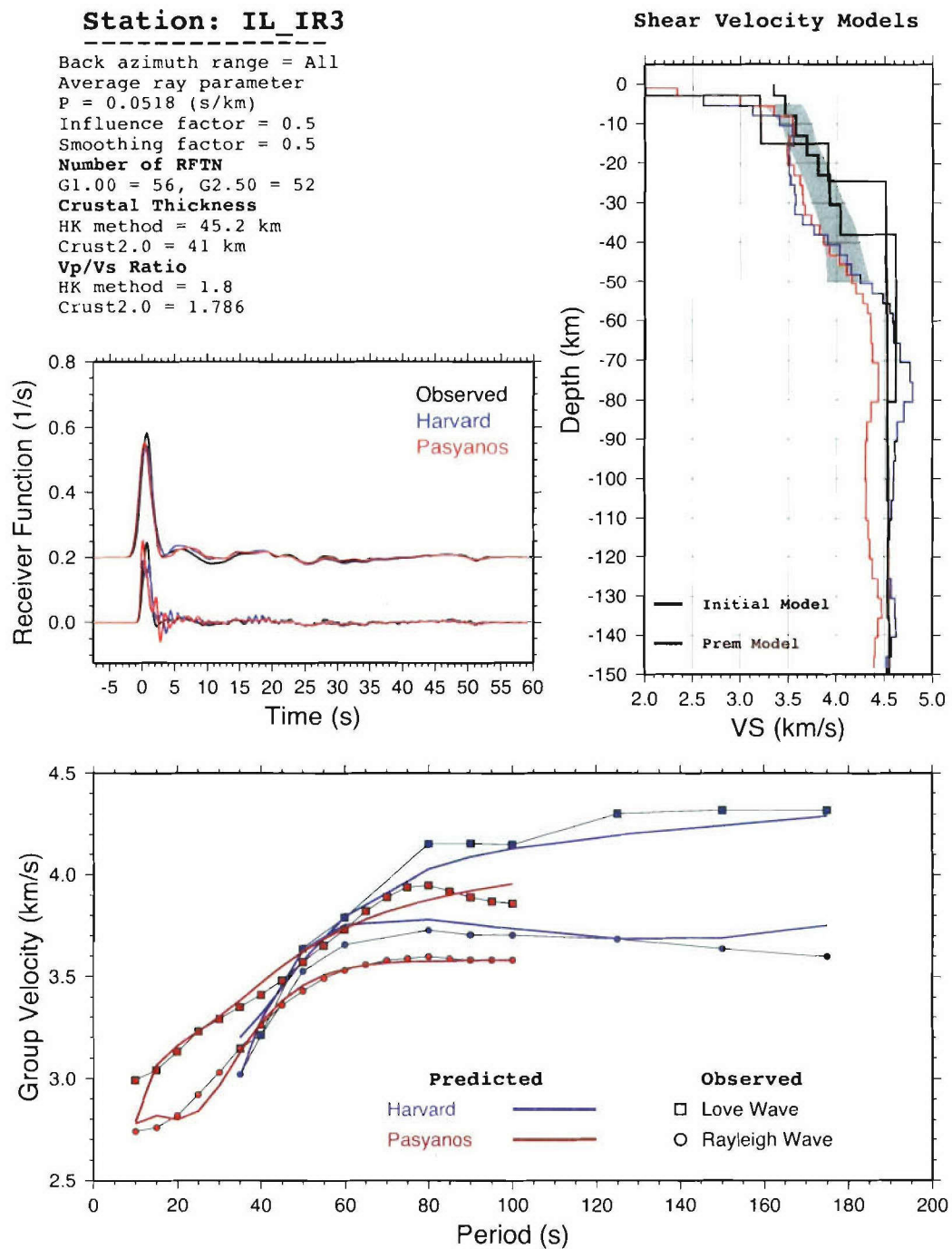


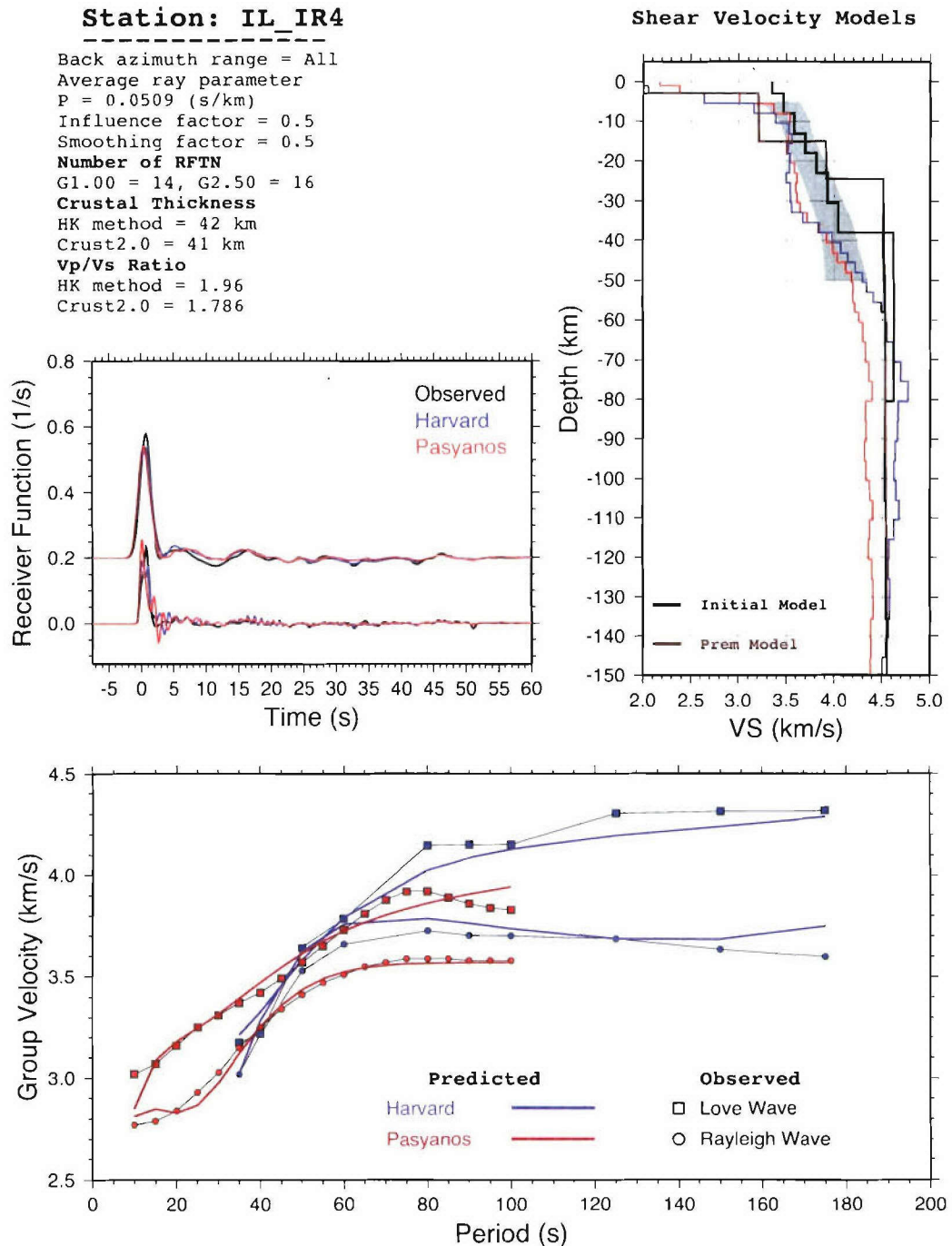


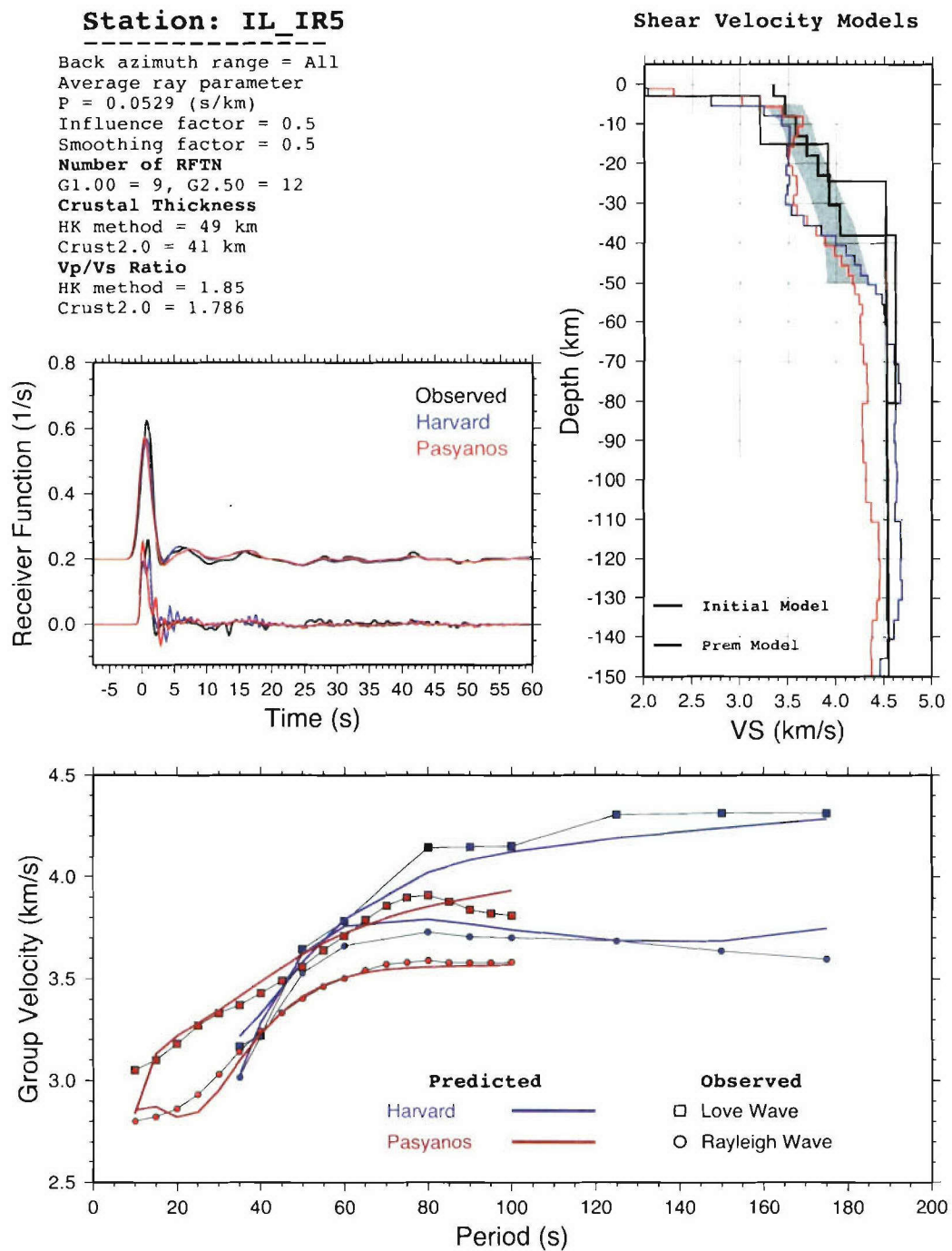


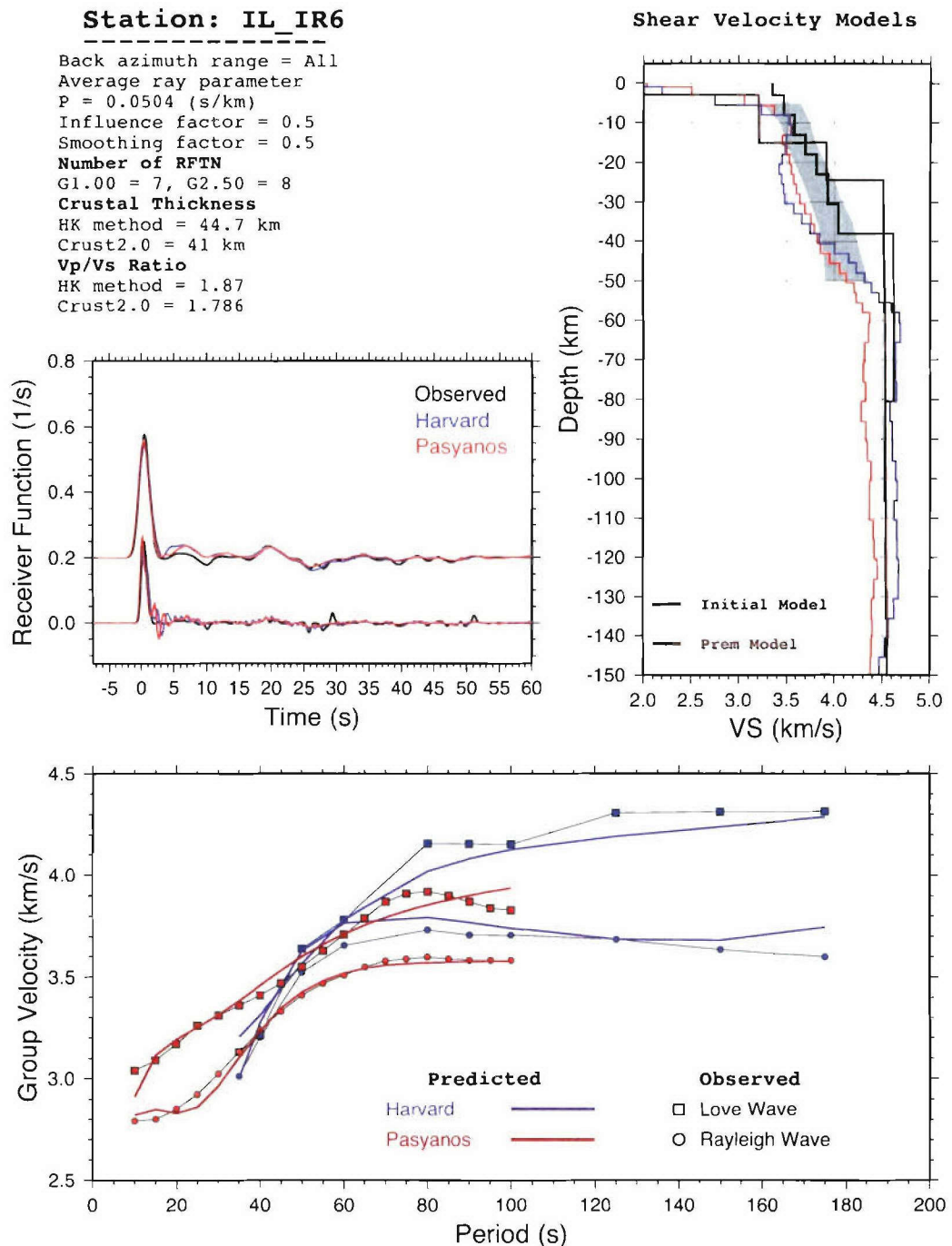


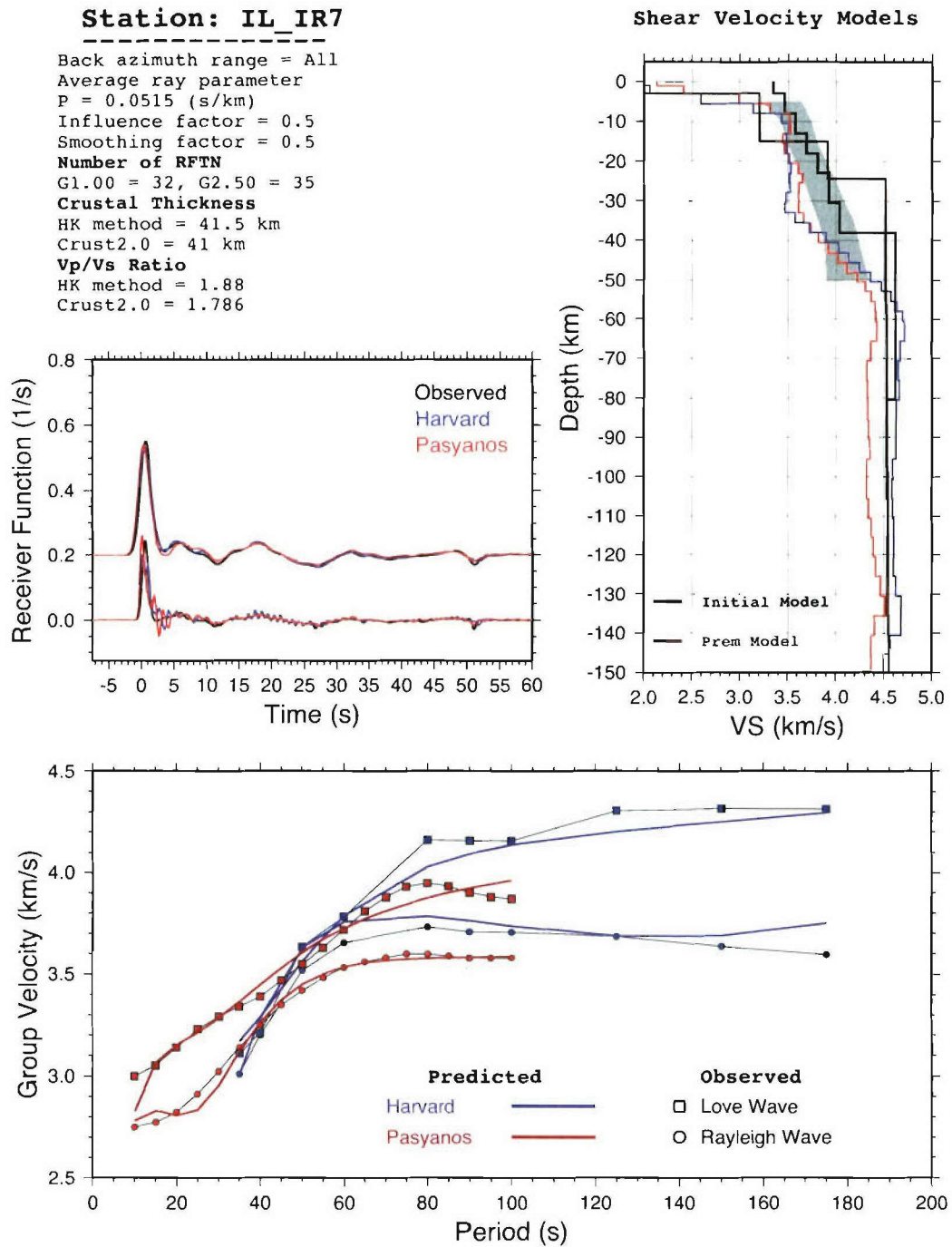


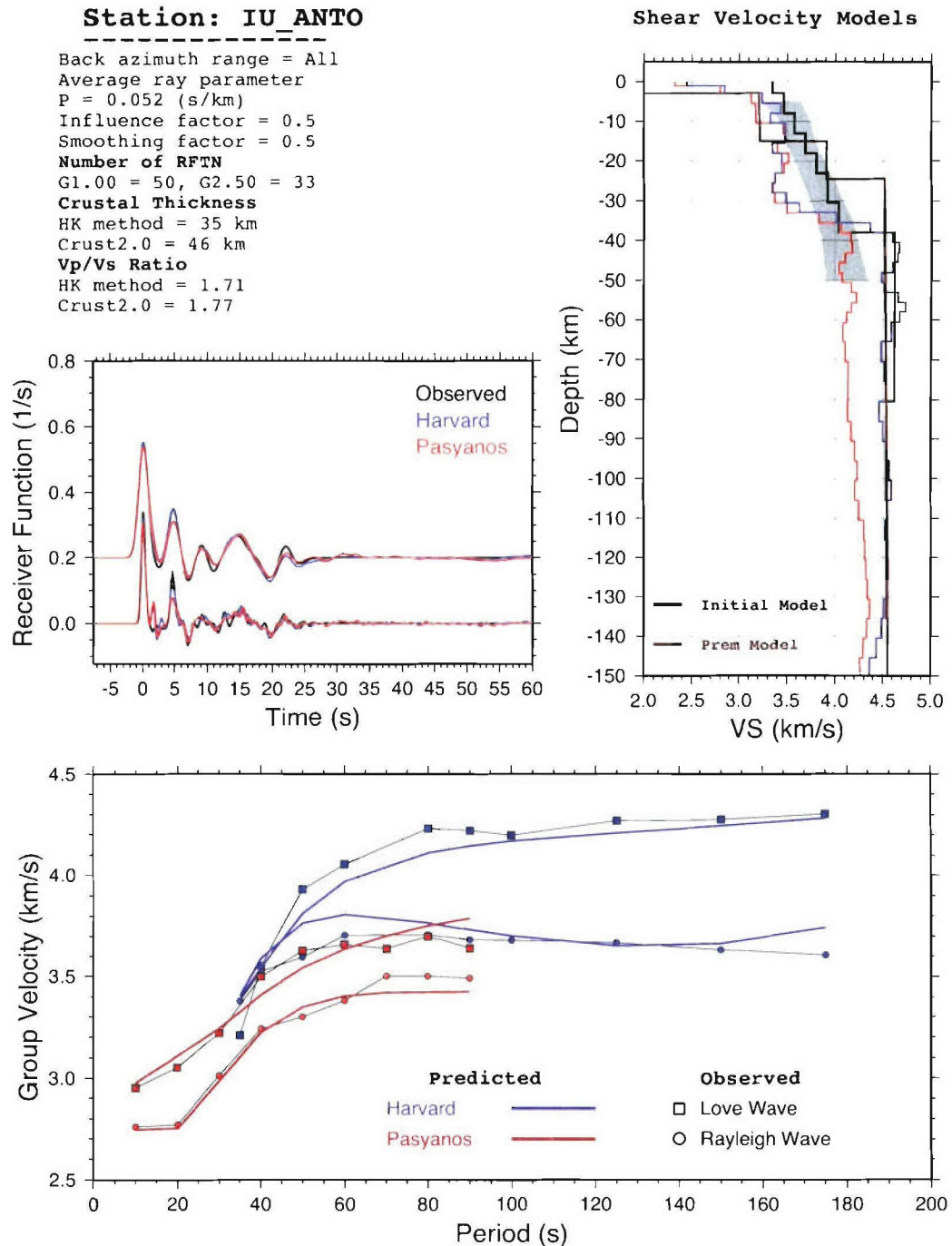


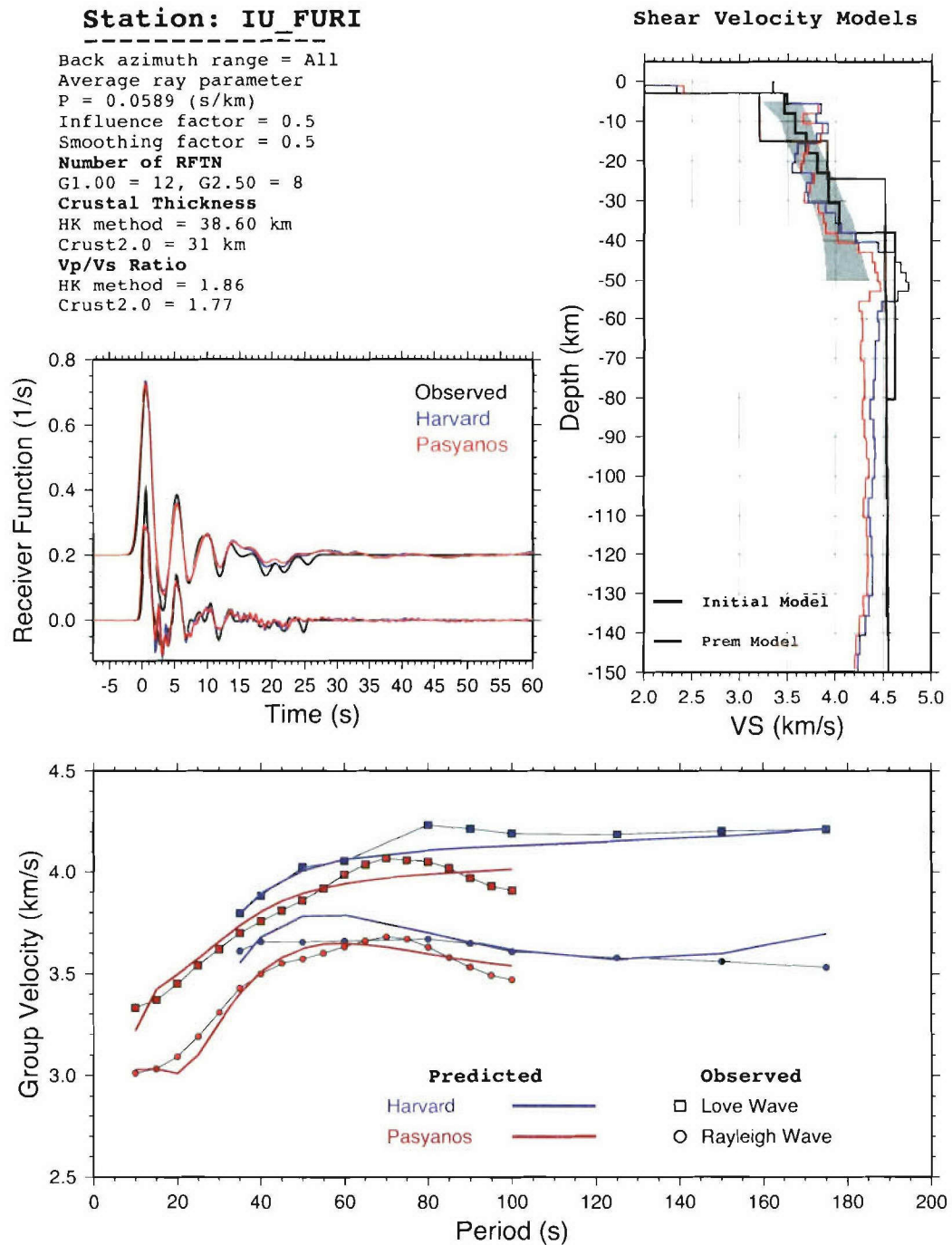


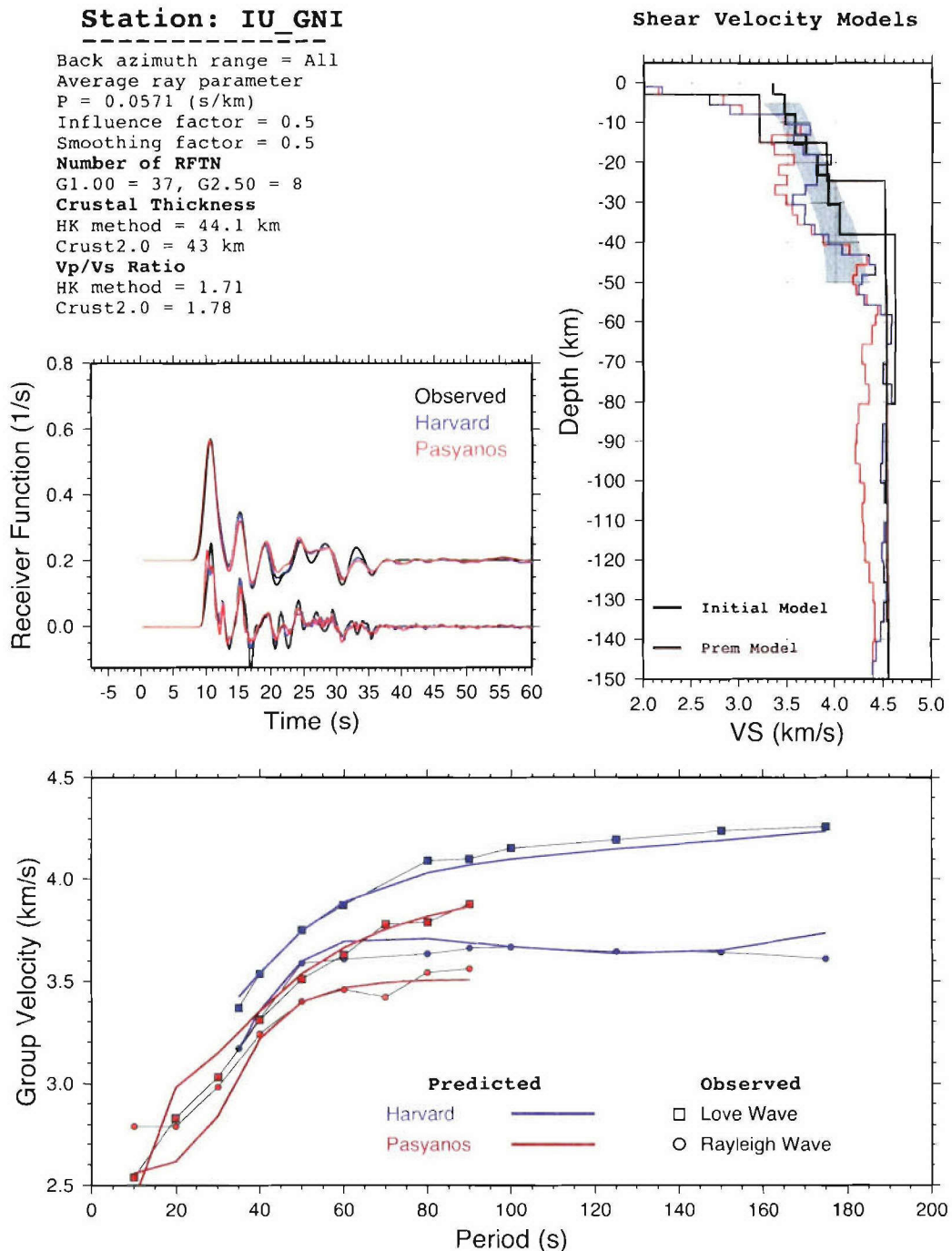


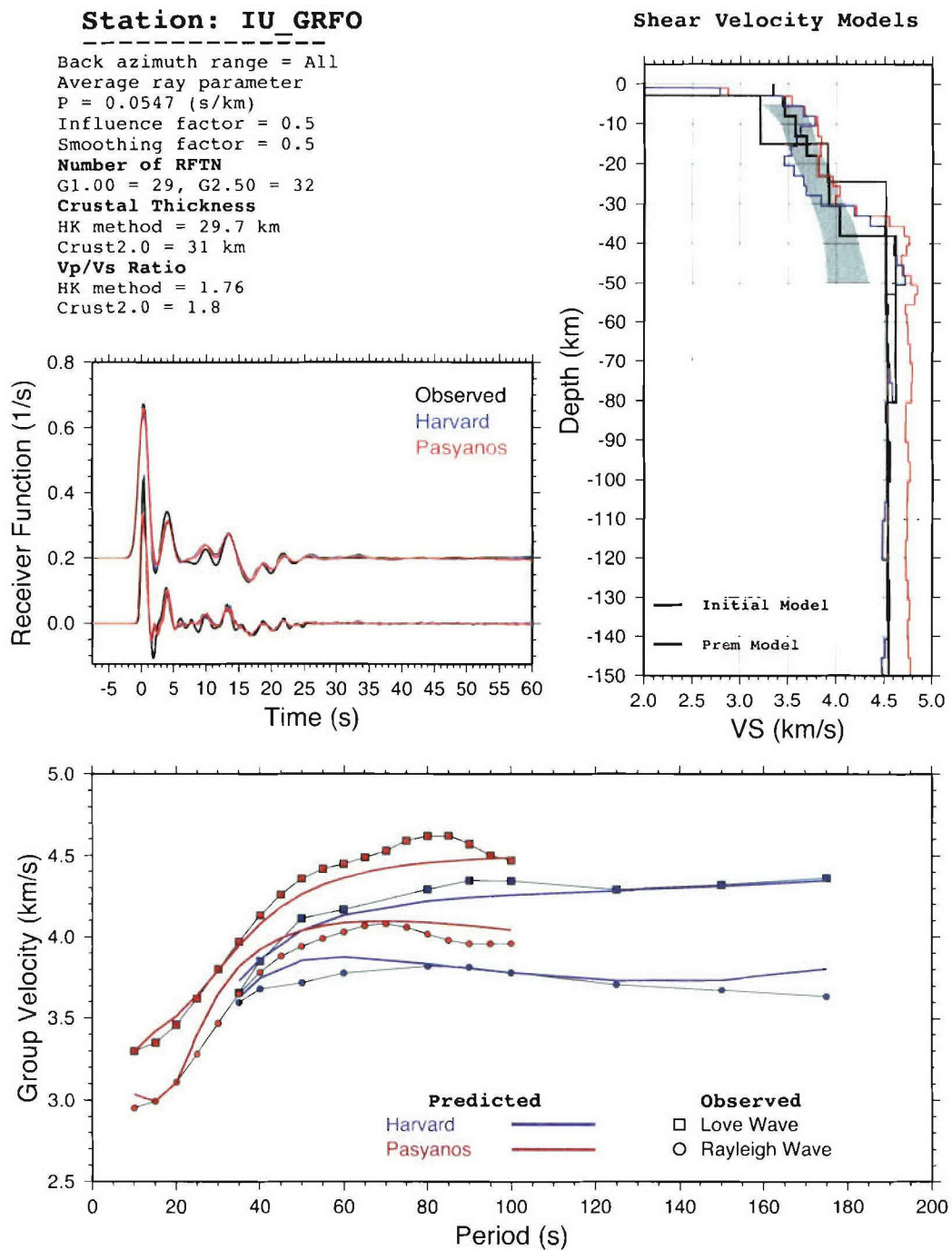


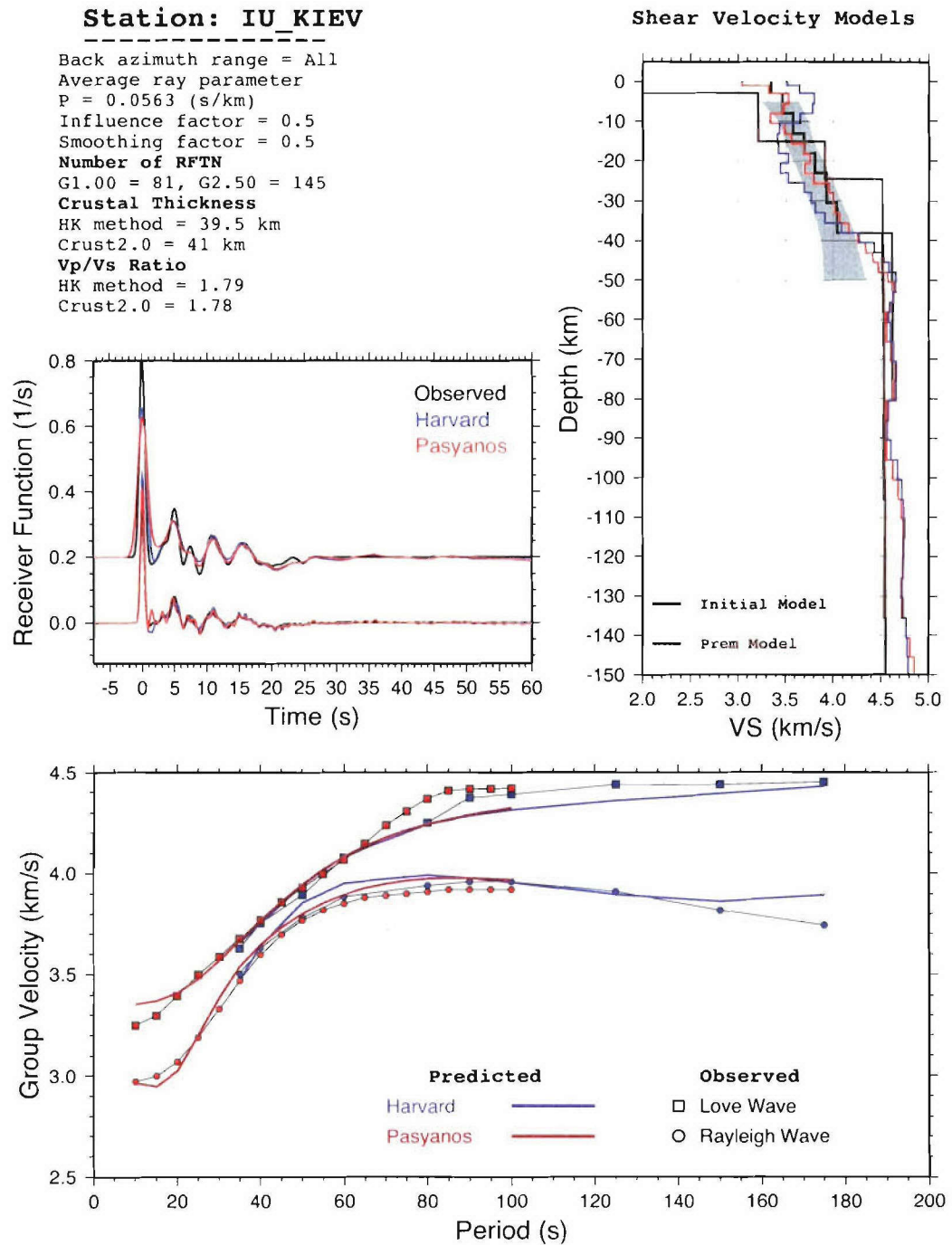


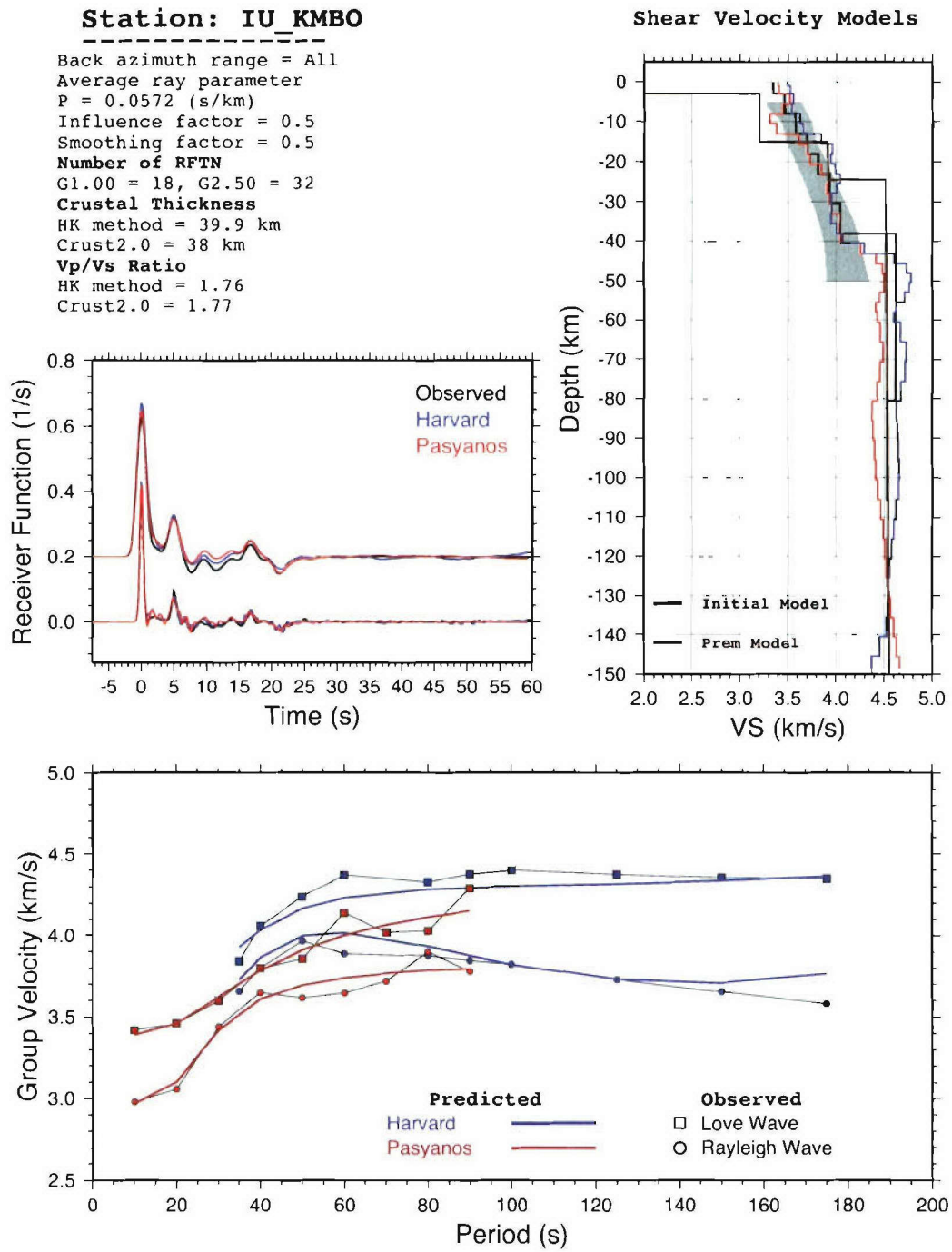


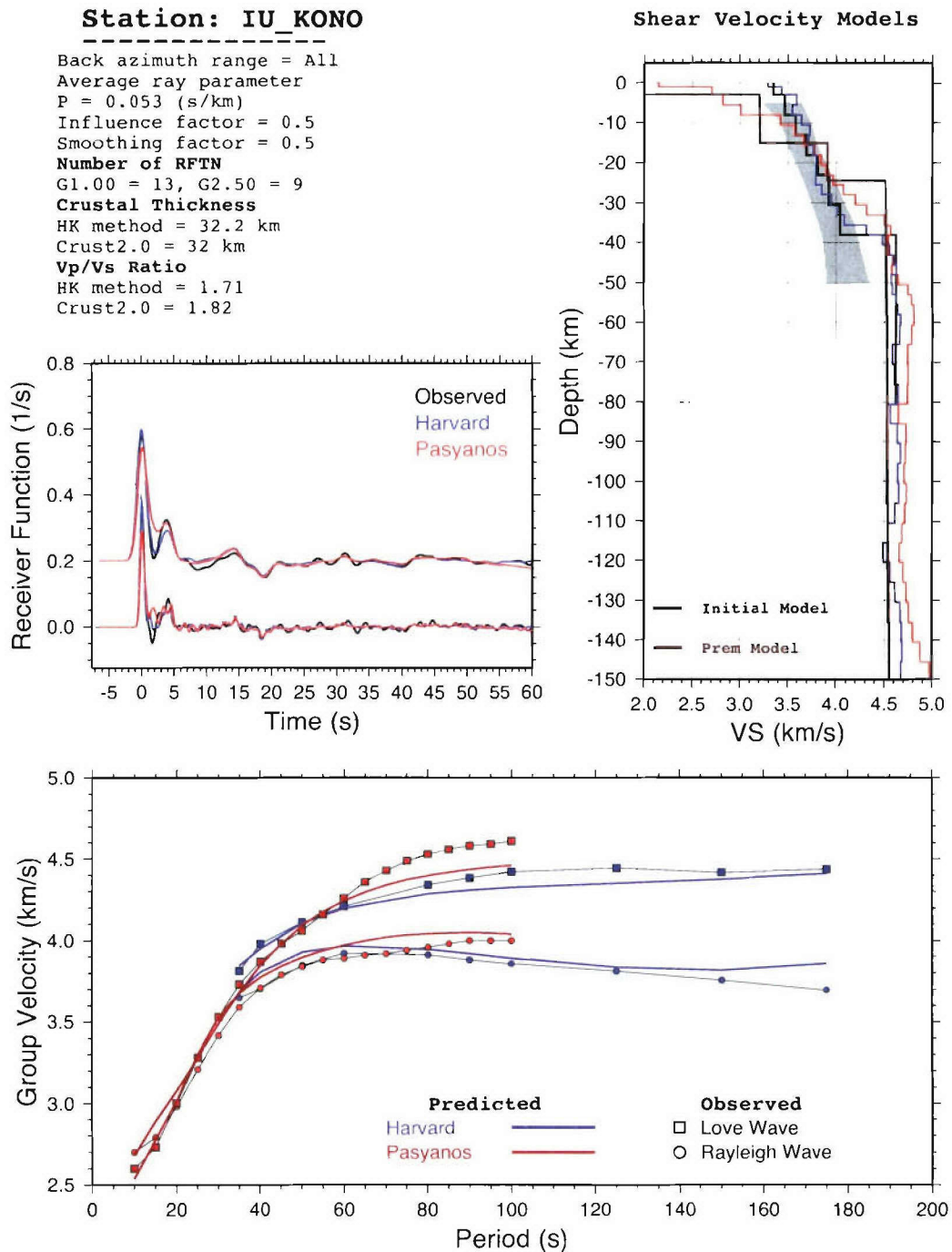


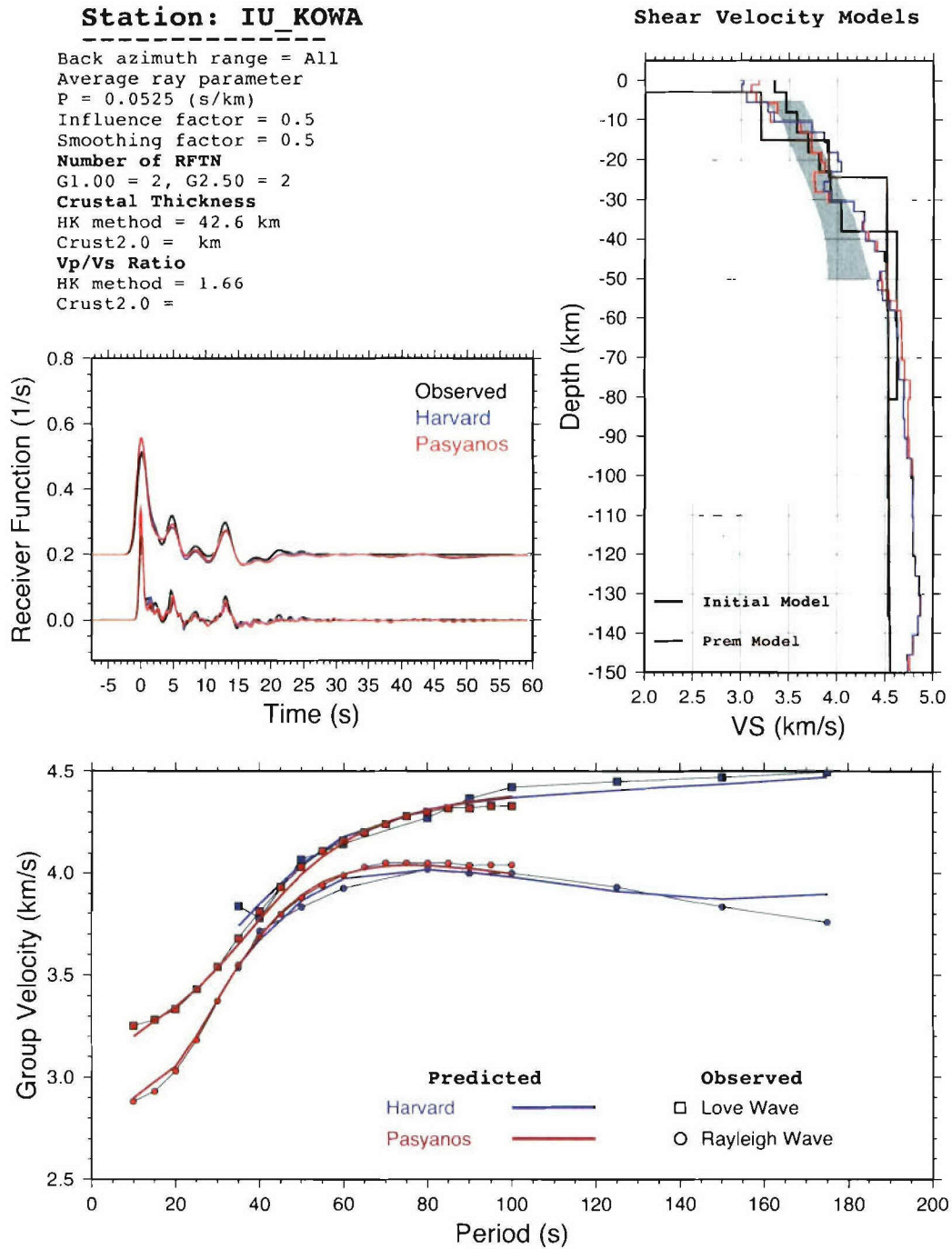


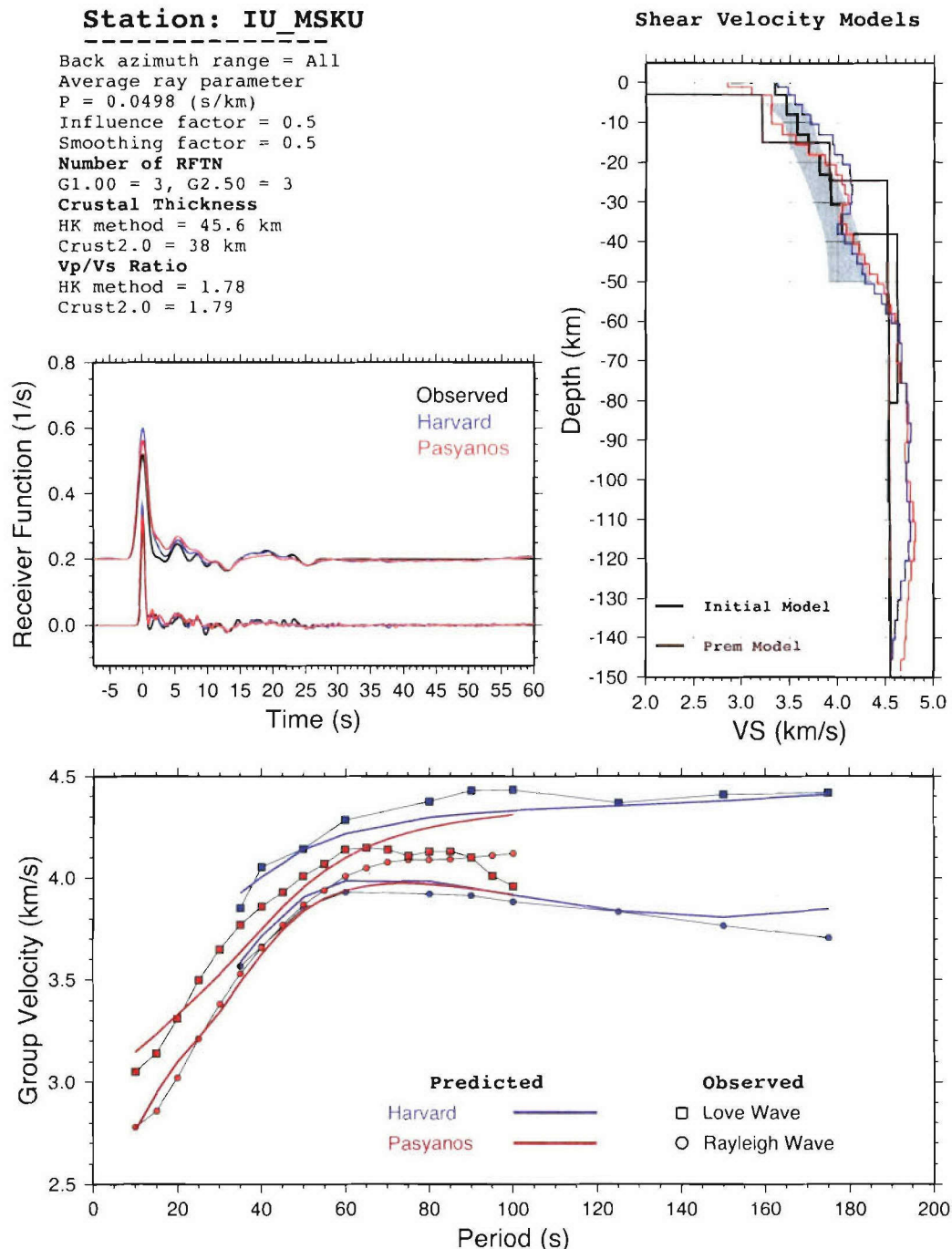


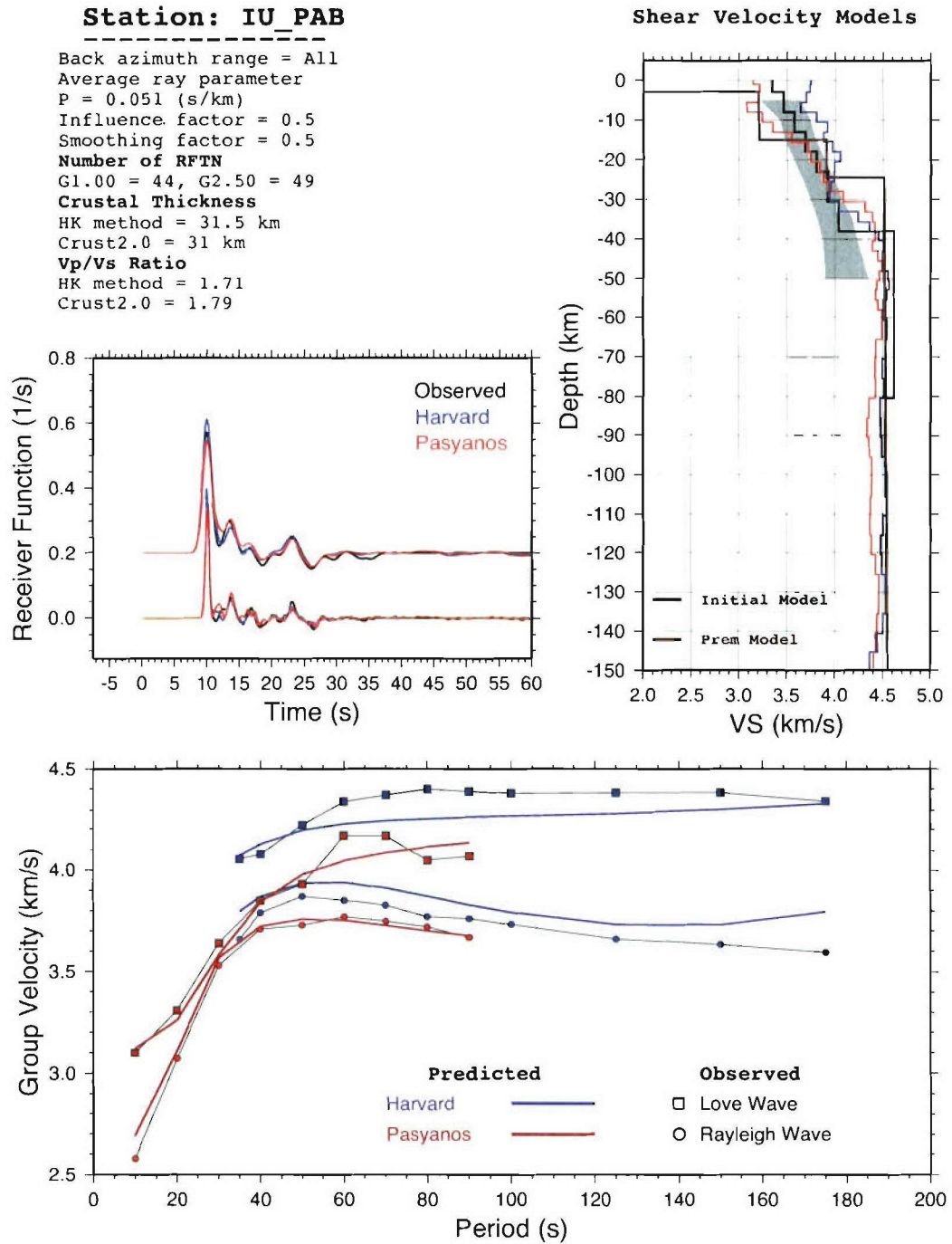


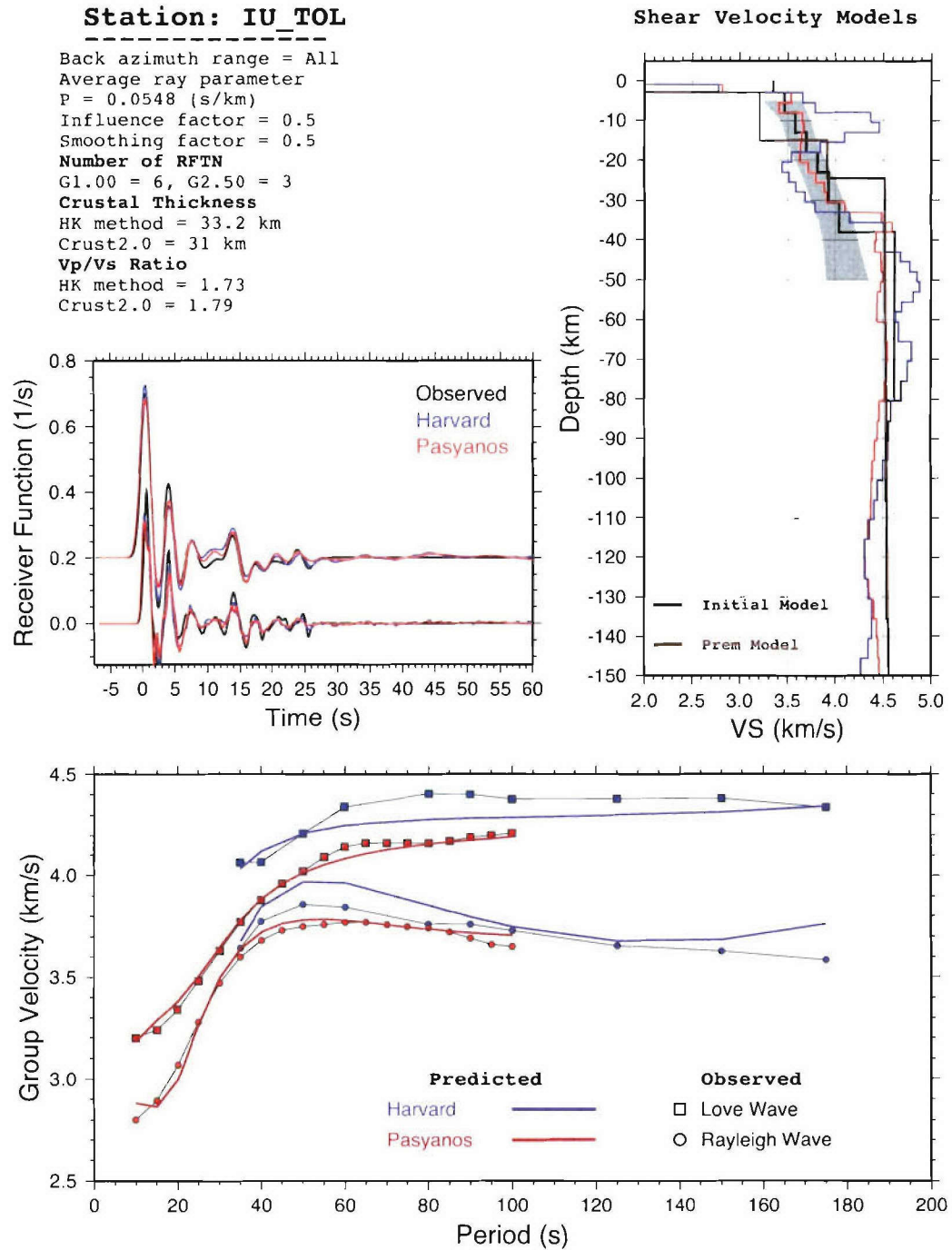


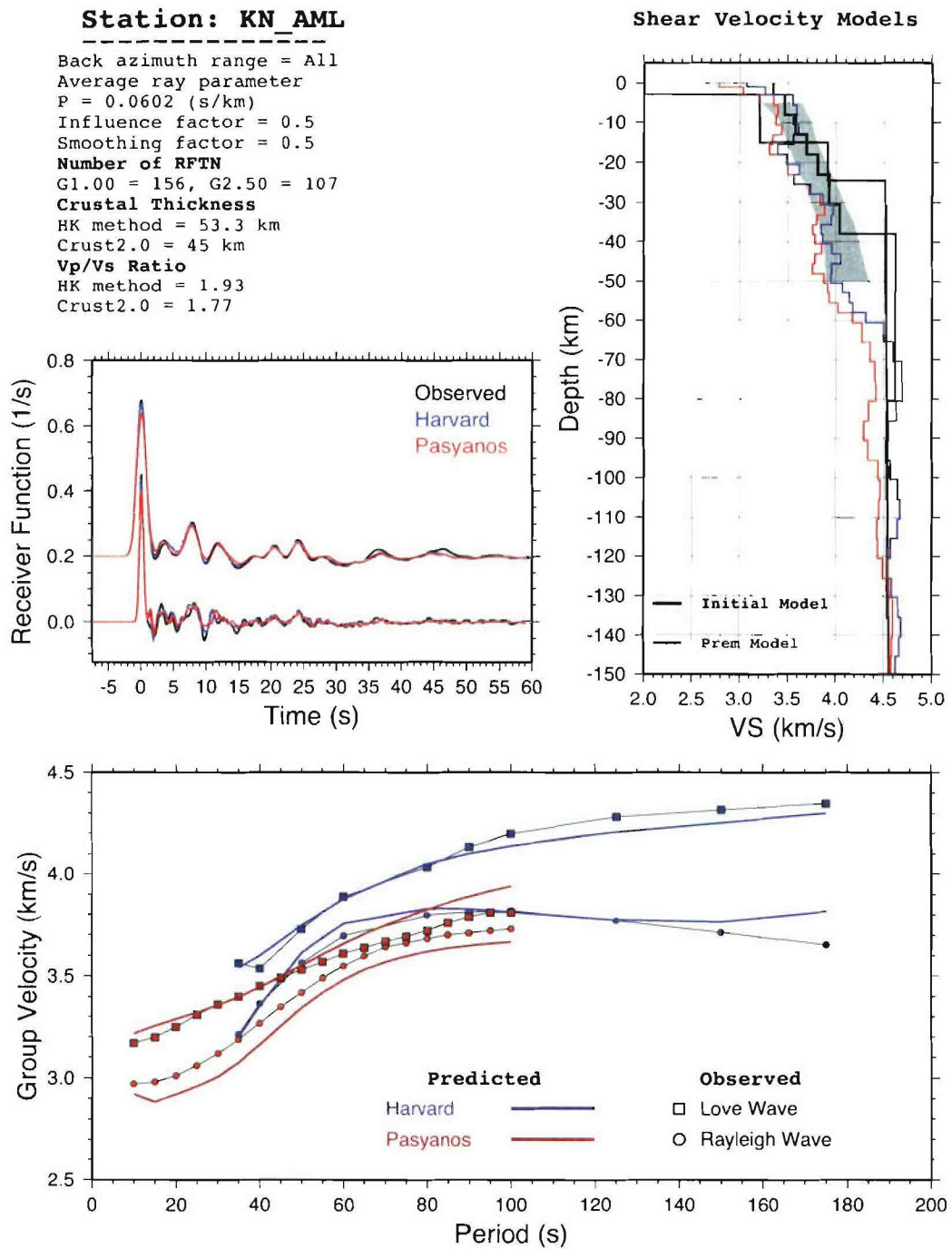


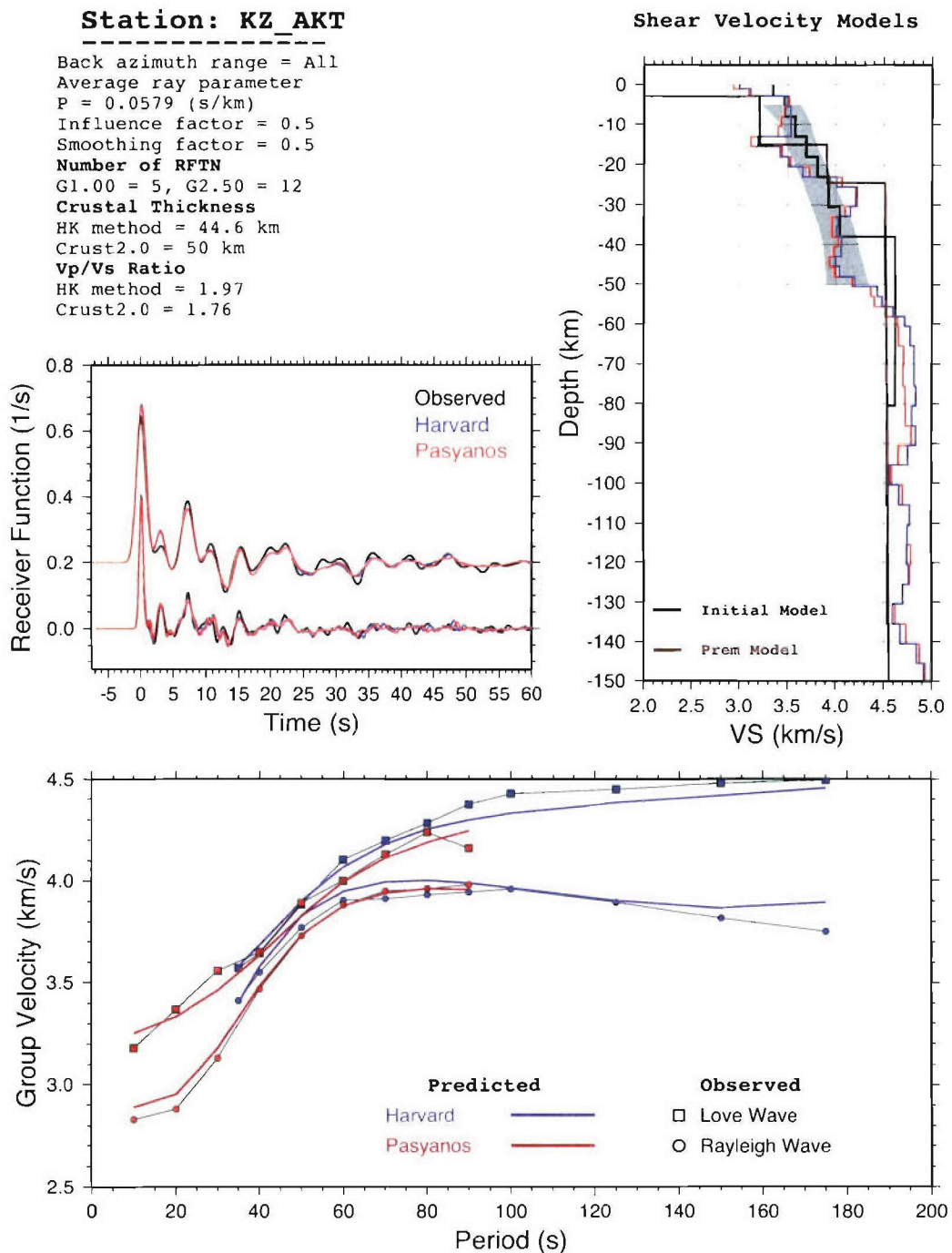


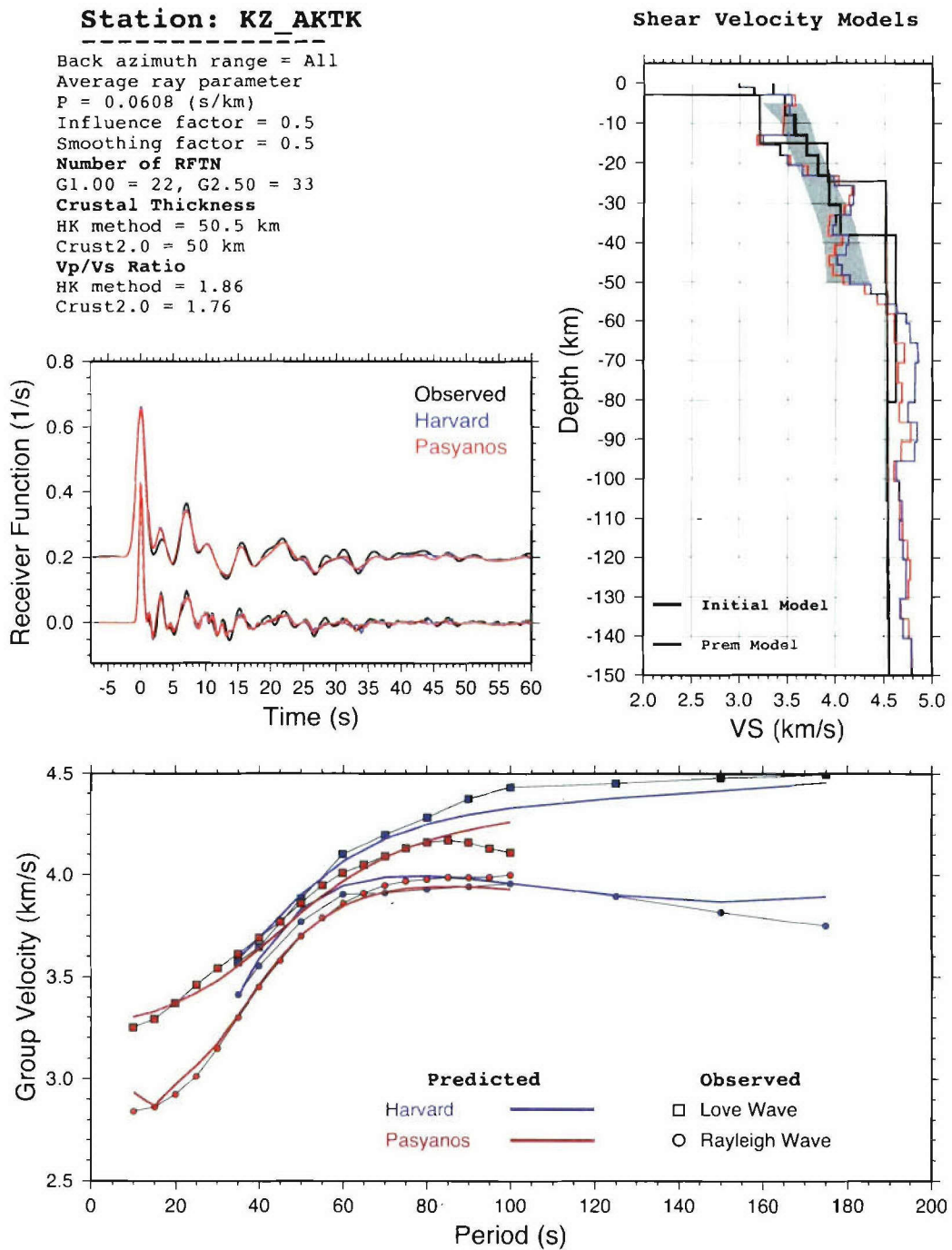


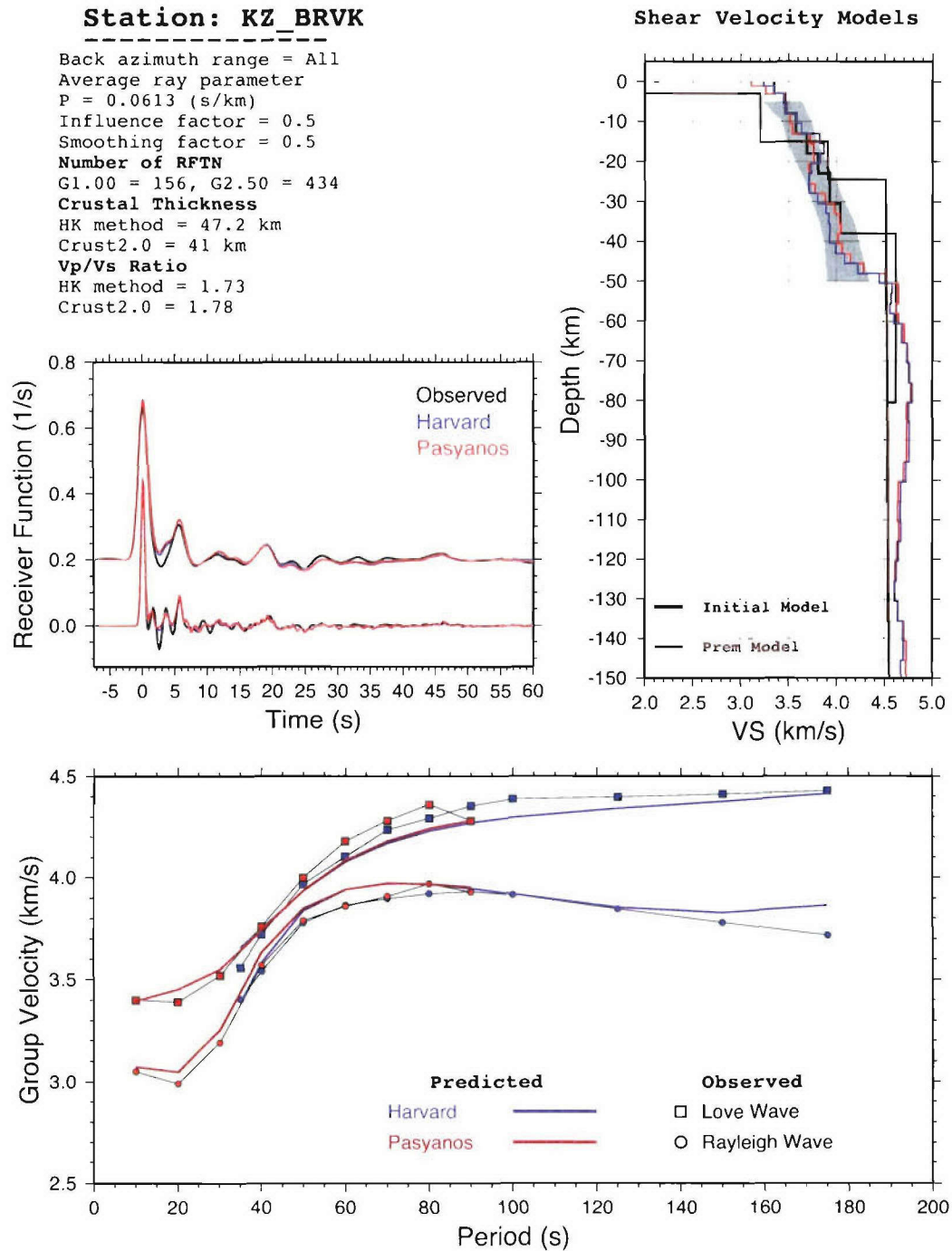


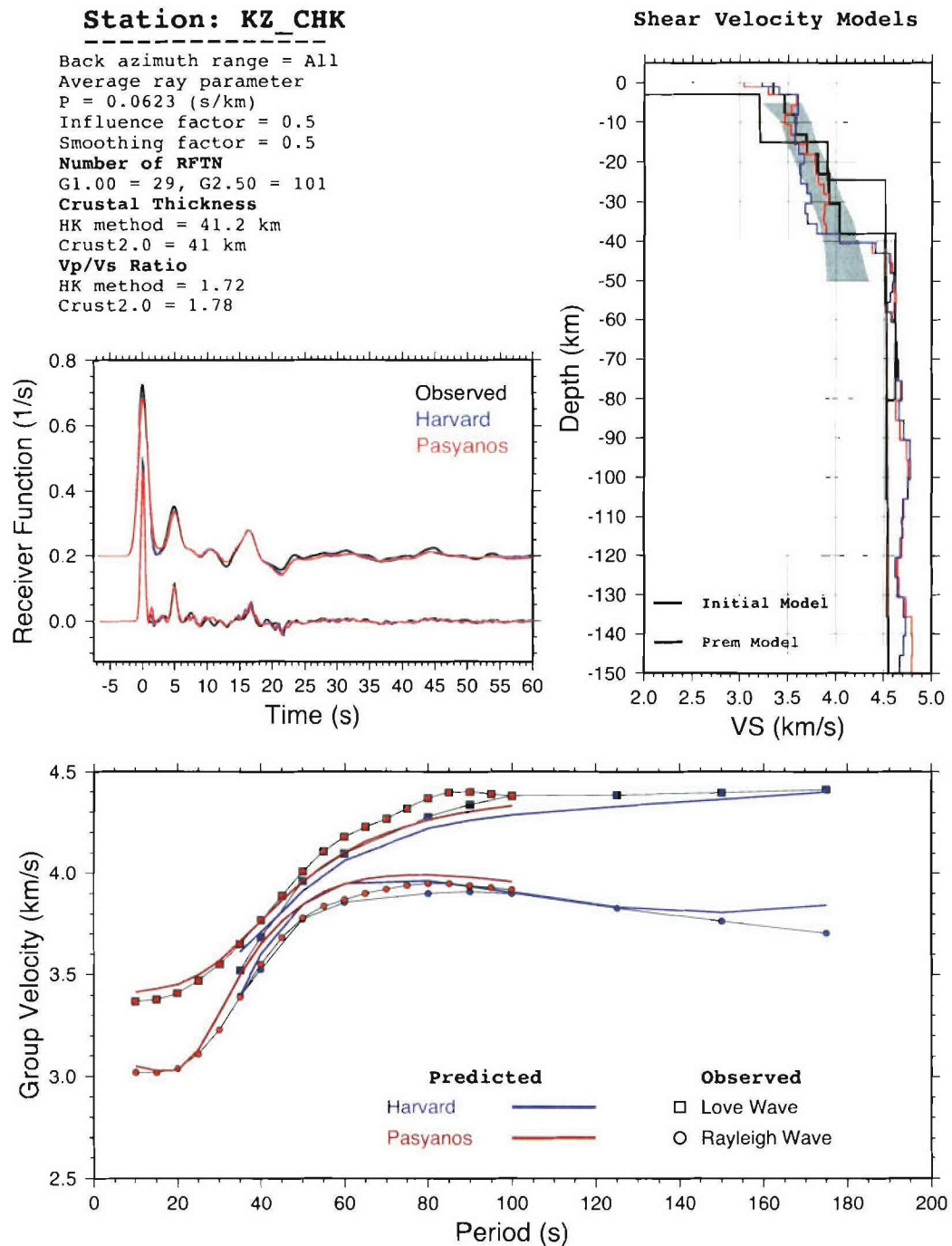


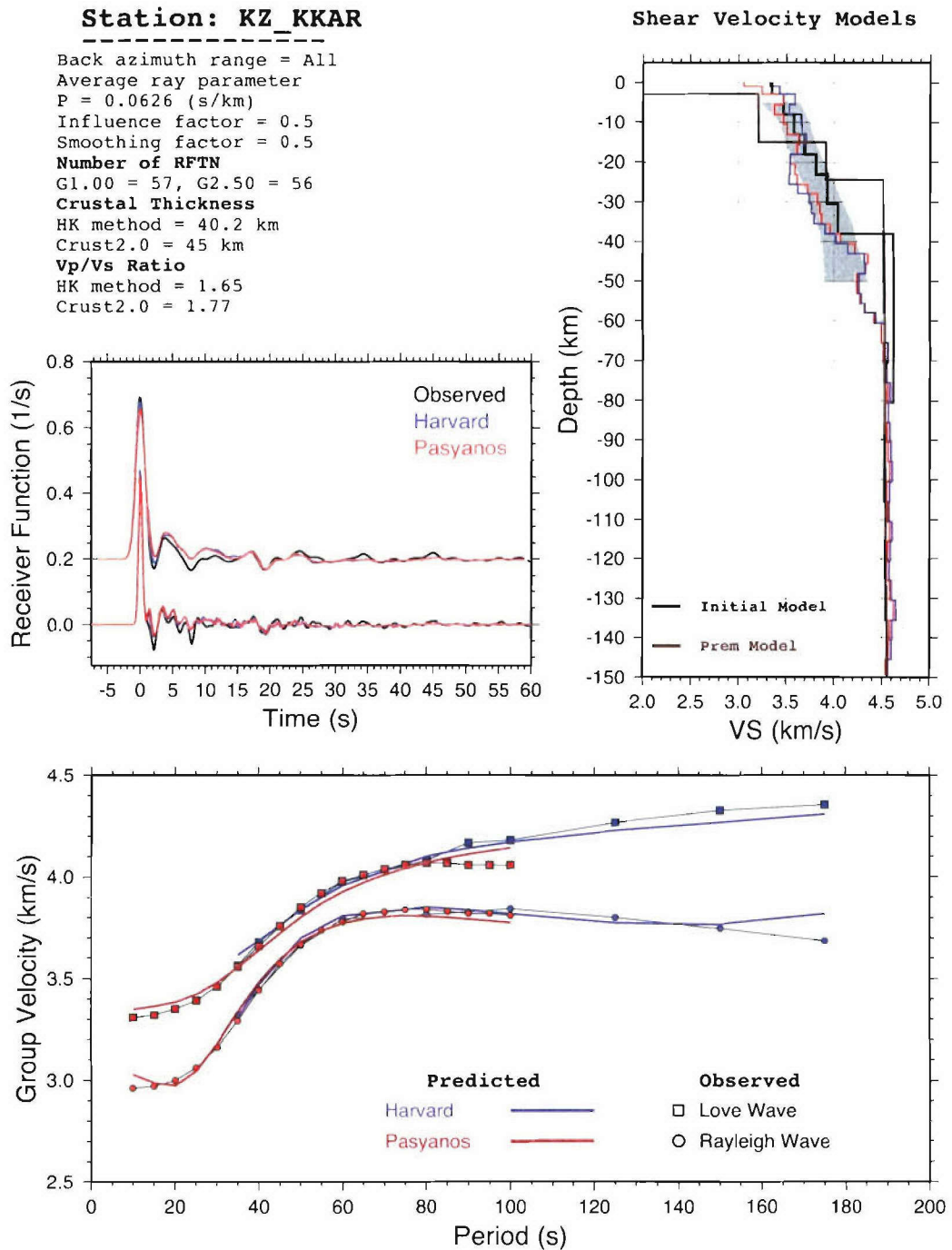


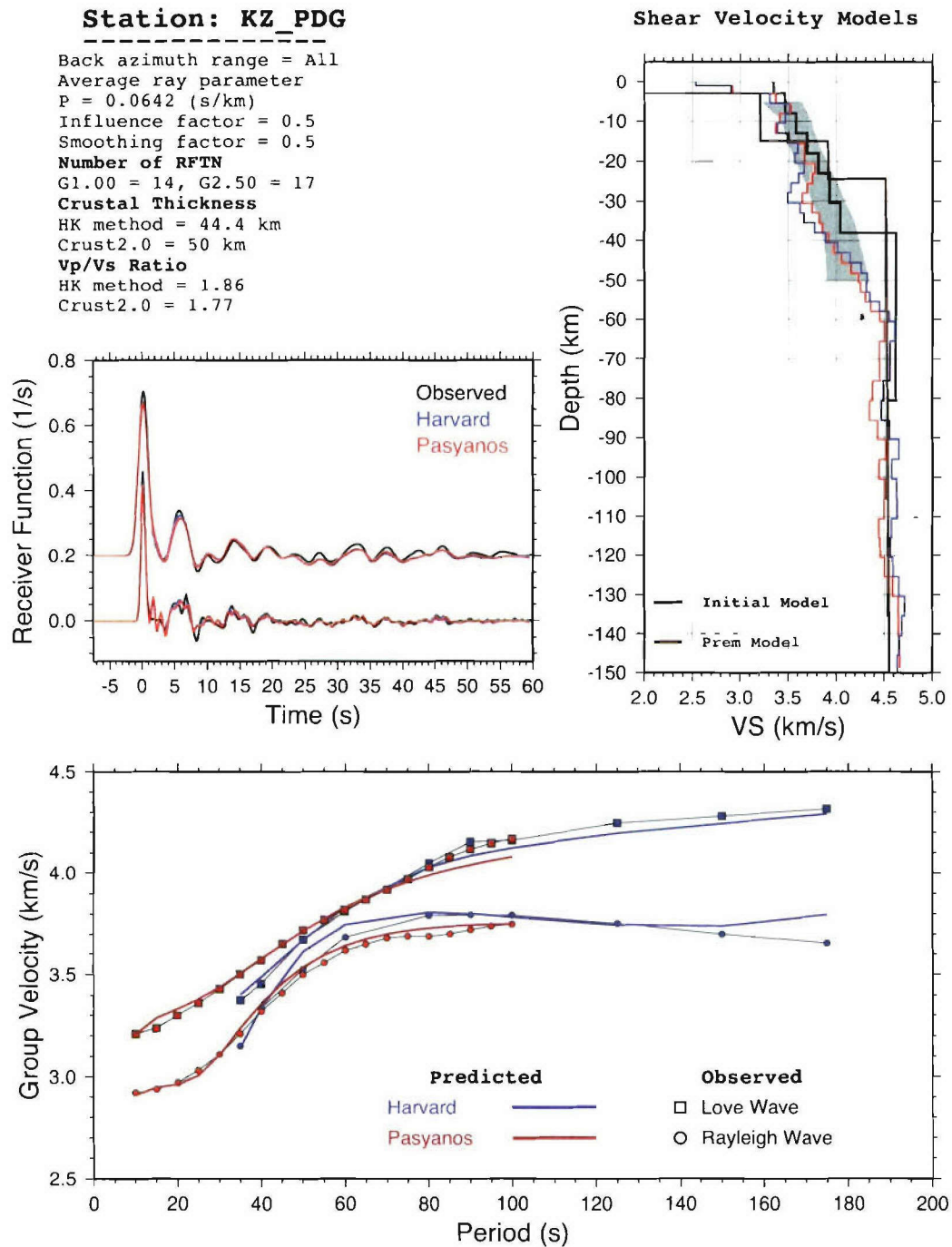


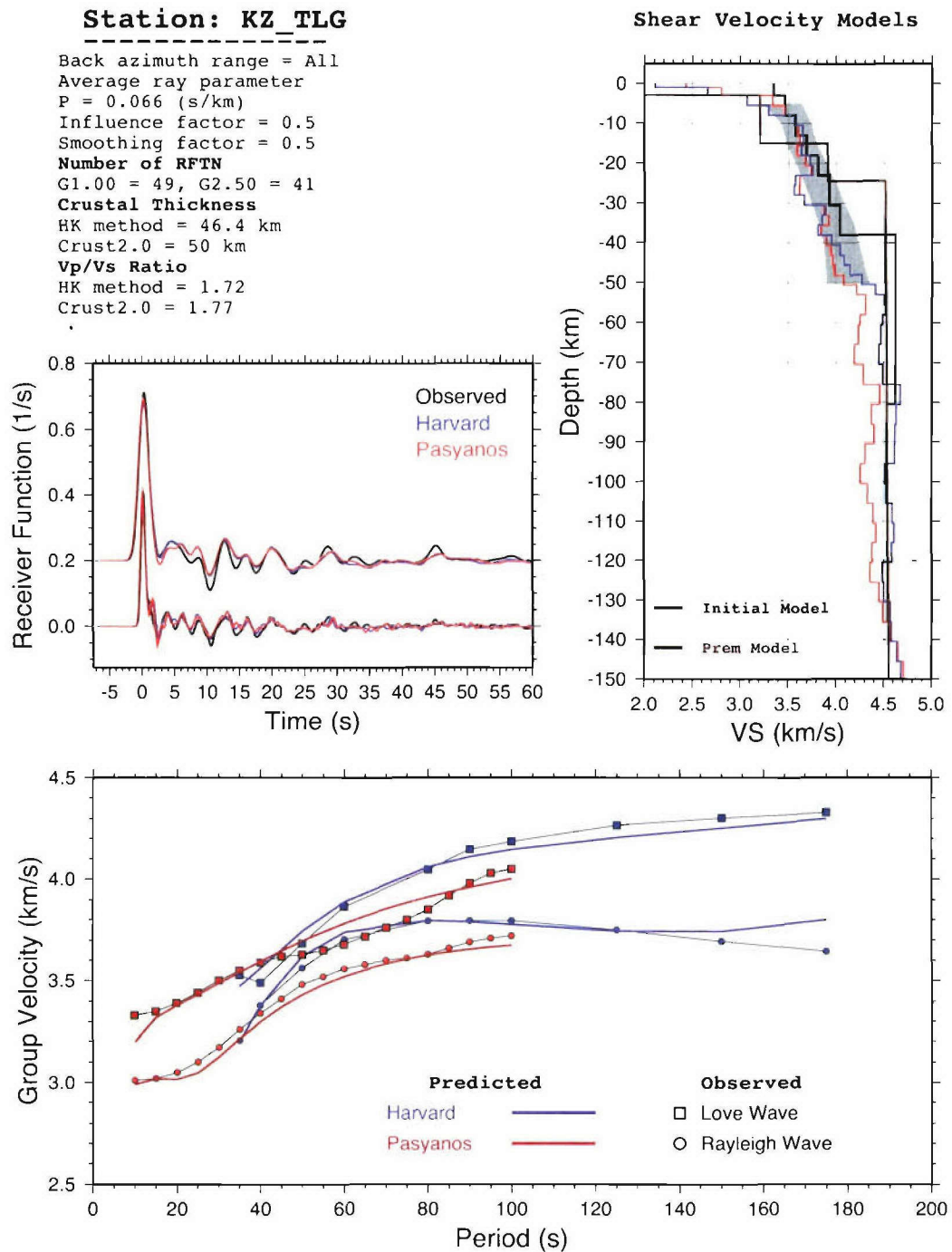


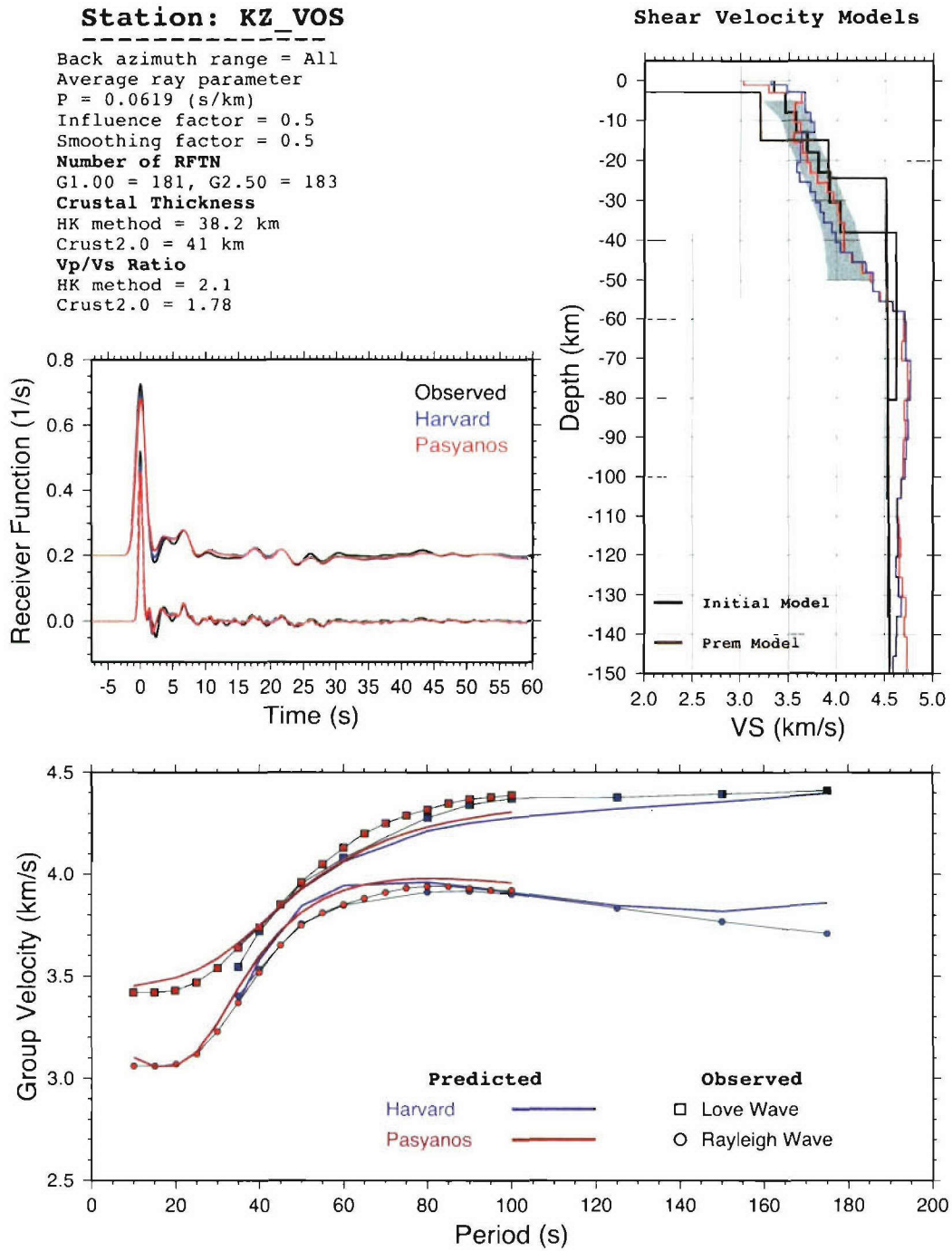


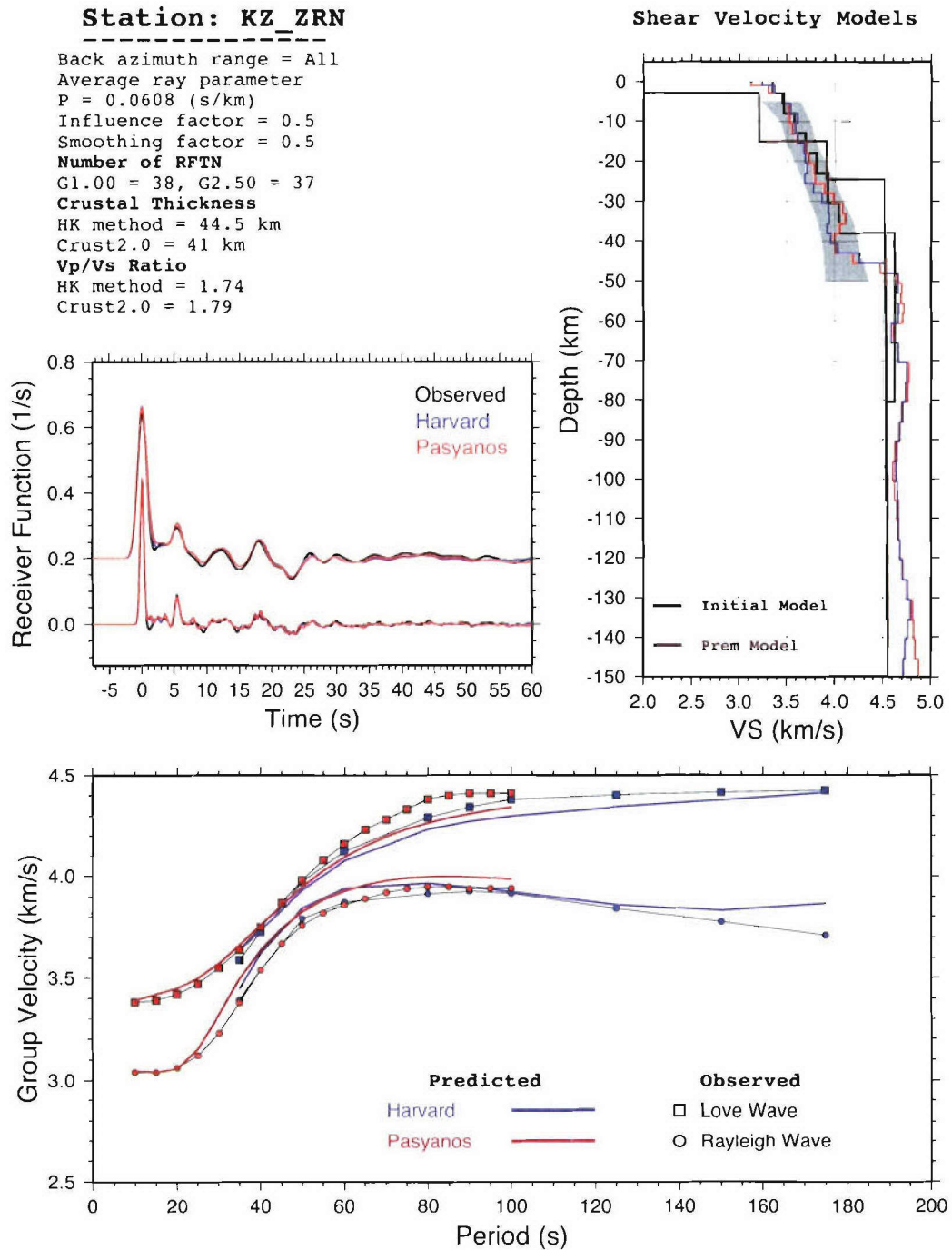


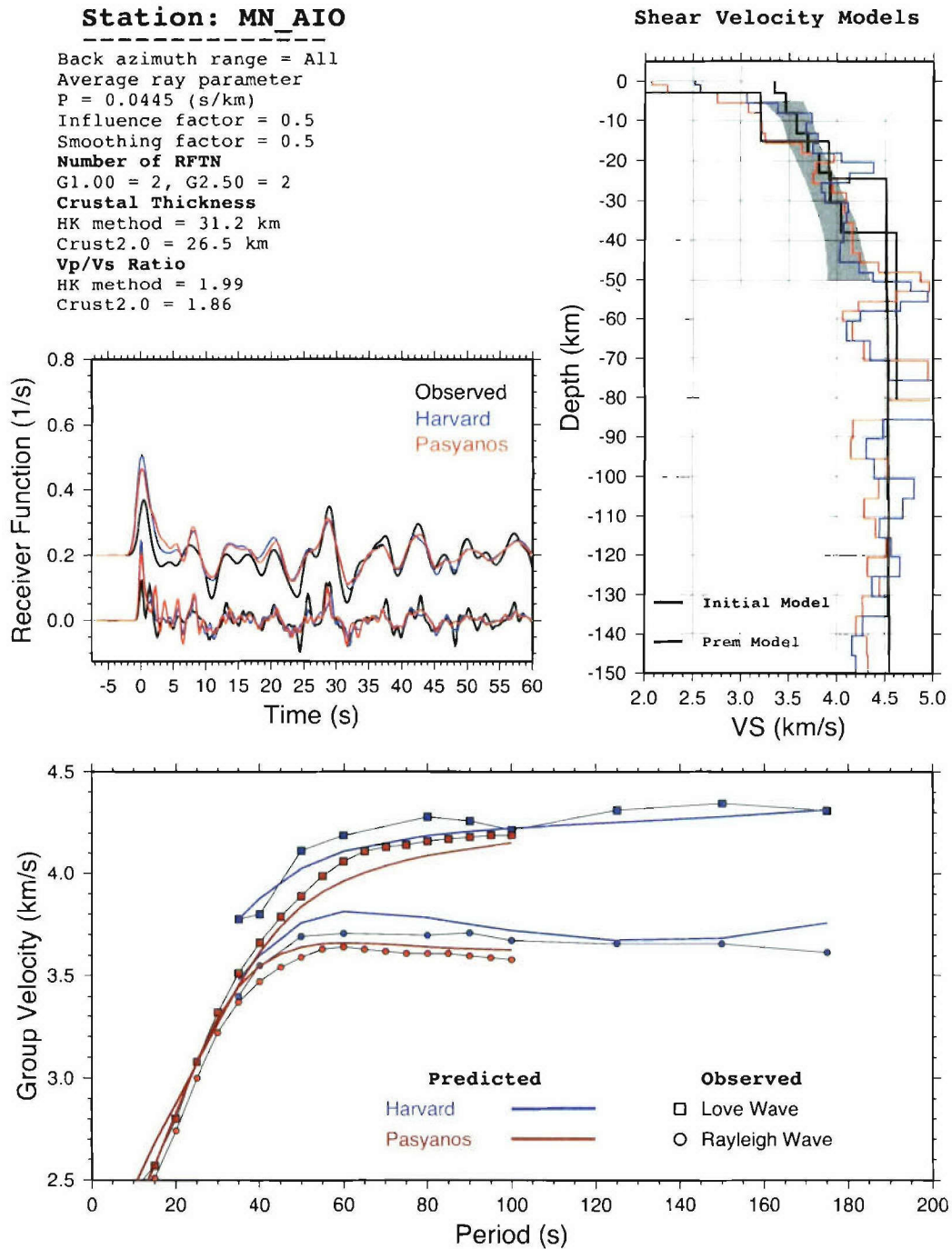


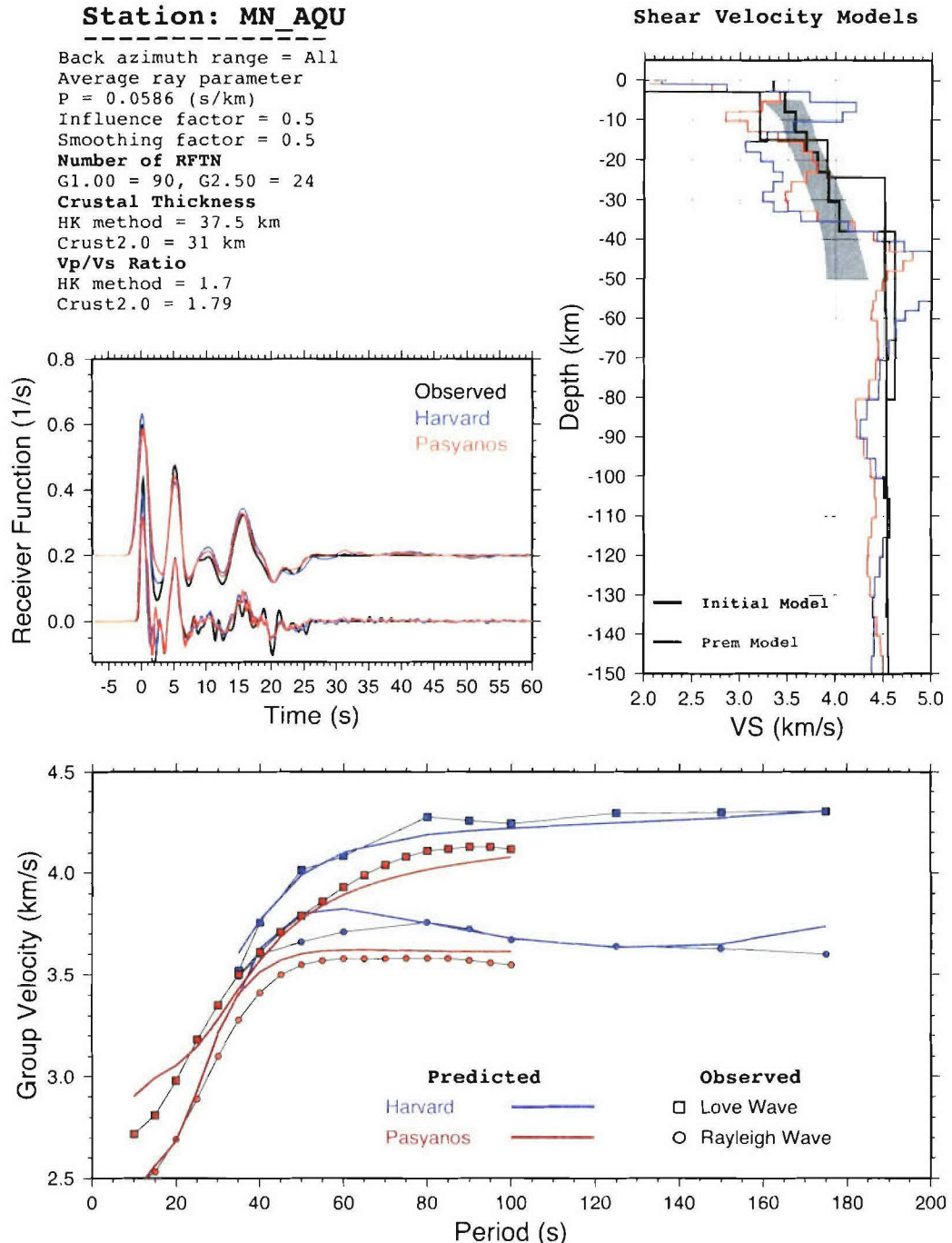


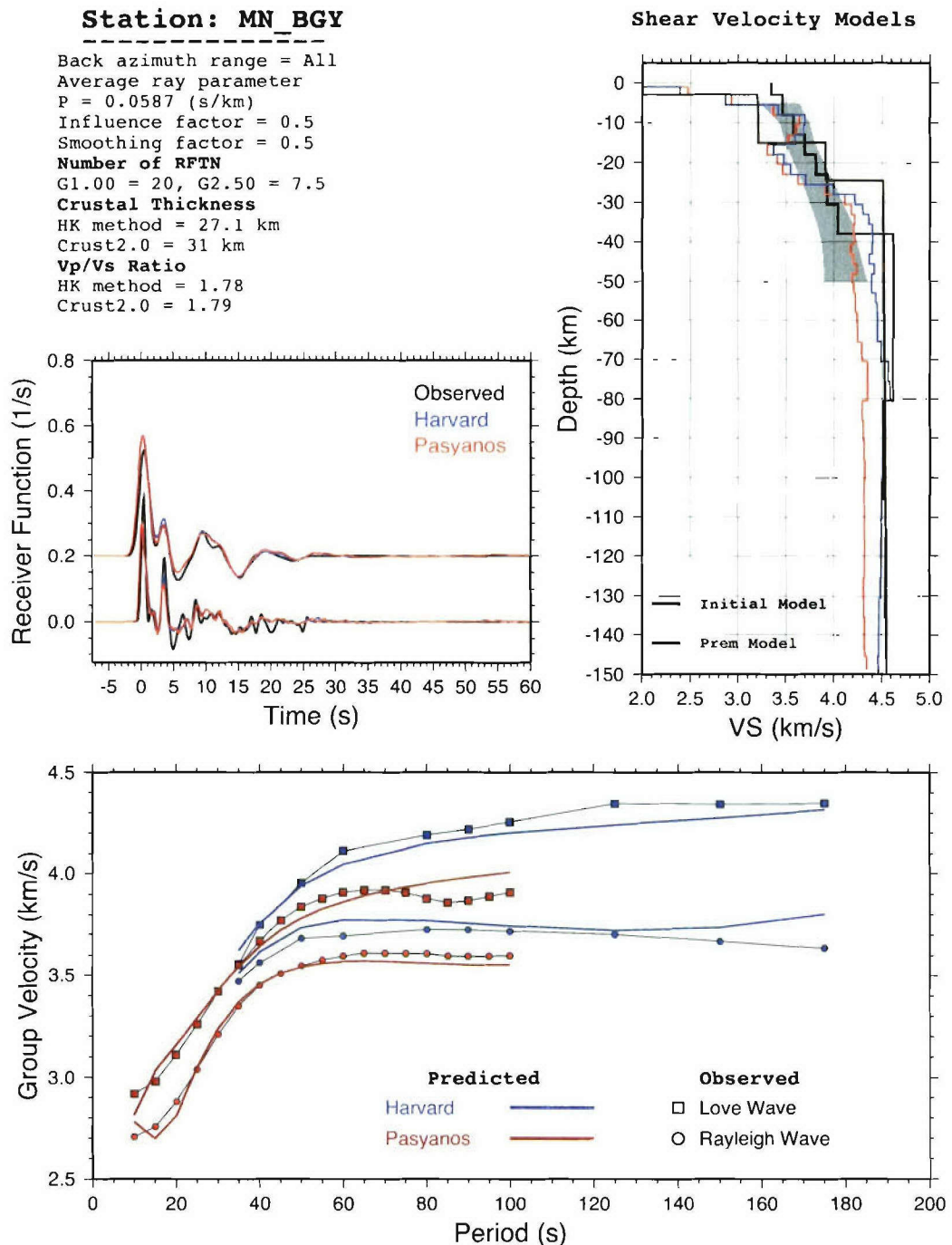


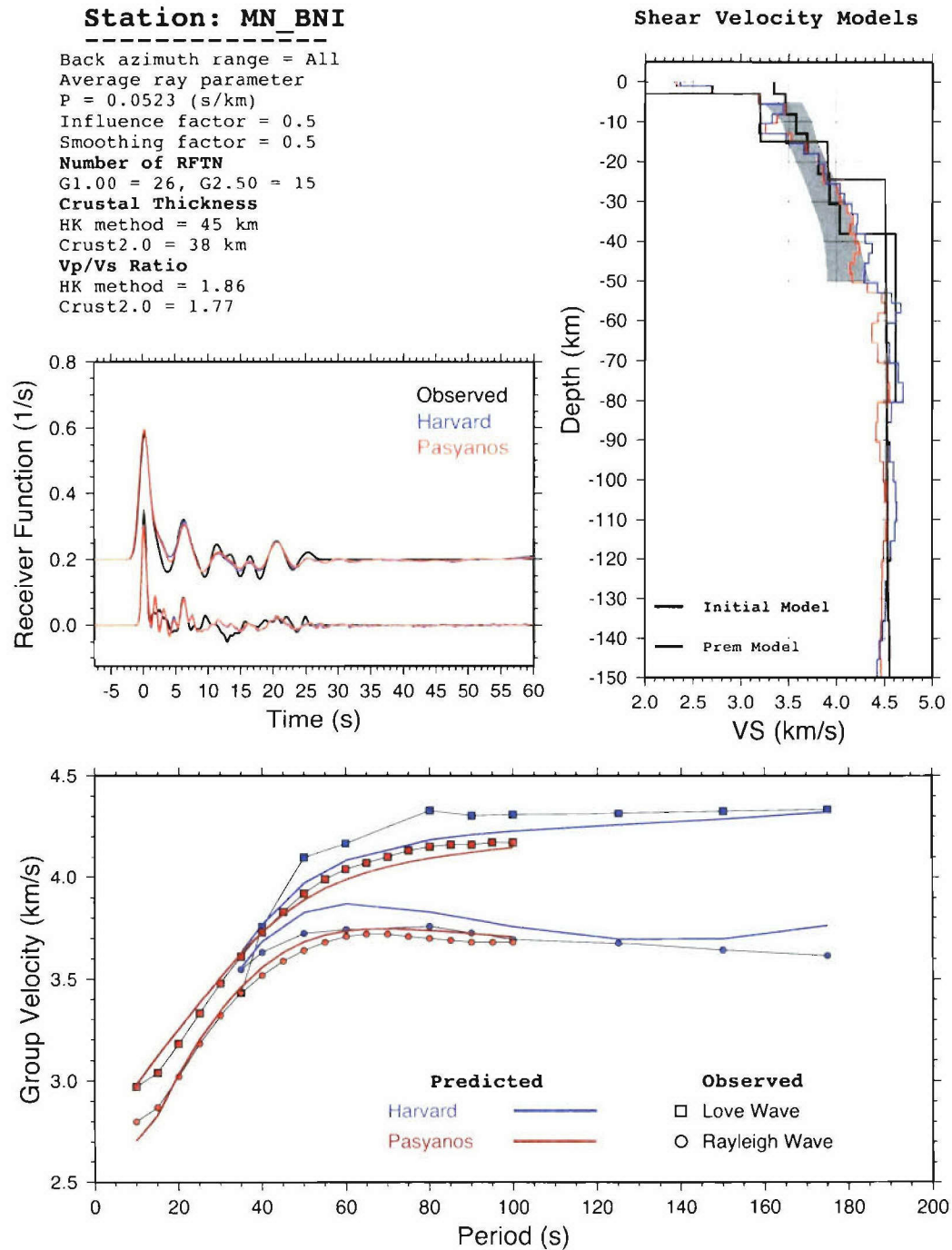


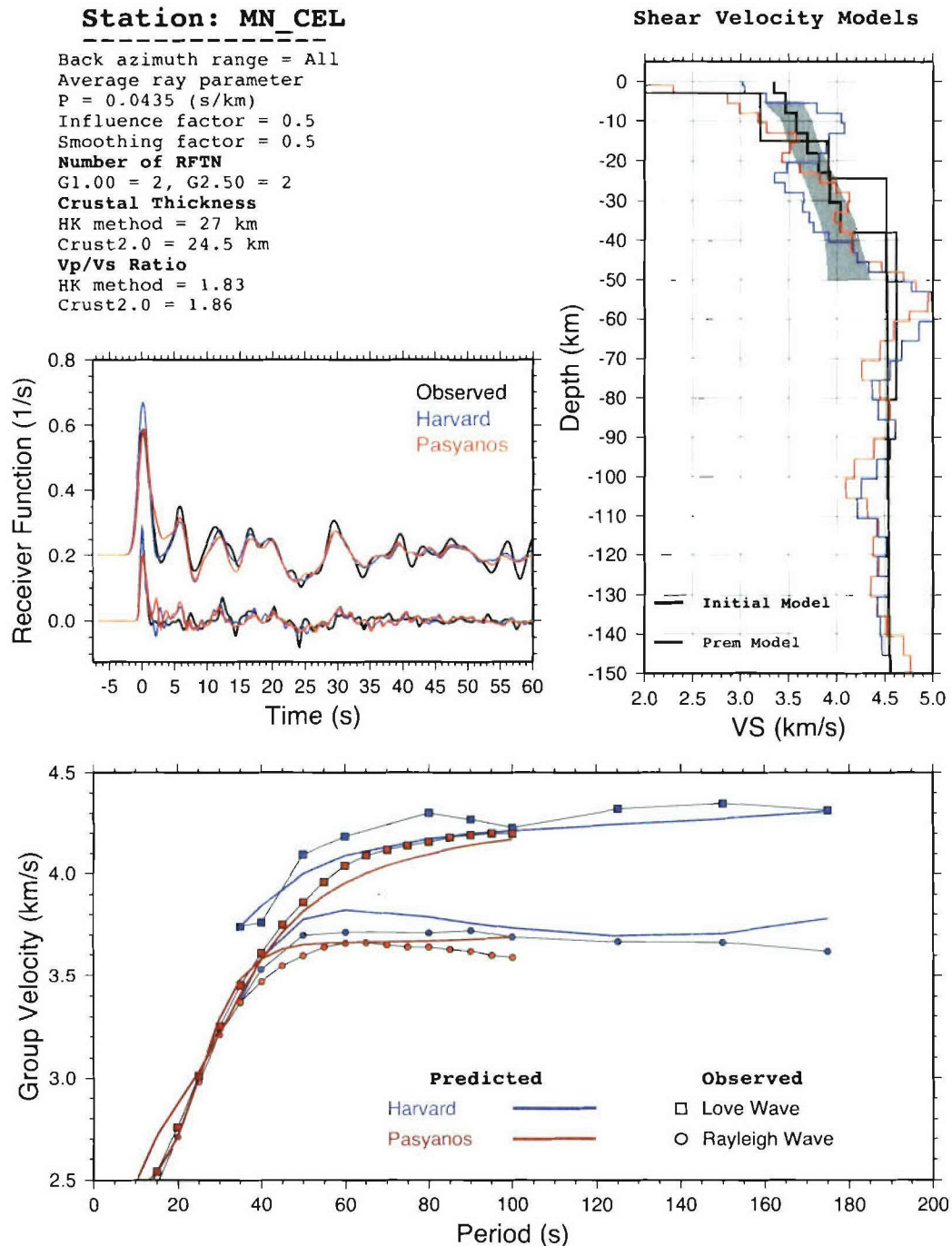


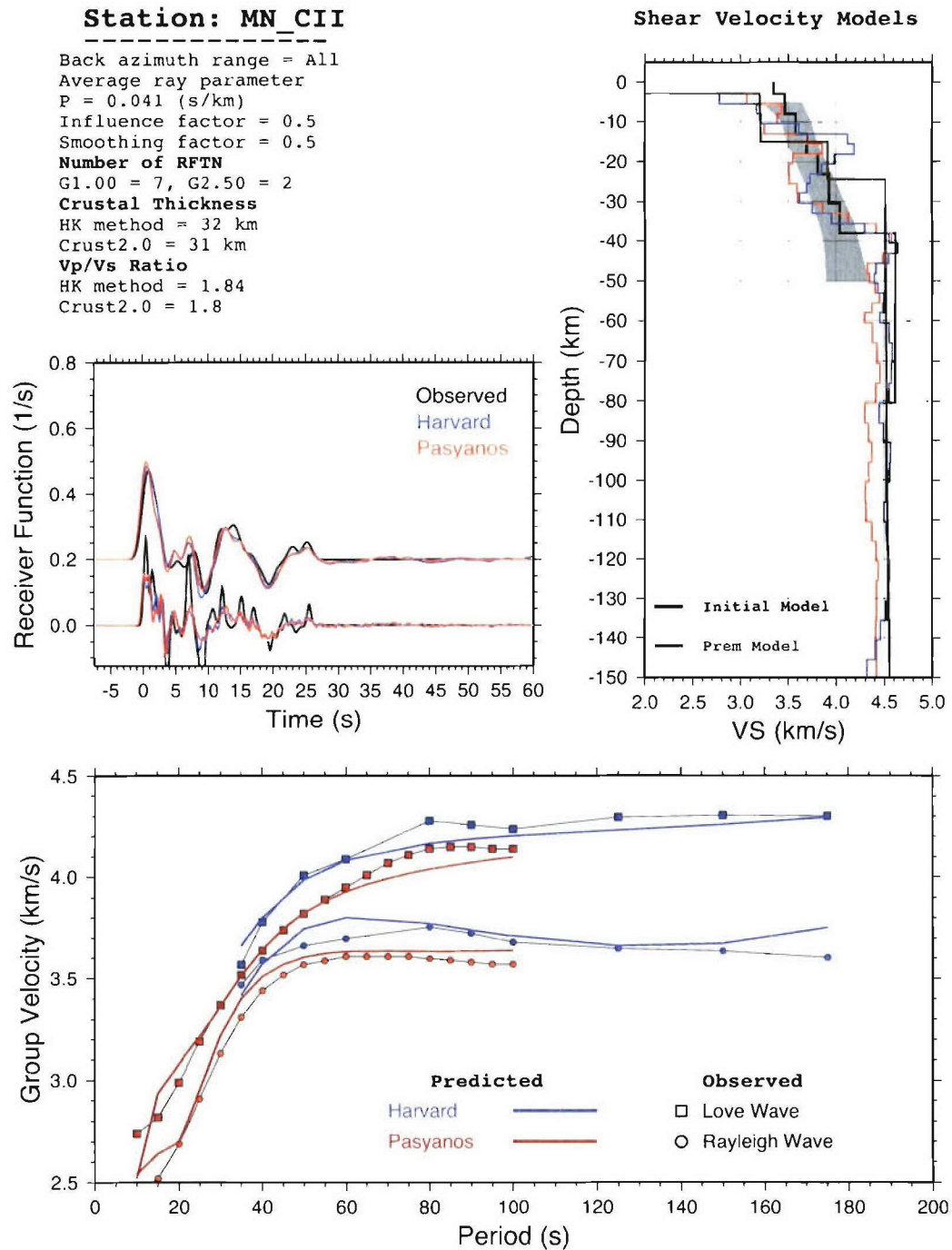


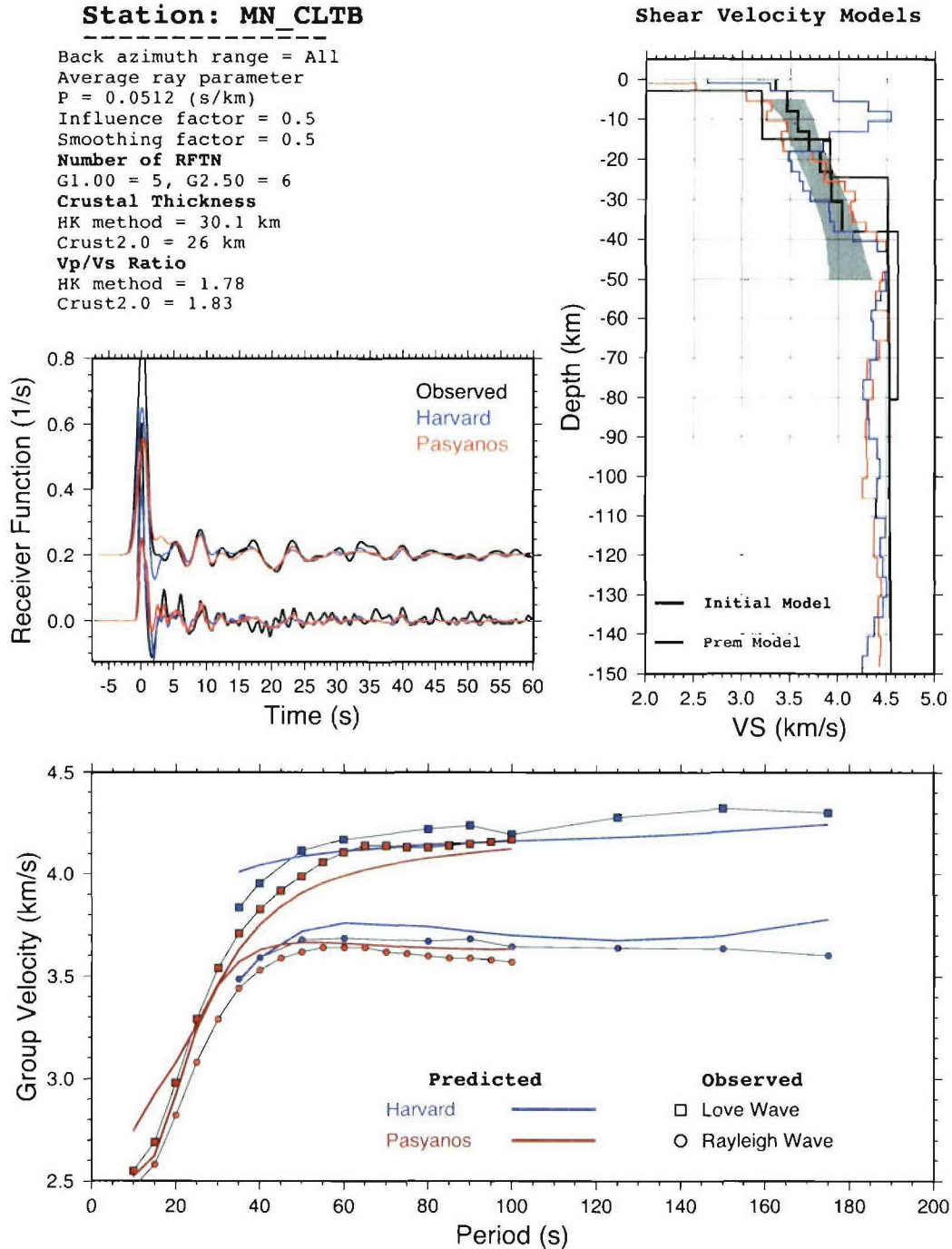


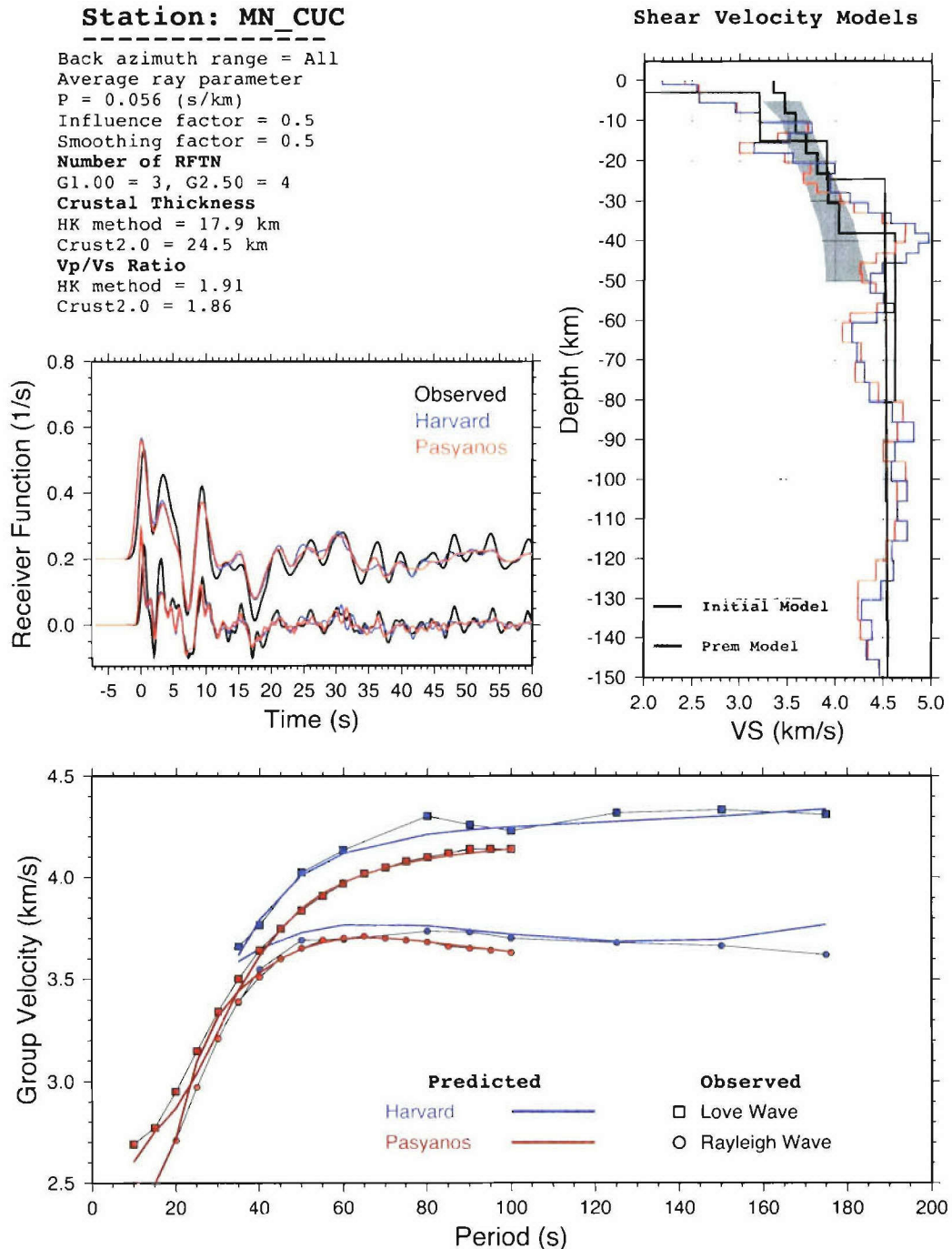


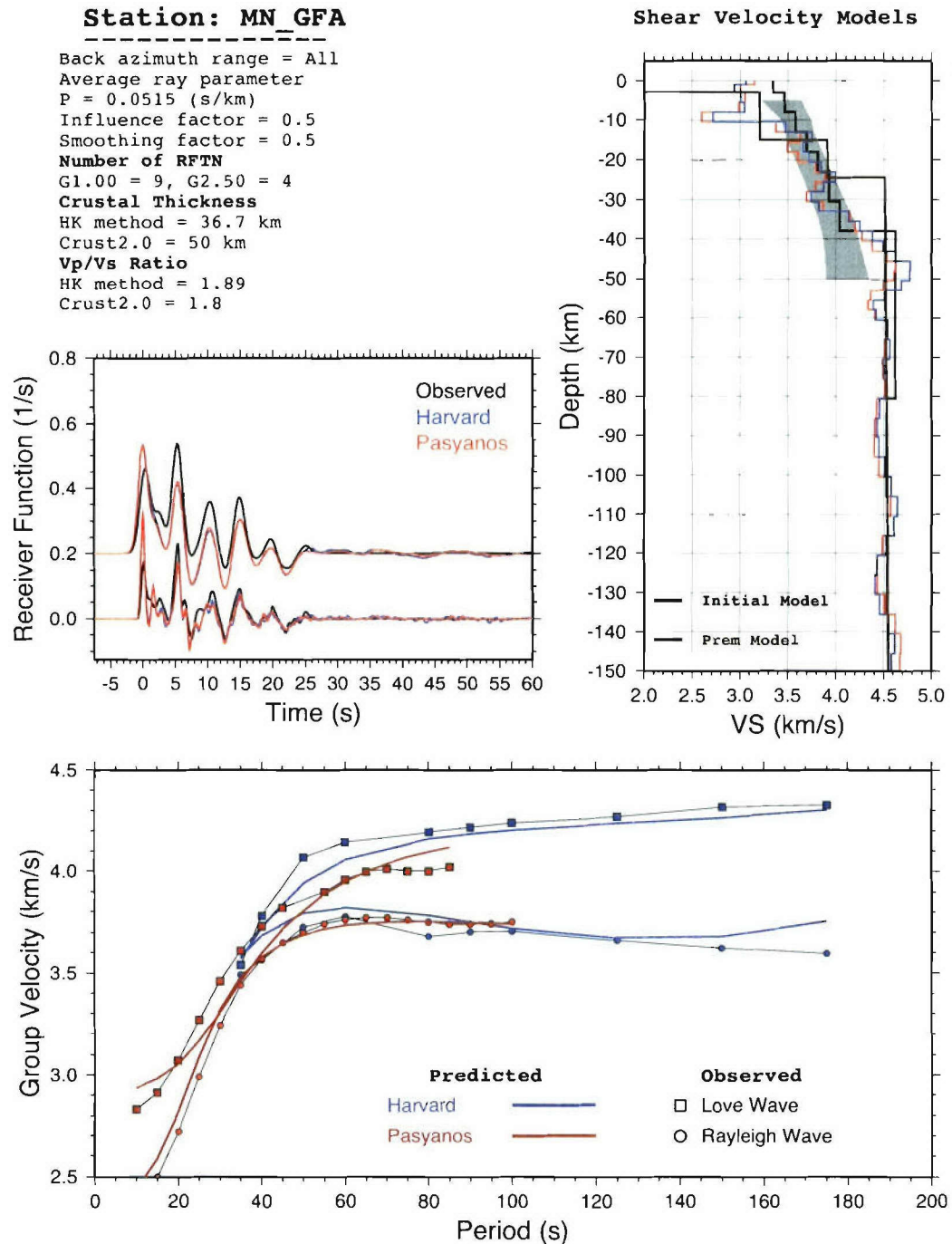


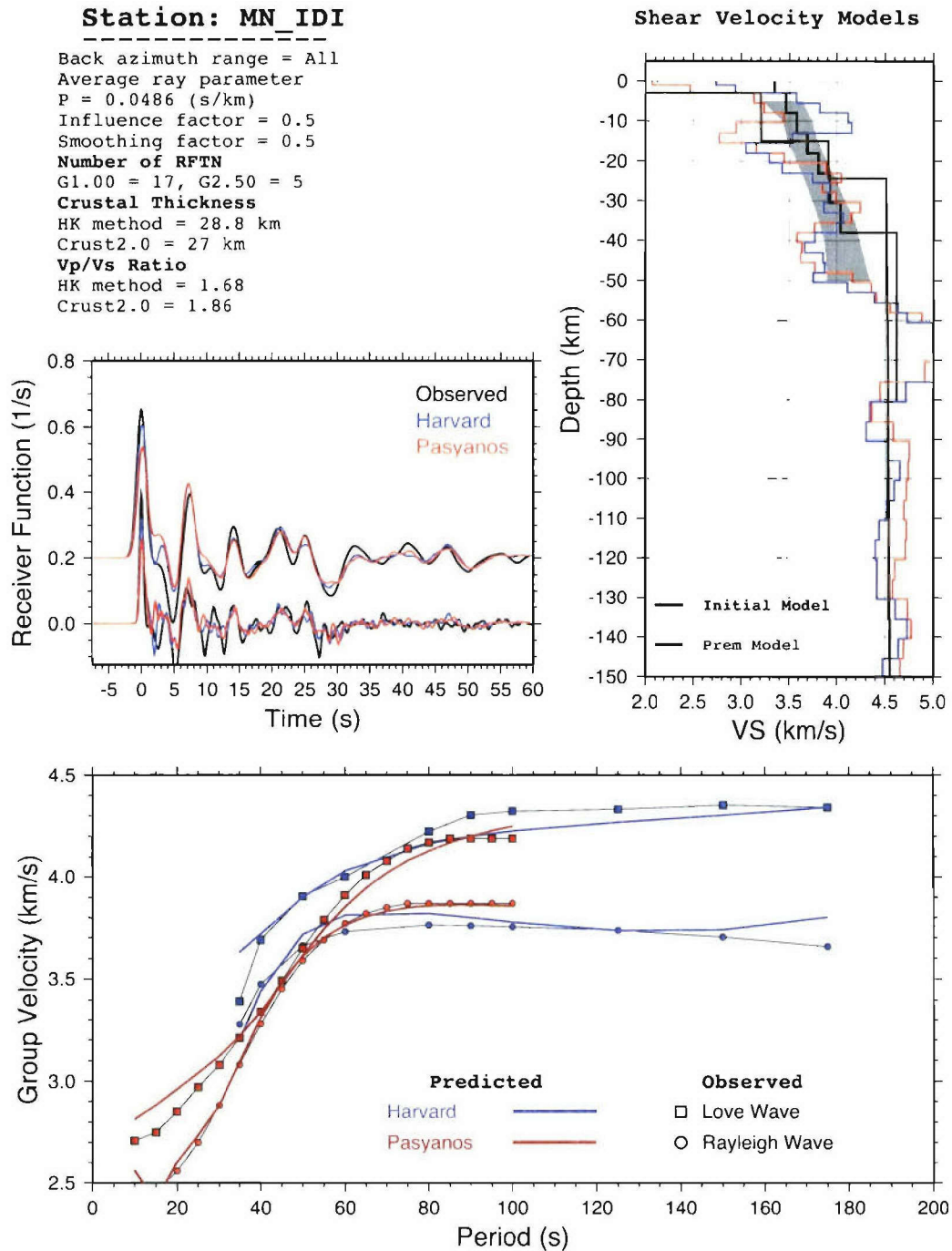


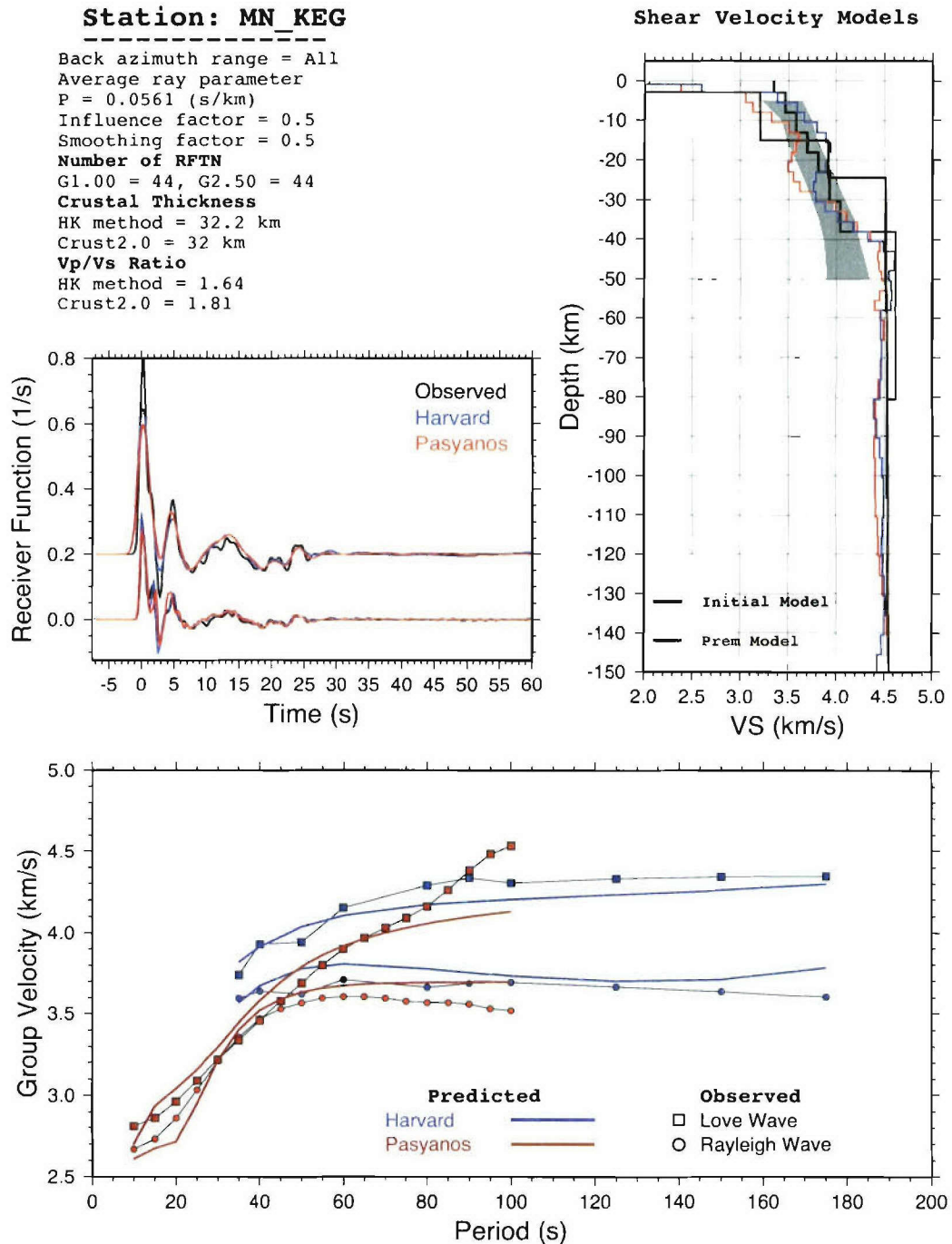


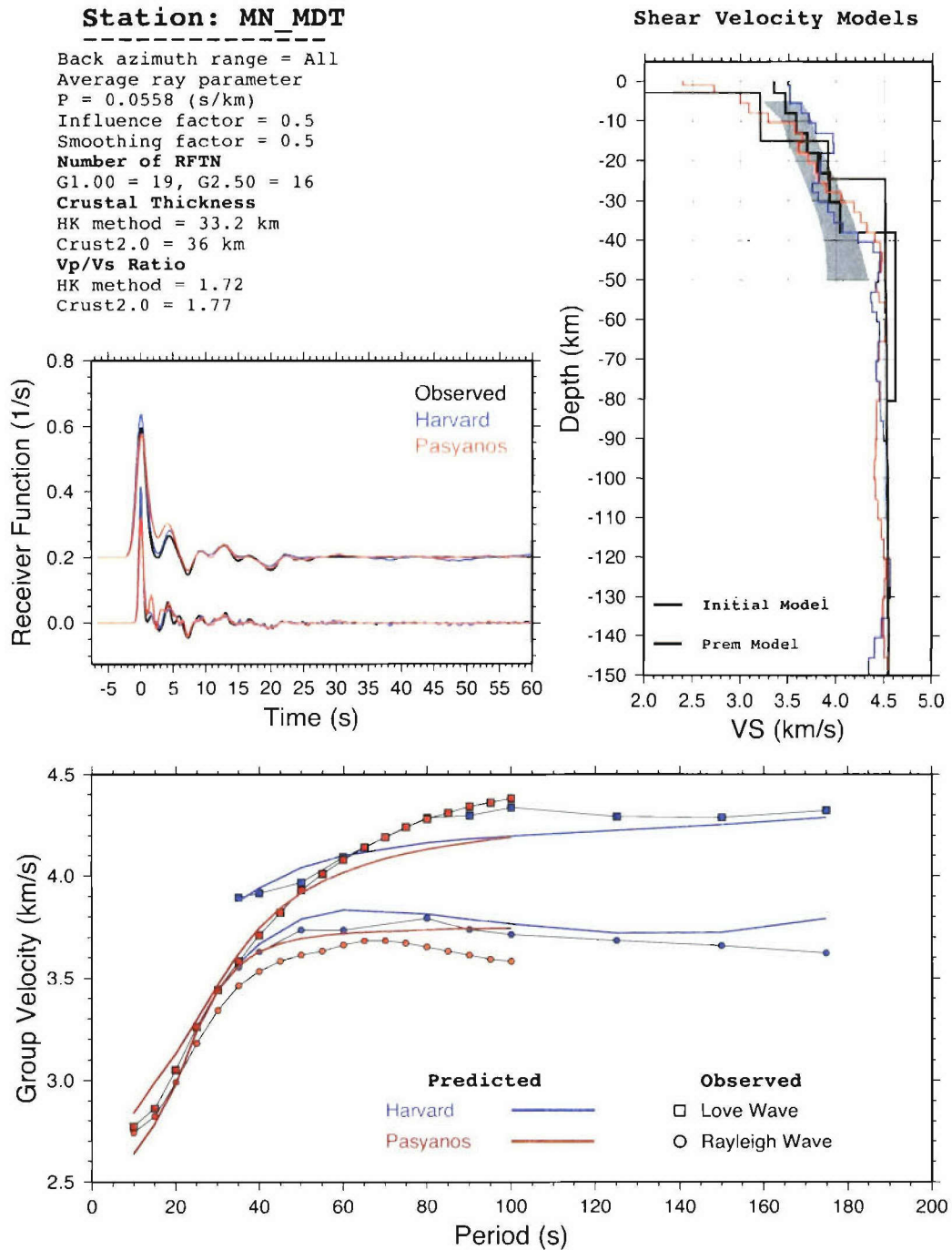


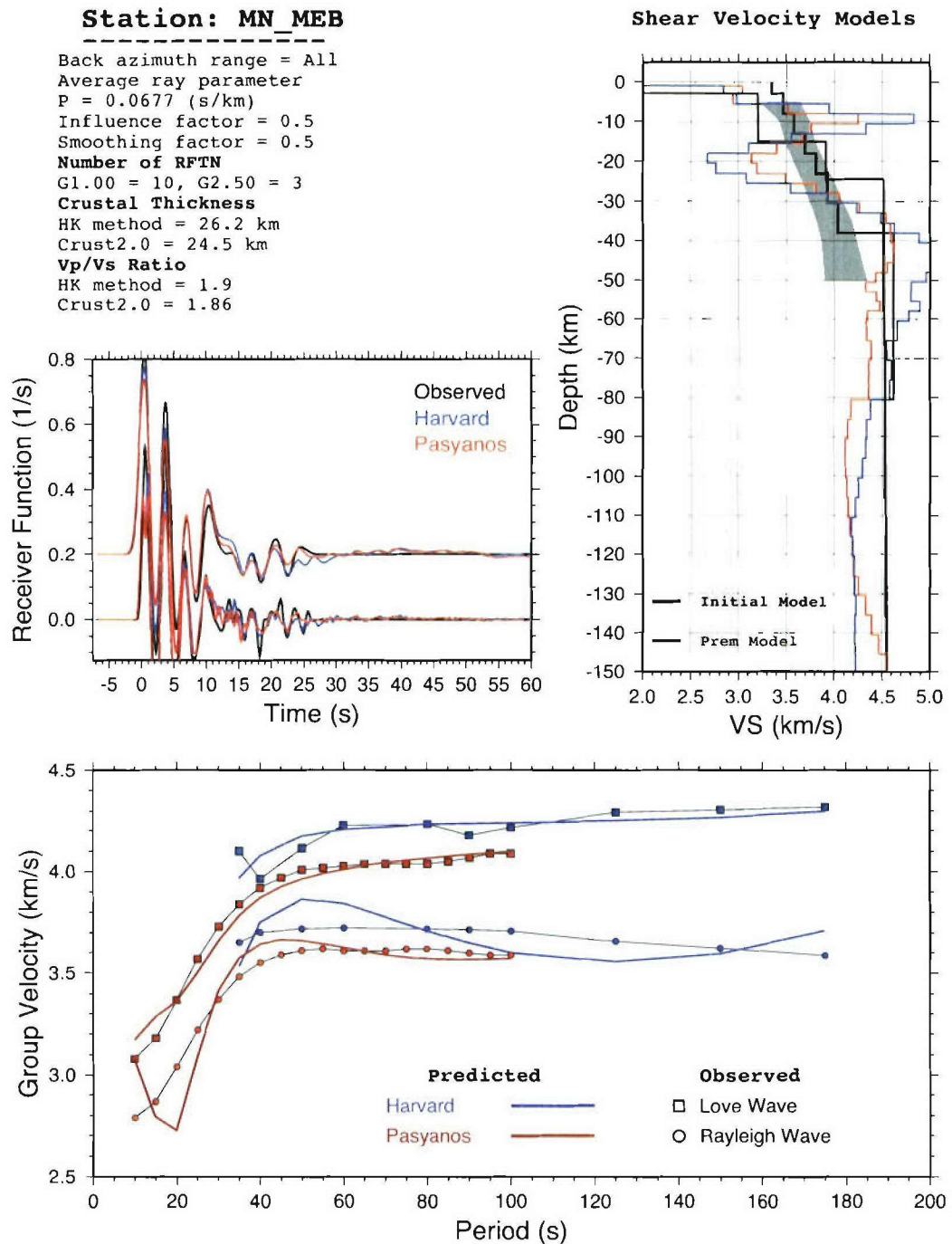


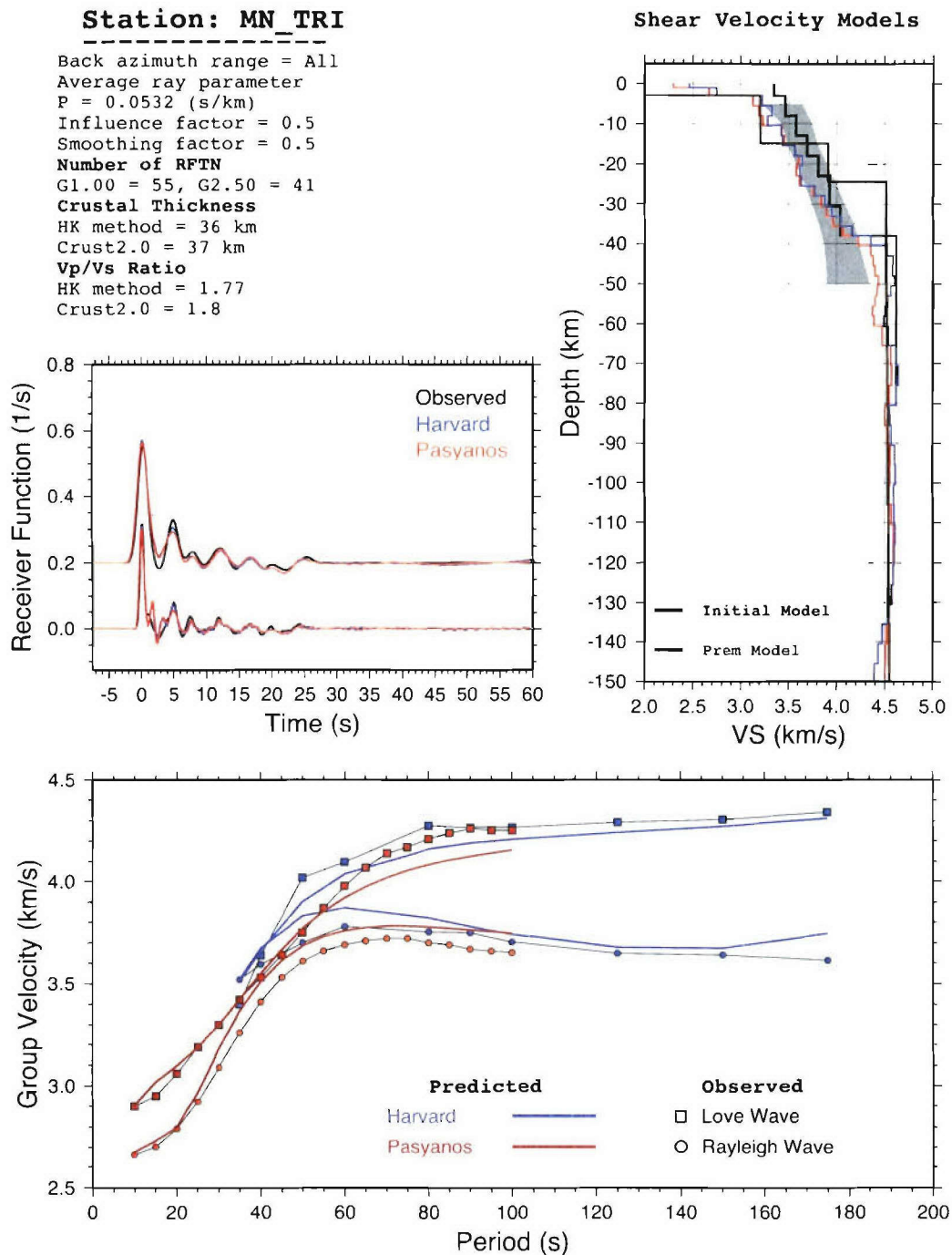


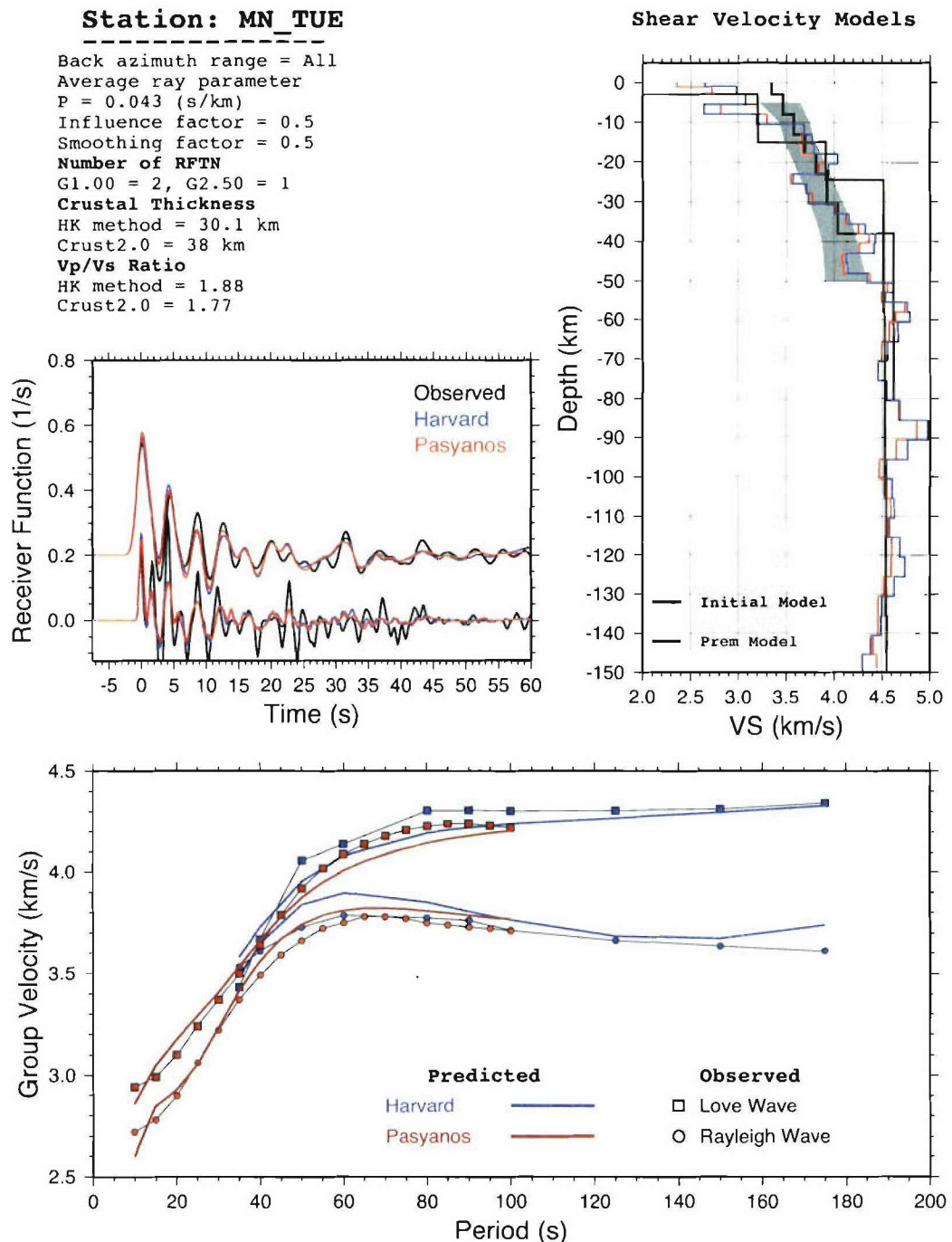


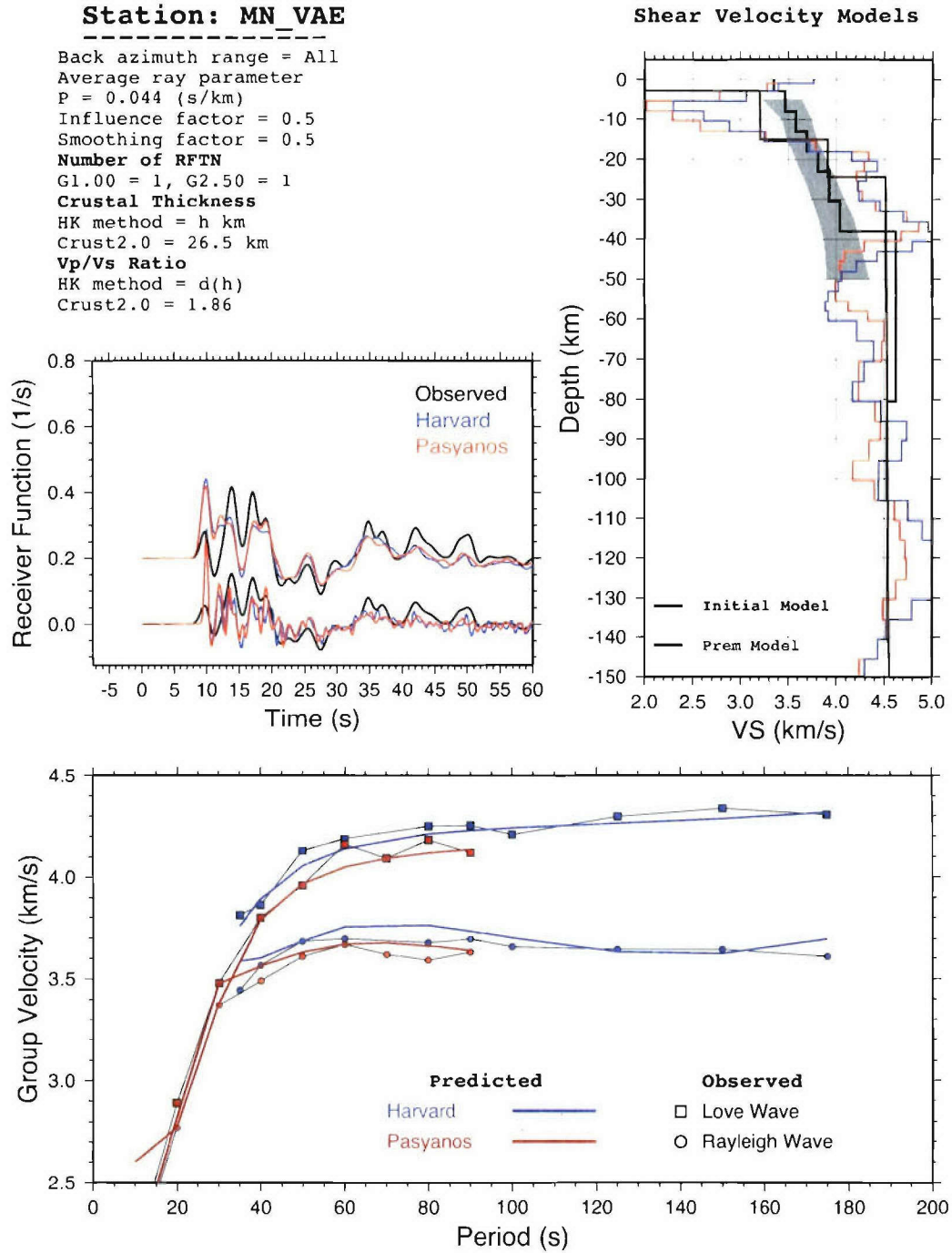


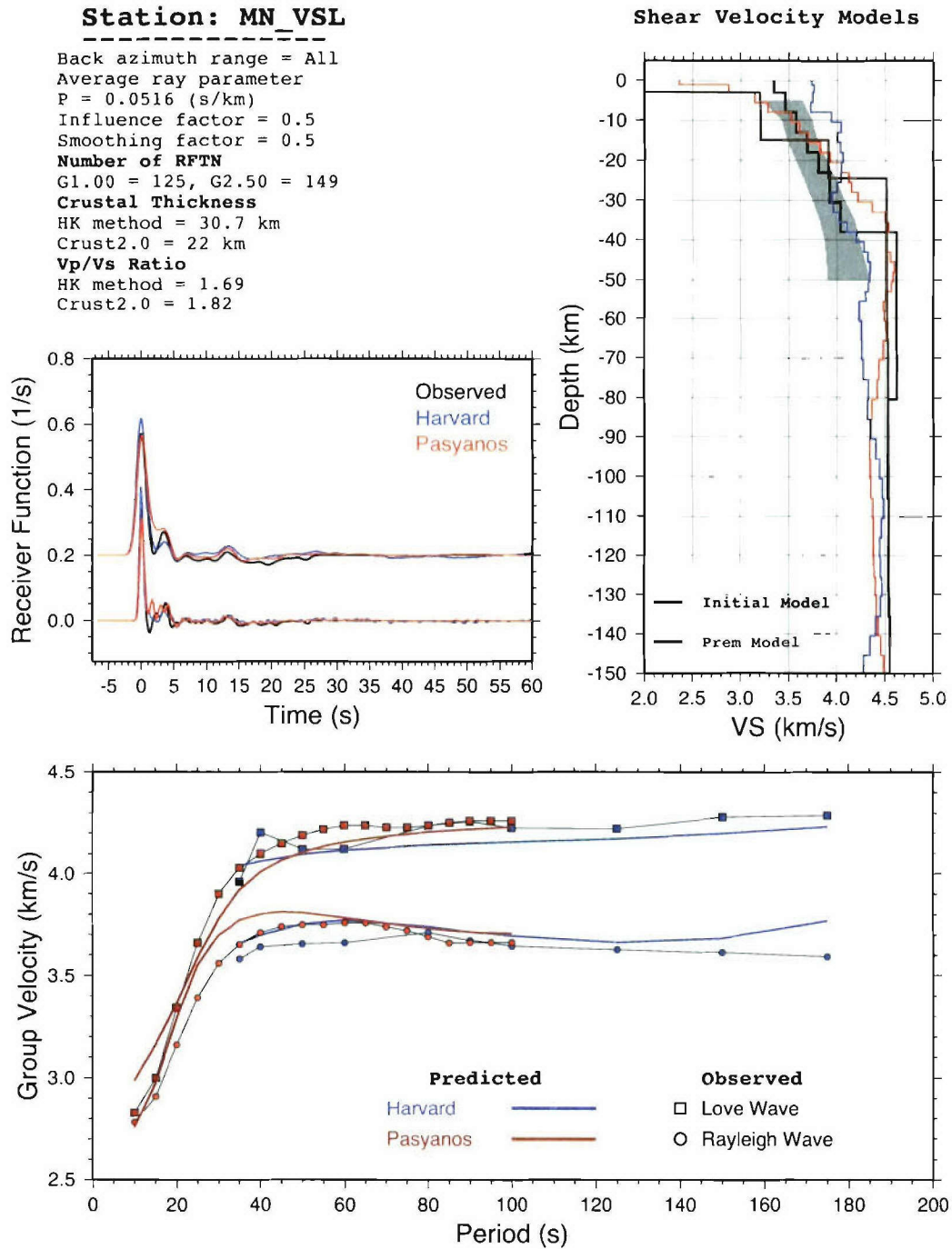


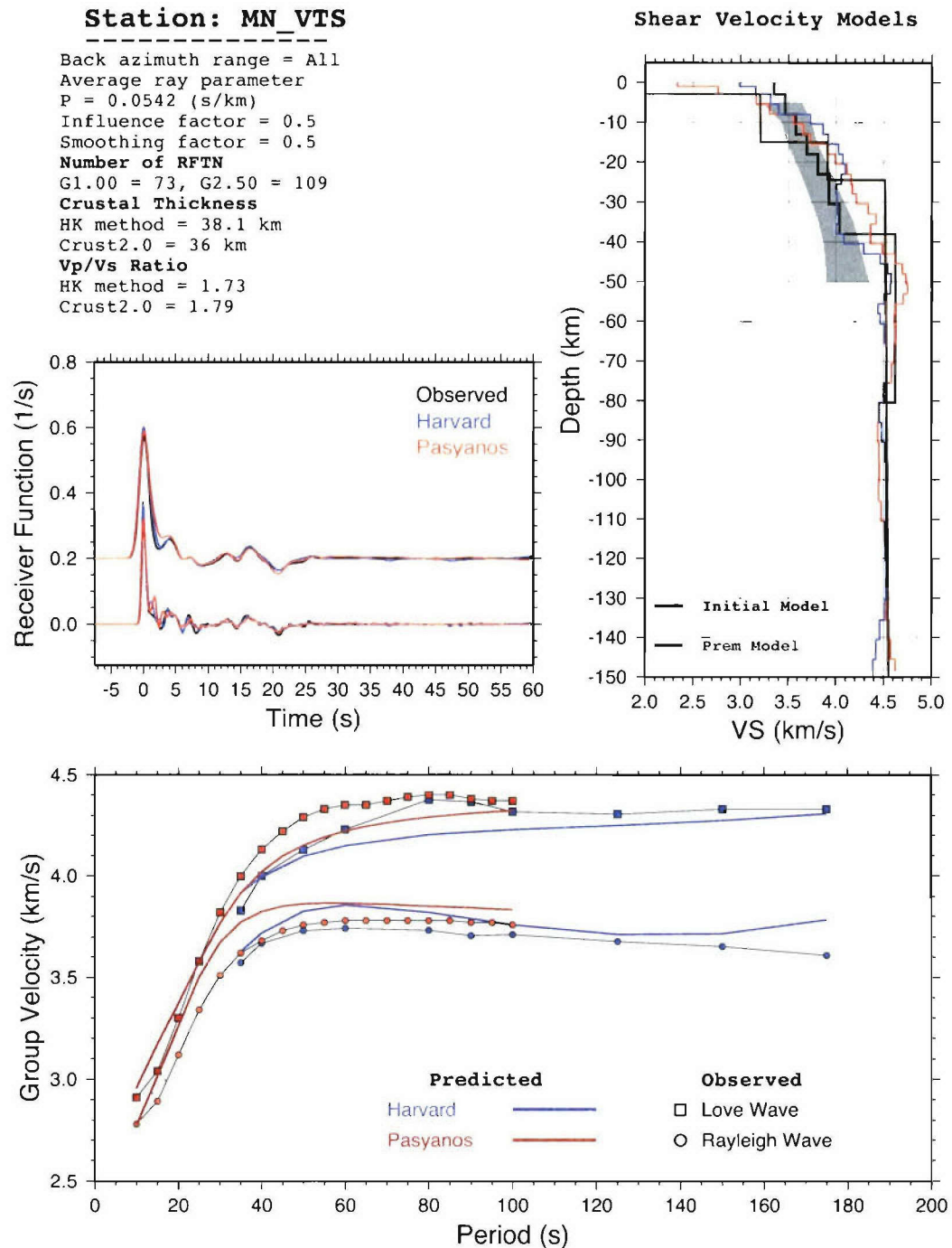


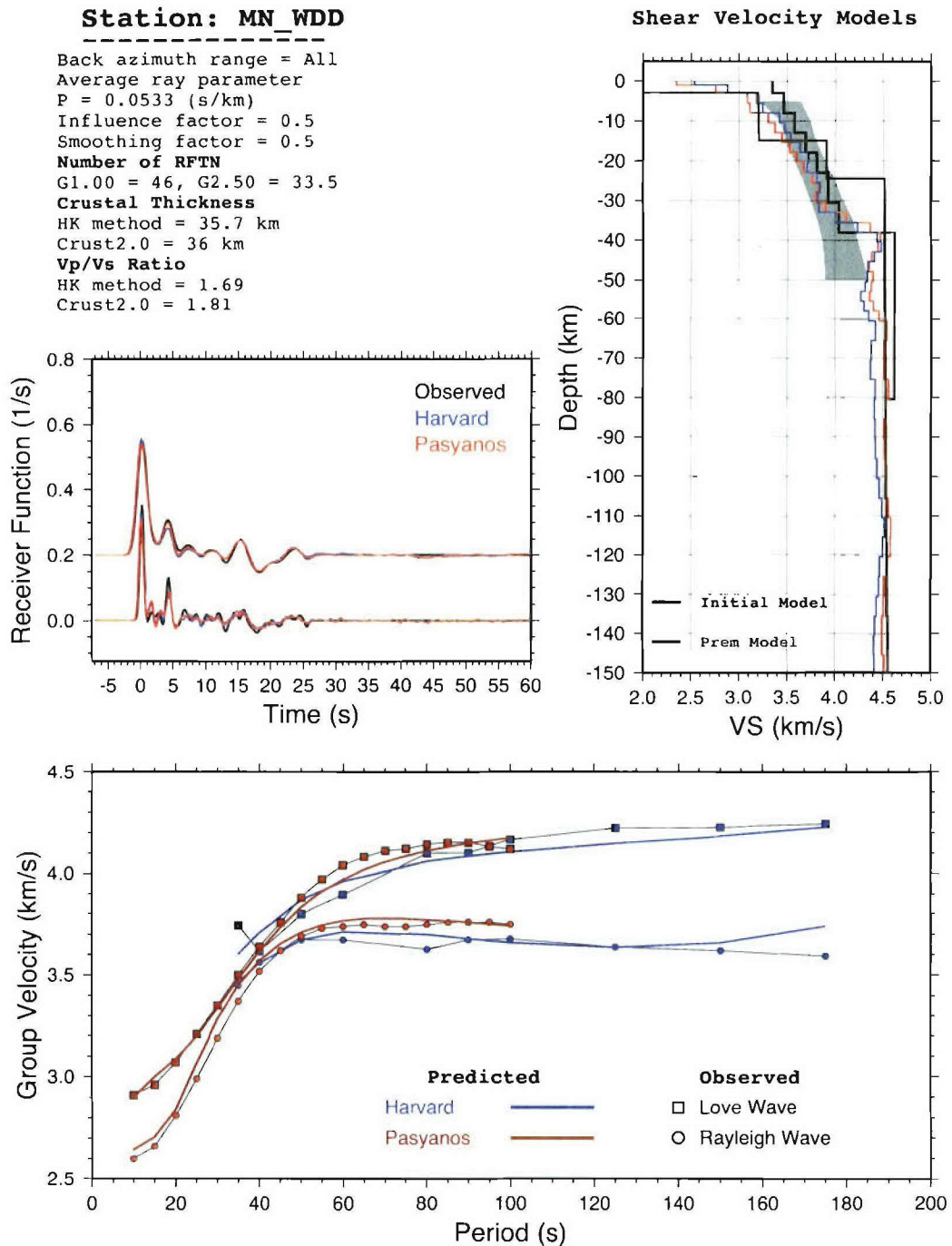


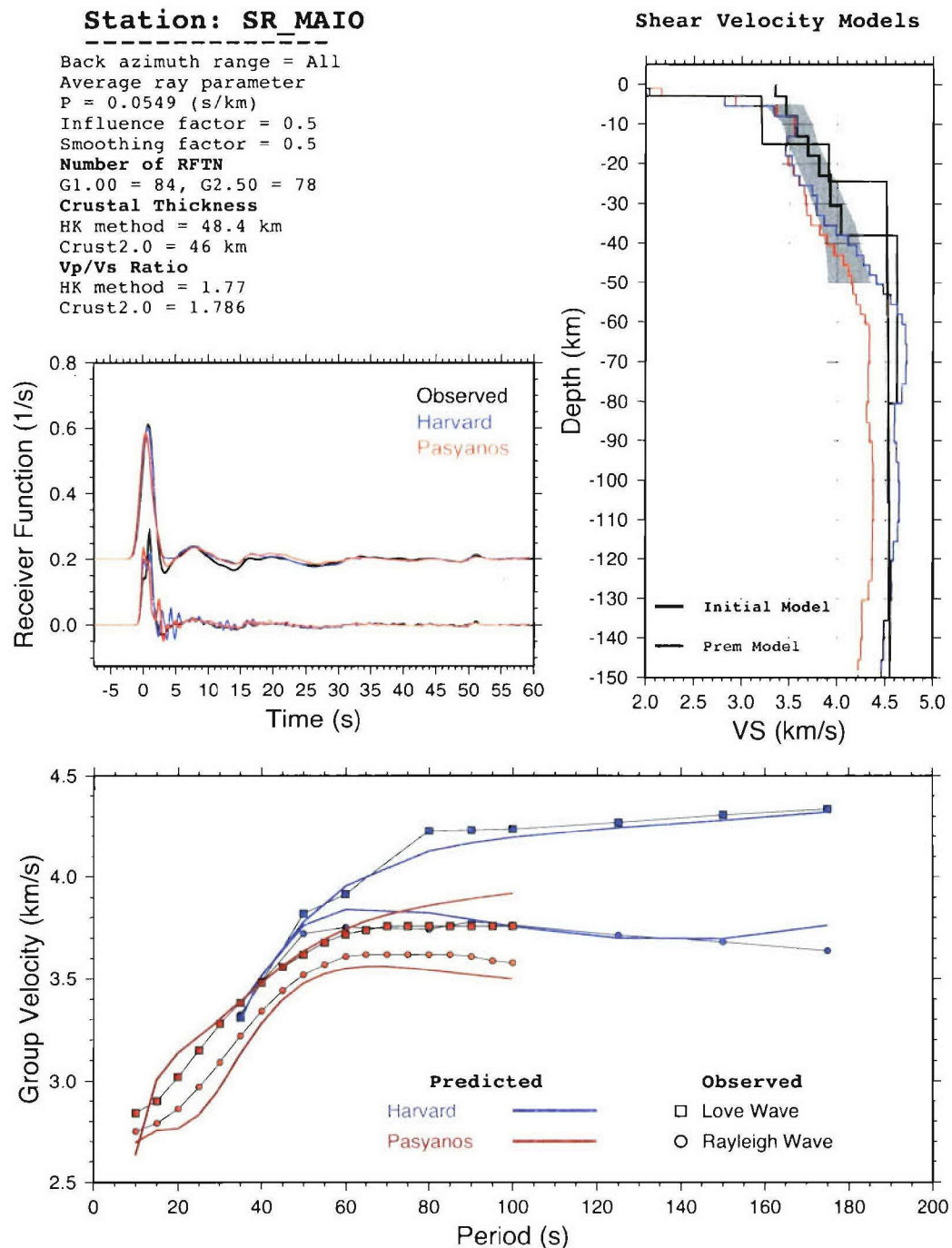


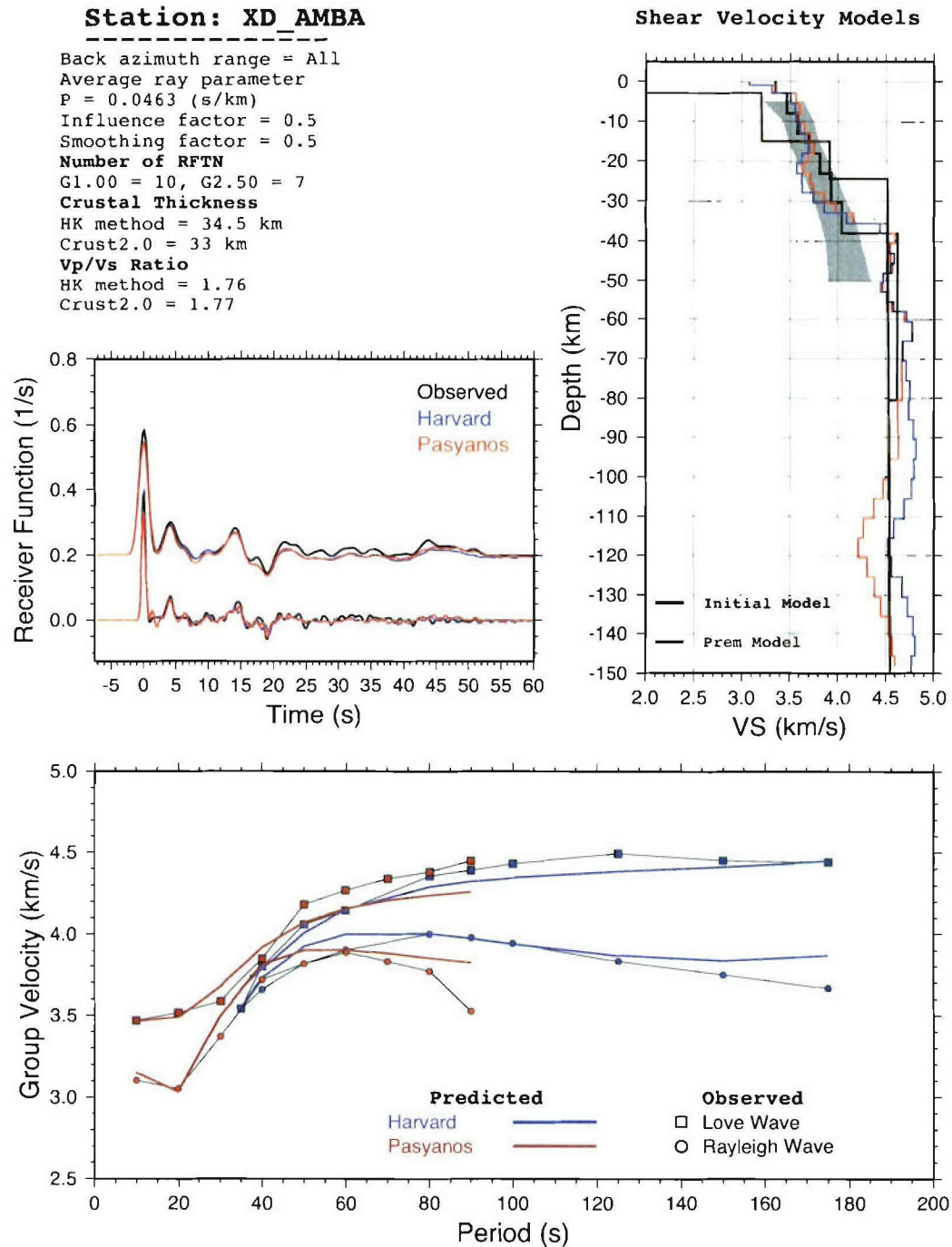


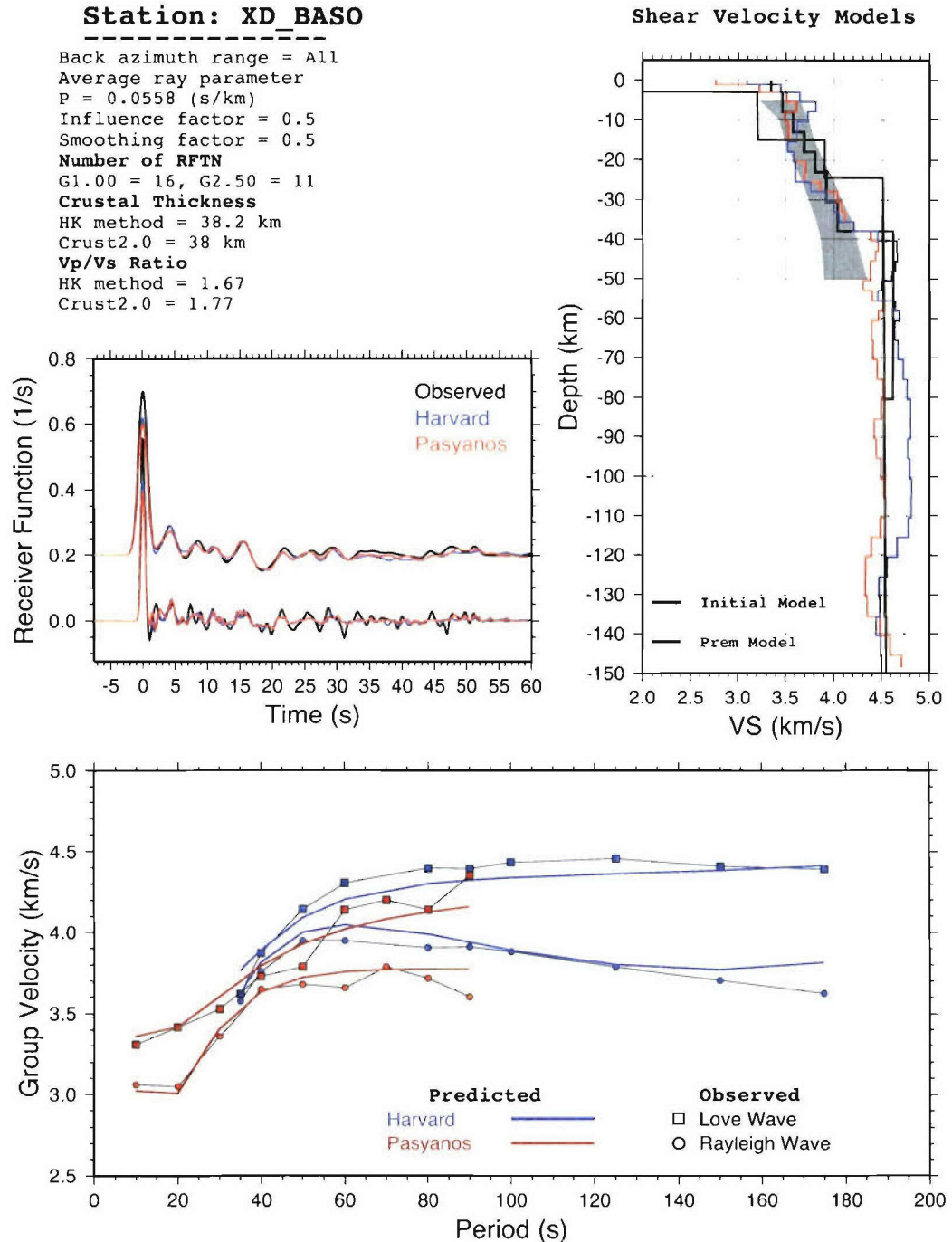


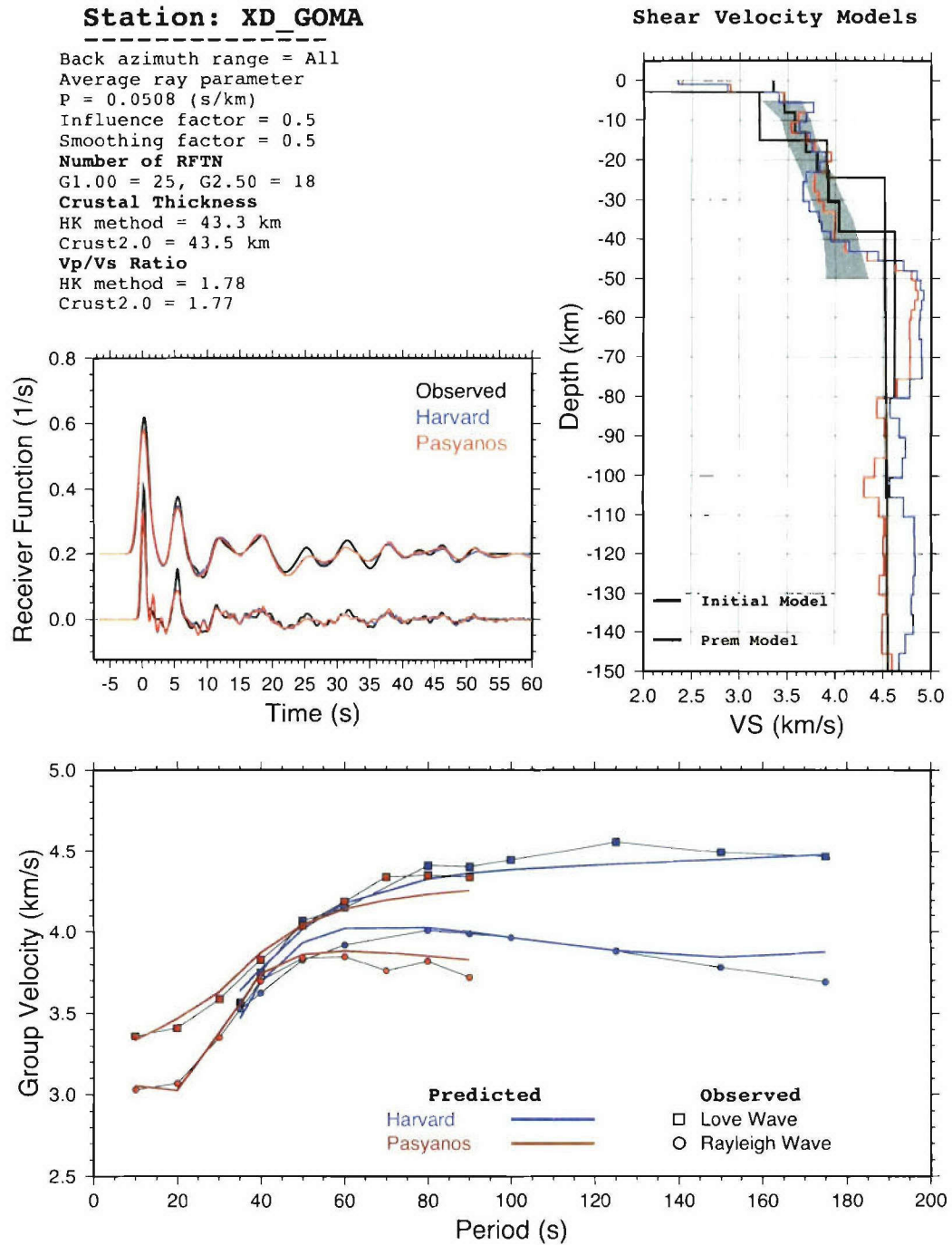


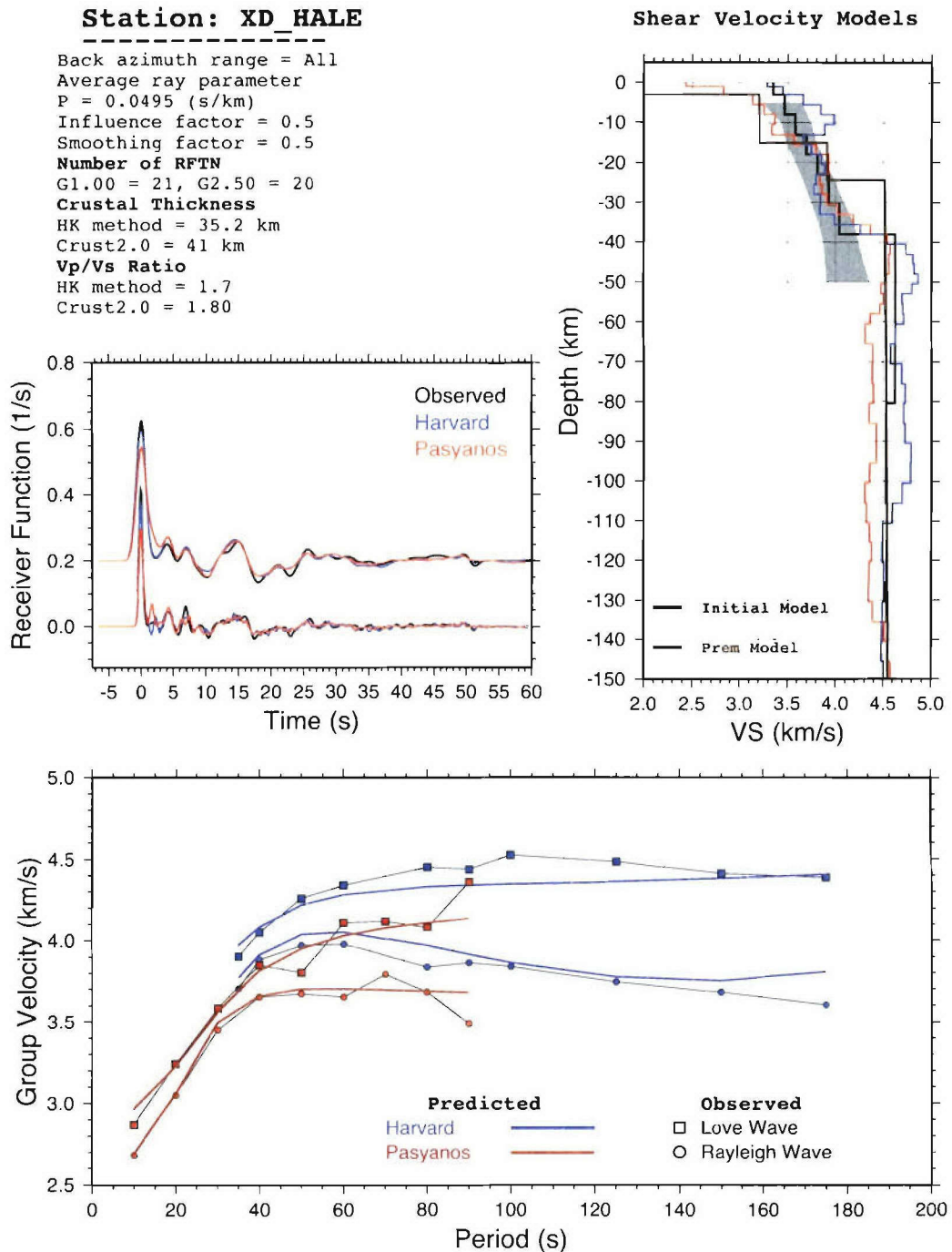


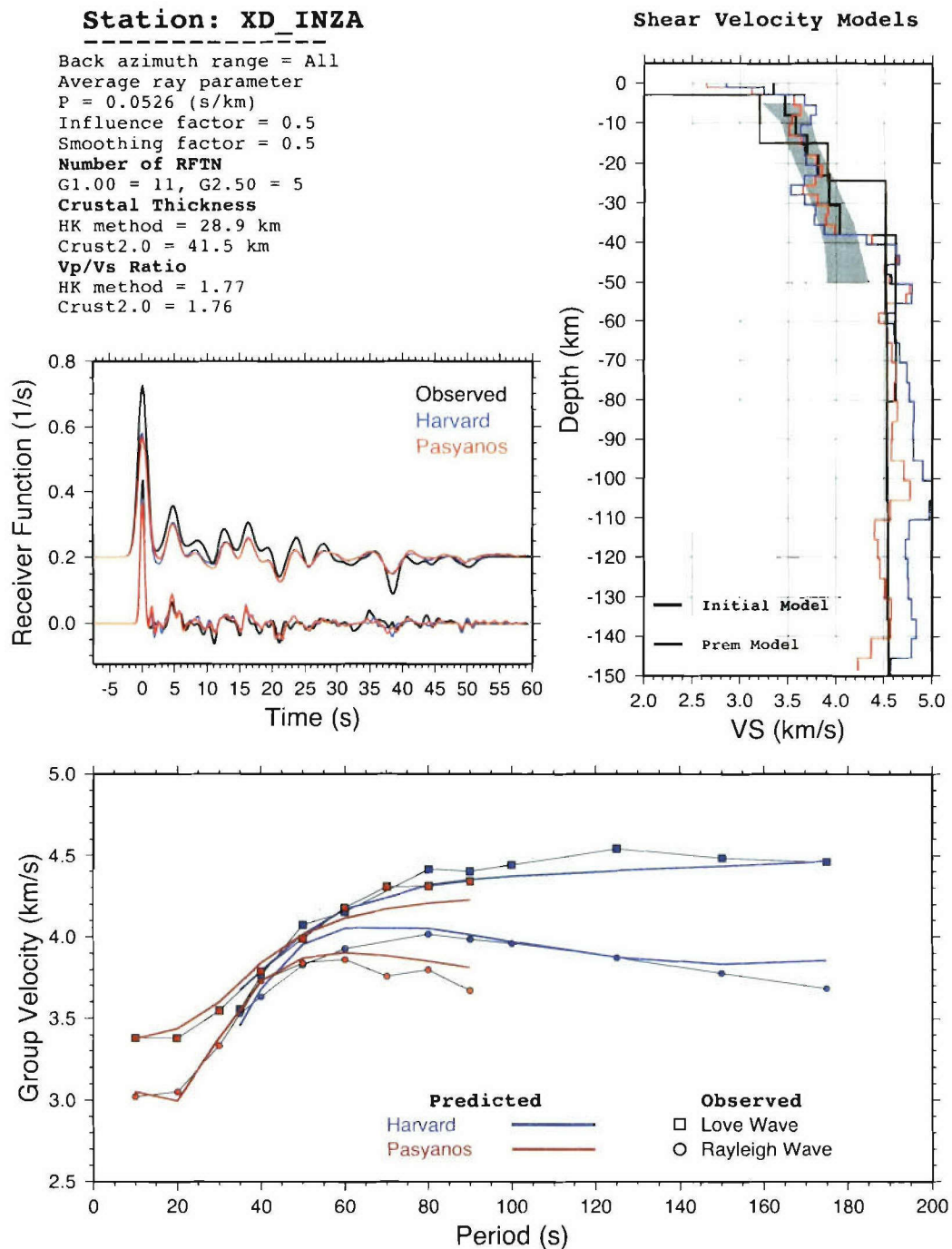


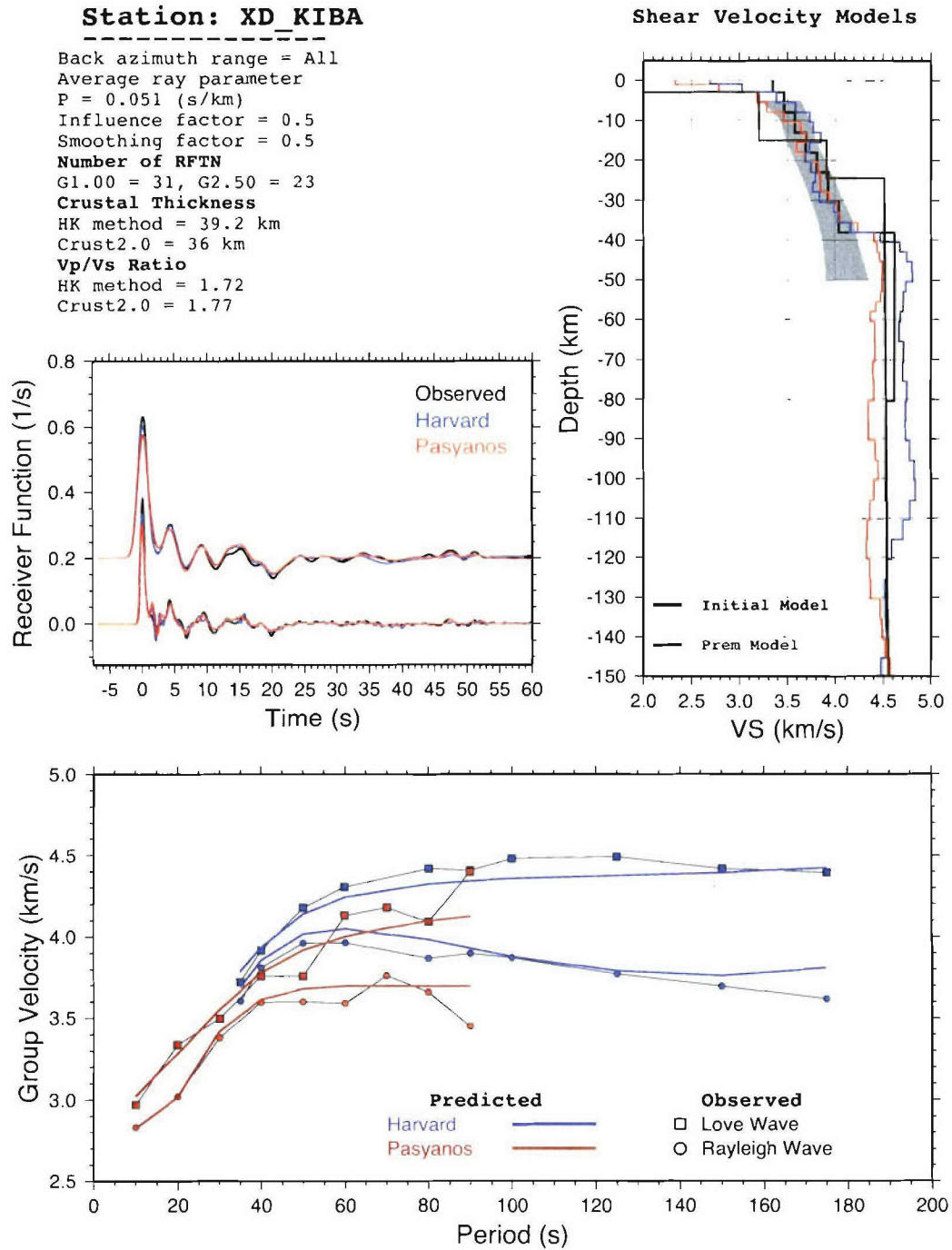


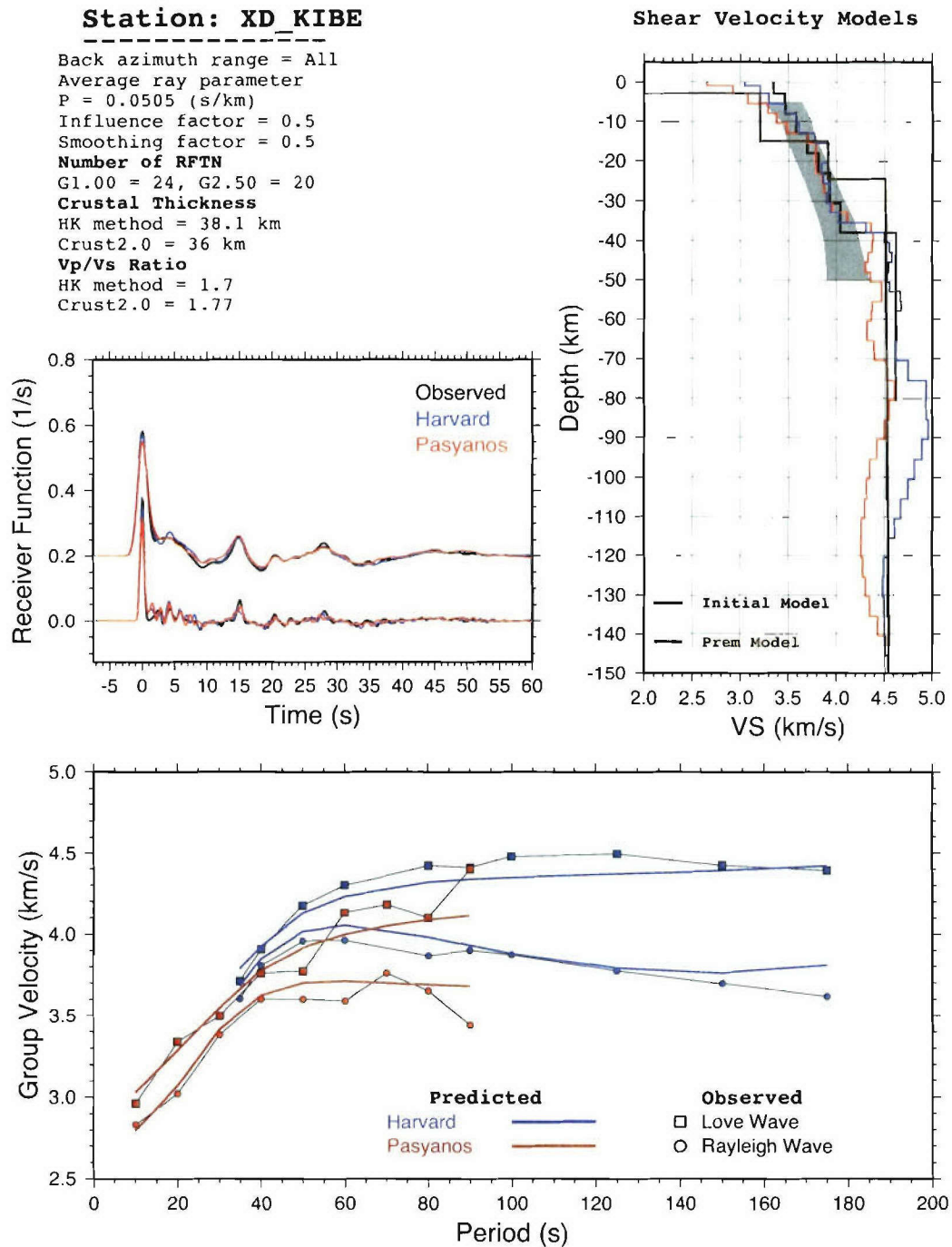


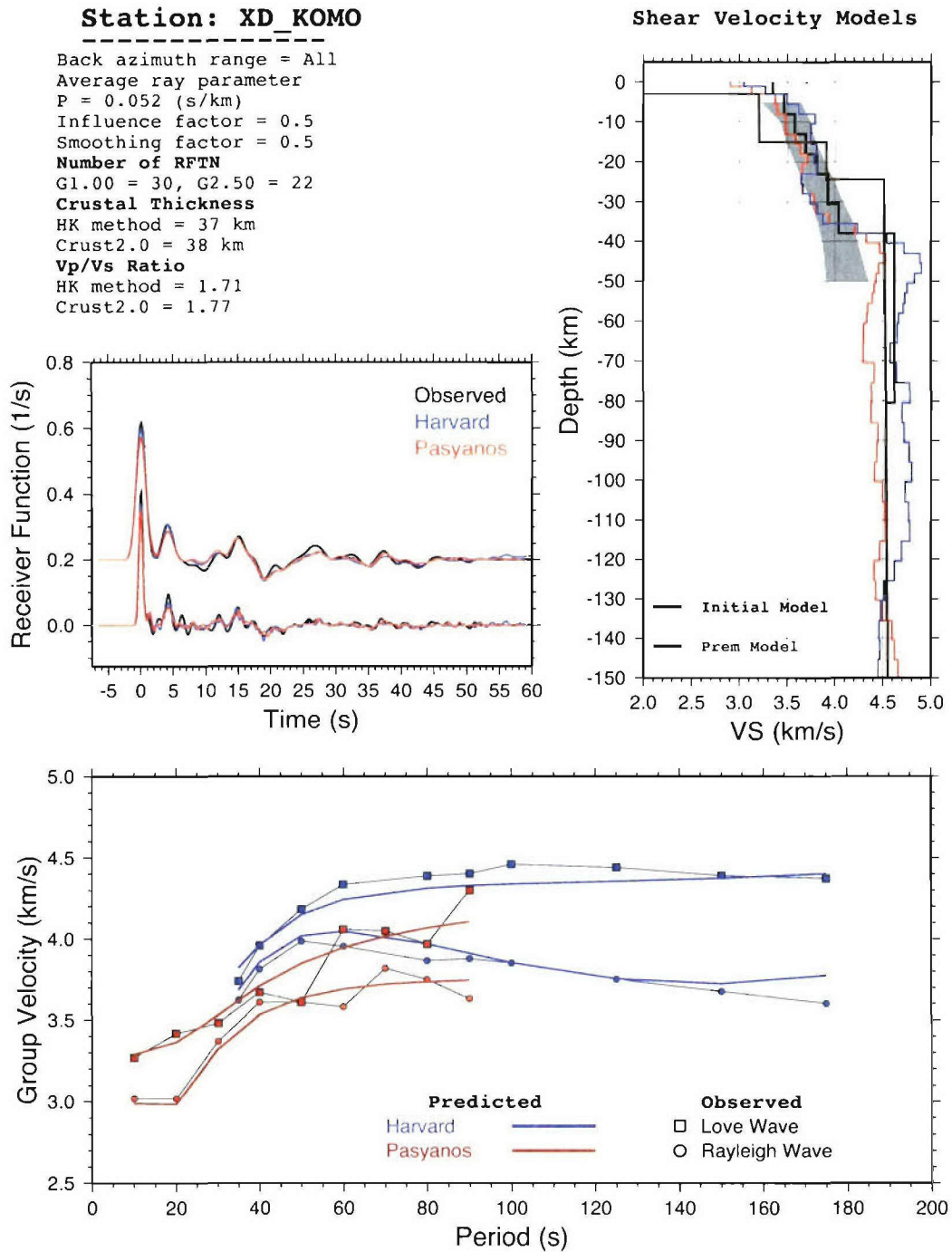


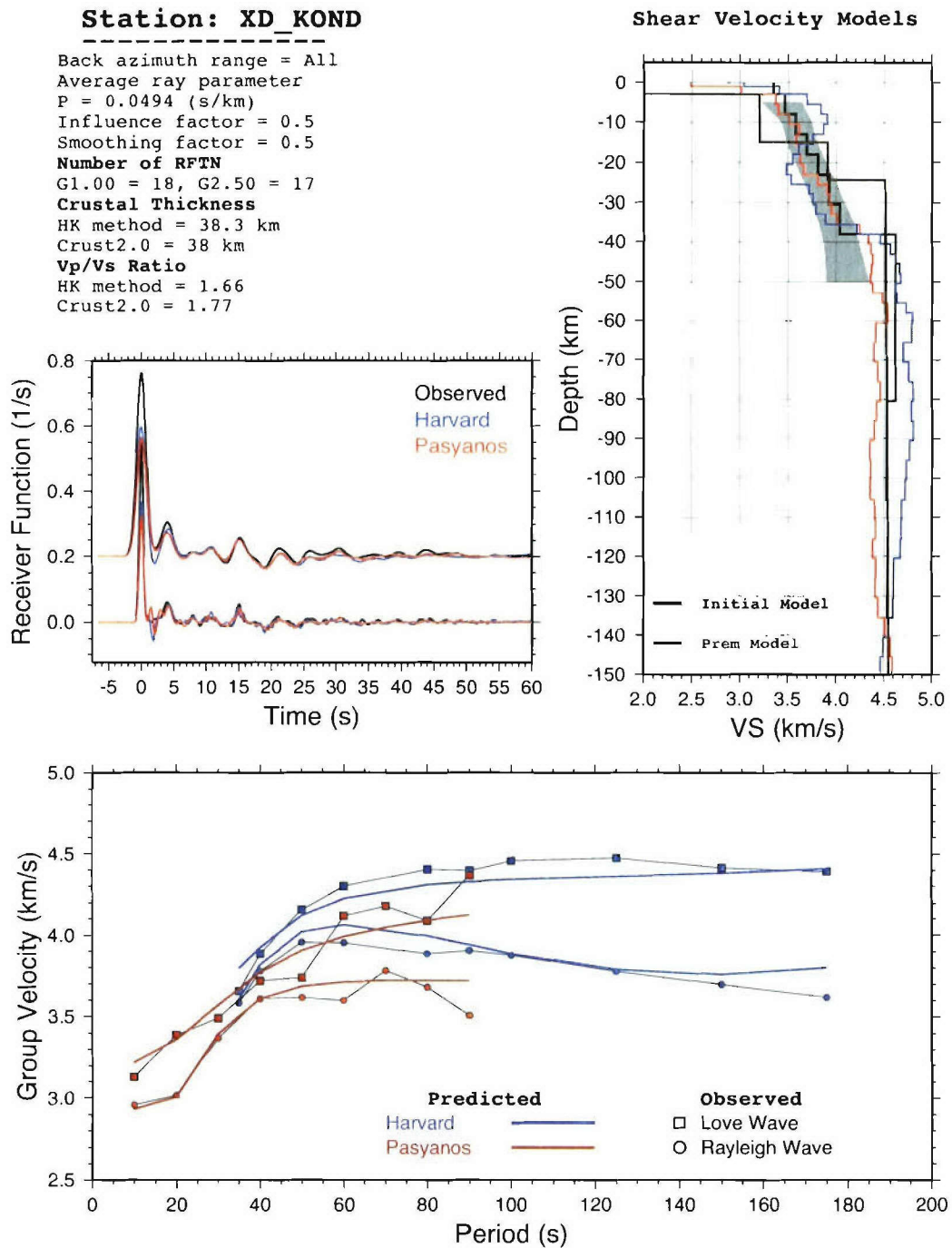


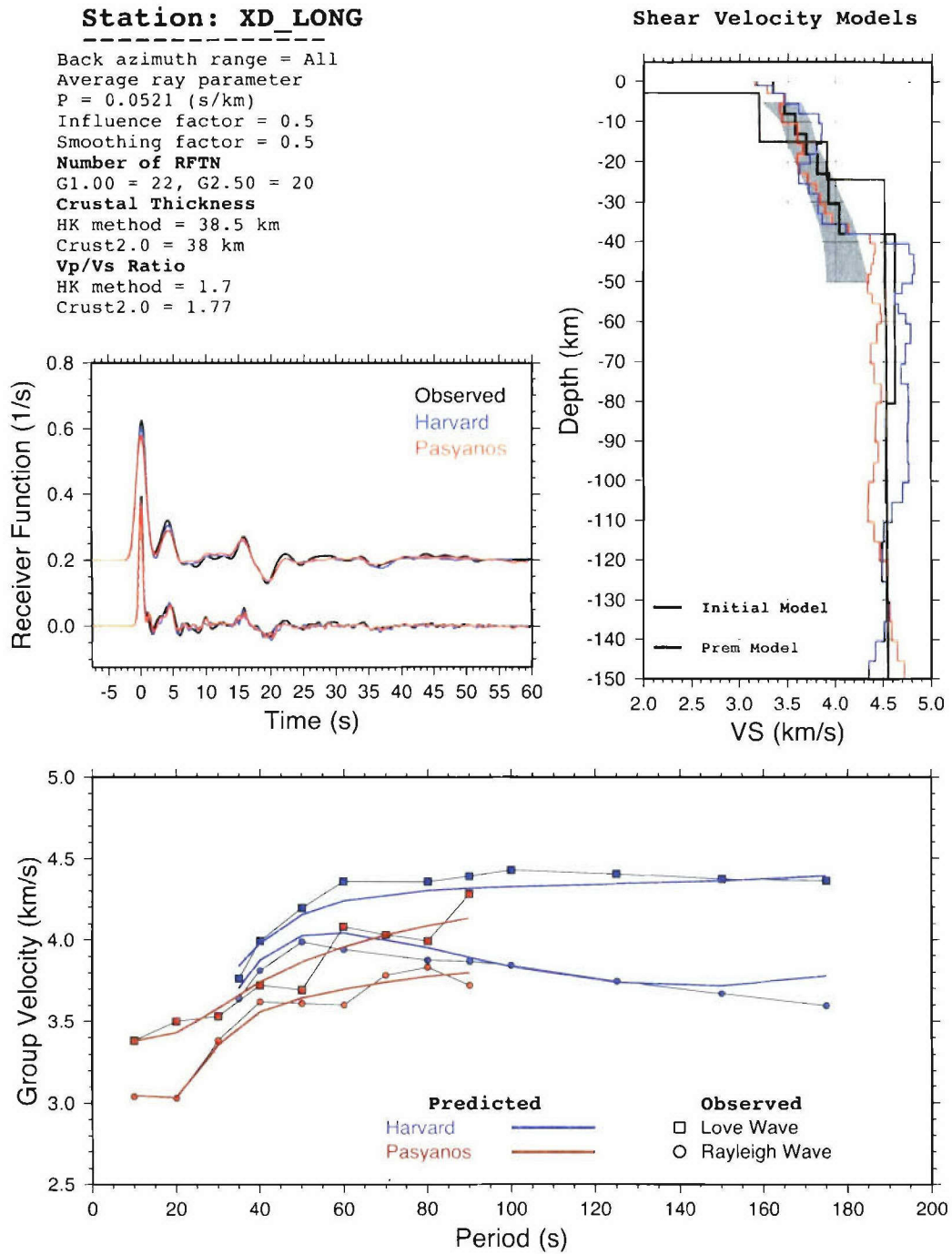


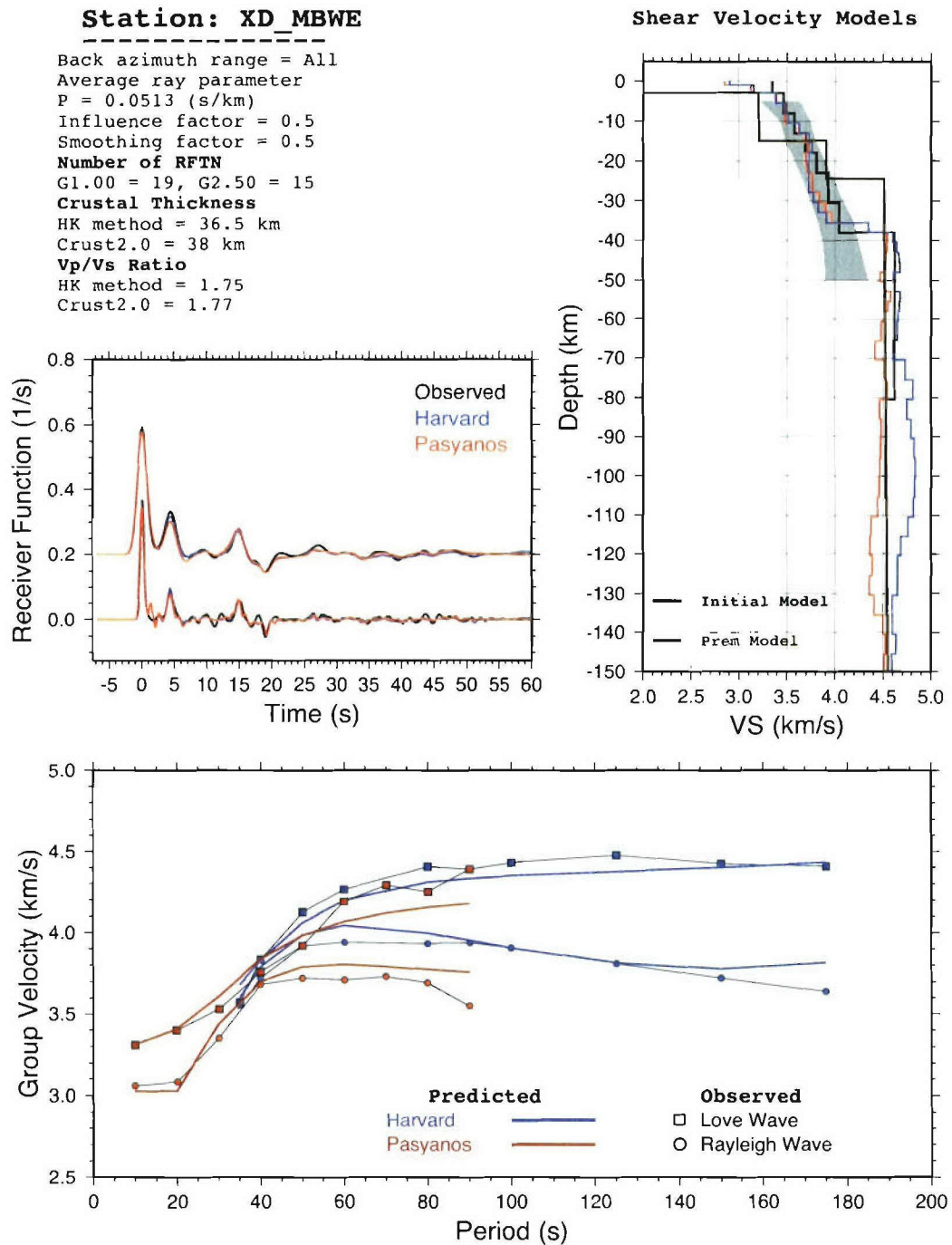


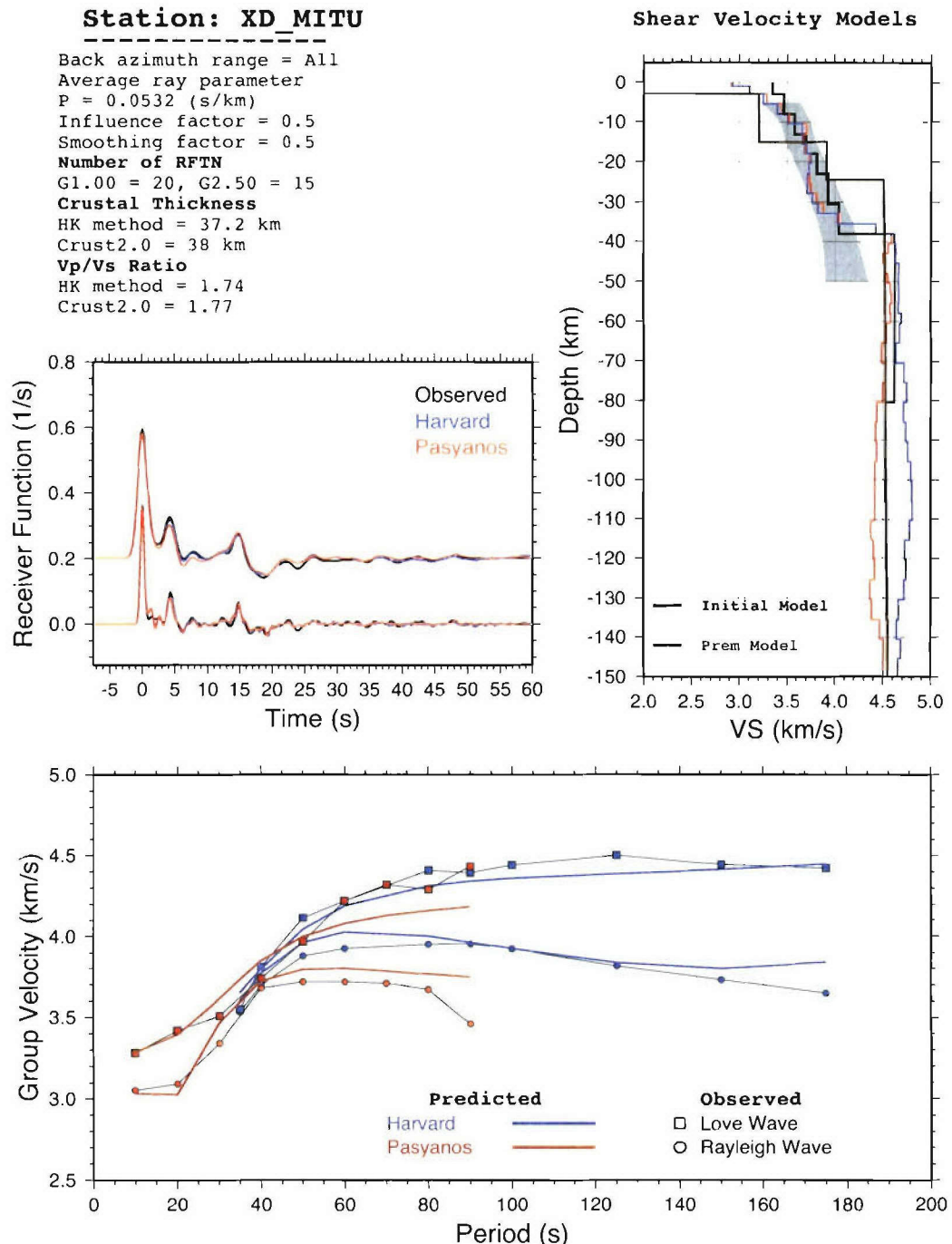


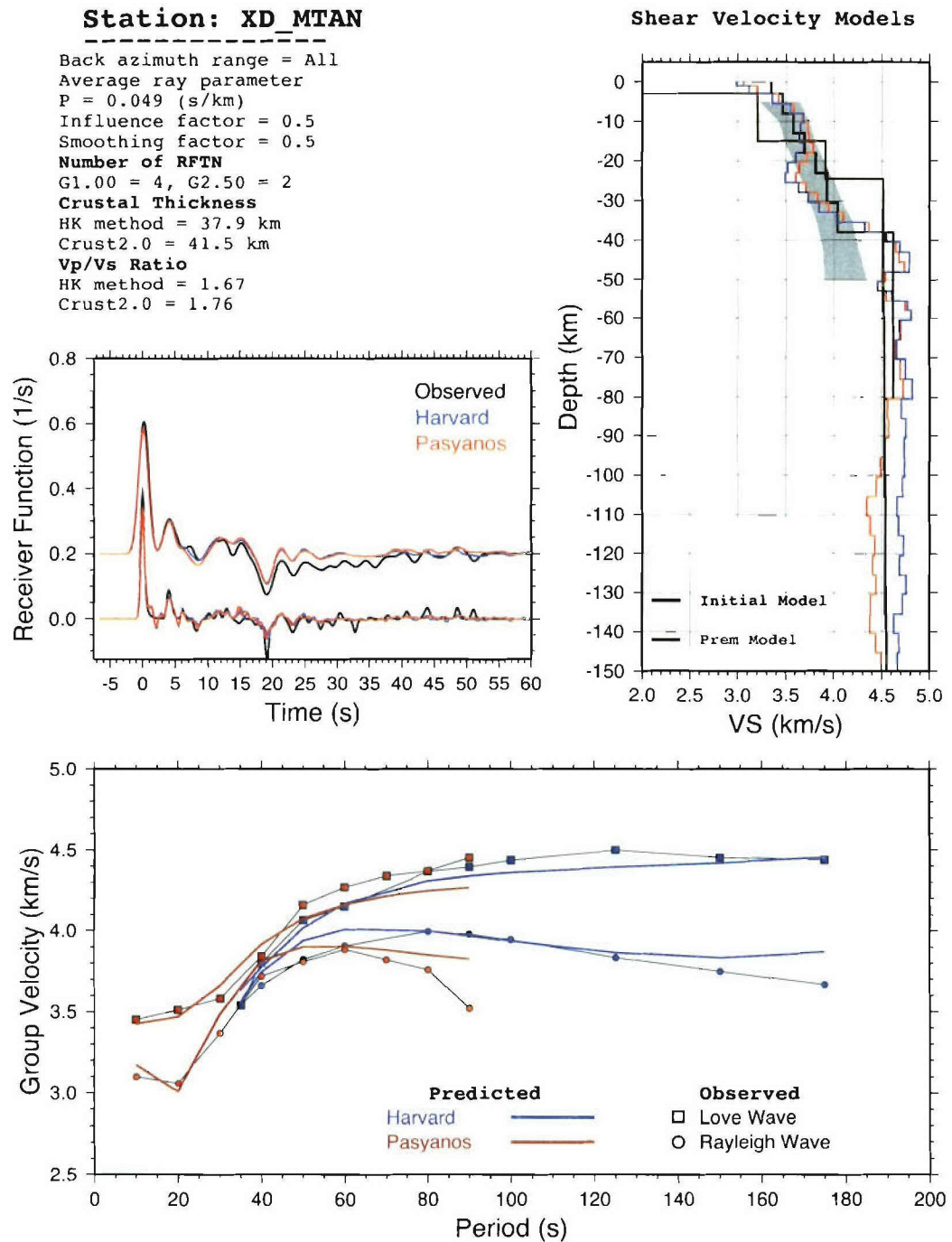


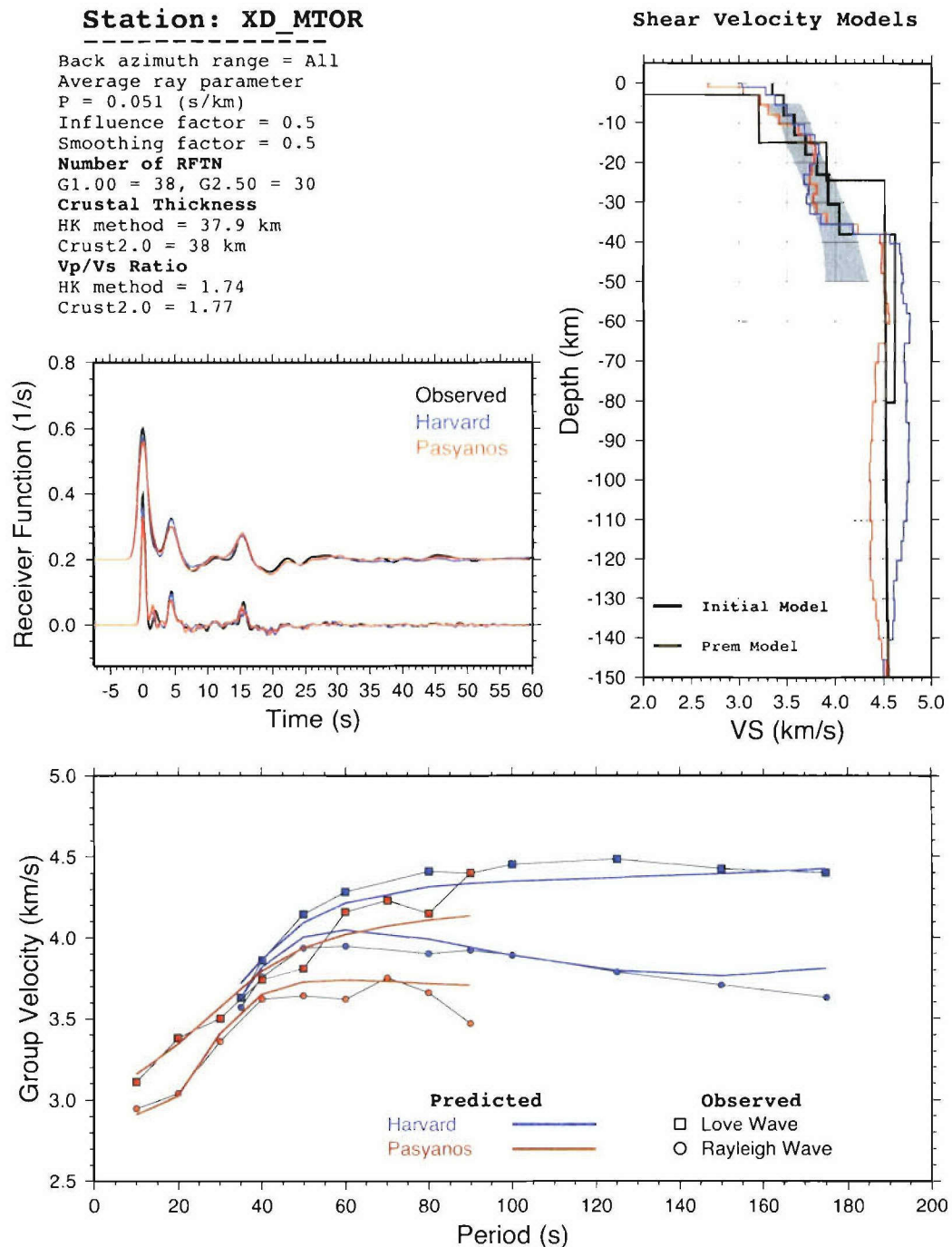


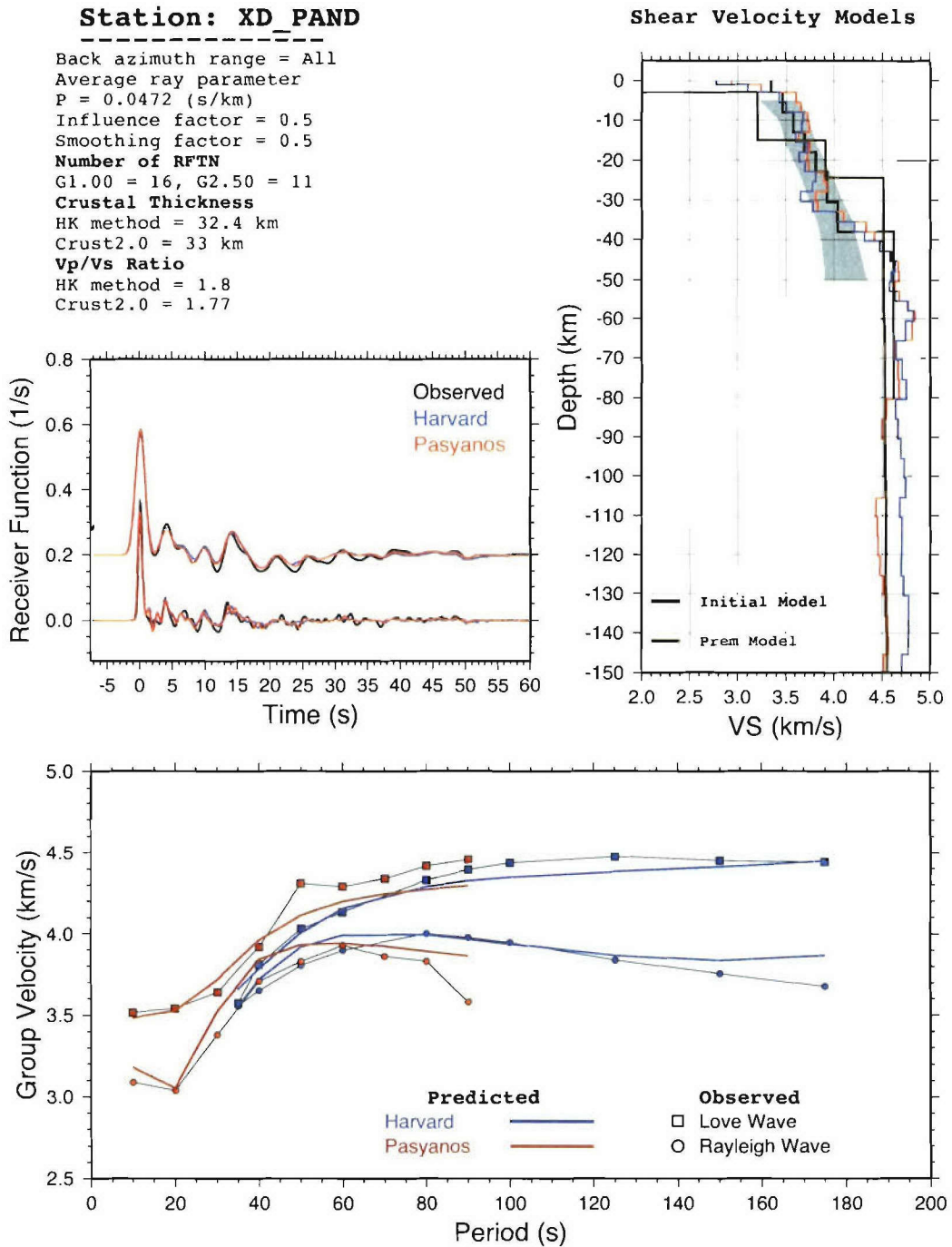


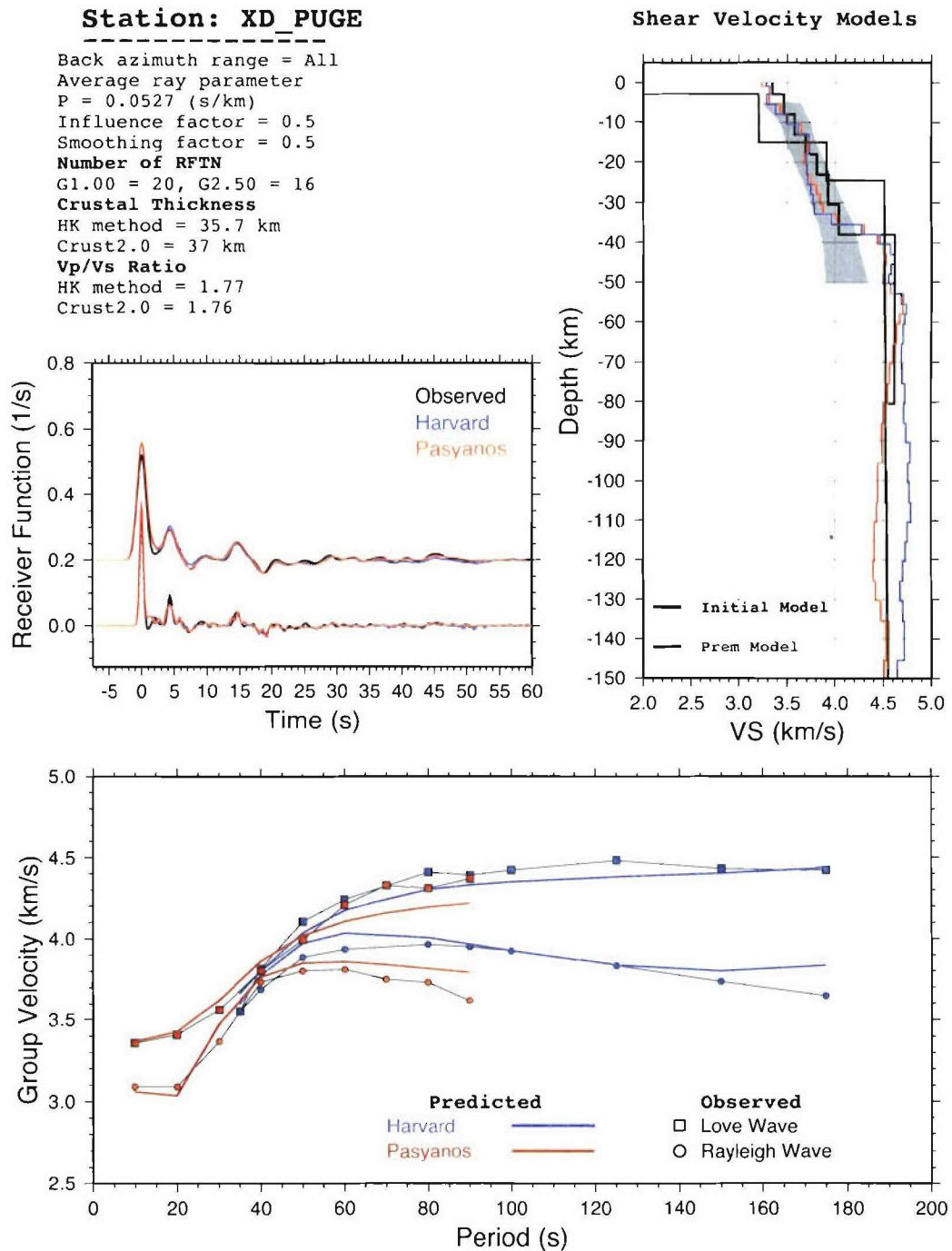


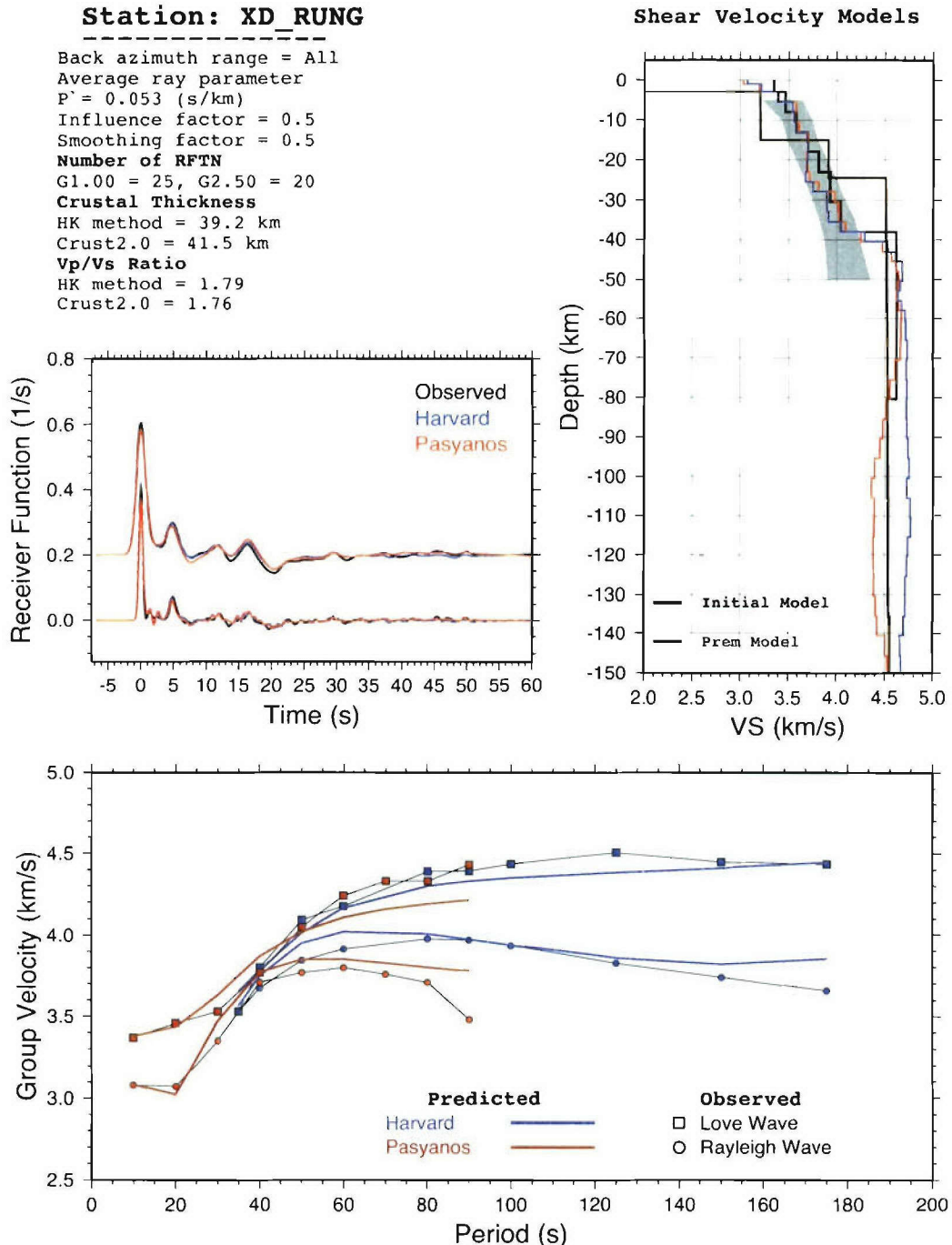


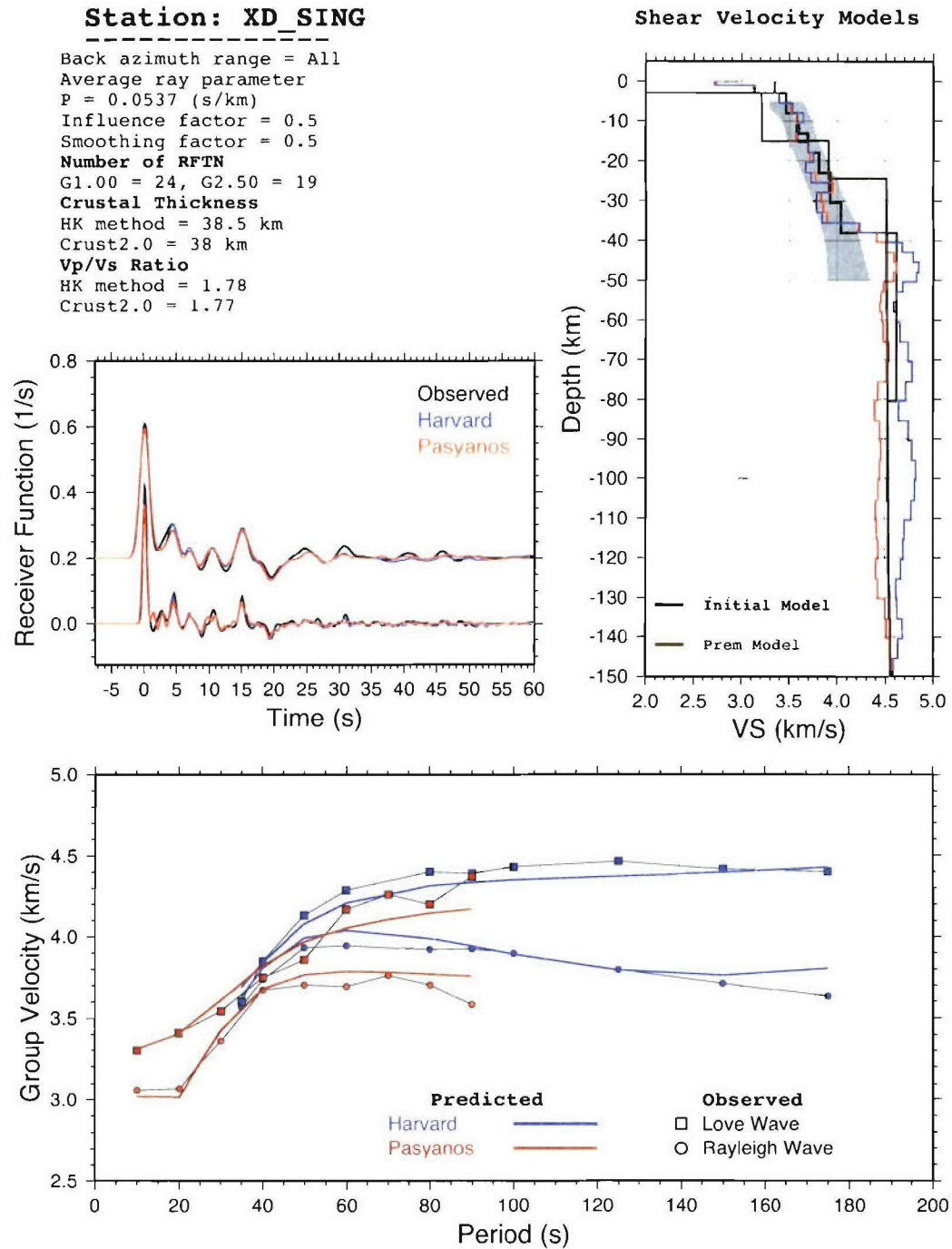


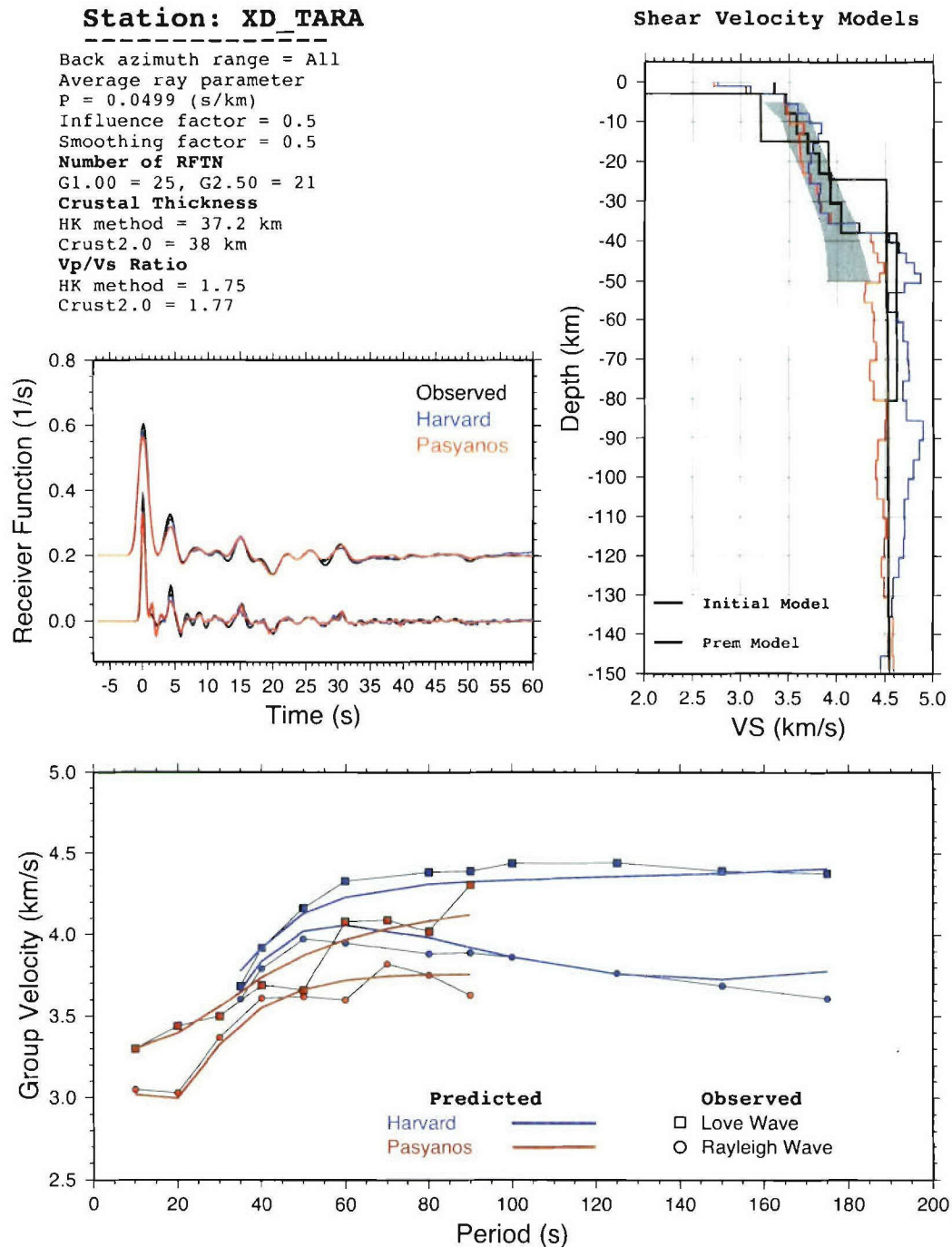


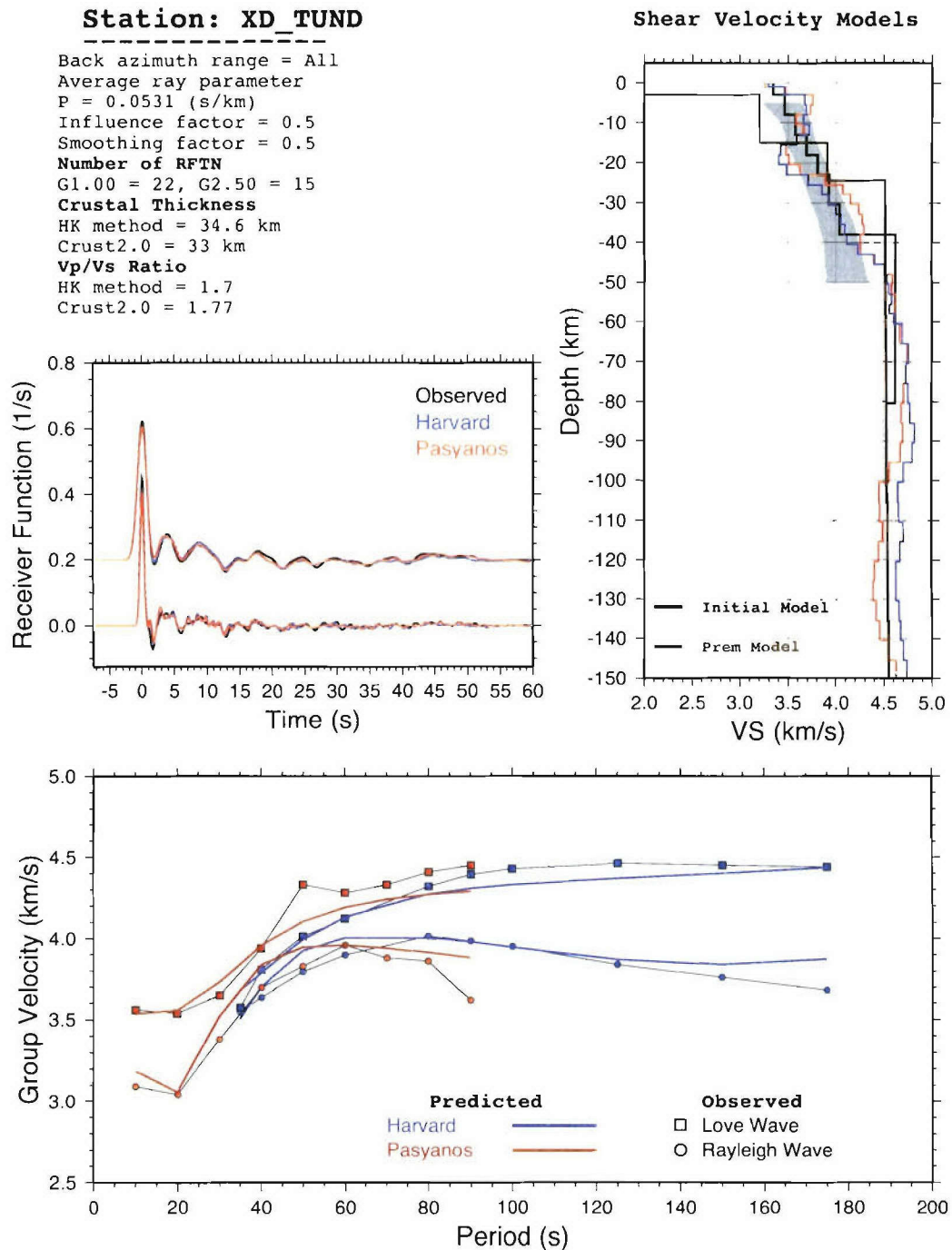


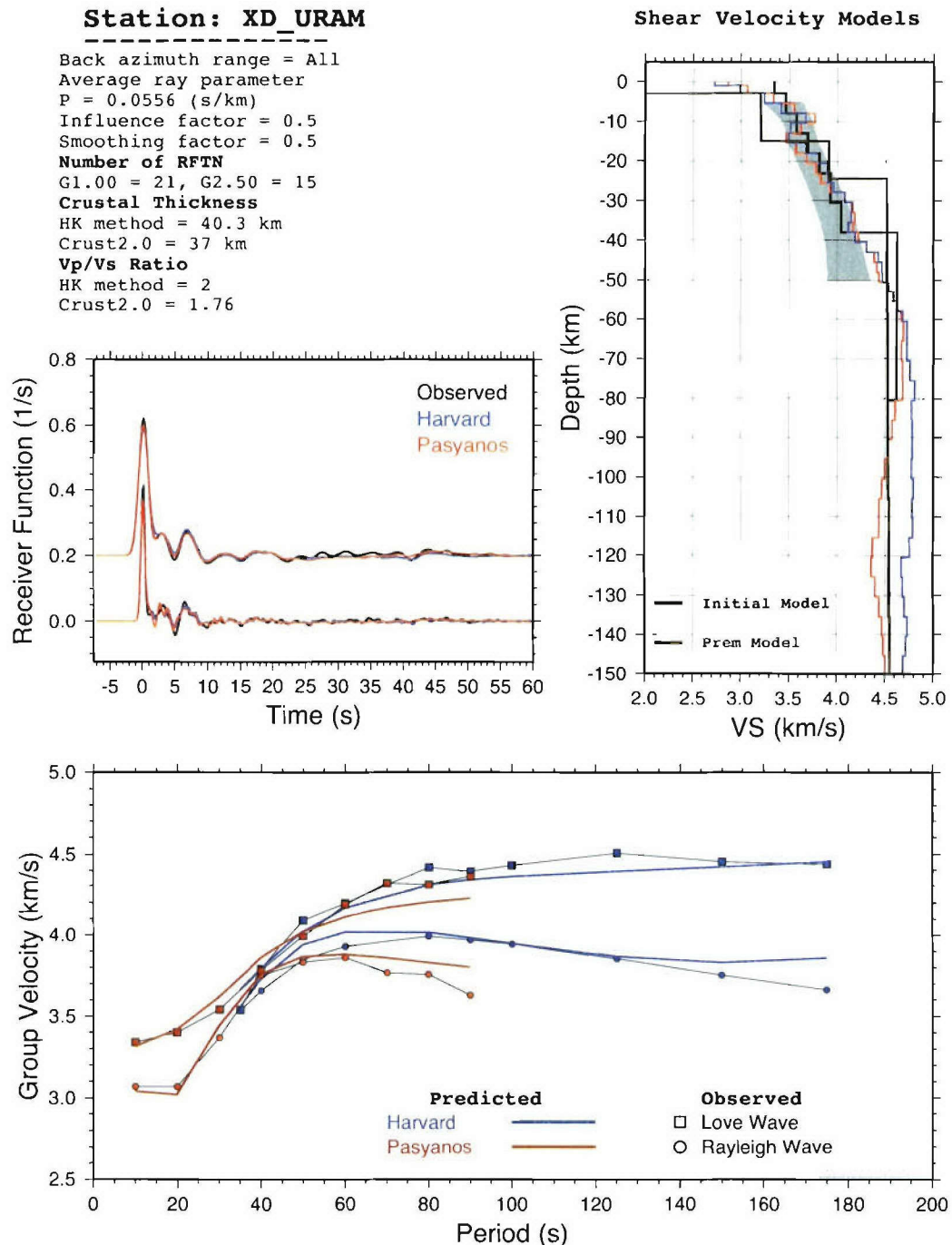


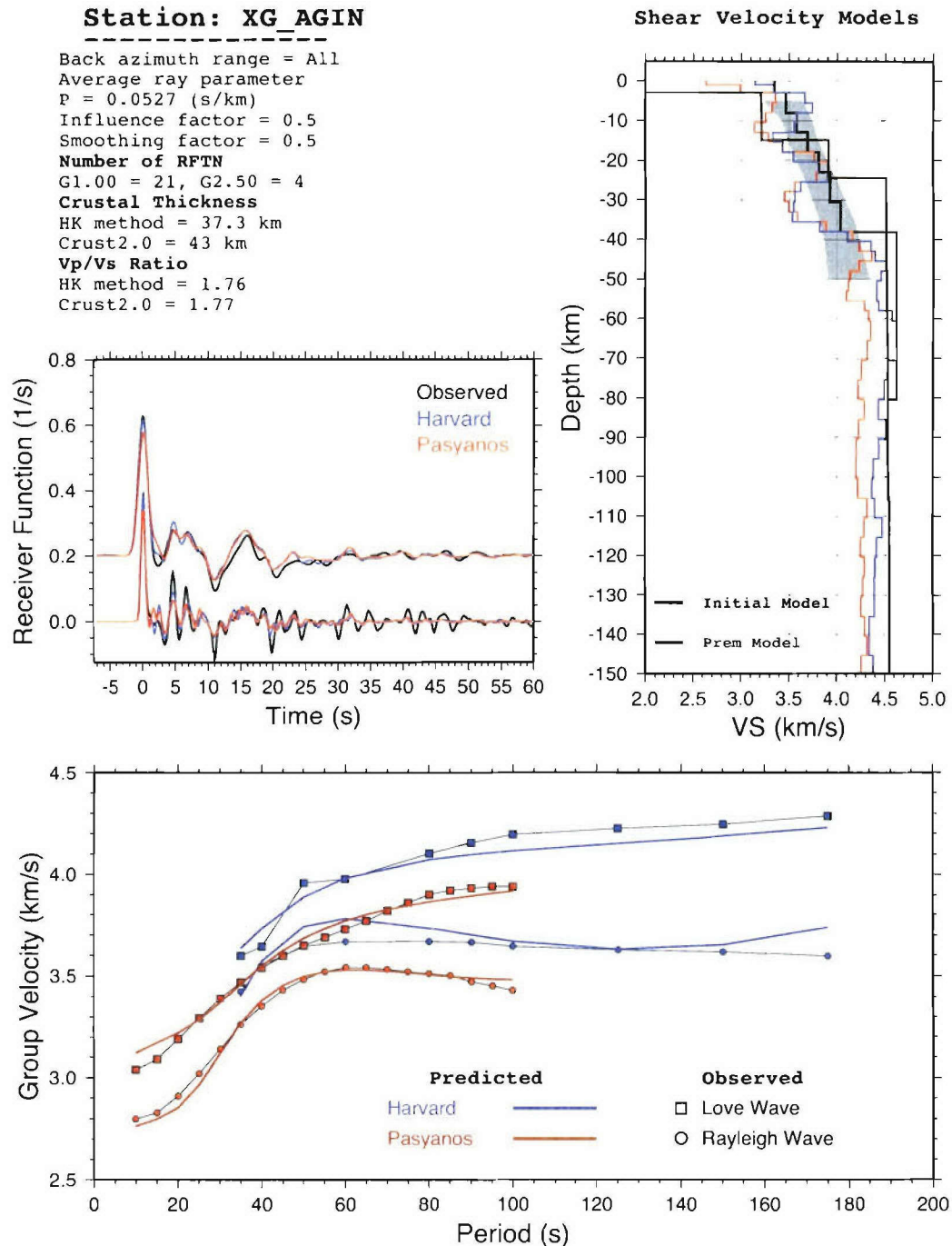


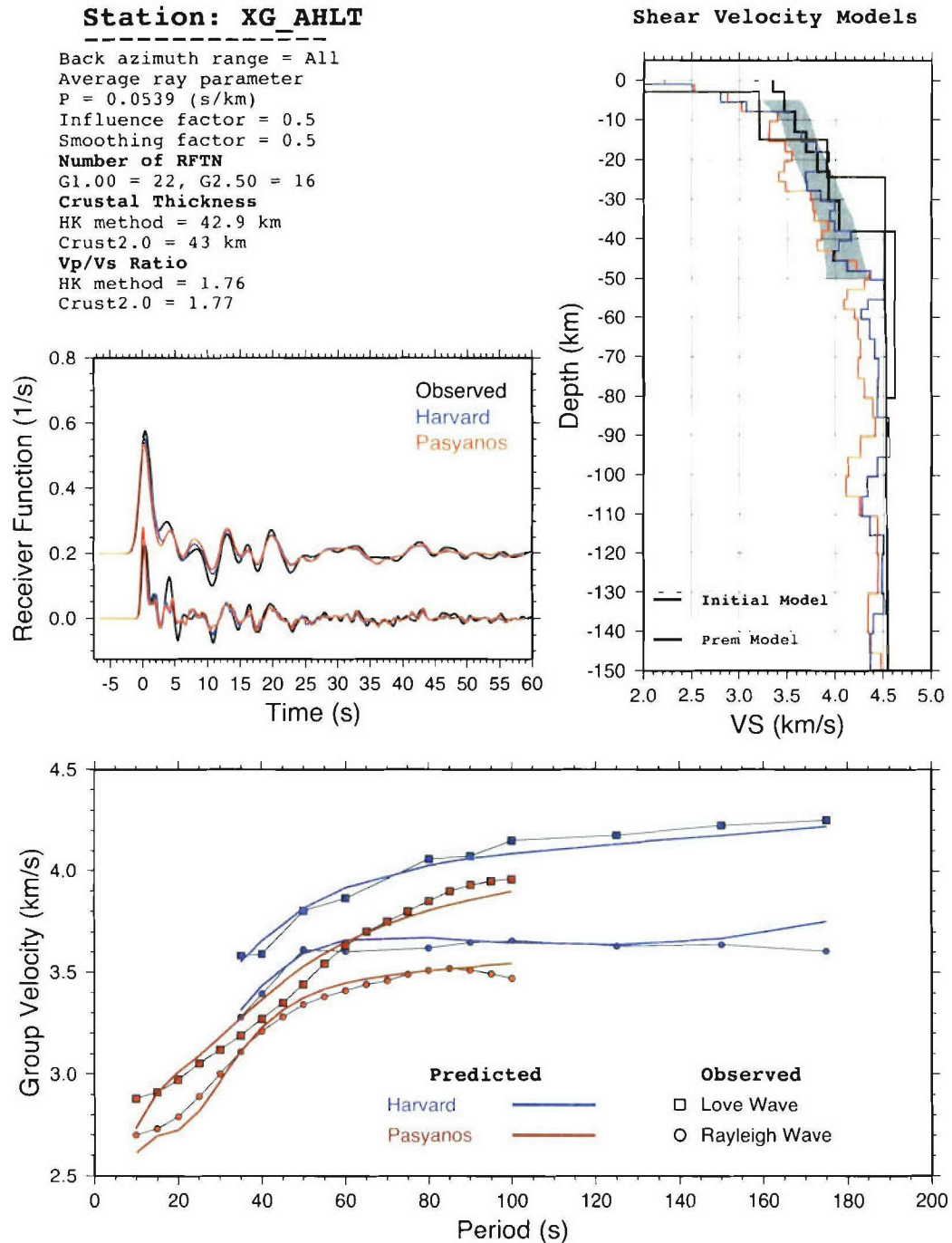


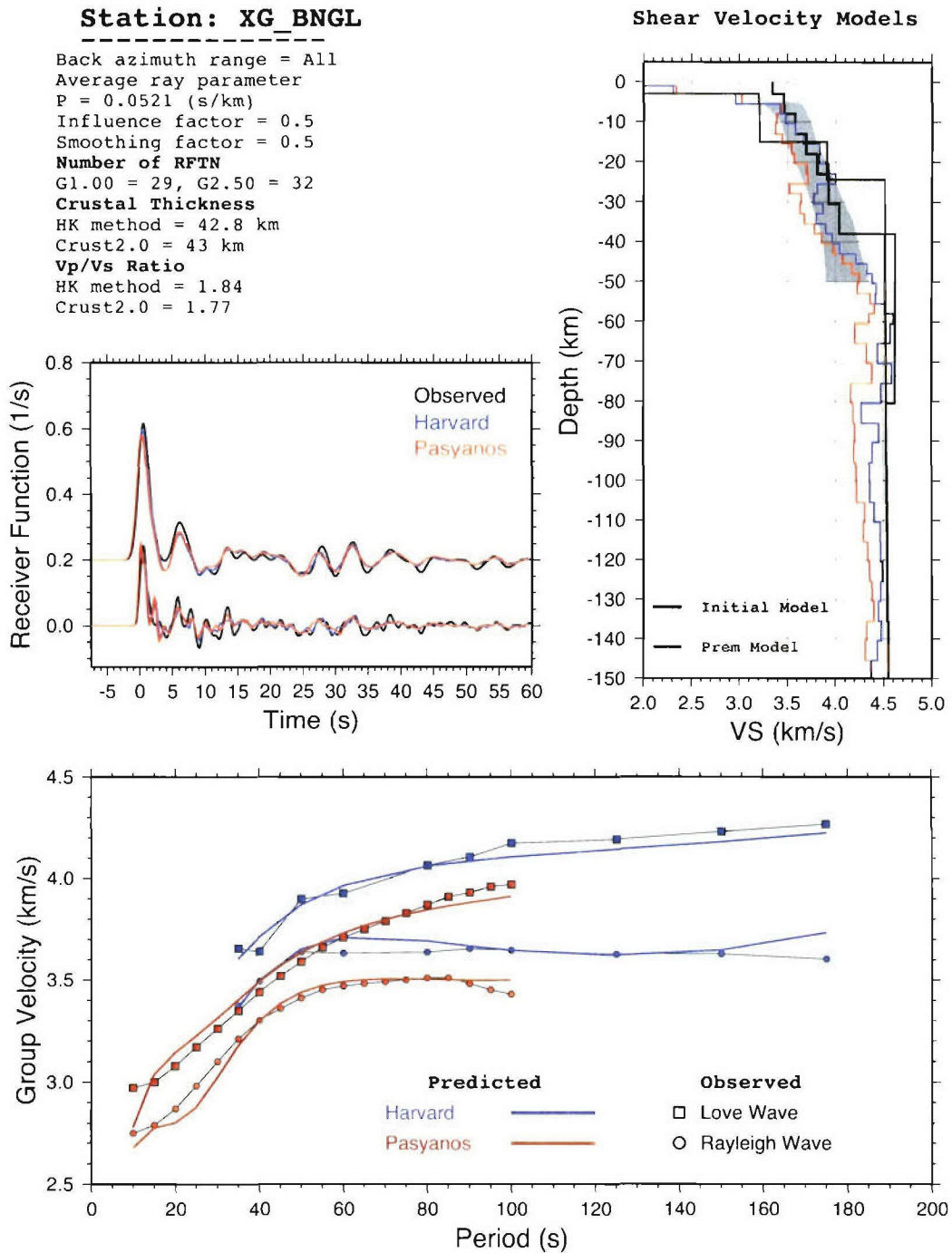


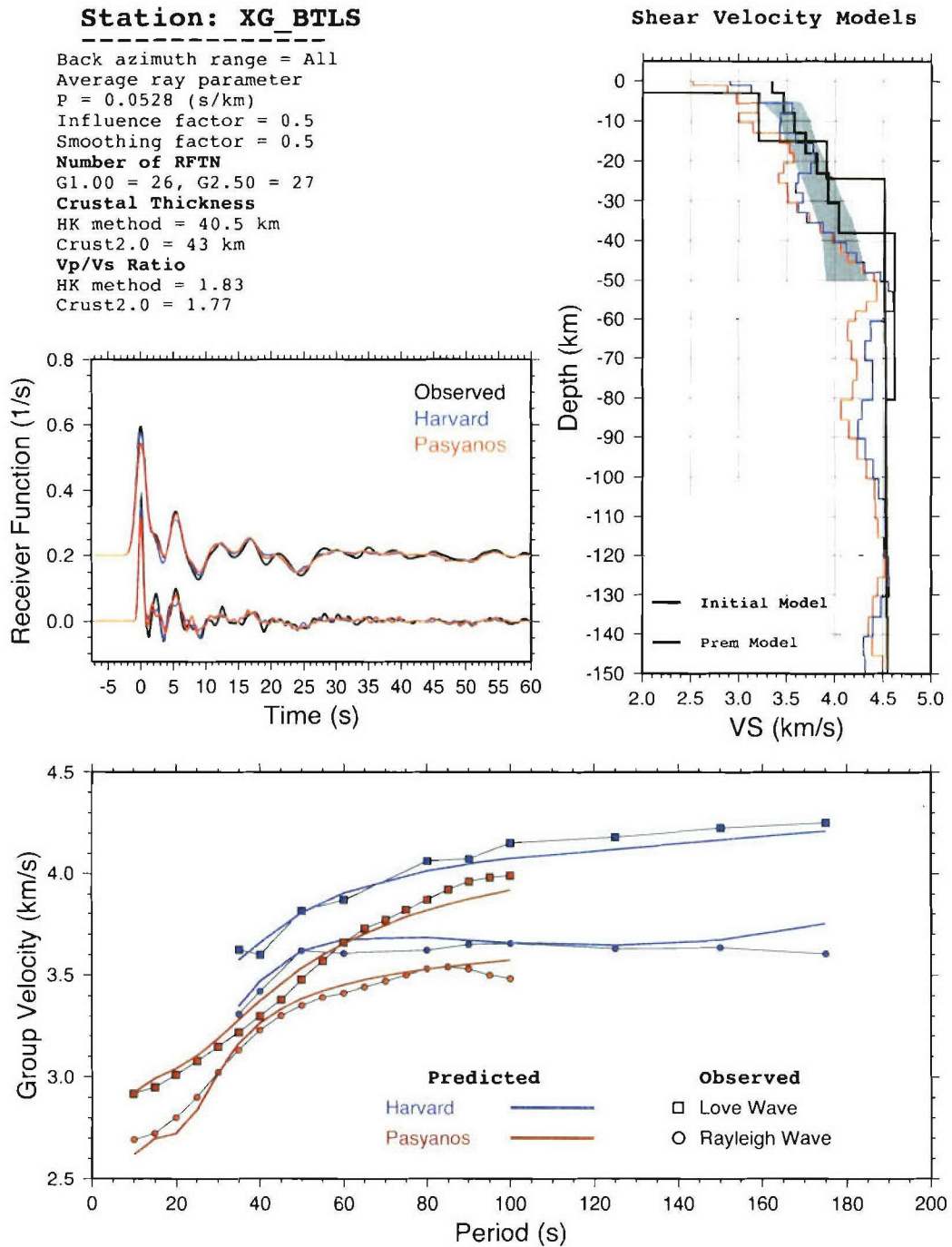


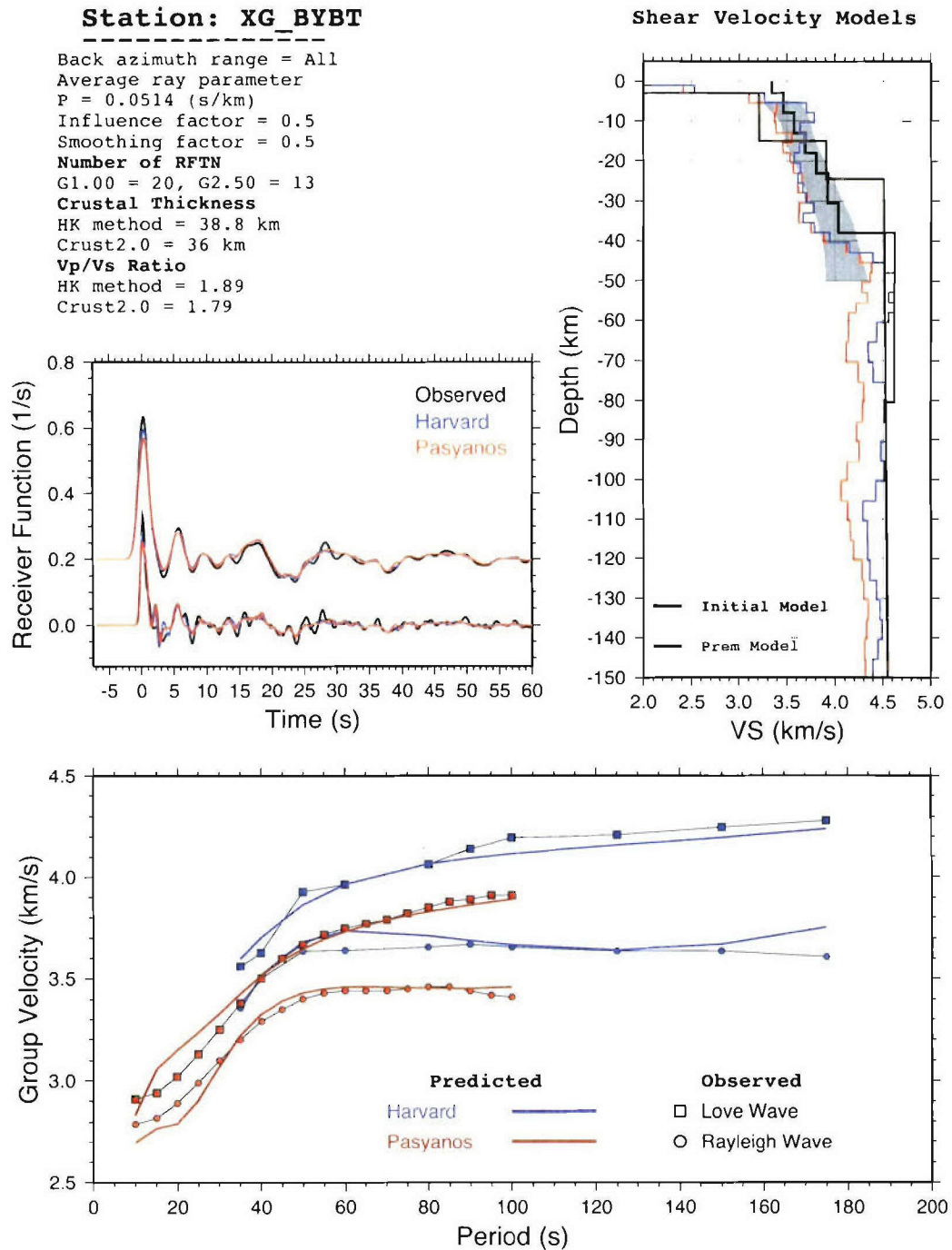


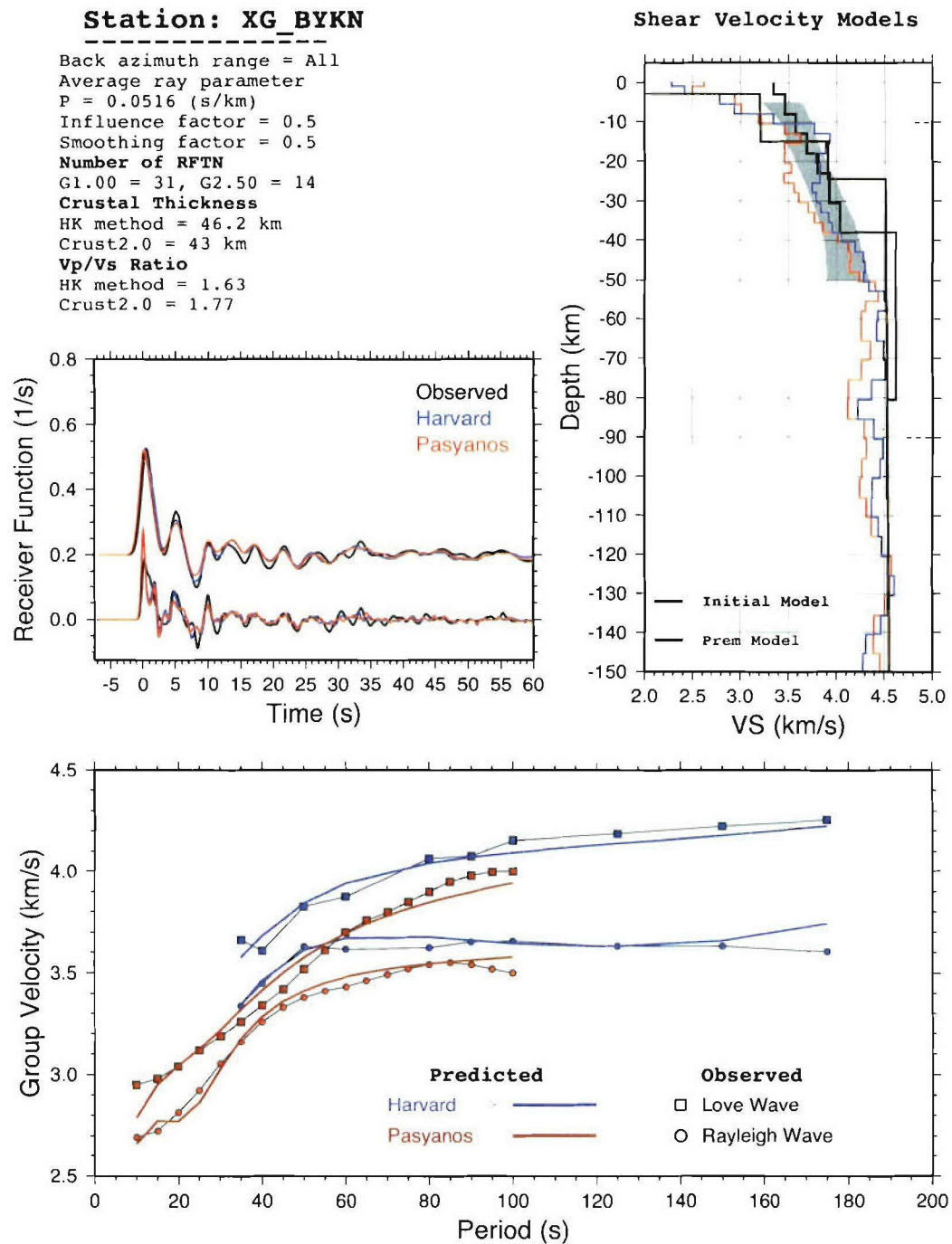


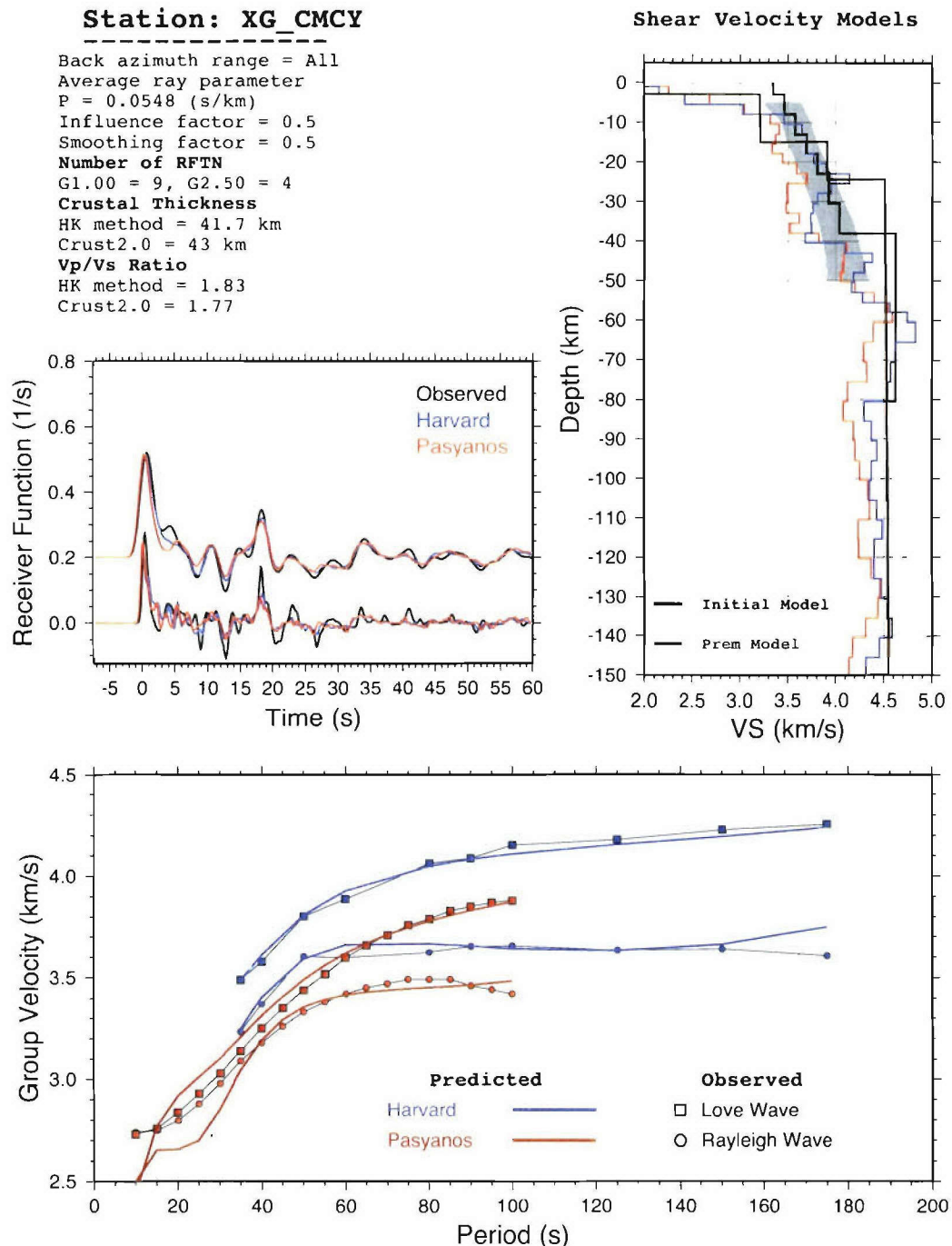


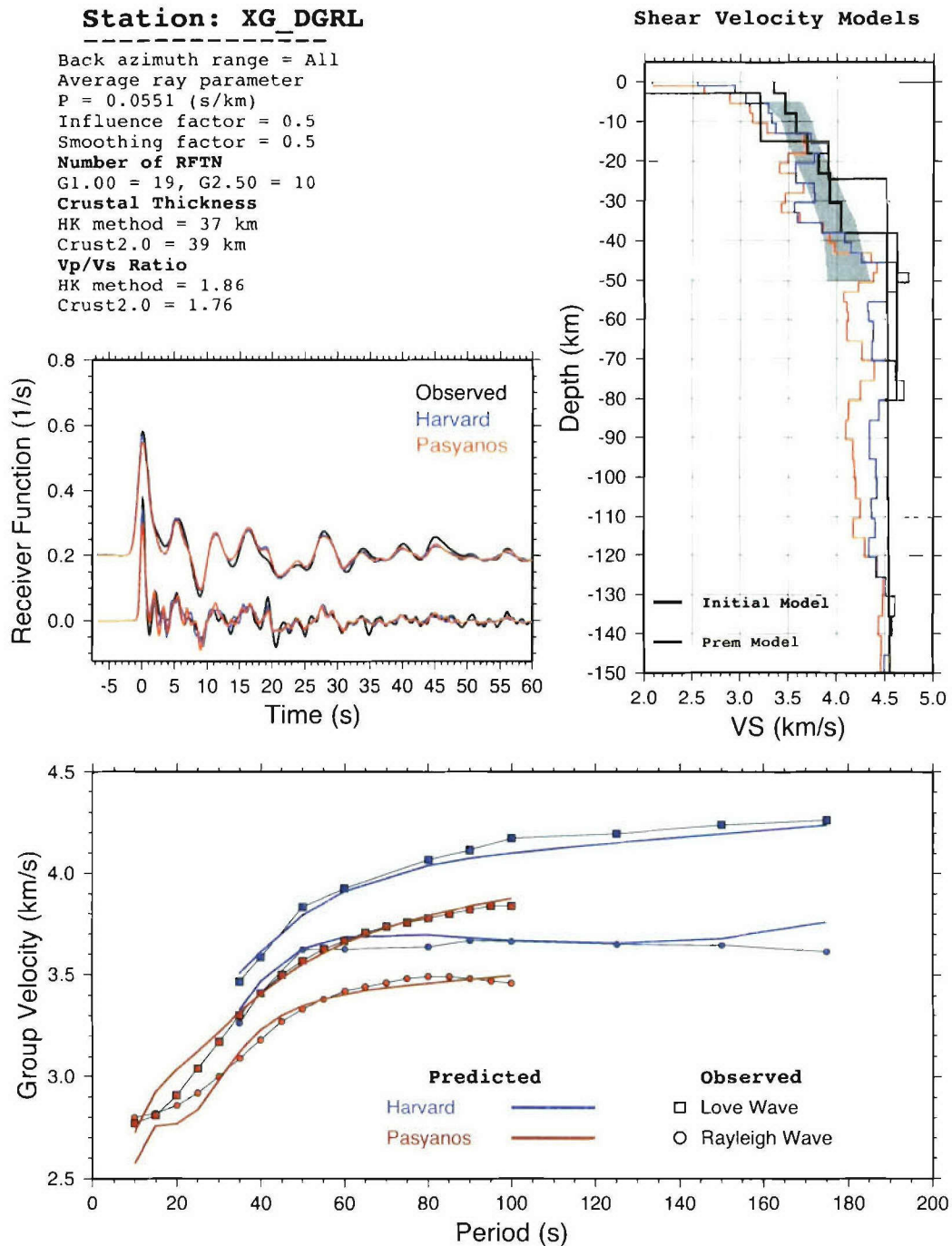


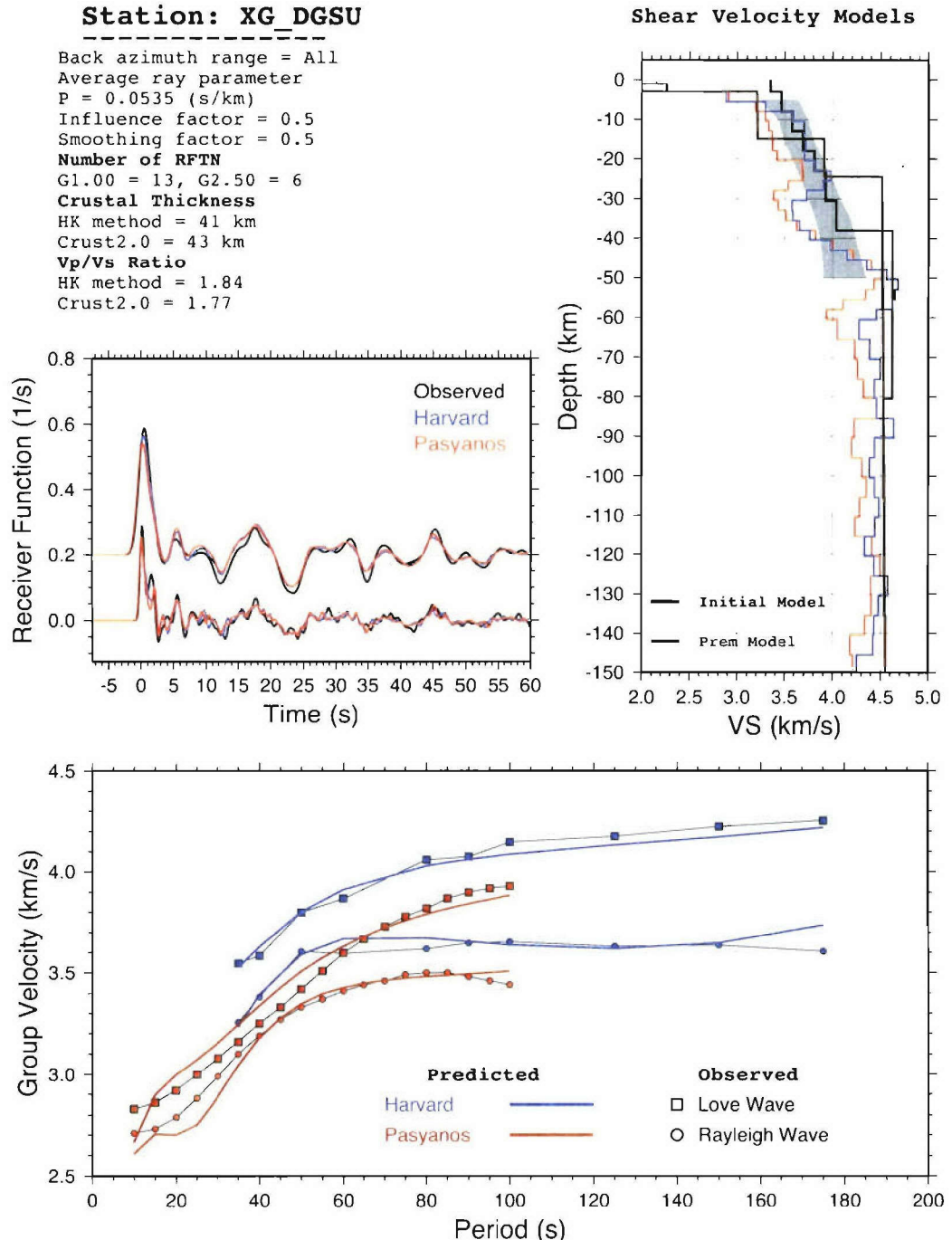


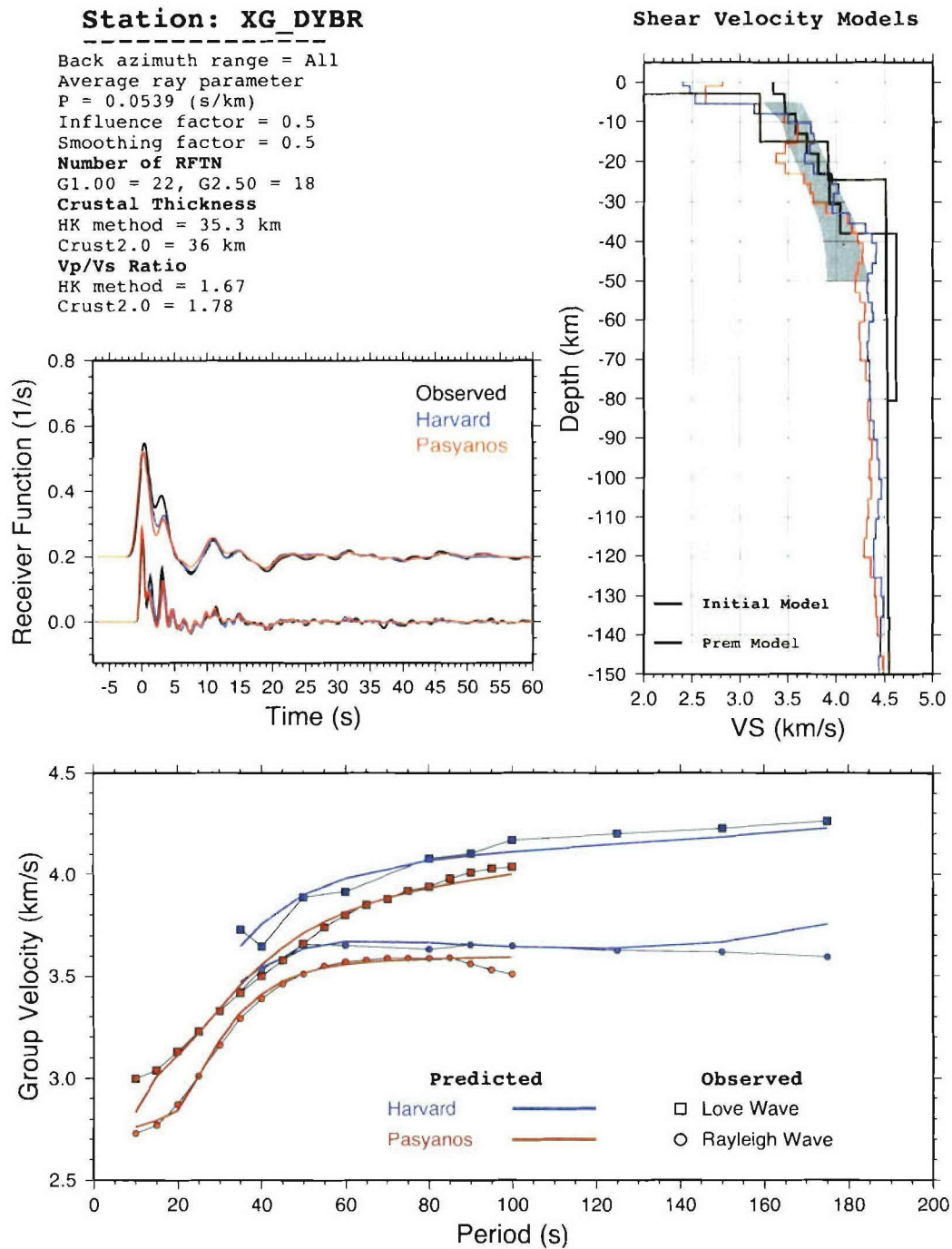


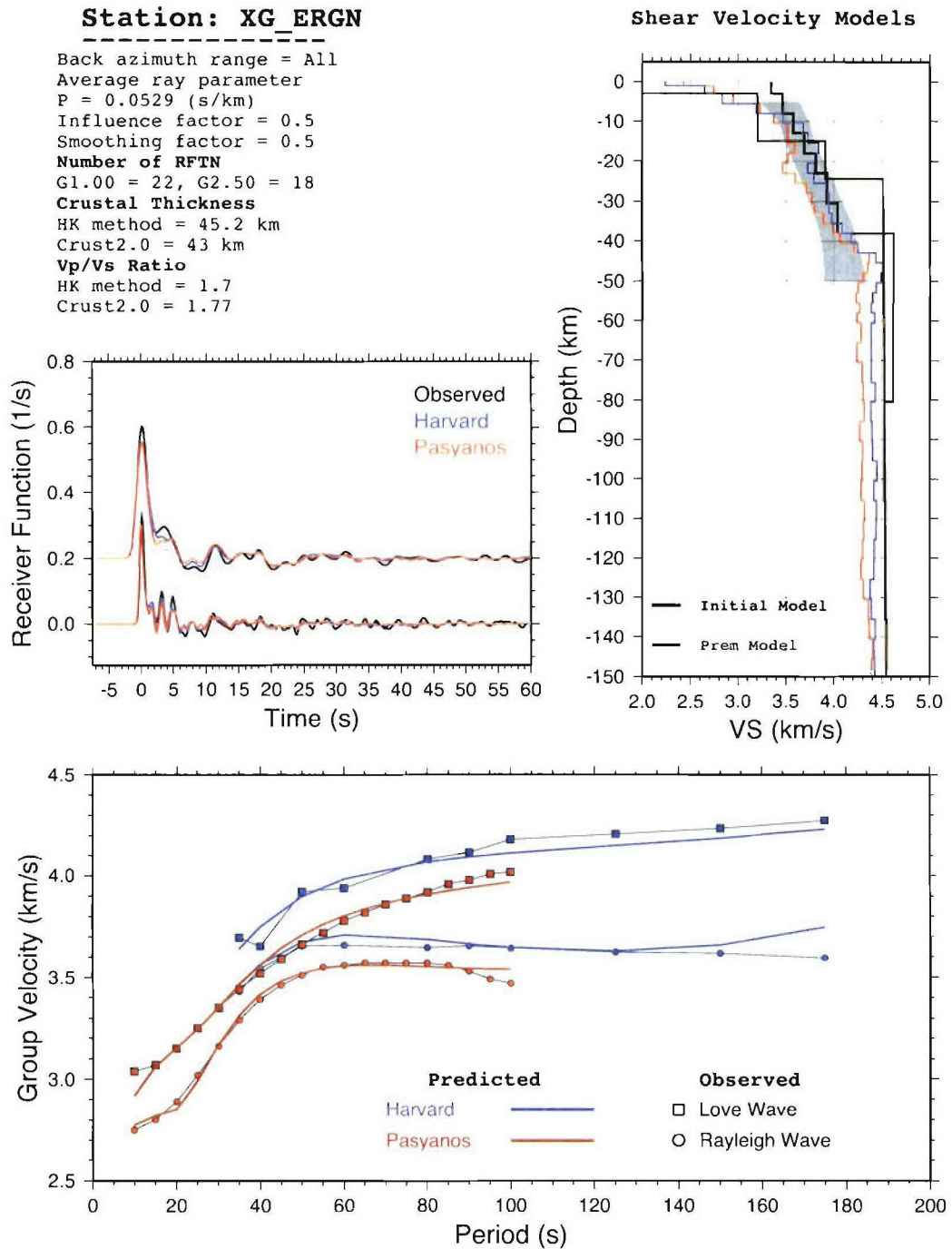


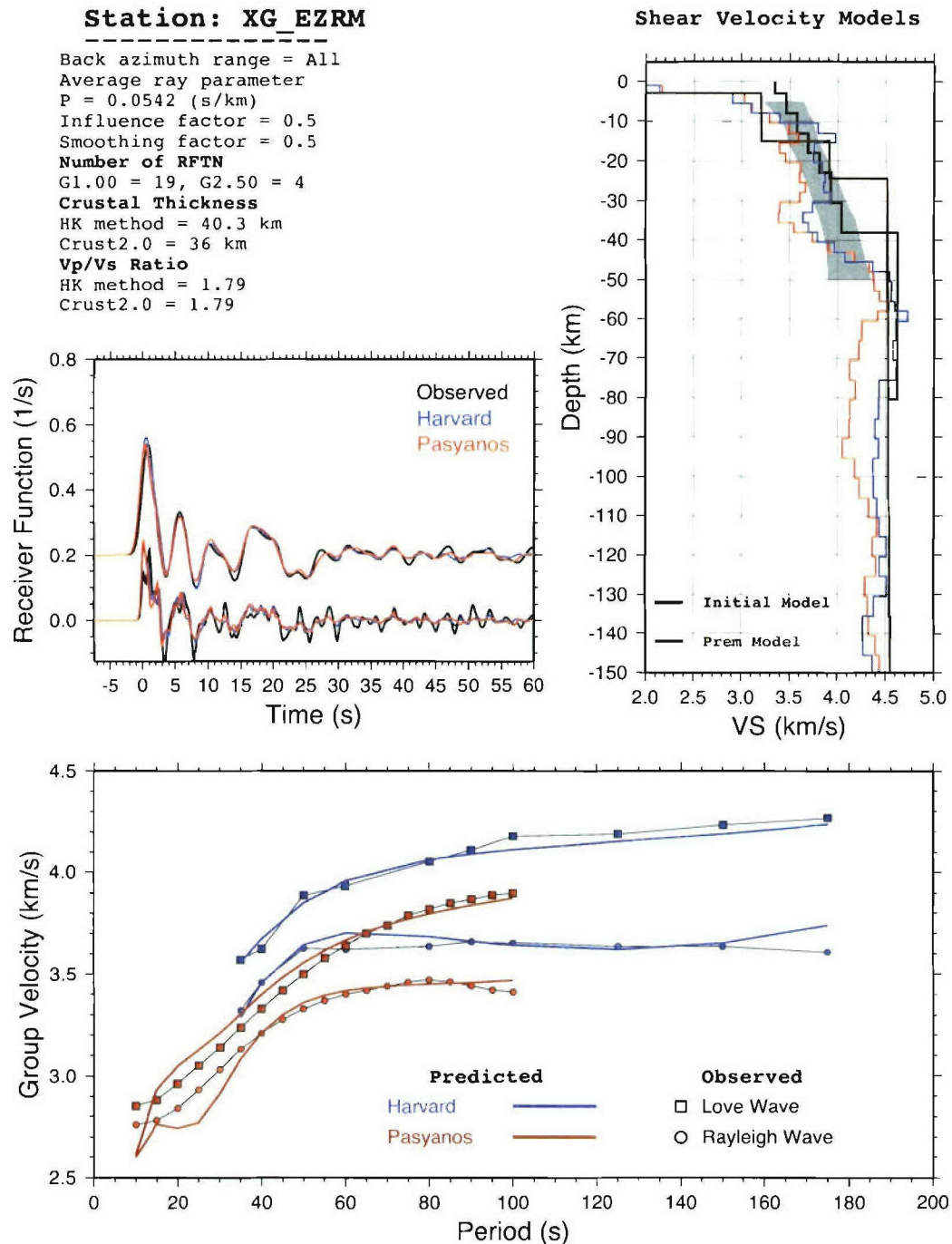


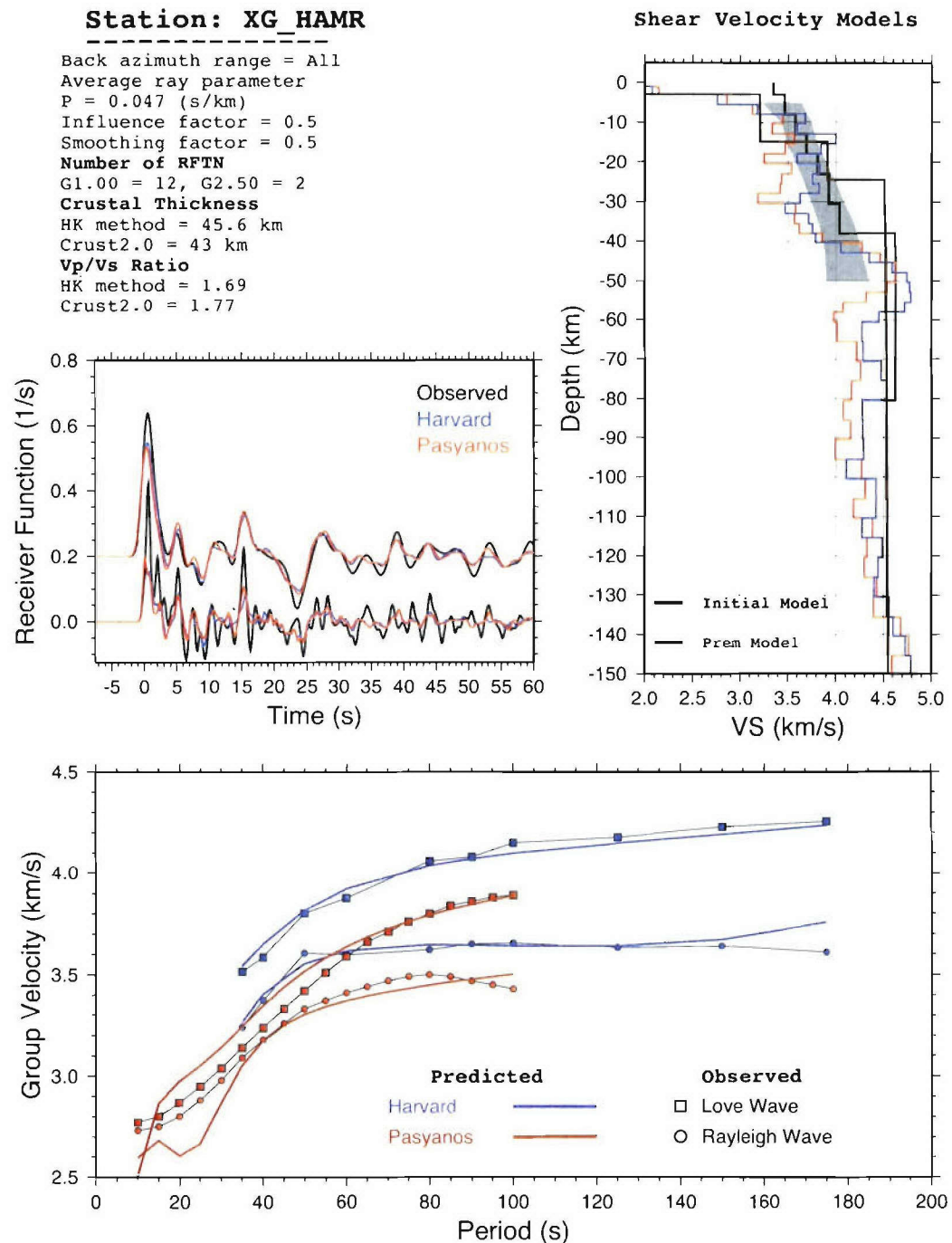


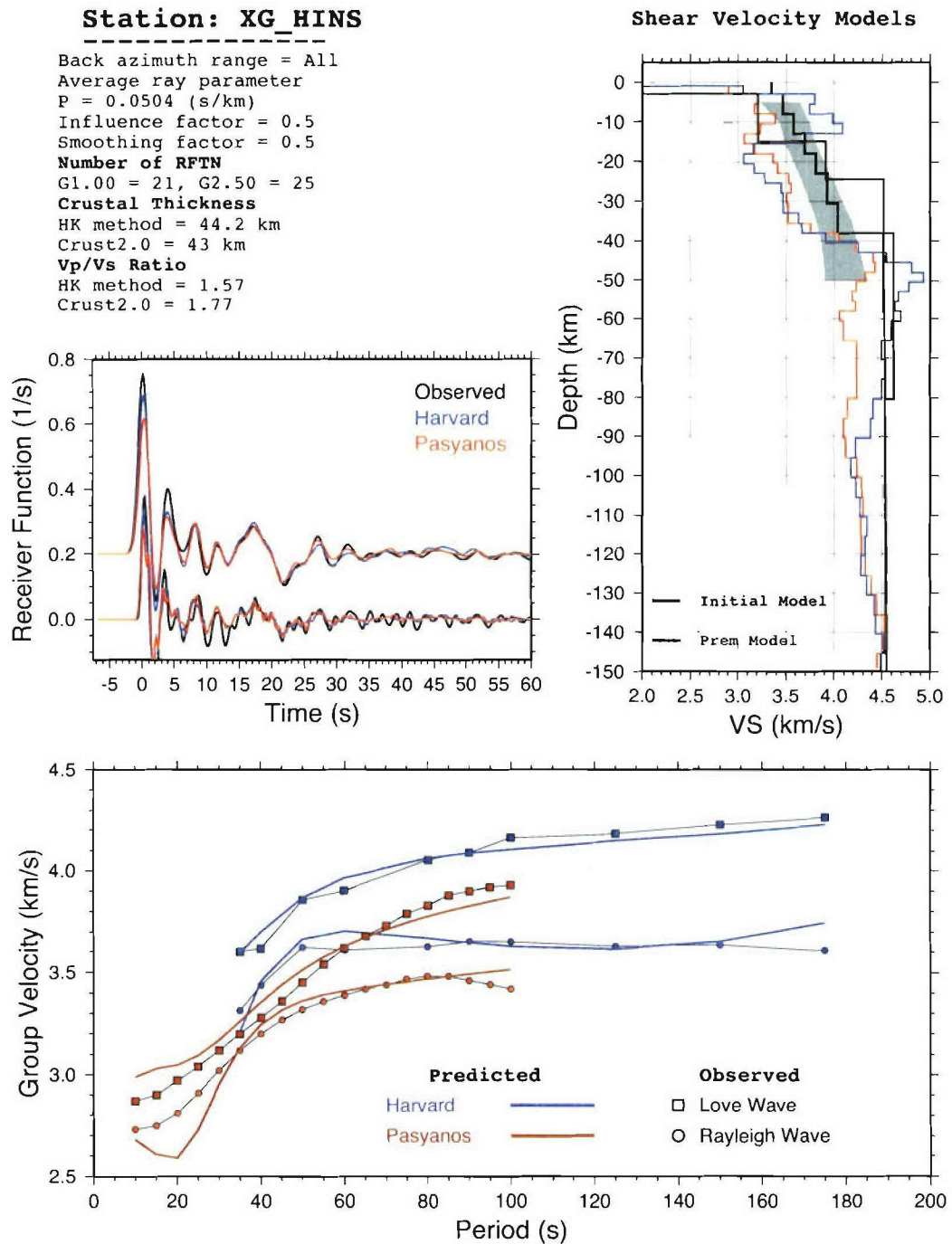


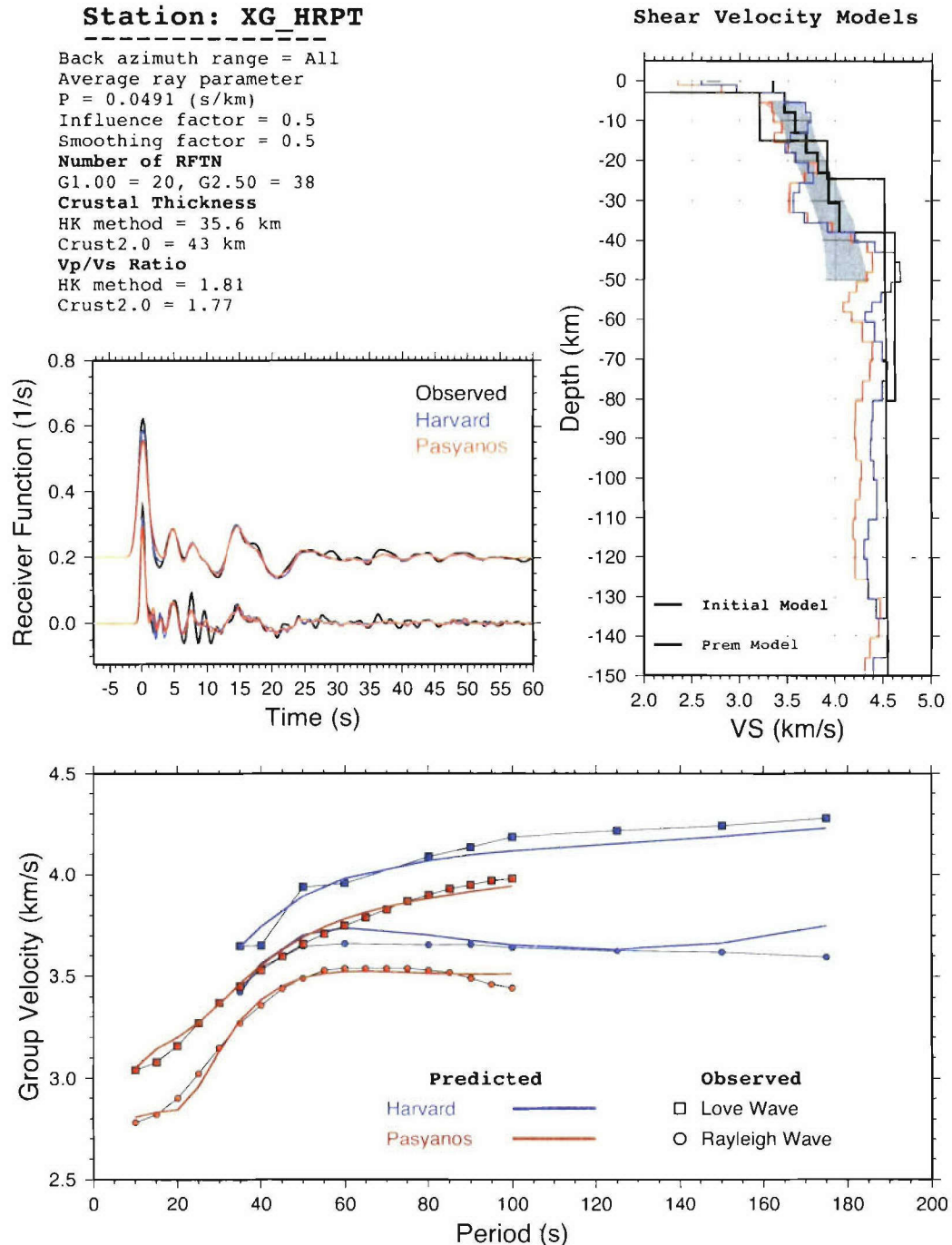


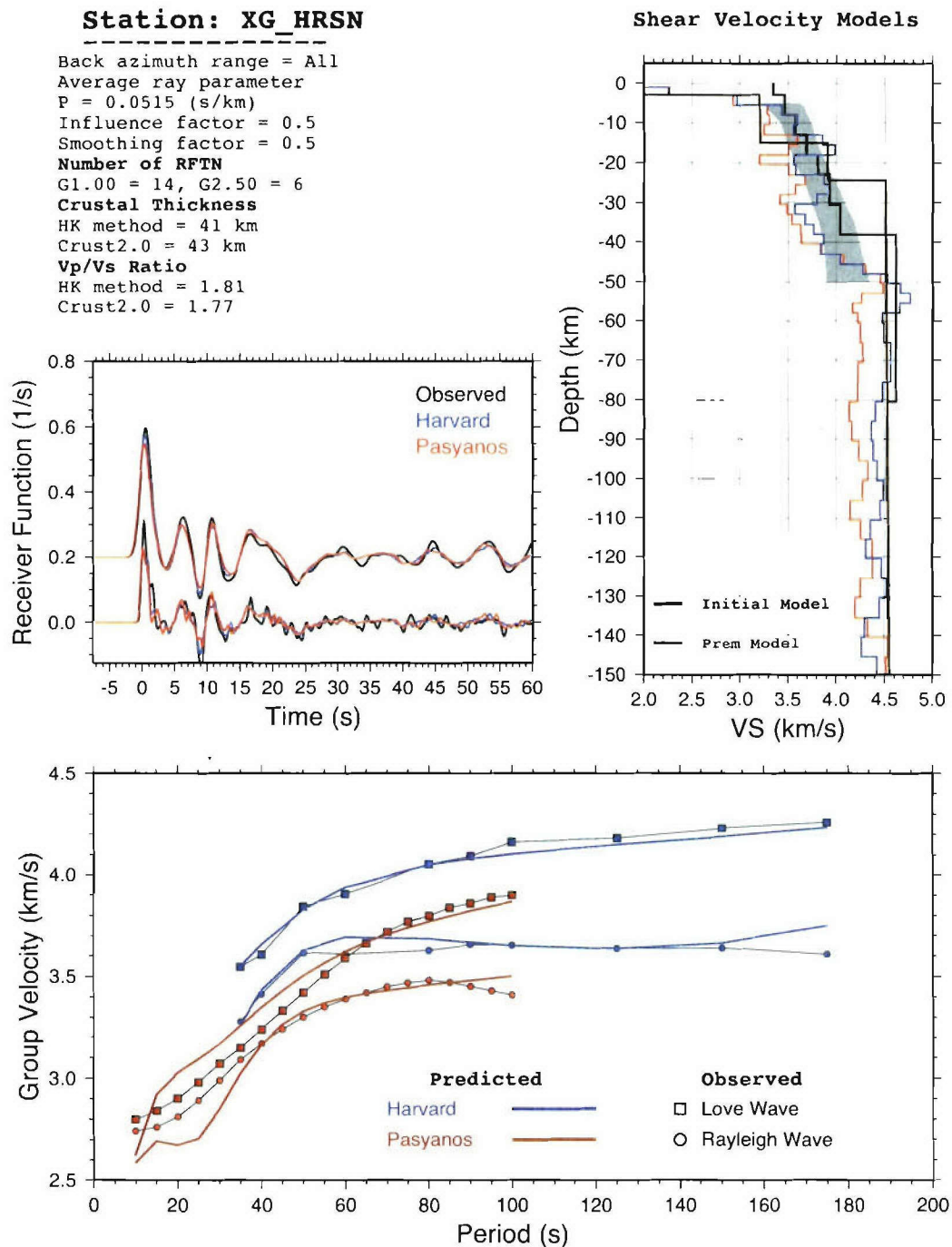


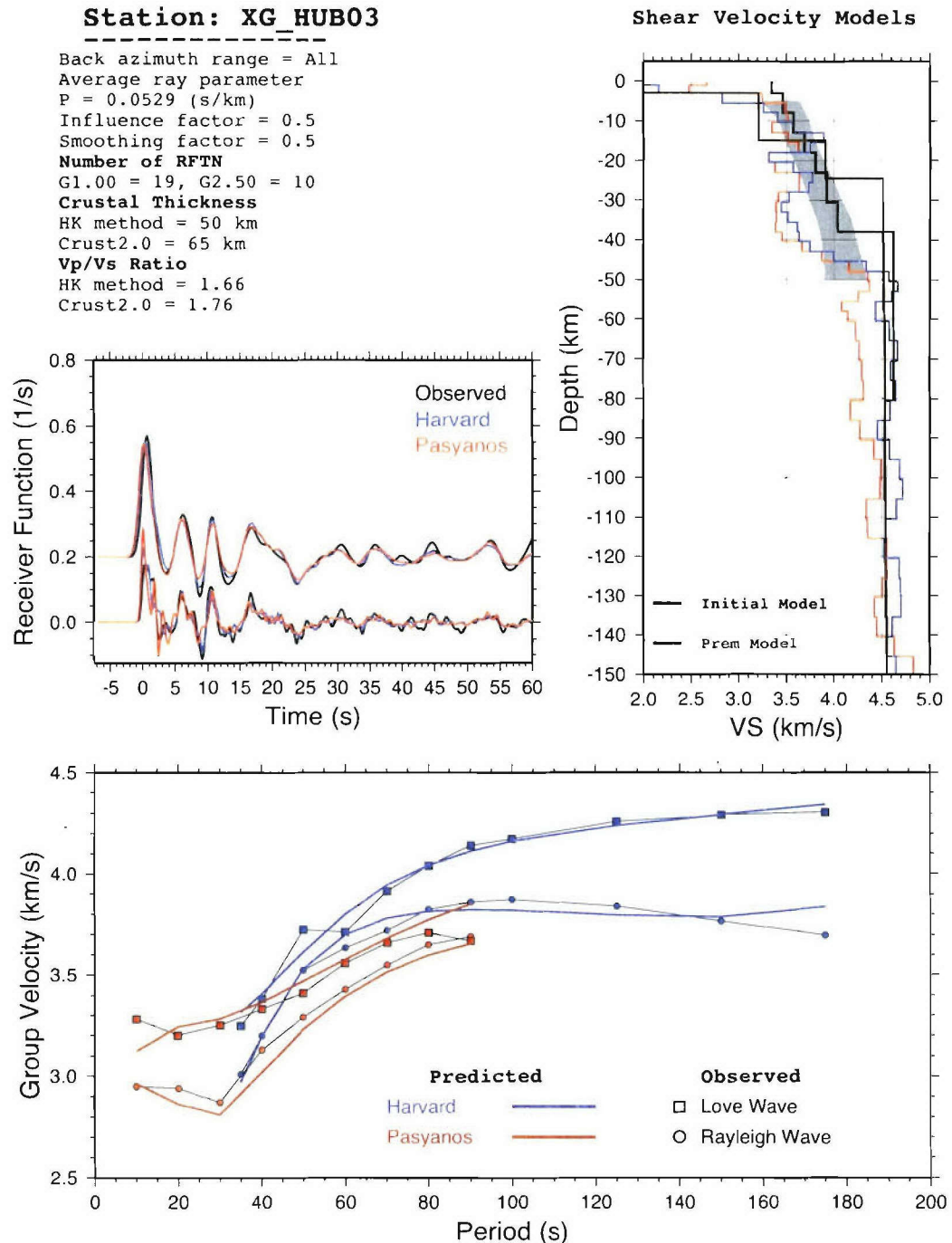


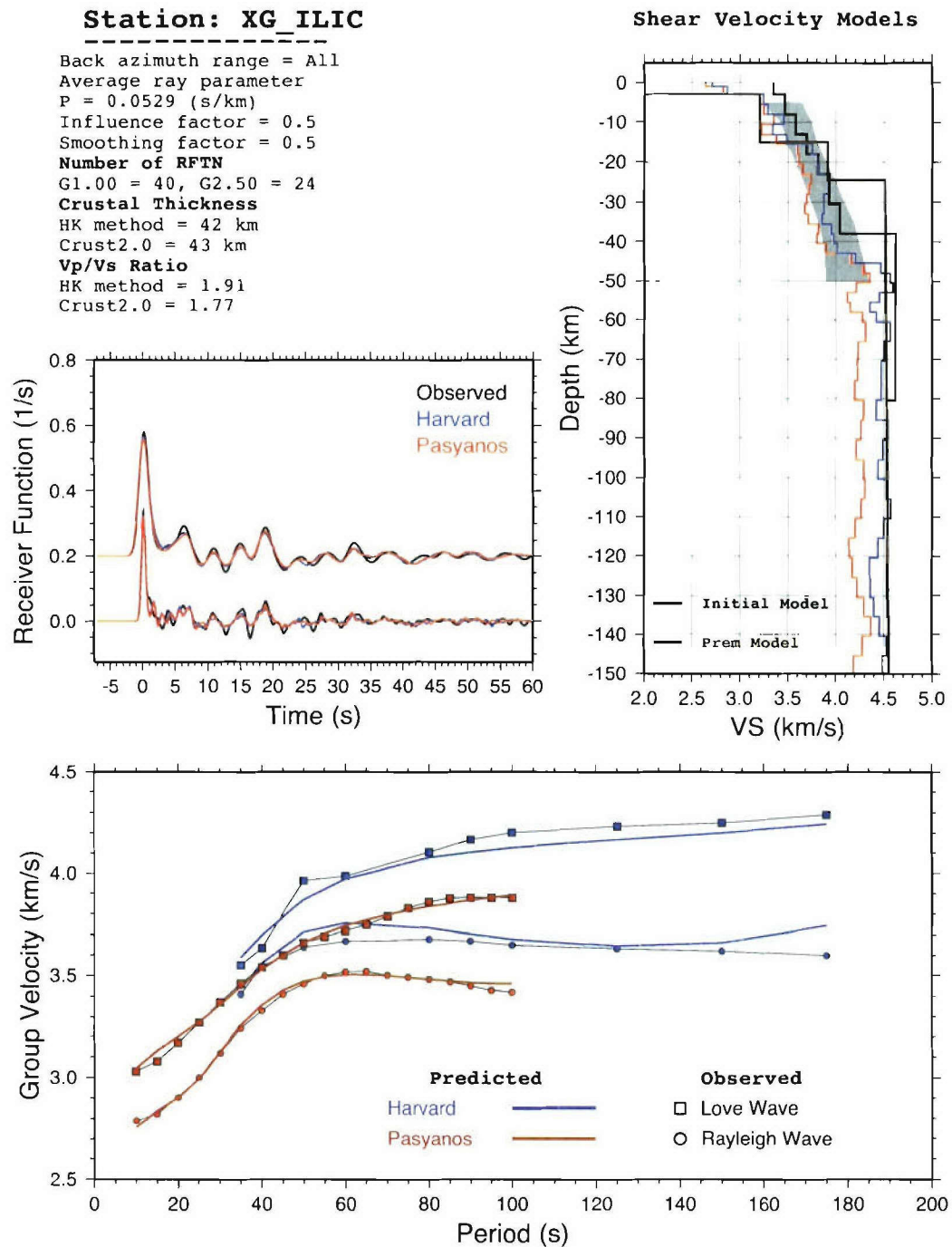


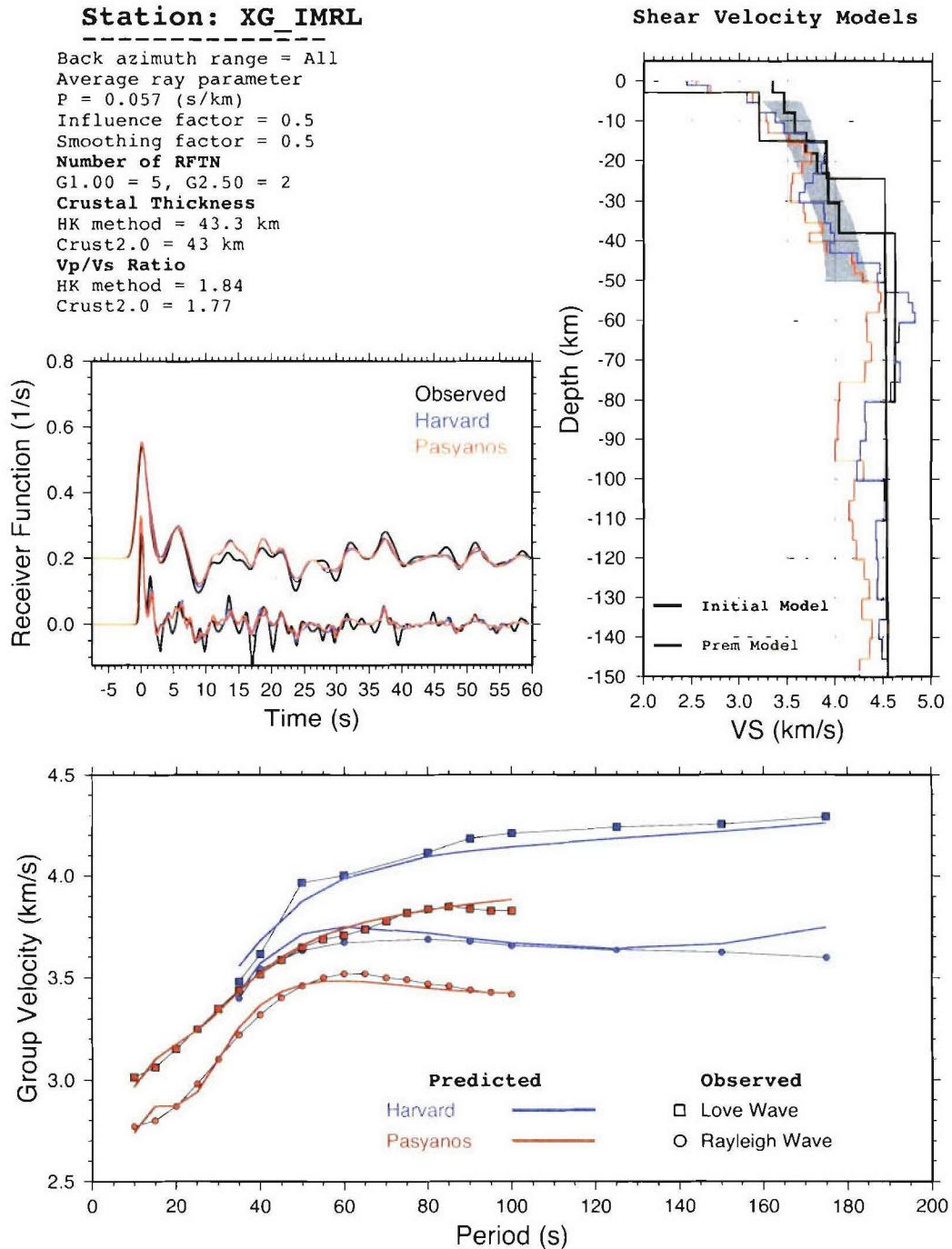


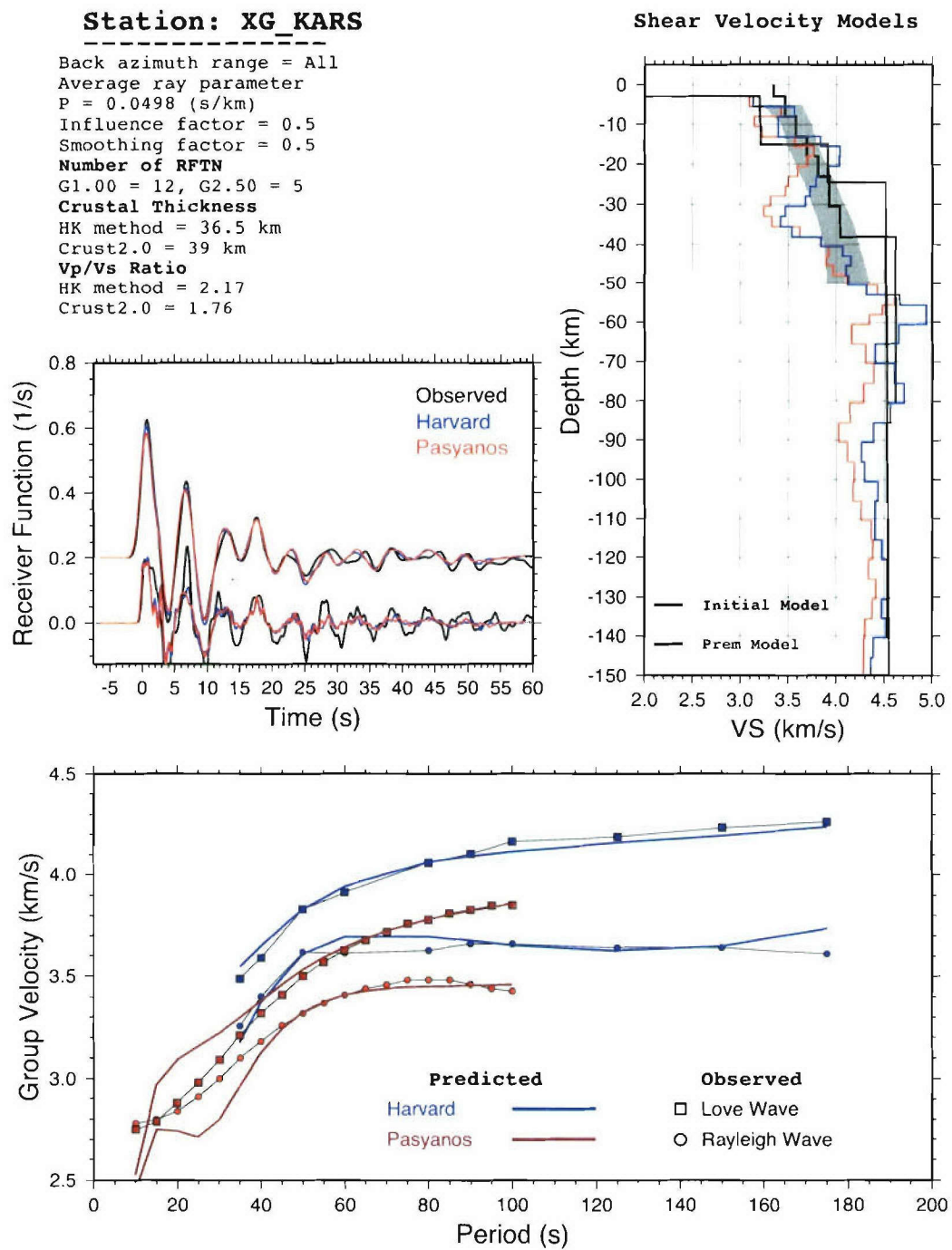


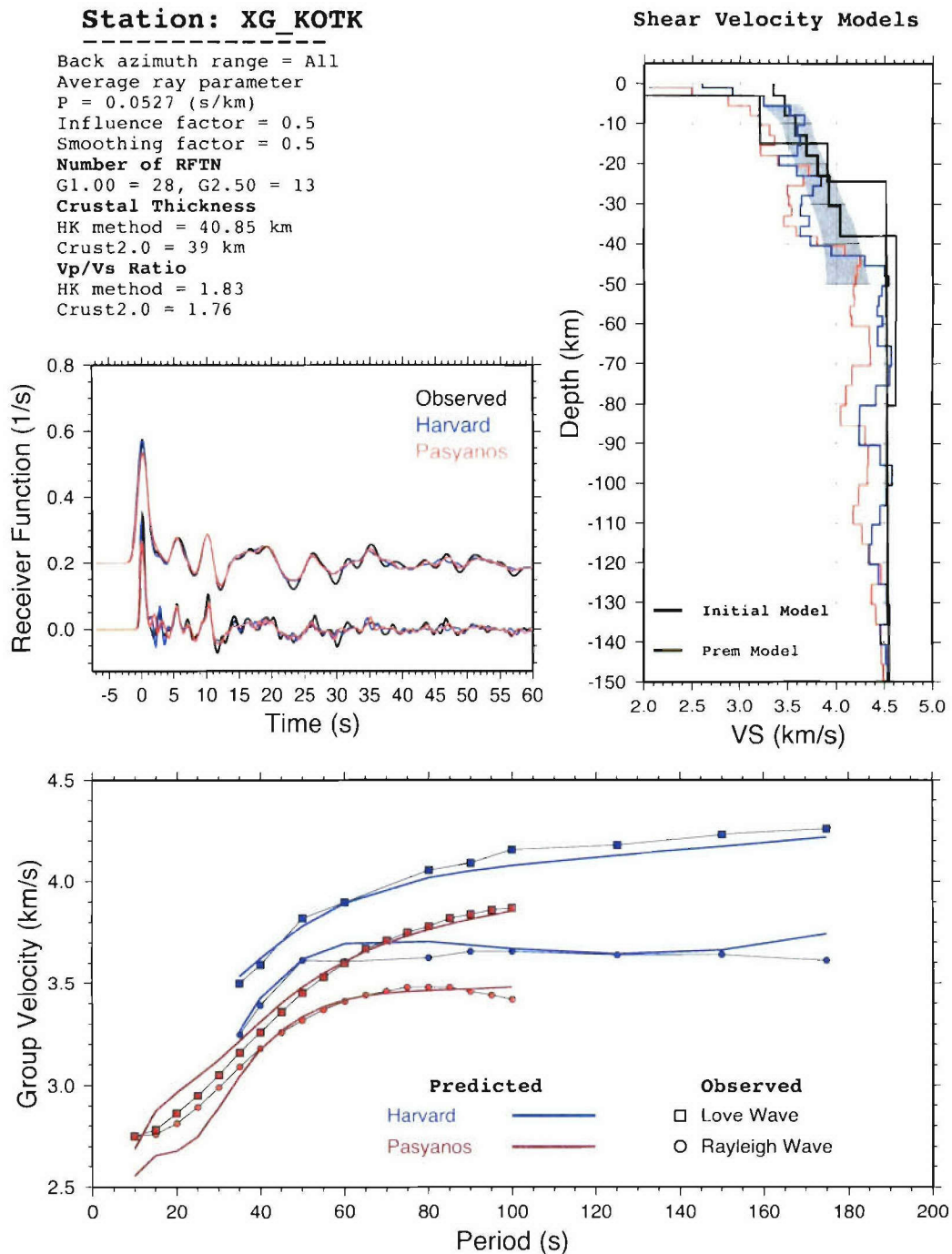


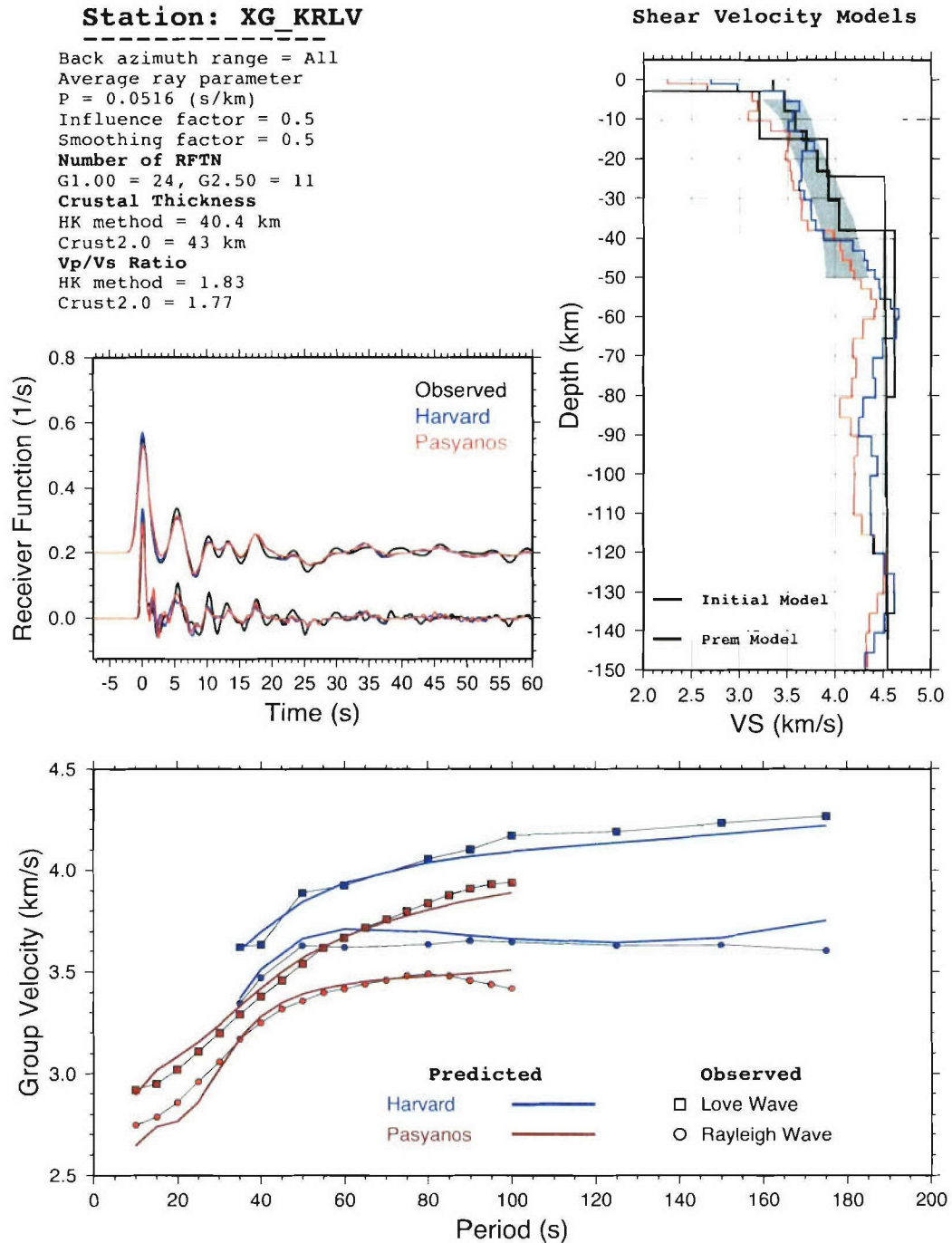


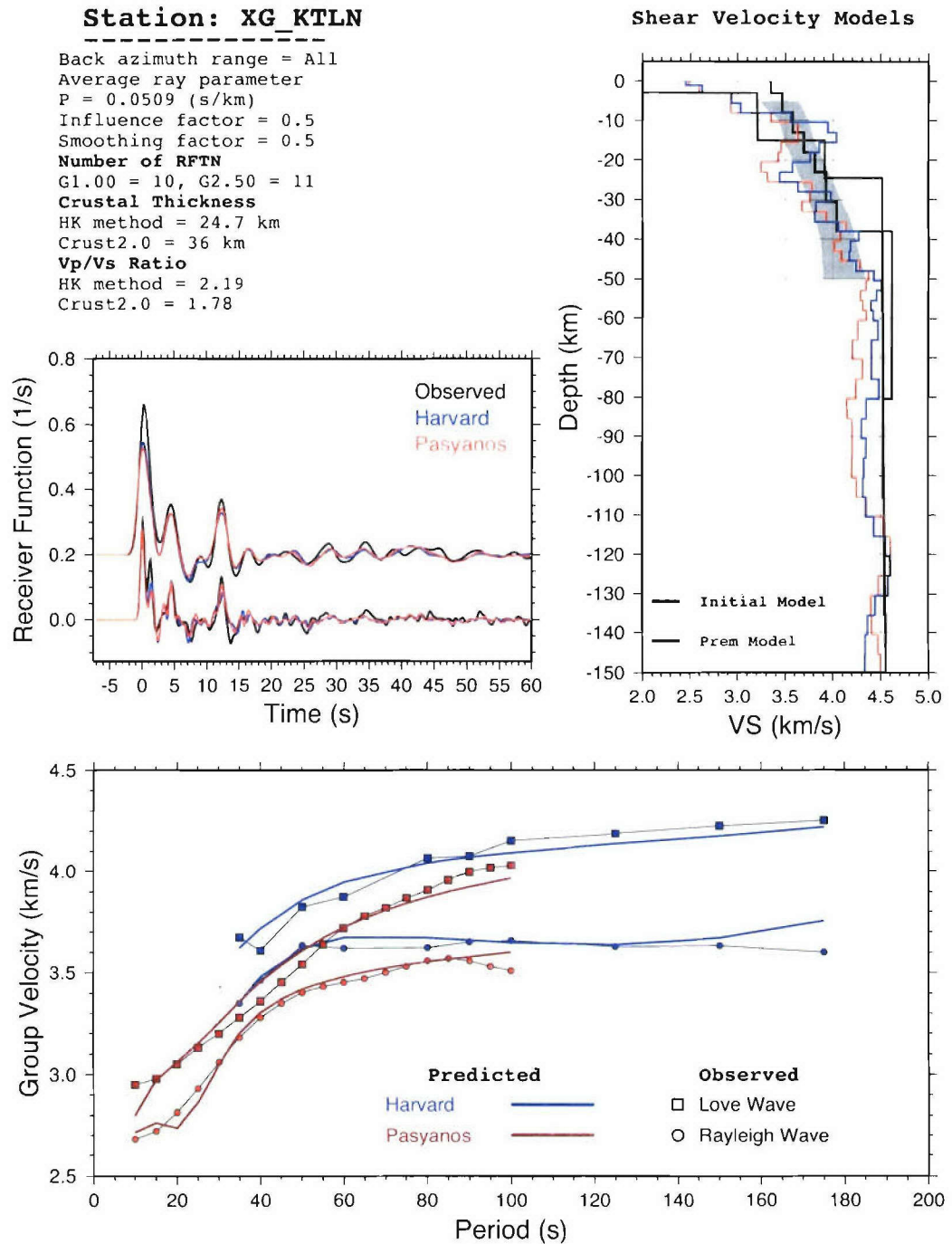


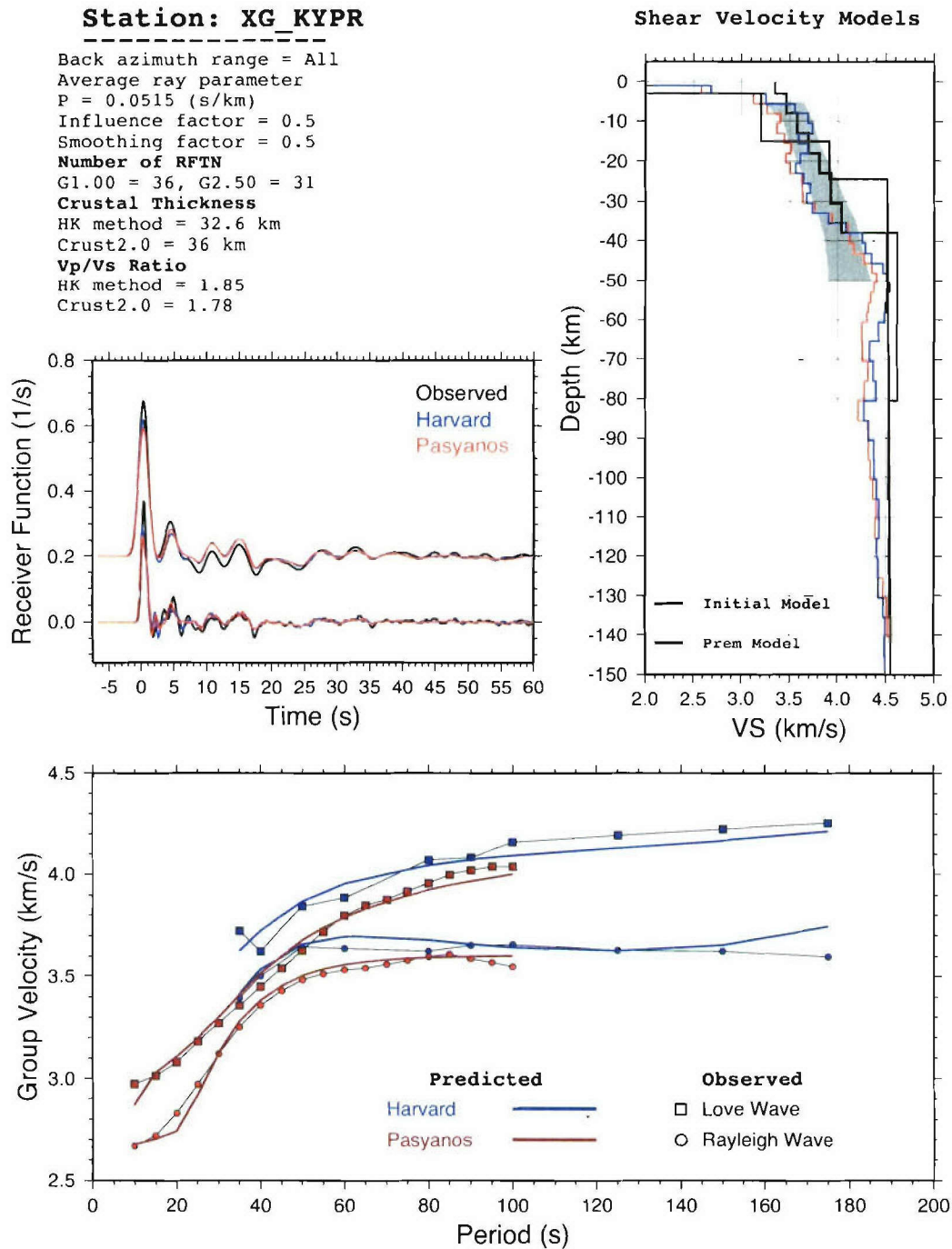


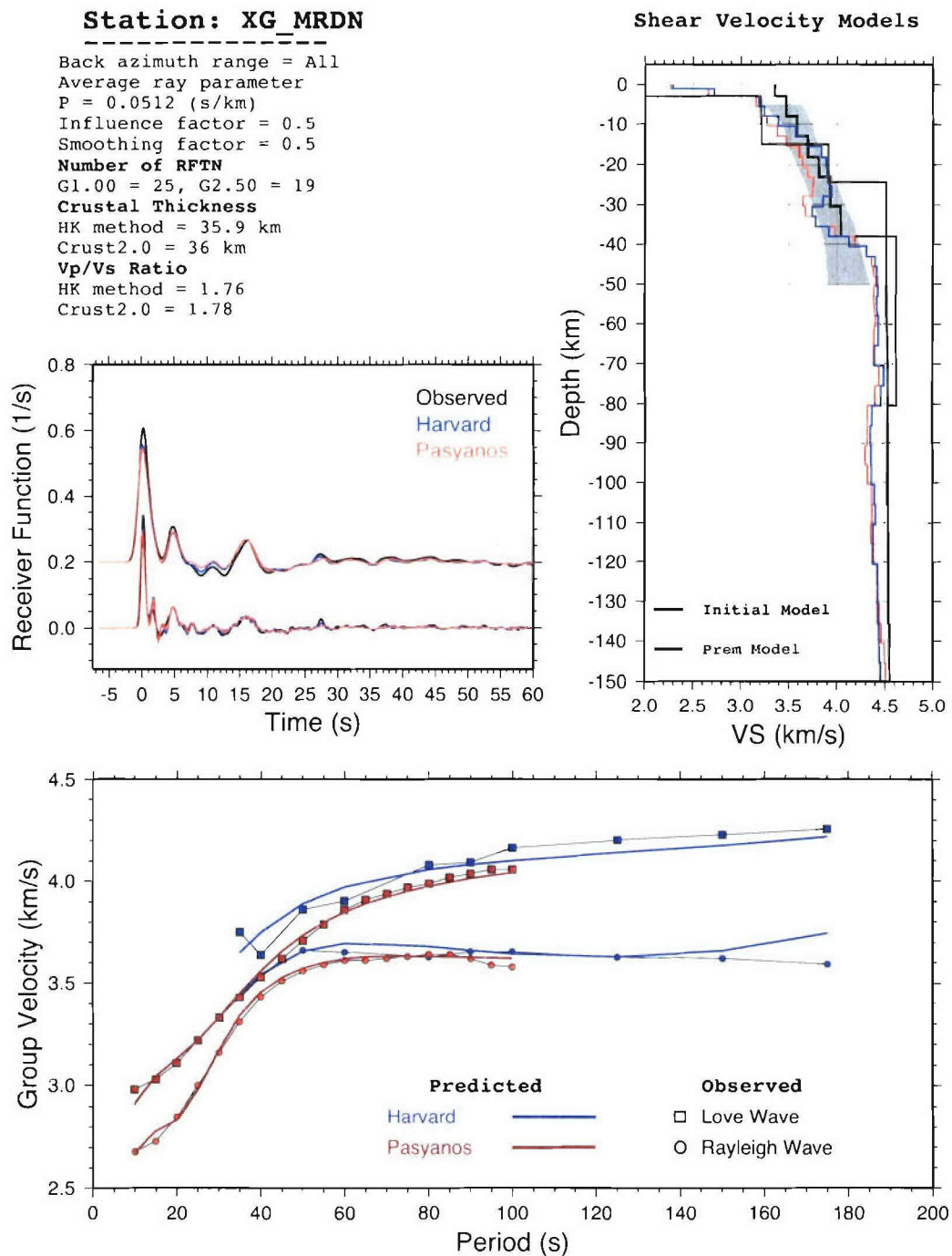


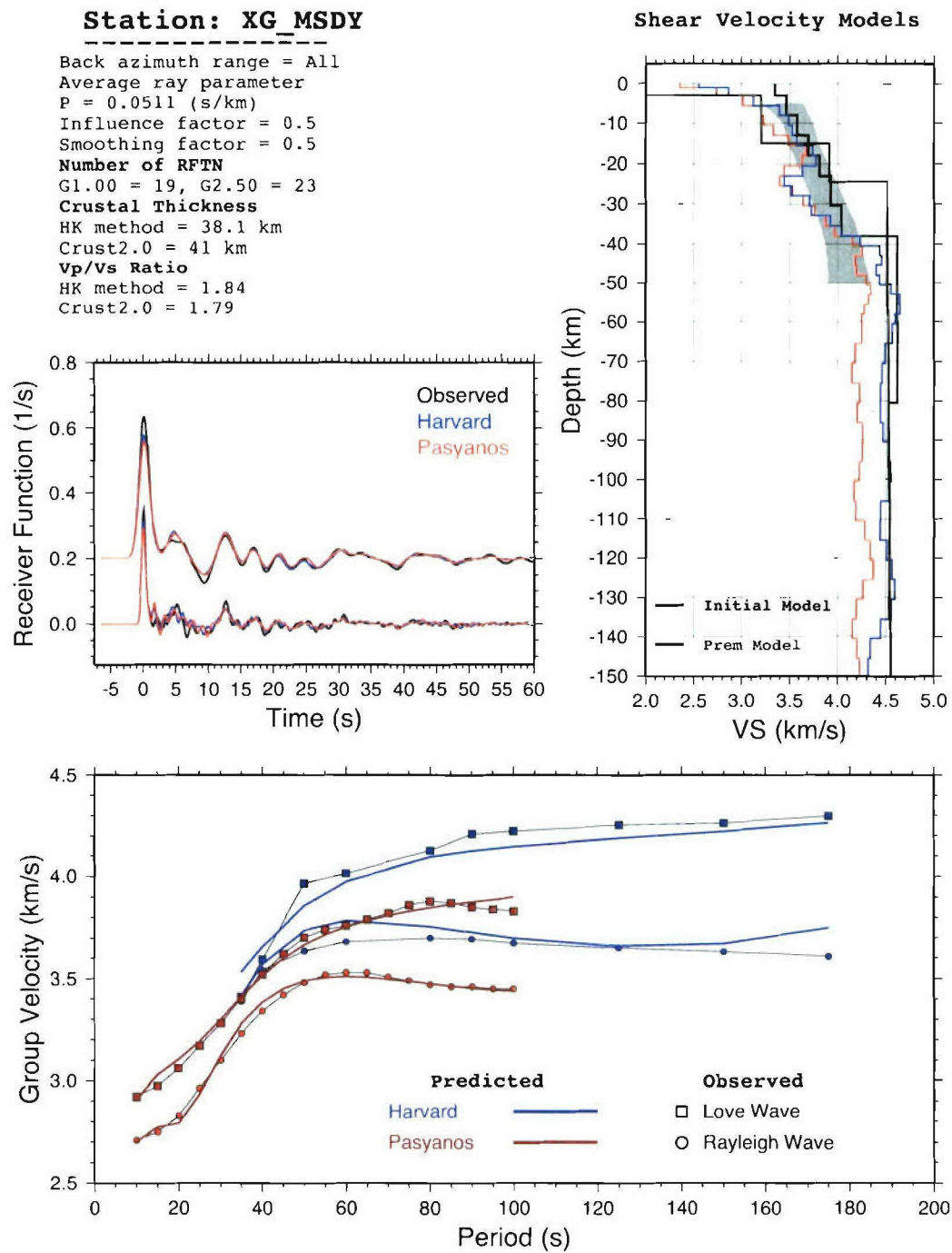


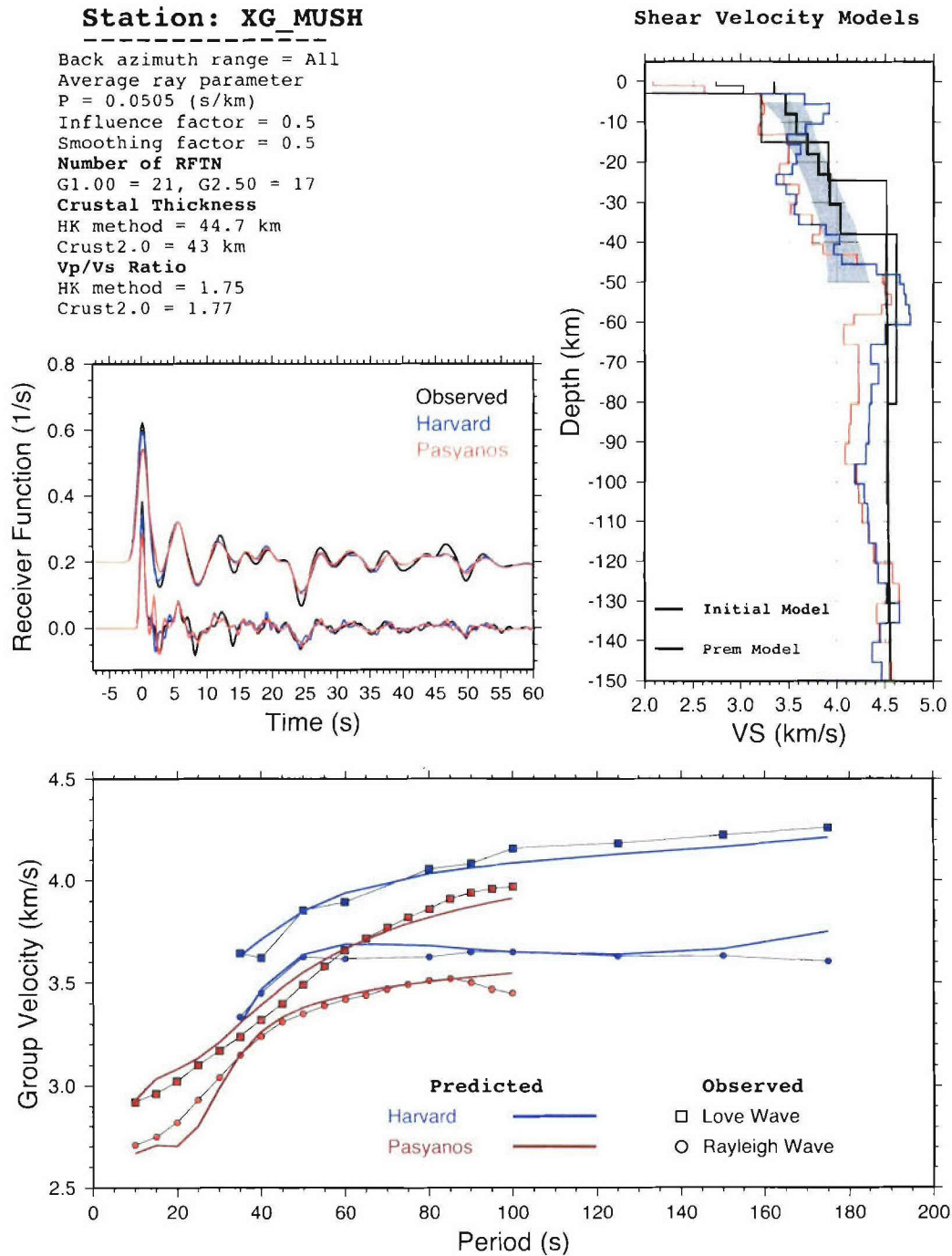


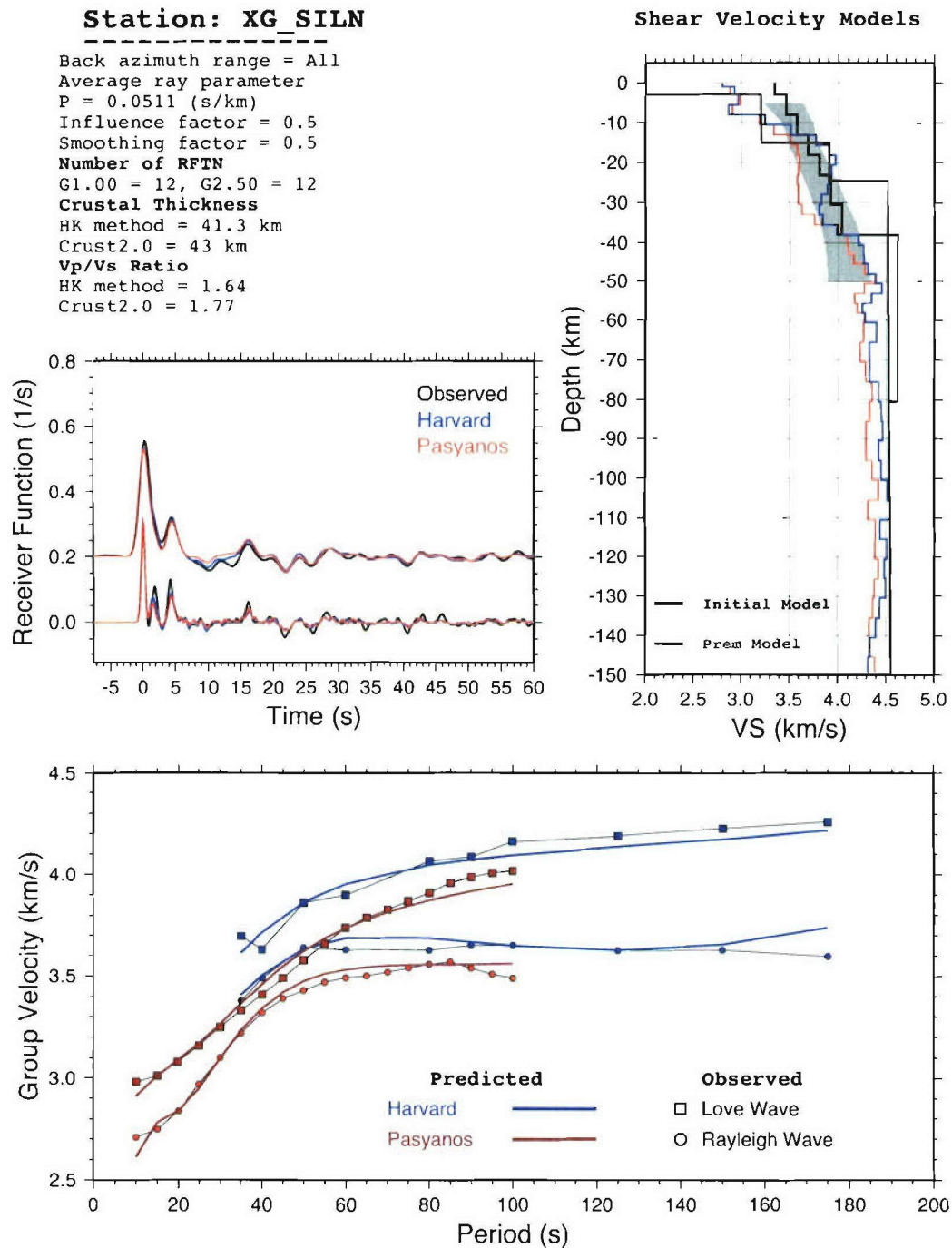


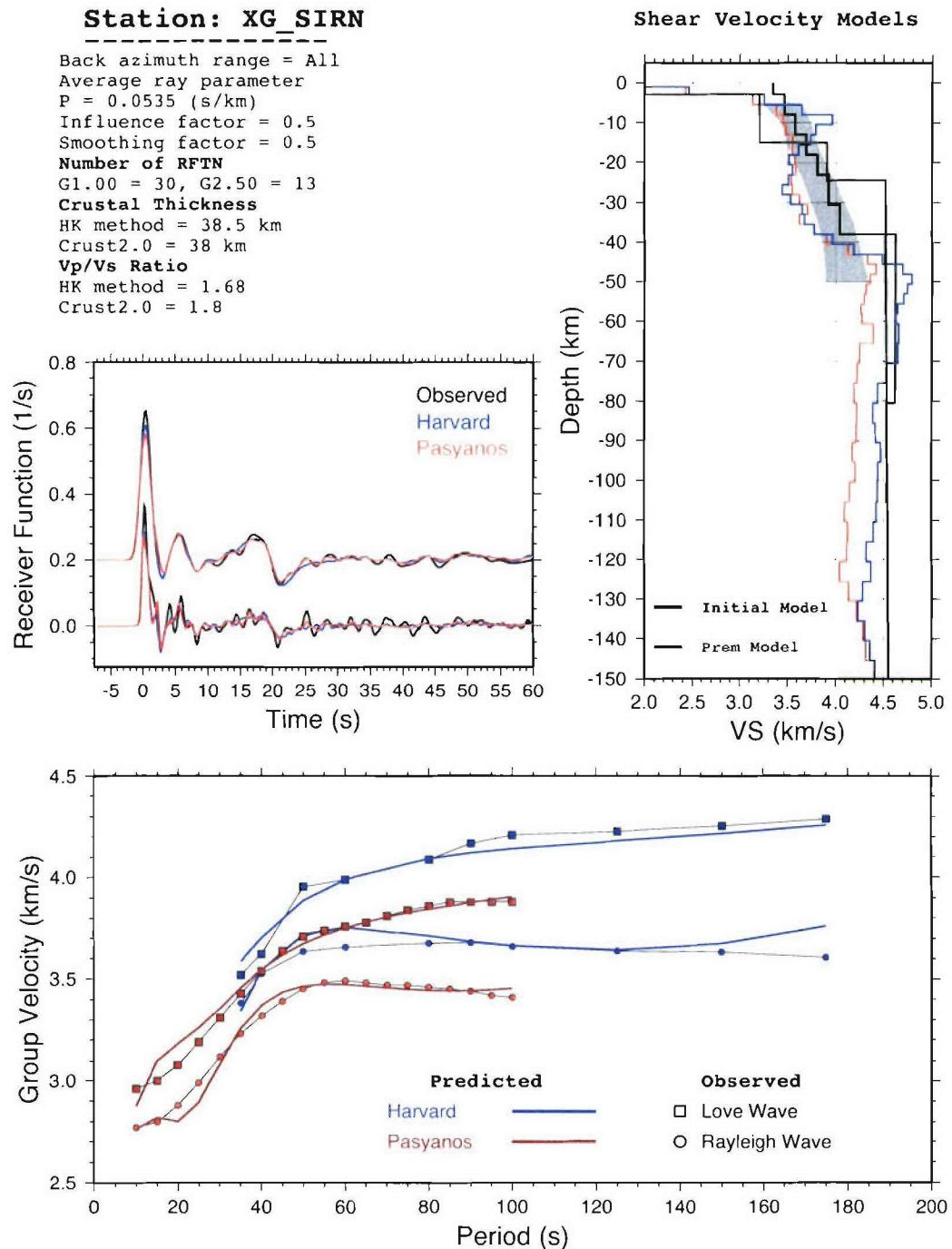


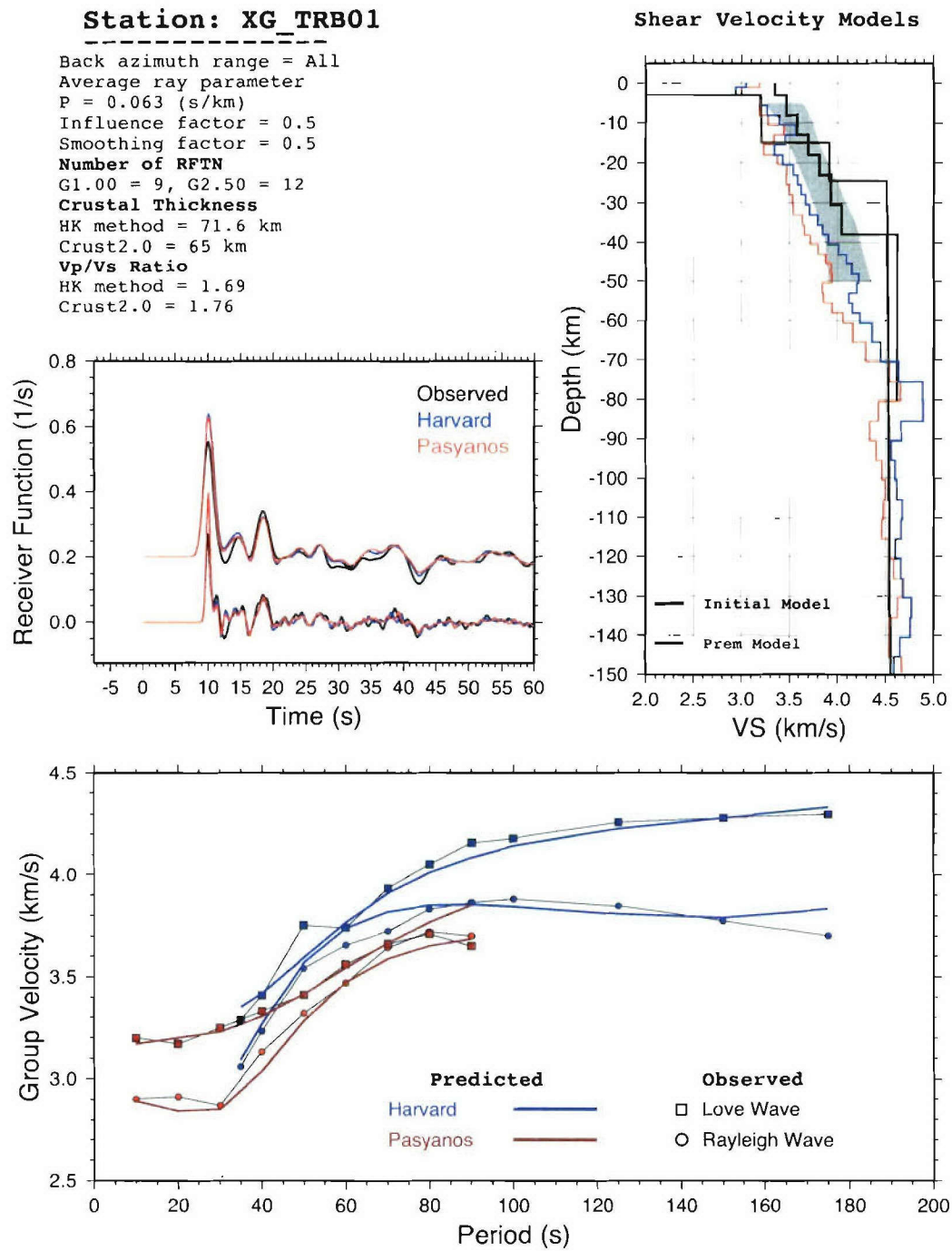


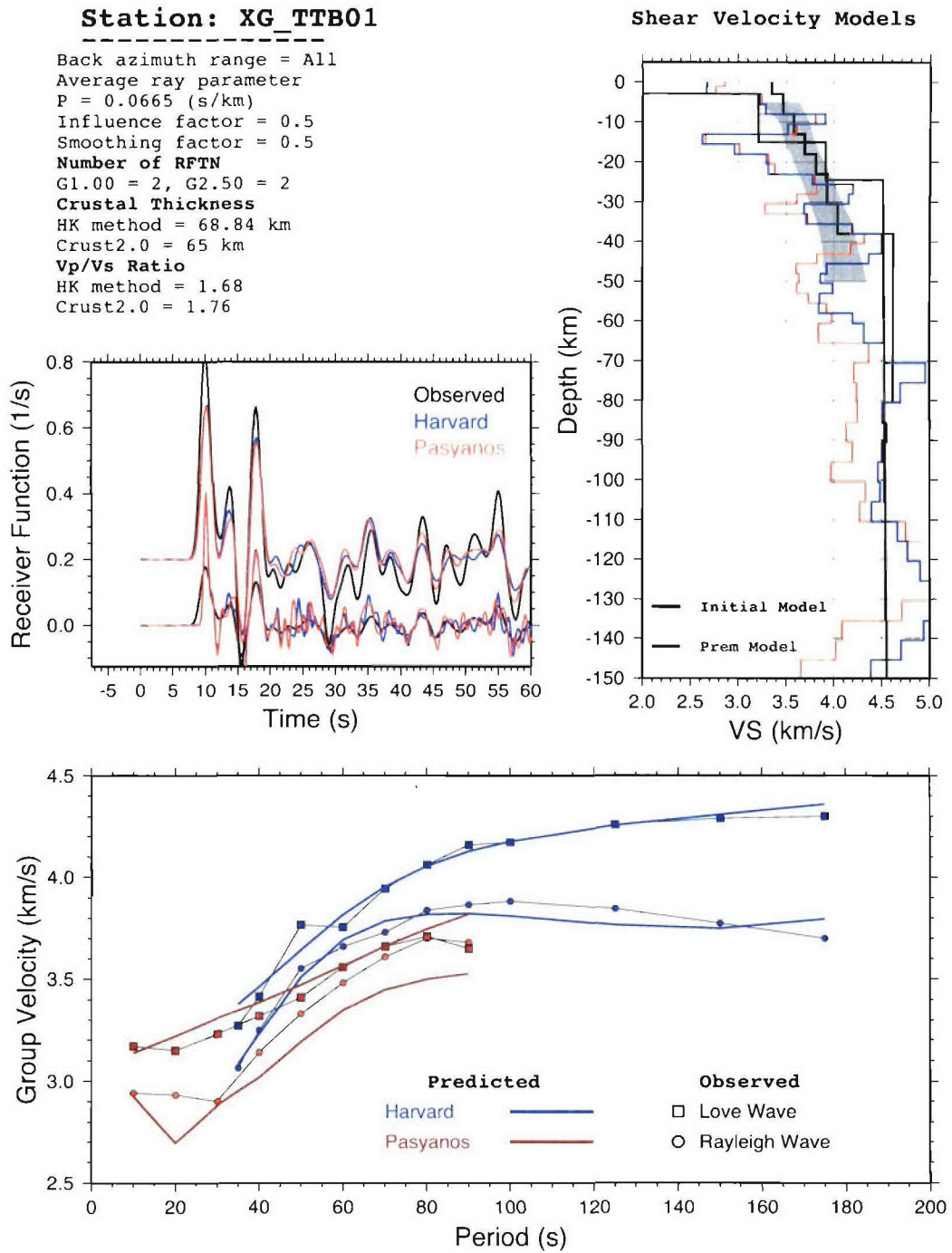


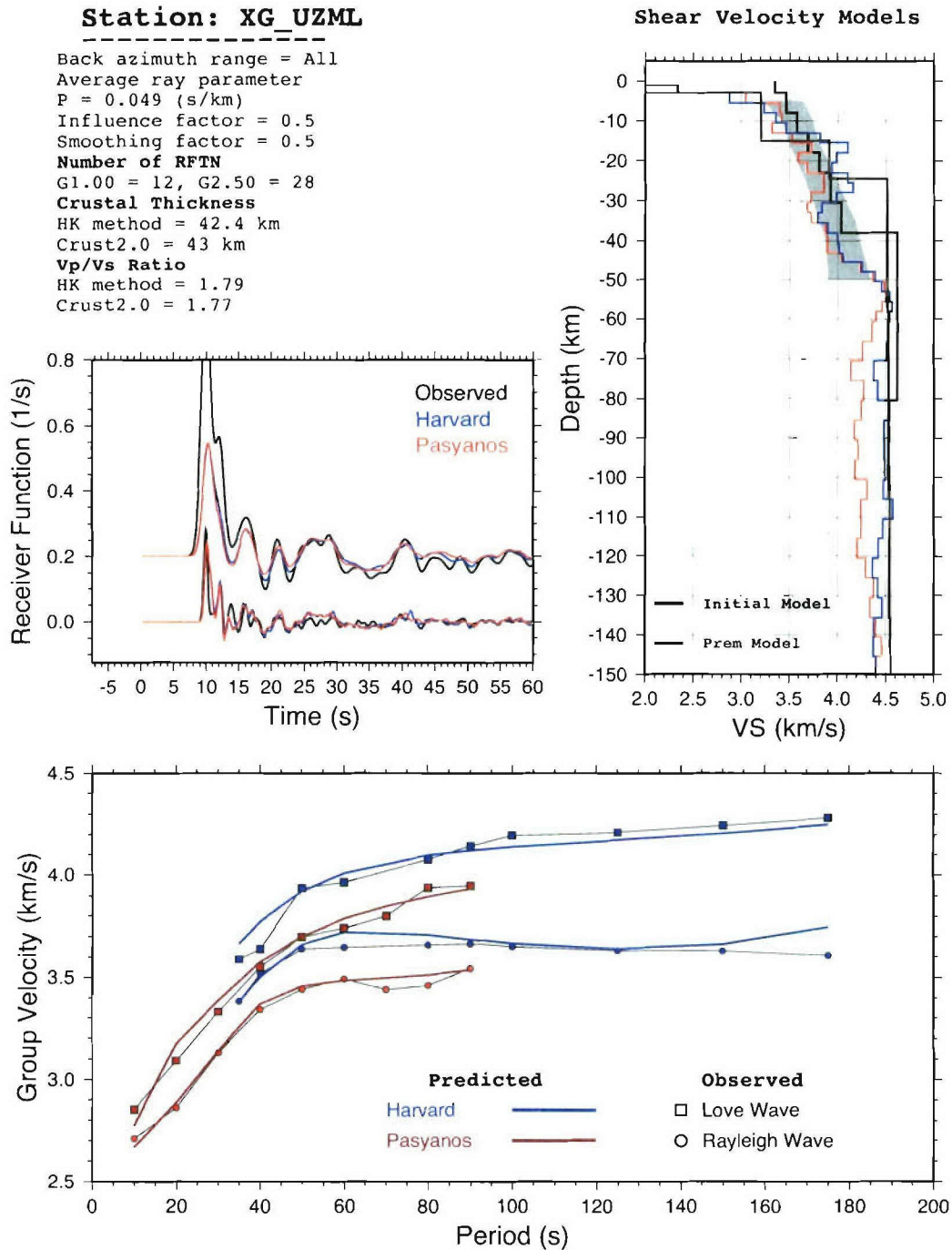


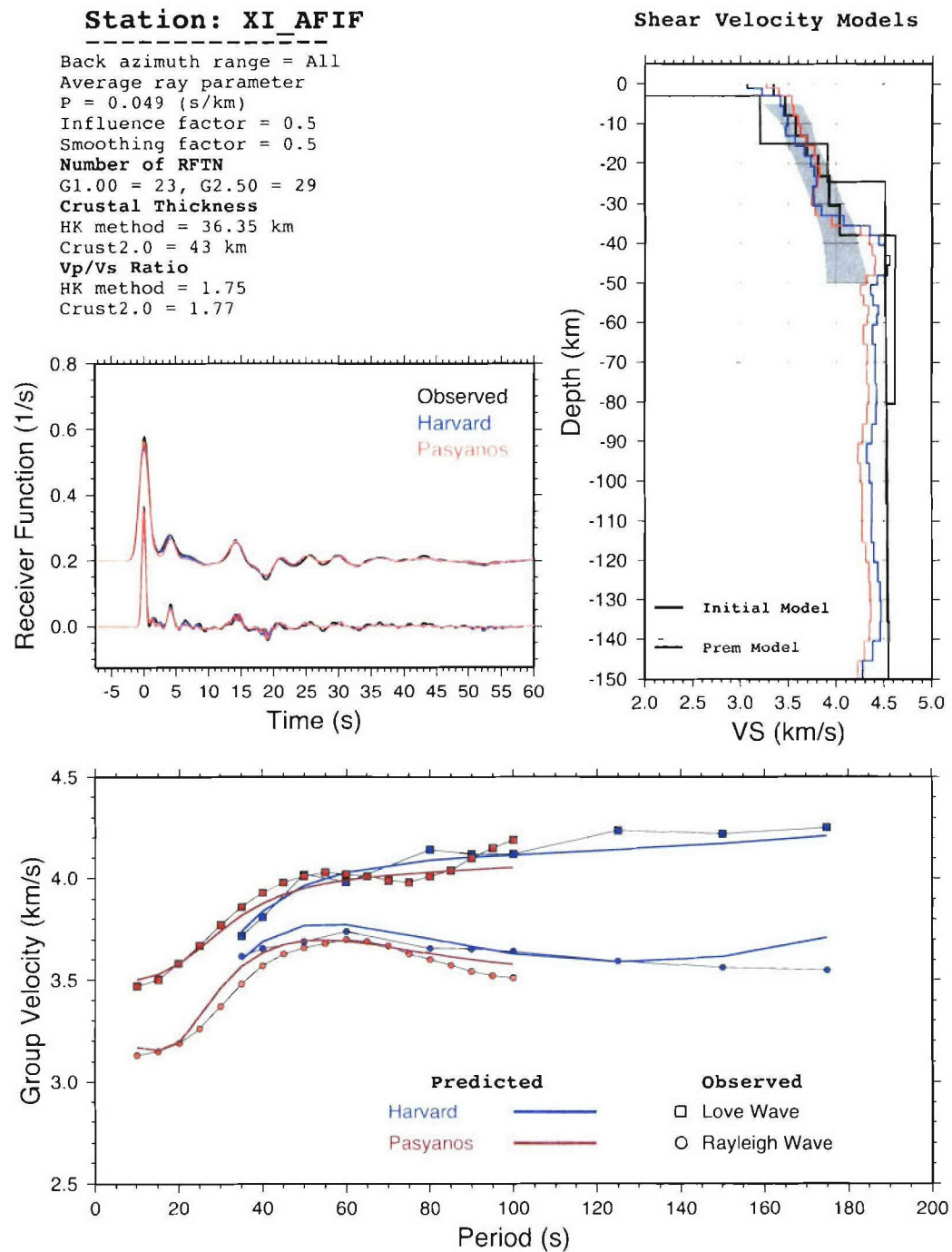


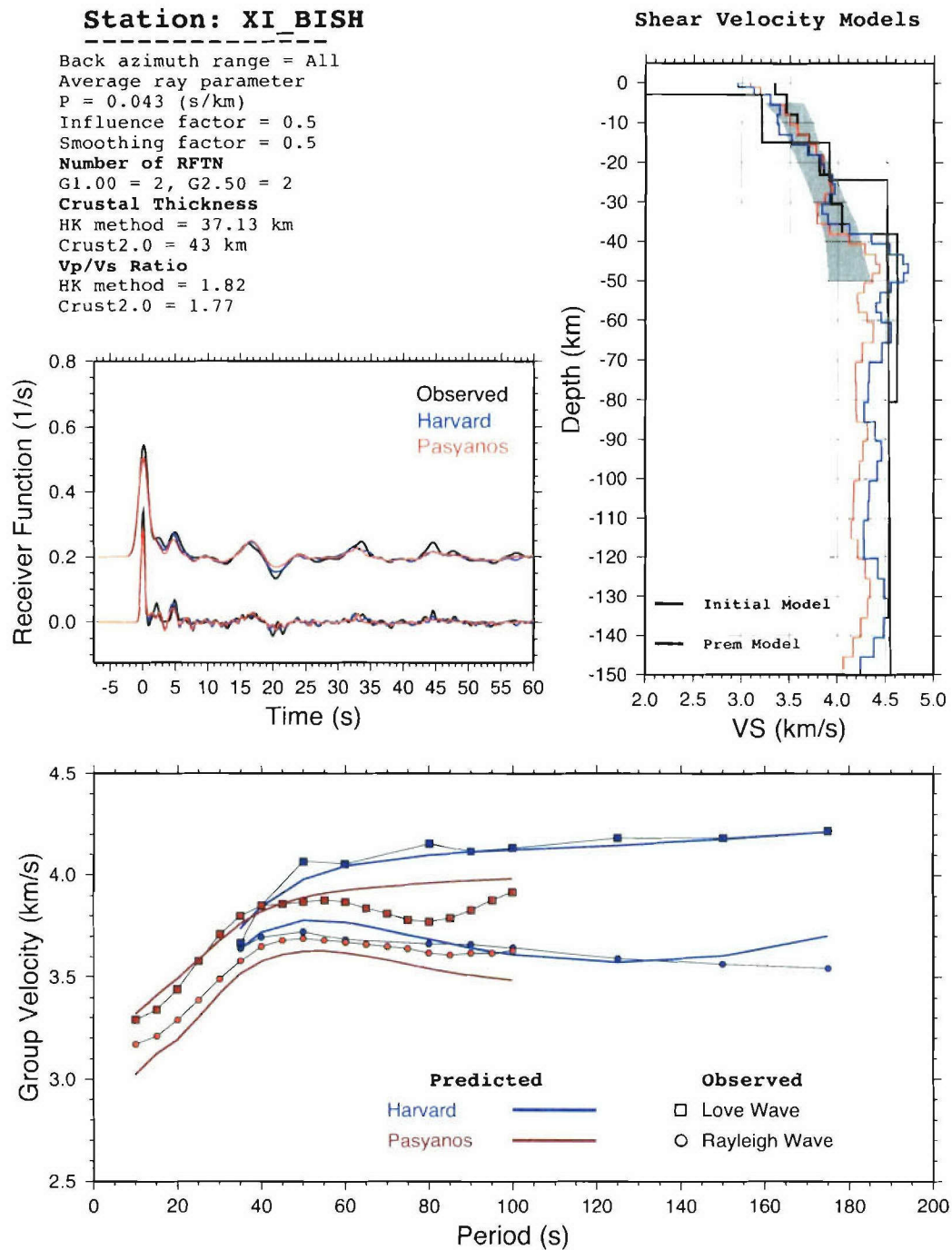


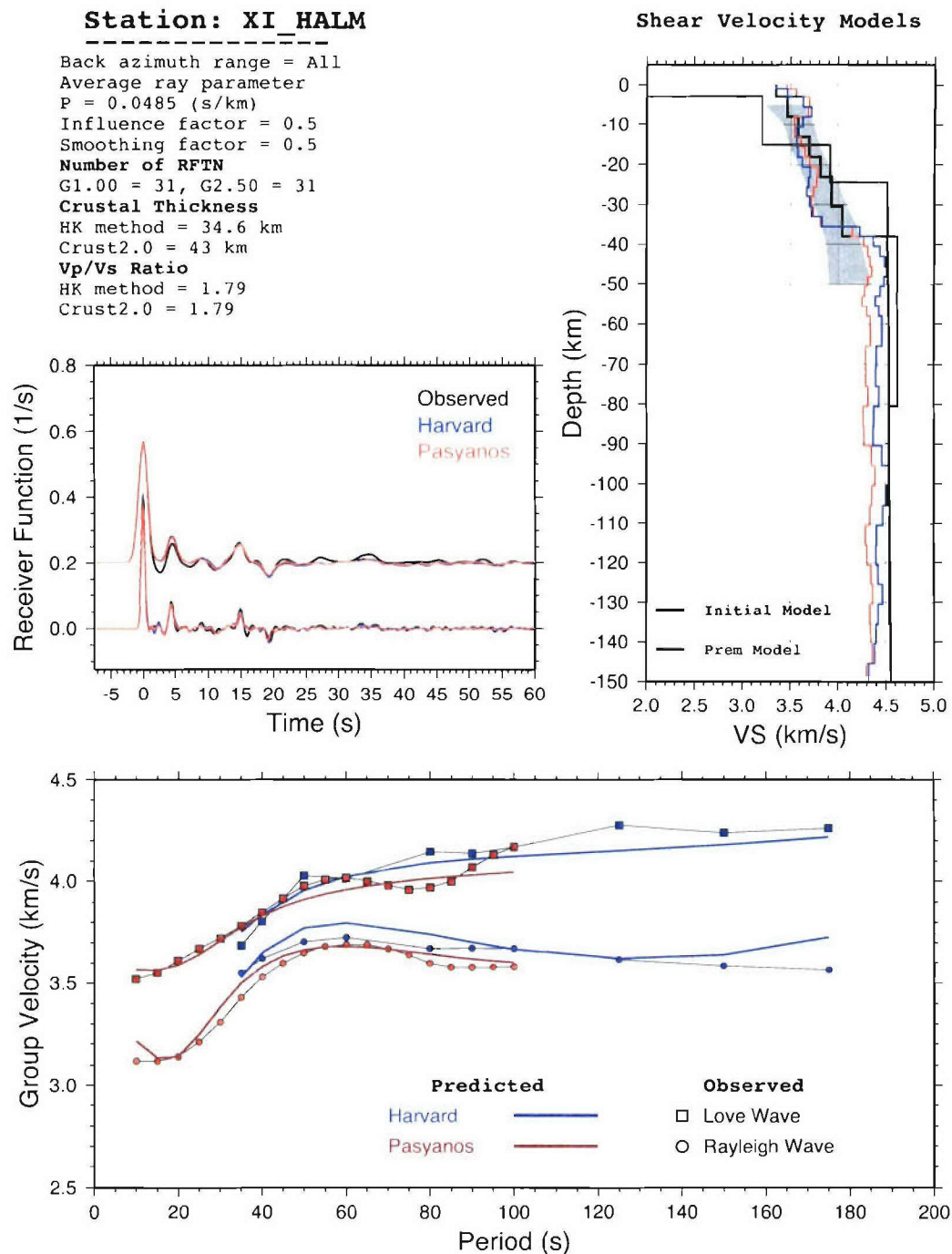


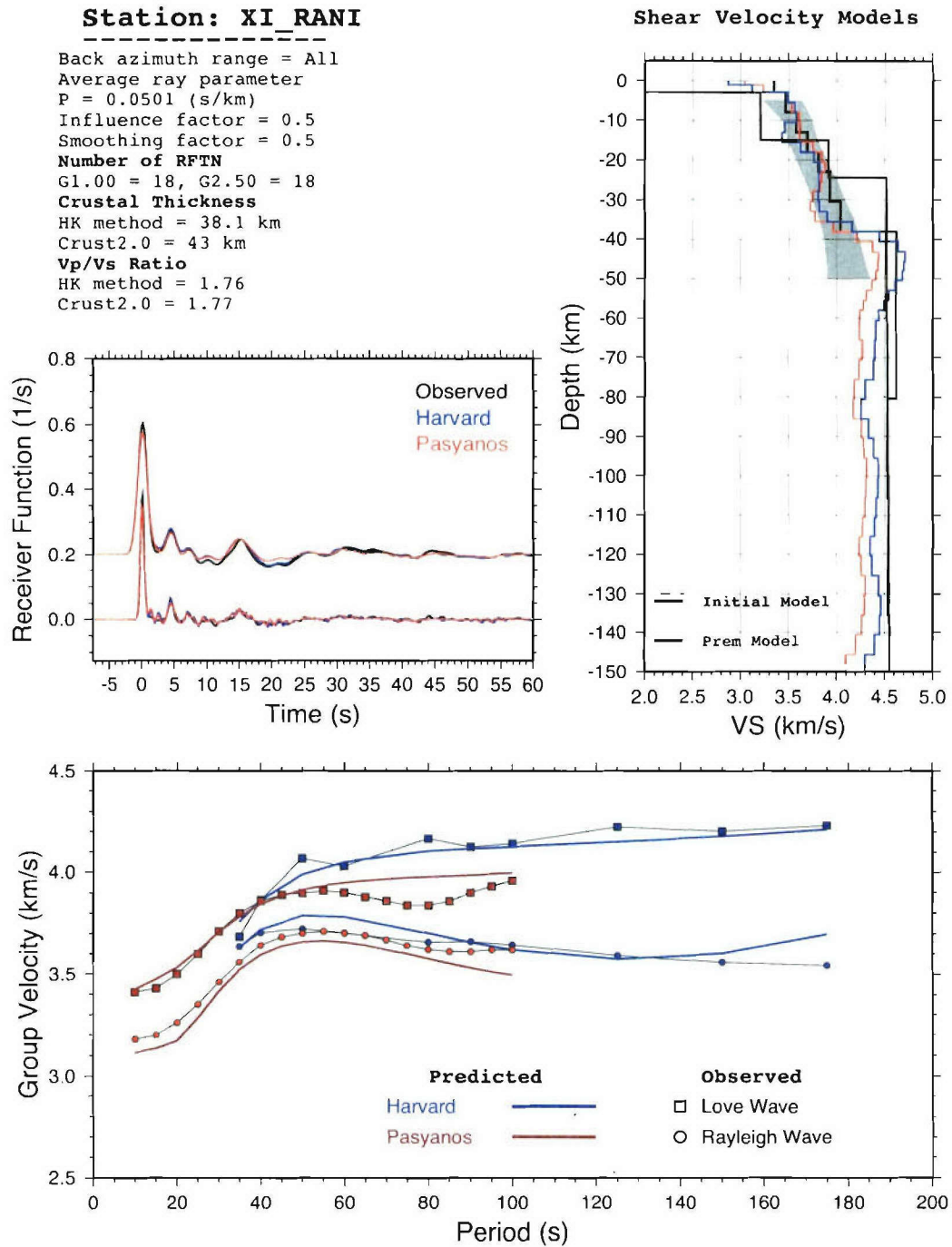


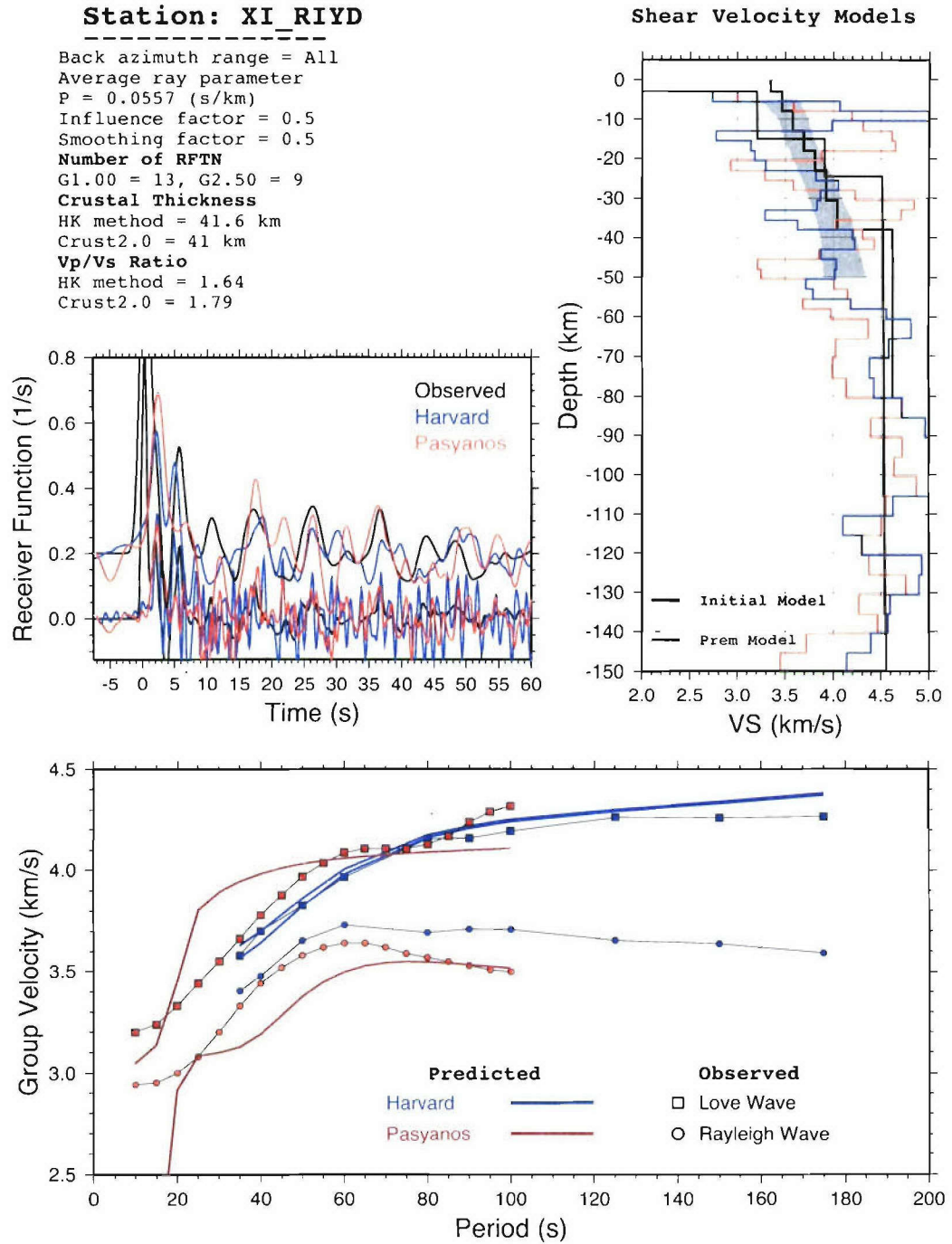


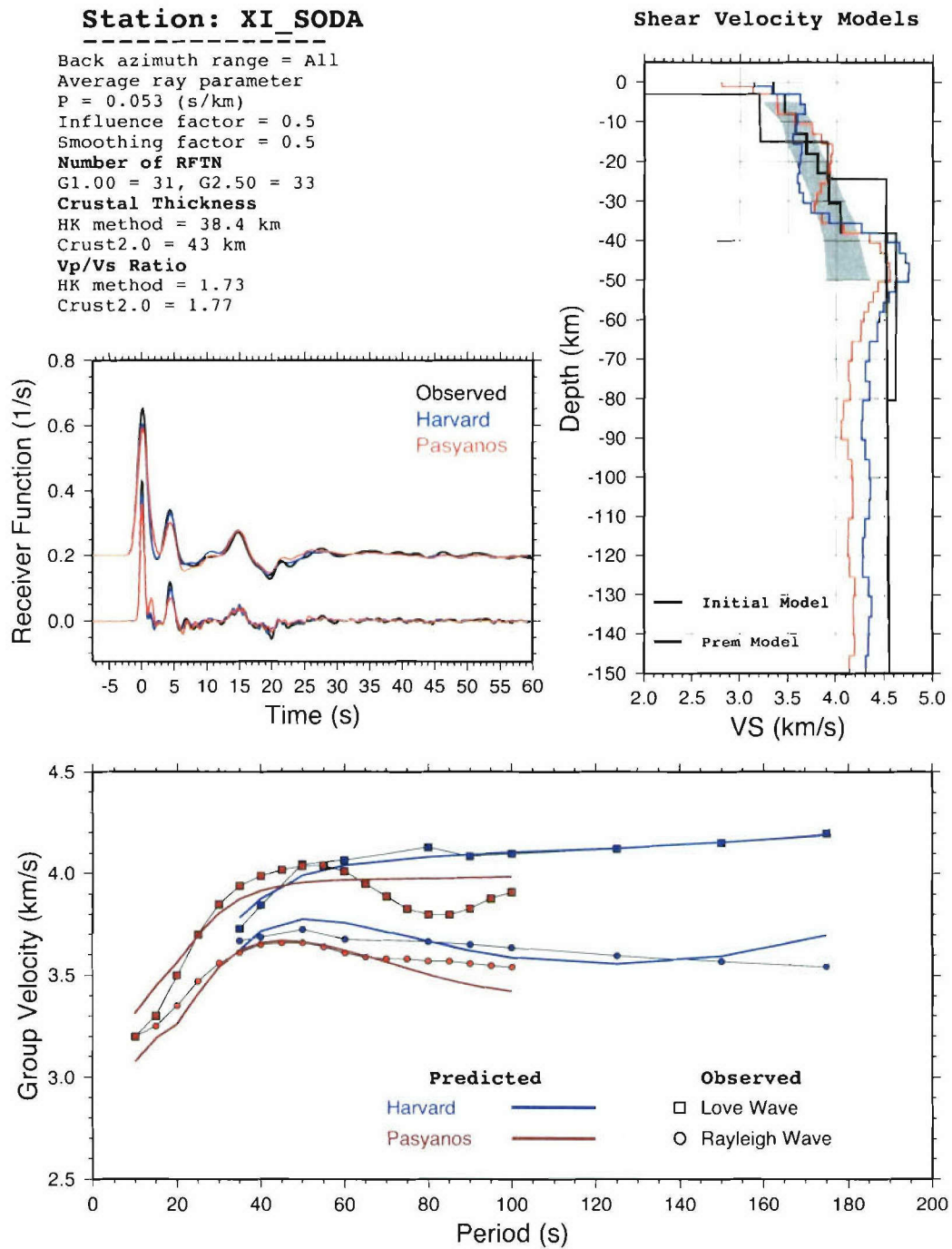


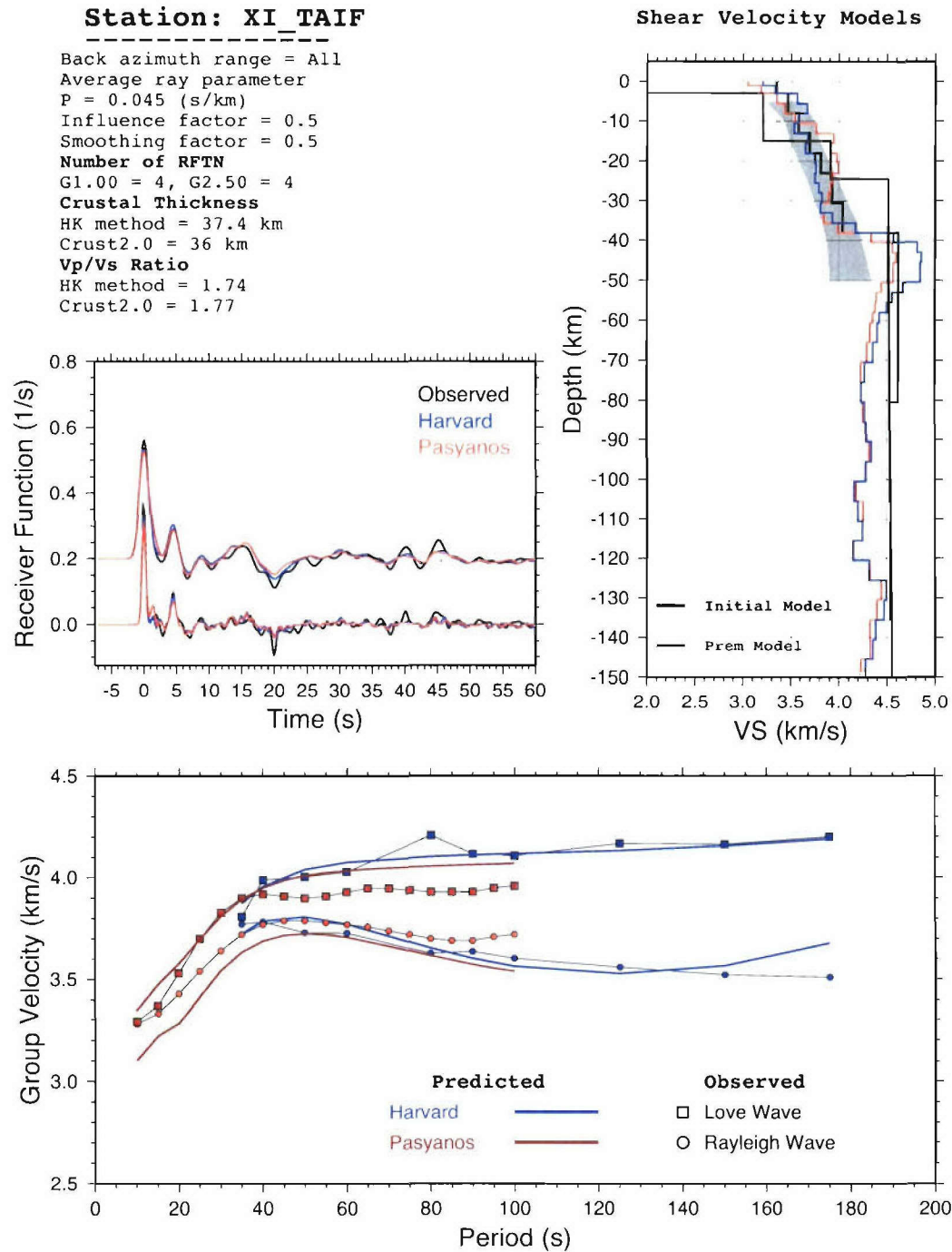


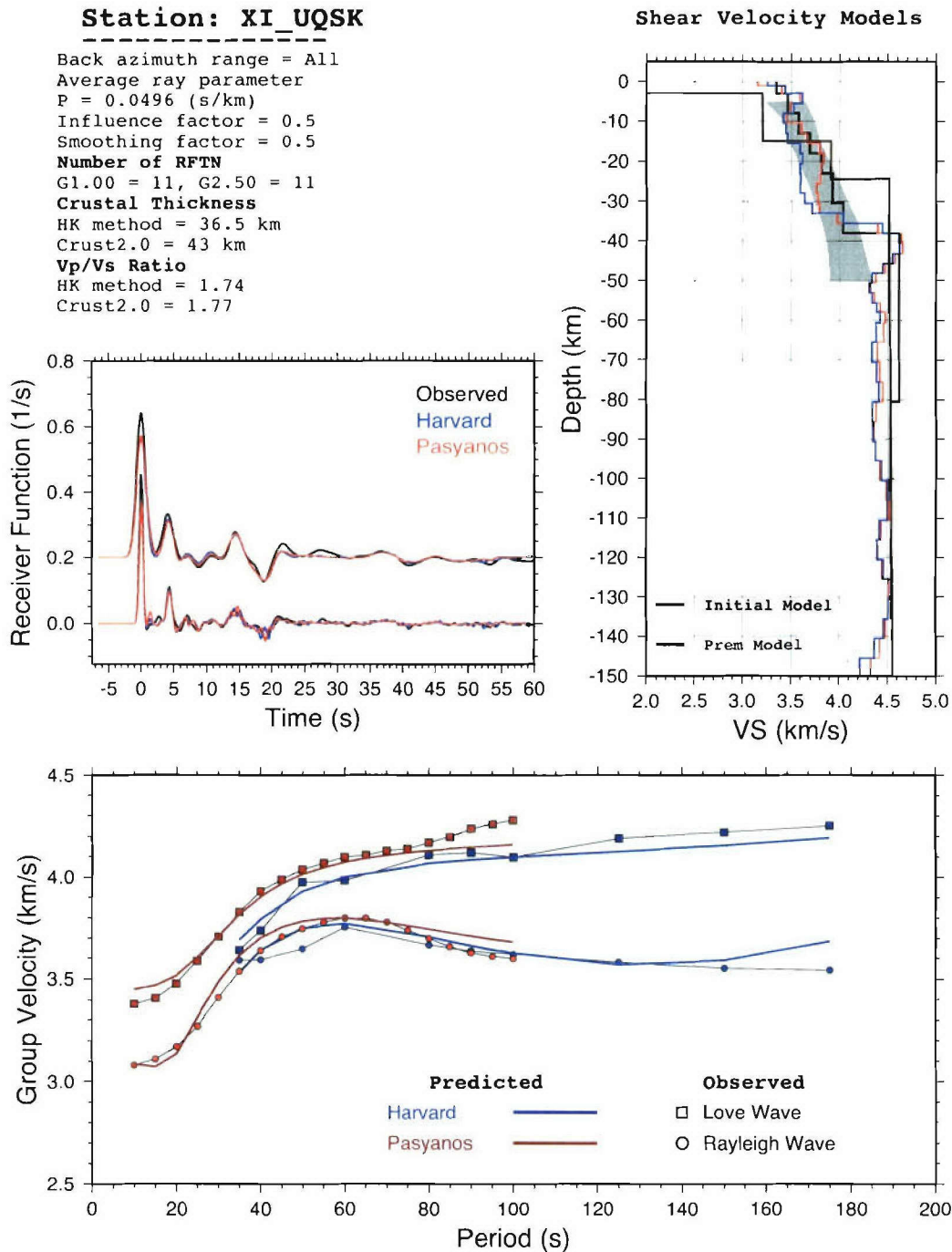


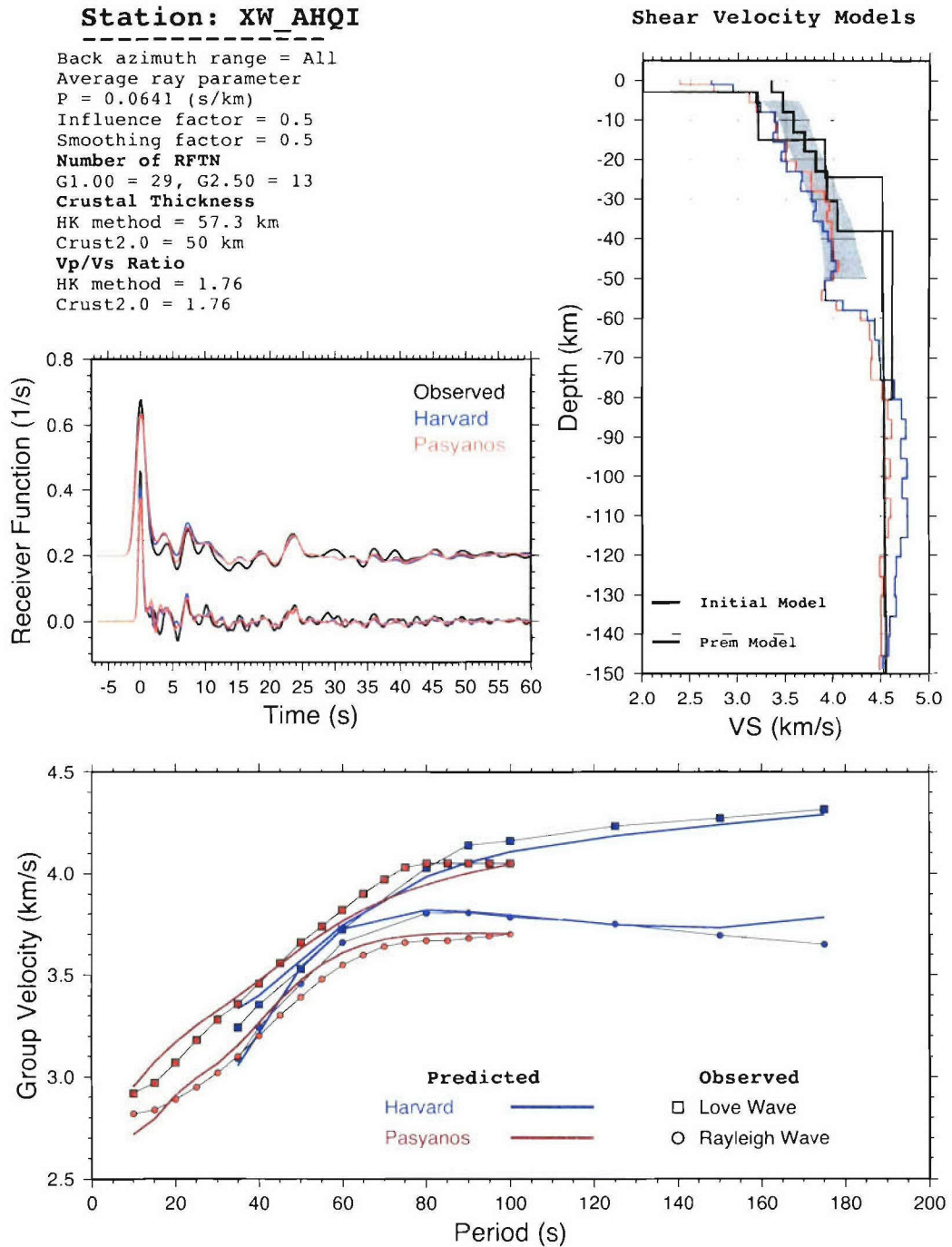












Bibliography

- [1] Ammon, C. J., G. E. Randall and G. Zandt, On the non-uniqueness of receiver function inversions, *J. Geophys. Res.*, 95, 15303-15318, 1990.
- [2] Ammon, C. J., The isolation of receiver effects from teleseismic P waveforms, *Bull. Seism. Soc. Am.*, 81, 2504-2510, 1991.
- [3] Ammon, C. J., and G. Zandt, The receiver structure beneath the southern Mojave Block, *Bull. Seism. Soc. Am.*, 83, 737-755, 1993.
- [4] Bassin, C., Laske, G., and G. Masters (2000), The current limits of resolution for Surface Wave Tomography in North America, *EOS Trans AGU*, 81, F897.
- [5] Braile, L., and G. R. Keller, Fine structure of the crust inferred from linear inversion of Rayleigh-wave dispersion, *Bull. Seism. Soc. Am.*, 65, 71-83, 1975.
- [6] Brune, J. N., Surface waves and crustal structure, in *The Earths Crust and Upper Mantle*, P. J. Hart Ed., American Geophysical Union, Washington, D.C., 230-242, 1969.
- [7] Cassidy, J.F., Numerical experiments in broadband receiver function analysis, *Bull. Seismol. Soc. Am.*, 82, 1453-1474, 1992.
- [8] Chevrot, S., and N. Girardin (2000), On the detection and identification of converted and reflected phases from receiver functions, *Geophys. J. Int.*, 141 (3), 801-808.
- [9] Christensen, N. I. (1995). Poissons ratio and crustal seismology, *J. Geophys. Res.*, 101, 3139-3156.
- [10] Christensen, N.I., and W.D. Mooney, Seismic velocity structure and the composition of the continental crust: A global view, *J. Geophys. Res.*, 100, 9761-9788, 1995.

- [11] Clitheroe, G., O. Gudmundsson, and B.L.N. Kennett (2000), Sedimentary and upper crustal structure of Australia from receiver functions, *Australian Journal of Earth Sciences*, 47 (2), 209-216.
- [12] Condie, K.C., *Plate Tectonics & Crustal Evolution*, Third Edition, 492 pp., Pergamon Press, Oxford, 1993.
- [13] Condie, K.C., *Plate tectonics and crustal evolution*, x, 282 pp., Butterworth Heinemann, Oxford, Boston, 1997.
- [14] Constable, S.C., R.L. Parker, and C.G. Constable, Occams inversion: A practical algorithm for generating smooth models from electromagnetic sounding data, *Geophysics*, 52, 289-300, 1987.
- [15] Crust 2.0, <http://mahi.ucsd.edu/Gabi/rem.dir/crust/crust2.html>.
- [16] Der, Z., R. Masse and M. Landisman, Effects of observational errors on the resolution of surface waves at intermediate distances, *J. Geophys. Res.*, 75, 3399-3409, 1970.
- [17] Diehl, T. M., Determining crustal Structure Beneath the Tibetan Plateau Using Receiver Functions, B. S. Thesis, Penn State University, University Park, PA, 2003.
- [18] Du, Z.J. and G.R. Foulger (1999), The crustal structure beneath the northwest fjords, Iceland, from receiver functions and surface waves, *Geophys. J. Int.*, 139, 419-432.
- [19] Durrheim, R.J., and W.D. Mooney, Archean and Proterozoic crustal evolution: Evidence from crustal seismology, *Geology*, 19, 606-609, 1991.
- [20] Durrheim, R.J., and W.D. Mooney, Evolution of the Precambrian Lithosphere: Seismological and geochemical constraints, *J. Geophys. Res.*, 99, 15,359-15,374, 1994.
- [21] Dziewonski, A.M., and D.L. Anderson (1981), Preliminary reference Earth model, *Phys. Earth Planet. Int.*, 25, 297-356.
- [22] Dziewonski, A.M., and D.L. Anderson, Preliminary reference Earth model, *Phys. Earth Planet. Int.*, 25, 297-356, 1981.
- [23] Haskell, N. A., The dispersion of surface waves on multilayered media, *Bull. Seism. Soc. Am.*, 43, 17-34, 1954.
- [24] Herrin, E., and T. Goforth, Phase-matched Filters: Application to the study of Rayleigh Waves, *Bull. Seism. Soc. Am.*, 67, 1259-1275, 1977.

- [25] Herrmann, R. B., Computer Programs in Seismology, 1995, Saint Louis University, St. Louis, MO, USA.
- [26] Jackson, D.D., Interpretation of inaccurate, insufficient and inconsistent data, *Geophys. J. R. Astron. Soc.*, 28, 97-109, 1972.
- [27] Julia, J., C. J. Ammon, R. B. Herrmann, and A. M. Correig, Joint Inversion of receiver function and surface-wave dispersion observations, *Geophys. J. Int.* 143, 99-112, 2000.
- [28] Julia, J., and J. Mejia (2004), Thickness and Vp/Vs ratio variations in the Iberian crust, *Geophys. J. Int.*, 156, 59-72.
- [29] Kikuchi, M., and H. Kanamori, Inversion of complex body waves (1982), *Bull. Seism. Soc. Am.*, 72, 491-506, 1982.
- [30] Kim, W. Y., L. Gao, and P. Richards, (1993) Crust and upper mantle seismic velocity structure beneath Borovoye Observatory, northern Kazakhstan, *EOS, Trans., AGU*, 74, Suppl., 433.
- [31] Kim, W. Y., and G. Ekstrom, (1996) Instrument responses of digital seismographs at Borovoye, Kazakhstan, by inversion of transient calibration pulses, *Bull. Seism. Soc. Am.*, 86, 191-203.
- [32] Kind, R., J. Yuan, J. Saul, D. Nelson, S.V. Sobolev, J. Mechie, W. Zhao, G. Kosarev, J. Ni, U. Achauer, and M. Jiang, Seismic Images of Crust and Upper Mantle Beneath Tibet: Evidence for Eurasian Plate Subduction, *Science*, 298, 1219-1221, 2002.
- [33] Langston, C. A., Structure under Mount Rainier, Washington, inferred from teleseismic body waves, *J. Geophys. Res.*, 84, 4749-4762, 1979.
- [34] Larson, E. W. F. and G. Ekstrom (2001), Global Models of Group Velocity, *Pure and Applied Geophys.*, 158, 1377-1399.
- [35] Last, R. J., A. A. Nyblade, C. A. Langston and T. J. Owens, Crustal structure of the East African Plateau from receiver functions and Rayleigh wave phase velocities, *J. Geophys. Res.*, 102, 24,469-24,483, 1997.
- [36] Lee, K., and S. G. Song, Crustal structure of the Korean peninsula by travel time inversion of local earthquakes, *Bull. Seis. Soc. Am.*, submitted, 2001.
- [37] Levin, V., and J. Park (1997), Crustal anisotropy in the Ural Mountains from teleseismic receiver functions, *Geophysical Research Letters*, 24 (11), 1283-1286.

- [38] Ligorra, J.P. (2000), An Investigation of the Crust-Mantle Transition Beneath North America and the Bulk Composition of the North American Crust, Ph.D. Thesis, Saint Louis University, 261 pages.
- [39] Ligorra, J.P. and C. J. Ammon, Iterative deconvolution and receiver function estimation, 89, 1395-1400, 1999.
- [40] McLennan, S.M., Continental Crust, in Encyclopedia of Earth System Science, pp. 581-592, Academic Press, Inc., 1992.
- [41] Mejia, J. (2001), Lithospheric structure beneath the Tibetan Plateau using simultaneous inversion of surface wave dispersion and receiver function, Ph.D. thesis, St. Louis University.
- [42] Mokhtar, T. A., C. J. Ammon, R. B. Herrmann (2001), and H. A. A. Ghalib, Lithospheric structure beneath Arabia, Pure and Applied Geophys, 158, 1445-1474.
- [43] Mokhtar, T. A., C. J. Ammon, R. B. Herrmann, and H. A. A. Ghalib, Lithospheric structure beneath Arabia, Pure and Appl. Geophys., in press, 2001.
- [44] Mokhtar, T. A., R. B. Herrmann, and D. R. Russell (1988), Seismic velocity and Q model for the shallow structure of the Arabian shield from short-period Rayleigh waves, Geophysics, 53, 1379-1387.
- [45] Mokhtar, T. A., R. B. Herrmann, and D. R. Russell, Seismic velocity and Q model for the shallow structure of the Arabian shield from short-period Rayleigh waves, Geophysics, 53, 1379-1387, 1988.
- [46] Mooney, W. D., M. E. Gettings, H. R. Blank, and J. H. Healy (1985). Saudi Arabian seismic refraction profile: a travel time interpretation and upper mantle structure, Tectonophysics 111, 173-246.
- [47] Myers, S.C., and S.L. Beck (1994), Evidence for a local crustal root beneath the Santa Catalina metamorphic core complex, Arizona, Geology, 22, 223-226.
- [48] Nelson, K.D., A unified view of craton evolution motivated by recent deep seismic reflection and refraction results, Geophys. J. Int., 105, 25-35, 1991.
- [49] Owens, T. J., G. Zandt and S. R. Taylor, Seismic evidence for an ancient rift beneath the Cumberland Plateau, Tennessee: A detailed analysis of broadband teleseismic P waveforms, J. Geophys. Res., 89, 7783-7795, 1984.

- [50] Ozalaybey, S., M. K. Savage, A. F. Sheehan, J. N. Louie and J. N. Brune, Shear-wave velocity structure in the northern Basin and Range Province from the combined analysis of receiver functions and surface waves, *Bull. Seism. Soc. Am.*, 87, 183-199, 1997.
- [51] Park, J., and V. Levin (2000), Receiver functions from multiple-taper spectral correlation estimates, *Bull. Seismol. Soc. Am.*, 90 (6), 1507-1520.
- [52] Pasyanos, M. E., Predicting Geophysical Measurements: Testing a combined empirical and model-based approach using surface waves, *Bull. Seism. Soc. Am.*, 90, 790-796, 2000.
- [53] Pasyanos, M. E., and W. R. Walter, A Surface Wave Dispersion Study of the Middle East and North Africa for Monitoring the Comprehensive Nuclear-Test-Ban Treaty, *Pure Appl. Geophys.*, in press, 2001.
- [54] Pasyanos, M.E. (2002), A Variable-resolution Surface Wave Dispersion Study of Western Eurasia and North Africa, submitted to *Journal of Geophysical Research*.
- [55] Pasyanos, M.E., W.R. Walter, and S.E. Hazler (2001), A Surface wave dispersion study of the Middle East and North Africa for Monitoring the Comprehensive Nuclear-Test-Ban Treaty, *Pure and Applied Geophys.*, 158, 1445-1474.
- [56] Pasyanos, M.E., and W.R. Walter, Crust and upper-mantle structure of North Africa, Europe and the Middle East from inversion of surface waves, *Geophys. J. Int.*, 149, 463-481, 2002.
- [57] Phillips, W. S., G. E. Randall, and S. R. Taylor (1998). Path corrections using interpolated amplitude residuals: an example from central China, *Geophys. Res. Lett.* 25, 2729-2732.
- [58] Phillips, W. Scott. Empirical path corrections of regional-phase amplitudes, *Bull. Seism. Soc. Am.* 89, 384-393, 1999.
- [59] Phinney, R. A., Structure of the Earth's crust from spectral behavior of long-period body waves, *J. Geophys. Res.*, 69, 2997-3017, 1964.
- [60] Randall, G. E., Efficient calculation of differential seismograms for lithospheric receiver functions, *Geophys. J. Int.*, 99, 469-481, 1989.
- [61] Richards, P., K. Won-Young, and G. Ekstrm (1992), Borovoye Geophysical Observatory, Kazakhstan, *EOS Trans AGU*, 73, 201-206.

- [62] Ritzwoller, M. H. and A. L. Levshin, Eurasian surface wave tomography: Group velocities, *J. Geophys. Res.*, 103, 1839-1878, 1998.
- [63] Rodgers, A. J., W. R. Walter, C. A. Schultz, S. C. Myers and Thorne Lay (1999) A comparison of methodologies for representing path effects on regional P/S discriminants, *Bull. Seism. Soc. Am.* 89, 394-408.
- [64] Rodi, W. L., P. Glover, T. M. C. Li and S. S. Alexander, A fast, accurate method for computing group-velocity partial derivatives for Rayleigh and Love modes, *Bull. Seism. Soc. Am.*, 65, 1105-1114, 1975.
- [65] Rudnick, R.L., Xenoliths - samples of the lower continental crust, in *Continental Lower Crust*, edited by D.M. Fountain, R. Arculus, and R. Kay, pp. 269-308, Elsevier, Amsterdam, 1992.
- [66] Ryberg, T., and M. Weber (2000), Receiver function arrays; a reflection seismic approach, *Geophys. J. Int.*, 141 (1), 1-11.
- [67] Sandvol, E., D. Seber, A. Calvert, M. Barazangi (1998), Grid search modeling of receiver functions: Implications for crustal structure in the Middle East and North Africa, *J. Geophys. Res.*, 103, 26,899-26,917.
- [68] Sandvol, E., D. Seber, A. Calvert, M. Barazangi, Grid search modeling of receiver functions: Implications for crustal structure in the Middle East and North Africa, *J. Geophys. Res.*, 103, 26,899-26,917, 1998.
- [69] Savage, M.K. (1998), Lower crustal anisotropy or dipping boundaries? Effects on receiver functions and a case study in New Zealand, *J. Geophys. Res.*, 103 (7), 15,069-15,087, 1998.
- [70] Schultz, C., S. Myers, J. Hipp and C. Young (1998). Nonstationary Bayesian kriging: application of spatial corrections to improve detection, location and identification, *Bull. Seism. Soc. Am.* 88, 1275-1288.
- [71] Stevens, J. L. and K. L. McLaughlin (2001), Optimization of Surface Wave Identification and Measurement, *Pure and Applied Geophys.*, 158, 1547-1582
- [72] Su, W., R. L. Woodward, and A. M. Dziewonski (1994), Degree 12 model of shear velocity heterogeneity in the mantle, *Nature*, 99, 6945-6980.
- [73] Su, W., R. L. Woodward, and A. M. Dziewonski, Degree 12 model of shear velocity heterogeneity in the mantle, 99, 6945-6980, 1994.
- [74] Walter, W. R., M. E. Pasyanos, J. Bhattacharyya, and J. O'Boyle, MENA 1.1 -An Updated Geophysical Regionalization of the Middle East and North Africa, LLNL Technical Report, UCRL-ID-138079, 2000.

- [75] Weeraratne, D.S., D.W. Forsyth, K.M. Fischer, and A.A. Nyblade, Evidence for an upper mantle plume beneath the Tanzanian craton from Rayleigh wave tomography, *J. Geophys. Res.*, 2002JB002273R, 2003.
- [76] Zandt, G., S.C. Myers, and T.C. Wallace (1995), Crust and mantle structure across the Basin and Range-Colorado Plateau boundary at 37 degrees N latitude and implications for Cenozoic extensional mechanism, *J. Geophys. Res.*, 100 (6), 10,529-10,548.
- [77] Zandt, G., and C. J. Ammon (1995), Continental Crustal composition constrained by measurements of crustal Poisson's ratio, *Nature*, 374, 152-154.
- [78] Zhu, L., and H. Kanamori (2000), Moho depth variation in Southern California from teleseismic receiver functions, *J. Geophys. Res.*, 105 (2), 2969-2980.